NOVEL ORGANIC CHROMOPHORES FOR APPLICATIONS IN PHOTOVOLTAICS AND PHOTODYNAMIC THERAPY

By

Matthew Bates

A DISSERTATION

Submitted to
Michigan State University
in partial fulfillment of the requirements
for the degree of

Chemical Engineering – Doctor of Philosophy

2022

ABSTRACT

Organic semiconducting chromophores have been used for a wide variety of electronic, optoelectronic, and biological applications. They offer solutions to global problems including the need for renewable energy and new and improved medical therapeutics and diagnostics. In optoelectronics, organic semiconductors can function as light harvesting materials in traditional photovoltaics (PVs) and transparent photovoltaics (TPVs). TPVs utilize organic semiconductors to absorb near-infrared and ultra-violet light, allowing visible light to pass through the device, and can be integrated with surfaces otherwise inaccessible for traditional PVs. In medical therapeutics and diagnostics, organic semiconducting chromophores function as active agents in light-based treatments such as photodynamic therapy, or as highly fluorescent imaging agents to aid in the detection of illnesses.

The first portion of this thesis details three projects focused on PVs. To begin, four new organic salt semiconductors, comprised of an organic chromophore and a counterion, are demonstrated in PVs. Device data is analyzed with experimental and computational methods to reveal a strong correlation between the total charge character on the chromophore and the carrier mobility in bulk films. In the second project, high efficiency TPVs are fabricated with a selectively near infrared absorbing polymer and non-fullerene acceptor via layer-by-layer deposition. TPVs achieved a power conversion efficiency of 8.8%, average visible transmittance of 40.9%, and light utilization efficiency of 3.6%, among the highest reported. Using the layer-by-layer approach, the impact of the full range of polymer thickness on electronic and optical device performance is evaluated. The last PV project presents the first demonstration of graphene nanoribbons as an active material in PVs with a detailed analysis of underlying exciton diffusion and charge collection mechanisms.

The second portion of this thesis demonstrates the translation of a series of fluorescent organic salts with various counterions developed as PV materials in the first half of the thesis into a platform for photodynamic therapy and fluorescent imaging. Organic salts are formulated into nanoparticles and found to selectively accumulate in tumor cells, where the counterion tunes the frontier energy levels and the toxicity of the salt. Organic chromophores paired with small, hard counterions are found to be cytotoxic while bulky and often halogenated counterions cause the salts to be nontoxic at high dosages, ideal agents for bioimaging. Between the two extremes are several organic salts that are selectively phototoxic and are excellent candidates for photodynamic therapy. Organic salt nanoparticles are characterized with a variety of spectroscopic techniques to understand the size and optical properties. Subsequently, organic salts are demonstrated as effective active agents for treating cancer via photodynamic therapy in a mouse model. Collectively, we demonstrate a vast range of processing, characterization, and applications for new organic semiconductors in two key fields that are united by their molecular chemistry.

ACKNOWLEDGEMENTS

I would like to begin by thanking my advisors, Dr. Richard Lunt and Dr. Sophia Lunt, for their consistent guidance and teaching throughout my PhD, and for their enthusiasm for our research. I would also like to thank the members of my PhD guidance committee, Dr. Carl Lira, Dr. Scott Calabrese-Barton, and Dr. Babak Borhan, for their helpful feedback and questions. The work entailed in this thesis would not have been possible without an awesome lab group. Starting with my first lab mentor, Peggy, thank you for your patience while training me, answering questions, and helping me figure stuff out as I was just getting started. Chris T., I learned a great deal watching how you handled the ups and downs of grad school and employed many of those lessons myself. Paddy, you had a huge impact on our group culture, and I really enjoyed working with you. Pei, your knowledge of our lab and its various intricacies was second to none and I had, perhaps not fun, but a good time taking apart half of the EvoVac with you. Dianyi and Lilli, you were outstanding role-models as postdocs for how a researcher should approach their work and I appreciate the time you both spent investing in the grad students. Alex, late night homework groups and cohort lunches with you and the guys was one of the best parts of my first couple years here. Nathan, I was impressed and thankful for the hard work you put in as an undergrad, and I hope the skills you picked up in lab techniques are proving useful to you. Isaac, you are an awesome friend, you and Chris H. helped me through a couple tough years while you were here. Lastly, for the folks who graduated before me, our tenured senior student Chenchen. Thank you for being the hardest worker in the group, even if it was at very odd hours, helping with just about everything, and for your dedication to scientific rigor. Thank you also for some of the best and deepest conversations I’ve had here while we were in lab, and for your willingness to share openly and vulnerably about all of the difficulties we ran into along the way.

For the current group members, Aungkan, I am thankful for your willingness to jump into our research. I hope you continue to find aspects of our work new and exciting, but also challenging in the best way. Chris H., I am super grateful for your friendship and willingness to hang out and talk about life and grad school. You have been a great resource for me and the group, and my PhD experience wouldn't have been the same without you.

Next, I'd like to acknowledge a lot of great people that I got to work with over the last few years. Deanna, I am very thankful for your hard work and sense of humor, even when things were really tough. Hyllana, I greatly appreciated your honesty and straightforwardness as a researcher and your willingness to ask questions and constantly learn. A big thank you to the following folks for their help, Austin Raithel from Dr. Hammond's group, Per Askaland and Mike Rich from the Composite Materials and Structures Center, Tony Schilmiller at the Mass Spectrometry and Metabolics Core, Ryan Malone and Dr. Wes Chalifoux at the University of Nevada, Reno, and Dr. Zhongrui Li at the Electron Microbeam Analysis Laboratory.

Two very important groups of friends during my time at MSU, my CHEMS cohort, Mr. Killian, Bubbles, Trey, Sami, Alex, and Sanket. You guys are awesome, we had a great time even when we were really having a bad time. My GradIV family, you were so important to me in every aspect of life.

I am of course grateful and thankful for my parents and their support, especially their patience when I've given the same answer for several years to questions about when I'll graduate and move back home. Lastly and most importantly, I need to thank my amazing wife and best friend, Caitlin, who has put up with so much over the last six years. From the highs and lows of experiments working or equipment breaking, to the constantly in-flux work schedule of a graduate student and the great adventure of moving across the country to live somewhere new. I love you, and am so excited for our next adventure. I’ll also even forgive you if you only read this far.

TABLE OF CONTENTS

LIST OF TABLES ix

LIST OF FIGURES x

LIST OF SYMBOLS AND ABBREVIATIONS xvi

Chapter 1 – Organic Photovoltaics 1
    1.1 Overview of organic semiconductors 1
    1.2 Introduction to organic photovoltaics 13
    1.3 Theoretical and experimental limits of organic photovoltaics 24
    1.4 Current OPV state of the art performance metrics 25
    1.5 Summary 26

Chapter 2 – Transparent Photovoltaics 28
    2.1 Introduction to transparent photovoltaics 28
    2.2 Optical and electronic evaluation of TPVs 28
    2.3 Categorization of transparent photovoltaics 32
    2.4 Limits for transparent photovoltaics 35
    2.5 Summary 36

Chapter 3 – Cyanine-based Organic Salt Photovoltaics Review 38
    3.1 Introduction 38
    3.2 Historical development of organic salt-based photovoltaics 40
    3.3 Weakly coordinating anions 49
    3.4 Role of the counterion in organic salt photovoltaics 50
    3.5 Ion mobility 53
    3.6 Exciton diffusion and charge carriers 55
    3.7 Organic salt transparent photovoltaics 61
    3.8 Stability of organic salt photovoltaic devices 63
    3.9 Conclusions 65

Chapter 4 – Experimental Techniques 66
    4.1 Synthesis 66
    4.2 Material characterization 70
    4.3 Device fabrication 77
    4.4 Device characterization 83
    4.5 Transfer matrix optical modeling and *EQE* fitting 88
    4.6 Fluorescent imaging 93

Chapter 5 – Charge Transfer in Organic Salt Photovoltaics 95
    5.1 Introduction 95
    5.2 Methods 97
    5.3 Results and discussion 101
    5.4 Conclusions 112

Chapter 6 – High Efficiency Transparent Photovoltaics 114

6.1 Introduction 114
6.2 Results 116
6.3 Discussion 128
6.4 Conclusions 136
6.5 Methods 136

Chapter 7 – Graphene Nanoribbon Photovoltaics 140
7.1 Introduction 140
7.2 Results 142
7.3 Discussion 154
7.4 Methods 155

Chapter 8 – Photodynamic Therapy and Fluorescent Imaging with Organic Salts 160
8.1 Introduction 160
8.2 Characterization of fluorescent organic salts 166
8.3 Tunable cellular toxicity 169
8.4 Mechanism of toxicity 171
8.5 Applications in imaging 176
8.6 Discussion 179
8.7 Experimental methods 180

Chapter 9 – *In Vivo* Photodynamic Therapy with Organic Salts 189
9.1 Introduction 189
9.2 Results 193
9.3 Discussion 209
9.4 Conclusions 211
9.5 Materials and methods 211

Chapter 10 - Future Directions for Research 219
10.1 Organic salt photovoltaics 219
10.2 Transparent photovoltaics 222
10.3 Graphene nanoribbons 225
10.4 Organic salts in photodynamic therapy and fluorescent imaging 227
10.5 Final conclusions 229

BIBLIOGRAPHY 230

Appendix – Photon balance checks for TPVs 248

LIST OF TABLES

Table 5.1. Organic salt photovoltaic device parameters. 104

Table 5.2. Characteristic parameters for anionic heptamethine based organic salts. 106

Table 6.1. *J-V* parameters for annealing temperature optimization. 117

Table 6.2. Solvent additive optimization device parameters. 118

Table 6.3. Dark *J-V* fit parameters for 1-chloronaphthalene and polymer thickness optimized devices. 120

Table 6.4. Polymer thickness optimization device parameters. 122

Table 6.5. *EQE* modeling fit parameters for polymer thickness dependent devices. 123

Table 6.6. PTB7-Th, Ag, and Alq_3 thickness dependent device optical parameters. 124

Table 6.7. Ag thickness dependent device parameters. 125

Table 6.8. Alq_3 thickness dependent device parameters. 126

Table 6.9. Optimized transparent photovoltaic device parameters. 128

Table 6.10. Impact of antireflection coating on optical performance. 130

Table 8.1. Zeta potential changes as a function of counterion pairing. 166

Table 8.2. Quantum yields for monomer CyX and Cy7X salts. 167

Table 8.3. CyX salt solubility in water and DMSO:H_2O mixtures. 167

Table 8.4. Toxicity of photoactive cyanine (Cy^+) is determined by counterion pairing............ 170

Table 8.5. Intracellular localization of CyX does not change with the counterion. 172

Table 9.1. Half maximal inhibitory concentrations (IC_{50}) of fluorescent organic salts with and without NIR irradiation in 6DT1 cells. 193

Table 9.2. 6DT1 gene expression values. 193

Table 9.3. Sigmoidal curve fitting values. 196

LIST OF FIGURES

Figure 1.1. Bandgaps of semiconductors, metals, and insulators. 2

Figure 1.2. Intrinsic and extrinsic semiconductors, and the formation of a p-n junction. 4

Figure 1.3. Hybridization of atomic orbitals. 6

Figure 1.4. Formation of the ethene double bond. 8

Figure 1.5. Reduction of the bandgap through an extended pi-conjugated network. 9

Figure 1.6. Potential energy curves. 10

Figure 1.7. Jablonski diagram. 11

Figure 1.8. Device architectures and example *J-V* curve. 14

Figure 1.9. Active layer architectures. 15

Figure 1.10. Current generation in OPVs. 16

Figure 1.11. Modes of exciton diffusion. 21

Figure 2.1. AM1.5G solar spectrum and photopic response. 29

Figure 2.2. *PCE* and *AVT* requirements for different PV applications. 30

Figure 2.3. Examples of low and high *CRI*. 31

Figure 2.4. Non-wavelength selective approaches to TPVs. 33

Figure 2.5. Wavelength selective approaches to TPVs. 34

Figure 2.6. *PCE* limit for TPVs as a function of bandgap and *AVT*. 35

Figure 3.1. Schematic of an organic salt-based PV. 39

Figure 3.2. Various cationic cyanines and common counterions. 40

Figure 3.3. Absorption spectra of various organic salts. 41

Figure 3.4. External quantum efficiency of organic salt-based PVs. 43

Figure 3.5. Impact of the counterion on organic salt-based PVs. 49

Figure 3.6. Impact of the counterion on V_{OC} and energy levels. 52

Figure 3.7. Impact of ion presence in organic salt-based PVs. 54

Figure 3.8. Crystallinity of organic salt thin films. 61

Figure 3.9. Organic salt-based transparent photovoltaics. 62

Figure 4.1. Ion exchange reaction purification. 67

Figure 4.2. Large scale synthesis purification. 68

Figure 4.3. Example mass spectrometry data for CyX compounds. 69

Figure 4.4. Ultraviolet visible near-infrared spectroscopy. 70

Figure 4.5. Ultraviolet visible near-infrared spectroscopy example data. 71

Figure 4.6. Photoluminescence and quantum yield setup. 73

Figure 4.7. Quantum yield example data. 74

Figure 4.8. Small angle x-ray scattering setup. 75

Figure 4.9. Example atomic force microscopy data for Ag thickness measurement. 76

Figure 4.10. Transparent device processing. 77

Figure 4.11. Encapsulated large area devices for lifetime testing. 78

Figure 4.12. Thin film thickness versus spin-coating rate. 79

Figure 4.13. High vacuum thermal vapor deposition system. 81

Figure 4.14. External quantum efficiency calibration and testing. 82

Figure 4.15. Mismatch factor calculation. 83

Figure 4.16. VASE thickness fitting. 85

Figure 4.17. VASE optical constant fitting. 86

Figure 4.18. Transient photovoltage setup. 88

Figure 4.19. Optical constants, electric field, and exciton generation rate. 89

Figure 4.20. Transfer matrix modeling and *EQE* fitting. 92

Figure 4.21. Fluorescent imaging operating principles. 93

Figure 5.1. Anionic heptamethines used as donor compounds in photovoltaics. 100

Figure 5.2. Mass spectrometry signals for anionic heptamethines. 101

Figure 5.3. Thickness dependent current-voltage (*J*-*V*) data. 102

Figure 5.4. Thickness dependent *EQE* data. 103

Figure 5.5. Thin film absorption profiles for organic salts. 105

Figure 5.6. Exciton diffusion fitting of fullerene and the organic salts. 107

Figure 5.7. Fitted *EQE* data with a fixed fullerene diffusion length... 108

Figure 5.8. Isolating hole collection losses in organic salt photovoltaics................................. 109

Figure 5.9. Hole mobility data and Mott-Gurney fit.. 110

Figure 5.10. Transient photovoltage measurements of organic salt photovoltaics. 111

Figure 6.1. Active materials and architecture used for photovoltaic devices. 116

Figure 6.2. *J*-*V* and *EQE* curves for annealing temperature optimization. 117

Figure 6.3. Solvent additive optimization. 118

Figure 6.4. Dark *J*-*V* for 1-chloronaphthalene and polymer thickness optimized devices. 119

Figure 6.5. Polymer thickness optimization. 121

Figure 6.6. Light intensity dependent V_{OC} and J_{SC} for polymer thickness devices.................... 122

Figure 6.7. Transfer matrix optical modeling and *EQE* fitting.. 123

Figure 6.8. Ag thickness dependence on device performance.. 125

Figure 6.9. Alq_3 thickness dependence on device performance. 126

Figure 6.10. Optimized transparent photovoltaic device data. 127

Figure 6.11. Aesthetic characterization of TPVs and literature comparison. 128

Figure 6.12. Calculated transmission through different top electrodes. 129

Figure 6.13. Impact of antireflection coating on optical performance. 129

Figure 6.14. Shelf life of bilayer photovoltaic devices. 130

Figure 7.1. Photoelectric effect from GNR thin films in photovoltaic devices. 143

Figure 7.2. Summary of the synthesis pathway for graphene nanoribbons. 144

Figure 7.3. Graphene nanoribbon photovoltaic device data. 145

Figure 7.4. Calculation of exciton diffusion and charge collection lengths. 146

Figure 7.5. Reflection, absorption, and integrated exciton generation rate profiles. 147

Figure 7.6. Exciton generation rate profiles for 3.0 and 3.5 nm GNR....................................... 149

Figure 7.7. Exciton generation rate profiles for 4.5 and 6.0 nm GNR....................................... 150

Figure 7.8. Exciton generation rate profiles for 7.0 and 9.0 nm GNR....................................... 151

Figure 7.9. Calculation of graphene nanoribbon bandgap and molecular orbitals. 153

Figure 8.1. Absorption coefficients of an organic salt and nanocrystal..................................... 161

Figure 8.2. Cyanine (Cy^+) with varying counterions enables tunable cellular toxicity. 163

Figure 8.3. Molecular structures of anions investigated in the study. 164

Figure 8.4. Differential pulse voltammetry measurements... 165

Figure 8.5. Photoluminescence measurements of Cy7X and CyX salts. 166

Figure 8.6. Nanoparticle size distribution is similar for all nanoparticles. 168

Figure 8.7. Nanoparticle lifetime and stability. 169

Figure 8.8. Organic salts with tunable toxicity can be used to target human cancer cells. 170

Figure 8.9. Organic salts with tunable toxicity used to target human melanoma cells.............. 171

Figure 8.10. $CyPF_6$ preferentially accumulates in mitochondria and lysosomes of cells. 172

Figure 8.11. CyFPhB and CyTPFB preferentially accumulate in the mitochondria and lysosomes of cells. 173

Figure 8.12. Fluorescent organic salts generate mitochondrial superoxide. 174

Figure 8.13. Ion pairings display varying degrees of nanoparticle stability in cell media. 175

Figure 8.14. Tunable phototoxicity is not due to accumulation or counterion toxicity. 176

Figure 8.15. Fluorescent dyes tuned to be nontoxic for brighter imaging. 177

Figure 8.16. Toxicity of organic salts correlates to changes in zeta potential. 178

Figure 9.1. Fluorescent organic salts can be used as photosensitizing agents to treat breast cancer cells. 192

Figure 9.2. Addition of Oatps inhibitor bromosulfophthalein (BSP) does not affect organic salt nanoparticle composition or absorption in cell media. 194

Figure 9.3. Oatps mediate cellular uptake of $CyPF_6$, but only partially account for CyTPFB and CyFPhB uptake. 195

Figure 9.4. Endocytotic inhibition does not inhibit uptake of organic salts. 197

Figure 9.5. Albumin plays a critical role in organic salt stability and uptake. 198

Figure 9.6. Impact of BSA on absorption profiles of organic salts. 199

Figure 9.7. Photoluminescence spectra of $CyPF_6$ monomers. 200

Figure 9.8. In vivo biodistribution data shows organic salts preferentially accumulate and are retained within 6DT1 mammary tumors. 201

Figure 9.9. Counterion tuning of organic salts produces a potent photosensitizer (PS) for photodynamic therapy (PDT) in a mouse model of breast cancer. 202

Figure 9.10. Tumor growth with 3 μmol/kg $CyPF_6$ in a mouse model of breast cancer. 203

Figure 9.11. Tumor growth with 1 μmol/kg $CyPF_6$ in a mouse model of breast cancer. 204

Figure 9.12. Tumor growth with 1 μmol/kg CyI in a mouse model of breast cancer. 204

Figure 9.13. CyFPhB irradiated with NIR light induces an antitumor effect via tumor necrosis and impedes cancer progression in a breast cancer mouse model. 205

Figure 9.14. TUNEL assay color thresholds for treatment groups at experimental endpoint (28 days). 206

Figure 9.15. Representative TUNEL assay color thresholds for Vehicle and CyFPhB + NIR treatment groups three days after PDT treatment. 207

Figure 9.16. Minimal systemic toxicity observed with CyFPhB + NIR treatment in mice........ 208

Figure 9.17. Serum levels of liver enzymes ALT and AST.. 209

Figure 10.1. Potential counterion exchanges for anionic heptamethine cyanines. 220

Figure 10.2. Potential failure mechanisms for LBL TPVs. 223

Figure 10.3. Vertically aligned graphene nanoribbons. 226

Figure 10.4. New series of carborane anions for PDT. 228

Figure A.1. Photon balances for Ag thickness dependent TPVs. 248

Figure A.2. Photon balances for PTB7-Th thickness dependent TPVs. 249

Figure A.3. Photon balances for Alq_3 thickness dependent TPVs. 249

LIST OF SYMBOLS AND ABBREVIATIONS

α	molecular extinction coefficient
χ	effective orbital radius of the final and initial electronic states
ε_0	permittivity of free space
ε_r	dielectric constant
η_A	absorption efficiency
η_{CC}	charge collection efficiency
η_{CT}	charge transfer efficiency
η_{DS}	exciton dissociation efficiency
η_{ED}	exciton diffusion efficiency
κ	transition dipole orientation factor
λ	wavelength
μ	mobility
μ_h	hole mobility
v	vibrational energetic state
v'	vibrational energetic state of the first excited electronic state
Φ	luminescence quantum yield
Φ_F	fluorescence quantum yield
π	pi bond or orbital
π^*	pi antibonding orbital
σ	sigma bond or orbital
σ^*	sigma antibonding orbital
σ_{DA}	overlap integral between the donor emission and acceptor absorption
σ_{DA}^*	normalized overlap integral between the donor emission and acceptor absorption

τ	lifetime
τ_e	exciton lifetime
τ_h	hole lifetime
A	area
A_0	pulse amplitude
a^*	red and green chromaticity coordinate
$A(\lambda)$	optical absorption
AVT	average visible transmittance
b^*	blue and yellow chromaticity coordinate
C	solution concentration of a compound
c	speed of light
CRI	color rendering index
d	distance or thickness, typically of an active layer material in a solar cell
D	diffusivity
d_0	nearest neighbor distance and/or donor-acceptor separation distance for energy transfer
E^*	energy
E	electric field
E_0	electric field incident on a device
$\|E\|^2$	electric field strength
E_B	binding energy
E_C	conduction band
E_f	fermi energy
E_G	bandgap
EQE	external quantum efficiency

$EQE_{fixed\ L_{ED,A}}$	external quantum efficiency calculated with a fixed acceptor exciton diffusion length
eV_0	potential barrier at the interface of a p-n junction
f	probability
FF	fill factor
G	exciton generation rate
h	Planck’s constant
$\hbar$	reduced Planck’s constant
I	sample light intensity
I_0	reference light intensity
IC_{50}	half maximal inhibitory concentration
$IPCE$	incident photon conversion efficiency, also known as external quantum efficiency
IQE	internal quantum efficiency
J	current density
J_0	reverse dark saturation current density
J_{MP}	current density at the maximum power point
J_{ph}	photocurrent density
J_{SC}	short-circuit current density
J-V	current-voltage characteristic curves
K	normalization factor
k	extinction coefficient
k_B	Boltzmann constant
k_D	Dexter energy transfer rate
k_F	Förster resonant energy transfer rate
k_{nr}	nonradiative recombination rate

k_r	radiative recombination rate
l	path length
L_{CC}	charge collection length
$L_{CC,A}$	charge collection length of the acceptor material
$L_{CC,D}$	charge collection length of the donor material
L_{Diff}	carrier diffusion length
L_{Drift}	carrier drift length
L_{ED}	exciton diffusion length
$L_{ED,A}$	exciton diffusion length of the acceptor material
$L_{ED,D}$	exciton diffusion length of the donor material
LUE	light utilization efficiency
M	spectral mismatch factor
m_e	effective mass of an electron
n	index of refraction
$\tilde{n}$	complex index of refraction
n_{e-}	number of electrons produced by a photovoltaic device
n_{id}	ideality factor
n_{ph}	number of photons incident on the surface of a photovoltaic device
$n_{ph\ absorbed}$	number of photons absorbed by a material in a quantum yield measurement
$n_{ph\ emitted}$	number of photons emitted by a material in a quantum yield measurement
p	exciton density
P_0	power incident on a photovoltaic device
PCE	power conversion efficiency
$PL(\lambda)$	photoluminescence emission spectra

PL_R	photoluminescence emission spectra of a reference solution
PL_S	photoluminescence emission spectra of a sample solution
q	elementary charge
Q	time average absorbed power
r	Fresnel coefficient of reflection
r_0	electron equilibrium position at the ground state energy level
R_0	Förster radius
r_1	electron equilibrium position at the first excited state energy level
$R(\lambda)$	reflectance
$R(\%)$	reflection
r_e	exciton Bohr radii
R_P	shunt or parallel resistance
R_S	series resistance
S	sum of electron spins
S_0	ground electronic state
S_1	first excited electronic singlet state
S_2	second excited electronic singlet state
$S(\lambda)$	solar spectrum
S_R	silicon diode responsivity used to calculate the spectral mismatch factor
S_T	optical transfer matrix for a device stack
T	temperature
t	Fresnel coefficient of transmission
T_1	first excited electronic triplet state
T_{80}	time until a device reaches 80% of the initial performance

$T(\lambda)$	transmittance
$T(\%)$	transmission
V	voltage, potential, or bias
V_0	baseline potential
V_{BI}	built-in voltage
V_{MP}	voltage at the maximum power point
V_{OC}	open-circuit voltage
w	depletion width
WF	work function
Z	dimensionality factor
3-GNR	graphene nanoribbon with three repeating units
6-GNR	graphene nanoribbon with six repeating units
A549	human lung carcinoma cell line
AFM	atomic force microscopy
Alq_3	aluminum hydroxyquinoline
ALT	alanine aminotransferase
AM1.5G	air-mass 1.5 global solar spectrum
ARC	anti-reflection coating
AST	aspartate aminotransferase
ATP	adrenosine triphosphate
BCP	bathocuproine
BF_4^-	tetrafluoroborate ion
BHJ	bulk heterojunction
BIPV	building-integrated photovoltaic
BPh_4^-	tetraphenylborate anion

BSP	bromosulfophthalein, an OATP inhibitor
C_6H_{13}	n-hexyl hydrocarbon chain
C_{60}	fullerene
CB^-	ortho-carborane anion
ClO_4^-	perchlorate anion
Cm-H2DCFDA	chloromethyl-2',7'-dichlorodihydrofluoecsein, general cytoplasmic reactive oxygen species probe
CN	1-chloronaphthalene
CNTs	carbon nanotubes
$CoCB^-$	cobalti-carborane anion
COi8DFIC	a non-fullerene acceptor used in organic photovoltaics, also known as NFA146, PCE146, O6T-4F
CuI	copper iodide
Cy^+	an organic cationic heptamethine cyanine
Cy3	commercially available trimethine cyanine dye
Cy5	commercially available pentamethine cyanine dye
$Cy7^+$	commercially available near-infrared responsive heptamethine cyanine cation
Cy7X	commercially available near-infrared responsive heptamethine cyanine cation paired with a generic counterion, X
CyX	organic cationic heptamethine cyanine paired with a generic counterion, X
DCM	dichloromethane
DI H_2O	deionized water
DMEM	Dulbecco’s modified eagle medium
DMF	dimethylformamide
DMOG	dimethyloxalylglycine, a HIF-1α stabilizer that promotes OATP

	expression
DMSO	dimethylsulfoxide
DNA	deoxyribonucleic acid
DPV	differential pulse voltammetry
DSSCs	dye-sensitized solar cells
EA	electroabsorption
ET	energy transfer
Et3N	triethylamine
ETL	electron transport layer
eV	electron volt
FPhB$^-$	tetrakis(4-fluorophenyl)borate anion
FRET	Förster resonant energy transfer
GNR	graphene nanoribbon
H_2O	water
HIF1α	hypoxia-inducible factor 1-alpha
HJ	heterojunction
Ho	Hoechst, a deoxyribonucleic acid stain
HOMO	highest occupied molecular orbital
HPLC-MS	high performance liquid chromatography-mass spectrometry
HTL	hole transport layer
IC	internal conversion
IEICO-4F	a non-fullerene acceptor used in organic photovoltaics
IPA	isopropanol
ISC	intersystem crossing
ITO	indium tin oxide

LBL	layer-by-layer
LDLs	low-density lipoproteins
LED	light emitting diode
LUMO	lowest unoccupied molecular orbital
MeI	iodomethane
MeOH	methanol
MEHPPV	organic polymer used in some organic photovoltaics
MO	molecular orbital
MoO_3	molybdenum trioxide
NaCy1	anionic heptamethine cyanine-based salt with a sodium counterion, Na783
Na_3Cy1’	anionic heptamethine cyanine-based salt with sodium counterions, $Na_3$789
NaCy2	anionic heptamethine cyanine-based salt with a sodium counterion, Na820
Na_3Cy2’	anionic heptamethine cyanine-based salt with sodium counterions, $Na_3$823
nBuLi	n-butyllithium
NFA	non-fullerene acceptor
NIR	near-infrared
NREL	National Renewable Energy Laboratory
OATP	organic anion transporter peptides
OPV	organic photovoltaic
PANI:DBS	polymer used as a hole transport layer or electrode modification layer in organic photovoltaics
PbS	lead sulfide semiconductor nanocrystal and quantum dots
PBS	phosphate buffered saline

PbSe	lead selenide semiconductor nanocrystal and quantum dots
PCBM	phenyl-C_{61}-butric acid methyl ester, a solution processable fullerene derivative used as an acceptor in organic photovoltaics
$Pd(PPh_3)_4$	tetrakis(triphenylphosphine)palladium (0)
$Pd(PPh_3)_2Cl_2$	bis(triphenylphosphine)palladium (II) dichloride
PDT	photodynamic therapy
PEDOT:PSS	poly(3,4-ethylenedioxythiophene) polystyrene sulfonate, a hole transport layer or electrode modification material in photovoltaics
PF_6^-	hexafluorophosphate anion
PL	photoluminescence
PS	photosensitizer
PTB7-Th	near-infrared absorbing polymer used in photovoltaics, also referred to as PCE-10
PV	photovoltaic
Rho123	rhodamine 123, mitochondrial stain
ROS	reactive oxygen species
r.t.	room temperature
SAXS	small angle x-ray scattering
SbF_6^-	hexafluoroantimonate anion
SC	solar cell
SCLC	space charge limited current
SEM	scanning electron microscopy
SQ	Shockley Queisser
STPVs	semitransparent photovoltaics
TBA^+	tetrabutylammonium cation
TCB	1,2,4-trichlorobenzene

TFM$^-$	tetrakis[3,5-bis(trifluoromethyl)phenyl]borate anion
TfOH	triflic acid
THF	tetrahydrofuran
TiO_X	titanium oxide, anode buffer layer
TLSC	transparent luminescent solar concentrator
TPFB$^-$	tetrakis(pentafluorophenyl)borate anion
TPV	transparent photovoltaic
TRIS$^-$	Δ-tris(tetrachloro-1,2-benzenediolato)phosphate(V) anion also called Δ-TRISPHAT-
TUNEL	terminal deoxynucleotidyl transferase dUTP nick end labeling
UHPLC-MS	ultra-high performance liquid chromatography mass spectrometry
UV	ultra-violet
VASE	variable angle spectroscopic ellipsometry
Veh	vehicle control
VIS	visible
VR	vibrational relaxation
WCAs	weakly coordinating anions
WM1158	metastatic human melanoma cell line
XRD	x-ray diffraction
ZnO	zinc oxide

Chapter 1 – Organic Photovoltaics

1.1 Overview of organic semiconductors

1.1.1 Introduction to semiconductor physics

Electrical conductivity is a measurement of the movement of electrons in a material in response to a potential gradient, and is therefore dictated by how loosely or tightly electrons are bound to the nuclei in a lattice or molecule. The electron energies are related directly to the energy band structure or molecular orbital (MO) energies, which arise from the overlap of atomic wavefunctions describing the electron density between nuclei in a lattice (typically inorganics) or a molecule (usually organics) and result in discrete energy values for locations within the lattice or molecular orbitals in the molecule. An important property for inorganic and organic materials is the size of the energetic difference between the highest energy occupied state and the lowest unoccupied state. The highest occupied and lowest unoccupied states are called the valence (E_V) and conduction (E_C) bands for inorganic materials, and the highest occupied molecular orbital (HOMO) and lowest unoccupied molecular orbital (LUMO) for organics. The energy difference between the valence (HOMO) and conduction (LUMO) bands define the bandgap (E_G) of a material, the minimum energy needed to move an electron from the ground state (S_0) to the first excited state (S_1). In conductors, the valence and conduction bands overlap, and electrons are considered to be delocalized from any particular nuclei and move freely from valence to conduction band in the lattice and consequently through the material itself (Figure 1.1). This gives rise to the high conductivity of metals and other conductors. Insulators generally have a bandgap larger than 3-4 eV, indicating that the electrons are tightly bound to the nuclei in the lattice or molecule and cannot move even in a large potential gradient and thus do not allow charge conduction.

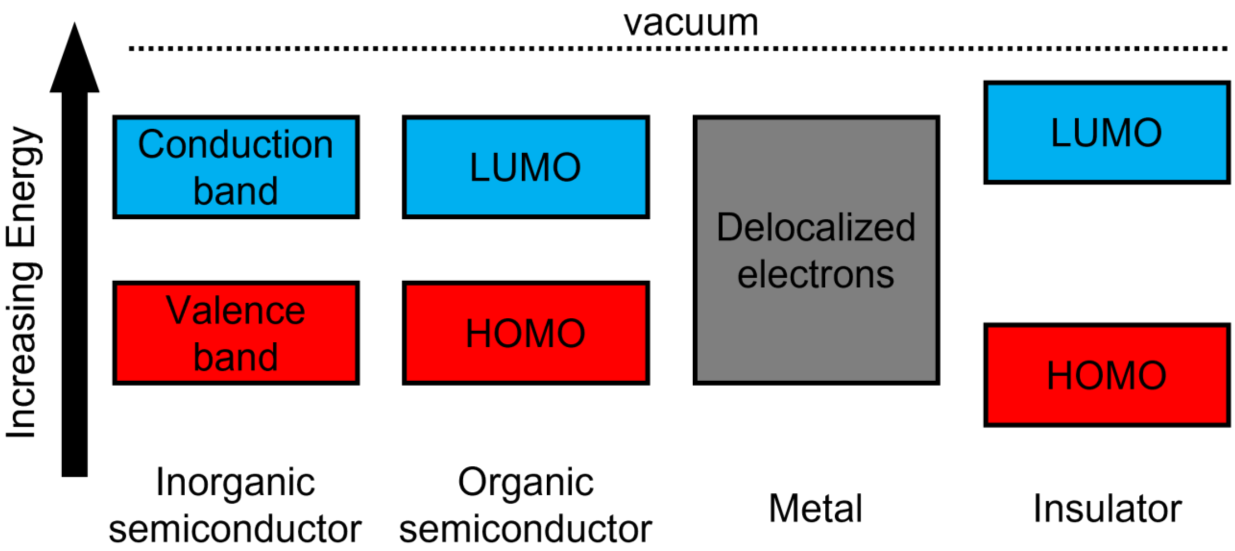

Figure 1.1. Bandgaps of semiconductors, metals, and insulators. Valence and conduction bands of inorganic semiconductors, highest occupied and lowest unoccupied molecular orbitals (HOMO and LUMO) of organic semiconductors, "sea of electrons" in metals, and the wide bandgap between the valence band or HOMO and conduction band or LUMO of insulators.

Large bandgap semiconductors can have bandgaps over 3 eV, including diamond (5.5 eV) and SiC (3.3 eV). Small bandgap semiconductors have a bandgap greater than the thermal energy at room temperature given by k_BT (~26 meV), where k_B is the Boltzmann constant and T is the temperature, so that there is some separation between the conduction and valence bands (Figure 1.1). Electrons in the ground state are considered localized and held in a general location relative to the lattice or molecule by coulombic forces between the electron and the nuclei. An excitation of the electron is needed to make the materials conductive, that is to overcome the electron-nuclei binding energy and allow the electron to move within the lattice or molecule (referred to as a free charge carrier). The absence of negative charge created by the movement of the electron to a location farther from the nuclei creates a positively charged hole in the lattice or molecule. In organic semiconductors, the excited state electron is often still coulombically bound to the hole to form an exciton, which will be discussed in section 1.2.5. The electron excitation can be achieved thermally by putting energy into the lattice or molecule and causing the distribution of electron energies described by the Fermi-Dirac distribution (Equation 1.1) to shift upwards in energy towards the conduction band, where E_F is the Fermi energy, the highest energy level occupied at absolute zero temperature (T = 0 K). The Fermi-Dirac distribution gives the probability (f) that an electron or hole has a given energy, E^*, at a temperature, T, given the Fermi energy.[1]

$$\boldsymbol{f(E^*) = \frac{1}{1+e^{\left(\frac{E^*-E_F}{k_B T}\right)}}} \tag{1.1}$$

Alternatively, an electron can be excited to a higher energy state radiatively by the absorption of a photon of sufficient energy to overcome the bandgap. In the case of in-direct bandgap semiconductors, a radiative excitation also requires the absorption of a phonon to traverse the band structure because the maximum valence band and minimum conduction band points do not overlap. The specifics of radiative excitation in organic semiconductors will be covered in detail in section 1.1.2. Photons with energy less than E_G will pass through the material, while those with energy greater than E_G will be absorbed by continuous bandgap semiconductors. Semiconductors with non-continuous bandgaps, such as many molecular semiconductors (i.e. organic semiconductors), will have molecular orbitals and higher excited states (not a continuous band) that allow certain photons with energy greater than E_G to pass through the material. This is a critical feature for the fabrication of transparent photovoltaics (TPVs) and will be discussed in Chapter 2.

The Fermi level of semiconductors, and consequently the work function (*WF*), the energy needed to move an electron from the Fermi level to the vacuum level, depends in part on the carrier concentration of the semiconductor. Intrinsic semiconductors like undoped silicon have an equal number of holes and electrons in the valence band, and consequently the Fermi level lies almost directly in the middle of the energy gap (Figure 1.2a). Extrinsic semiconductors, most commonly

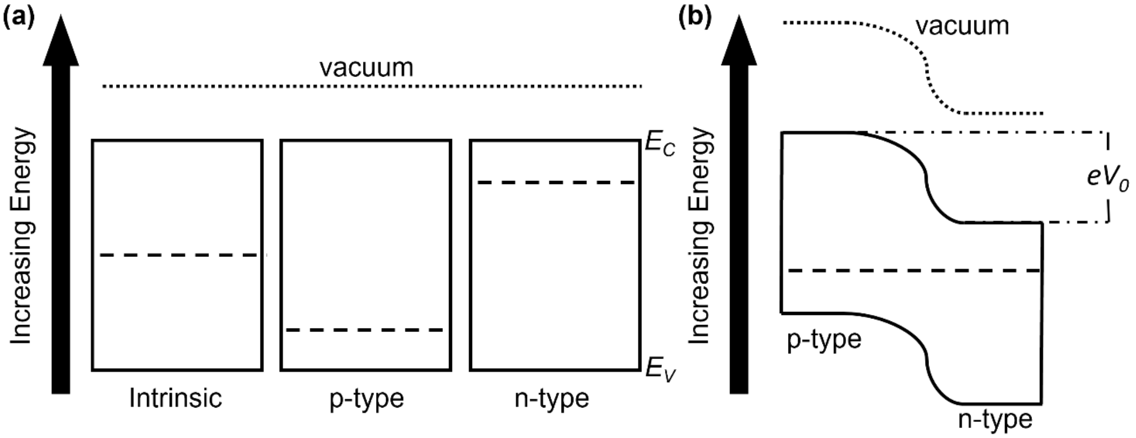

Figure 1.2. Intrinsic and extrinsic semiconductors, and the formation of a p-n junction. Energy diagrams and relative work functions of **(a)** intrinsic and extrinsic (p and n-type) semiconductors with valence and conduction band energies denoted E_V and E_C, respectively. **(b)** A p-n junction formed by a shared interface between a p-type and an n-type semiconductor. The Fermi levels are indicated with a dashed line.

doped semiconductors such as p- and n-type silicon, have unequal concentrations of holes and electrons. In p-type semiconductors, there are a greater number of holes than electrons, shifting the Fermi level down in energy (Figure 1.2a). This is achieved in silicon by doping with an element that has a less than half-filled valence shell, such as boron, which has an entirely empty 2p orbital creating a hole in one of the four boron-silicon bonds. Charge is then able to move through the doped silicon via the impurity created holes. Doping can also be achieved with elements that contribute an extra electron, such as phosphorus, which brings the four electrons needed to bond with four silicon atoms and contributes an extra electron to allow current to pass through the n-type semiconductor. The Fermi level of an n-type semiconductor lies closer to the conduction band due to the greater concentration of electrons than holes (Figure 1.2a). In organic semiconductors, a semiconductor with p-type behavior is commonly referred to as a donor material and a material with n-type semiconducting properties is called an acceptor. When a p-type and n-type semiconductor are brought together to form a junction (called a p-n junction or a diode), the carrier concentration gradient causes carrier diffusion of electrons into the p-type material and holes into the n-type material near the interface. Carrier diffusion results in a space charge region (or depletion region) around the p-n interface, and the space charge build-up creates an electric field. An equilibrium is reached when the carrier concentration diffusion is balanced with drift current due to the electric field. At equilibrium, the fermi level is constant across the junction (Figure 1.2b) and a potential barrier (eV_0) at the interface caused by the space charge allows current to flow in a single direction through the diode. A forward bias across the diode will reduce the potential barrier and allow charge carriers to move more freely across the interface, creating a current. A reverse bias enhances the built-in potential barrier and further reduces charge carrier movement. These conditions are described by the Shockley diode equation (Equation 1.2), where J is the current density, J_0 is the reverse dark saturation current density, and eV is the potential barrier at the interface.[2]

$$J = J_0\left[e^{\left(\frac{eV}{k_BT}\right)} - 1\right] \tag{1.2}$$

Including series (R_S) and parallel (R_P) resistance, the ideality factor (n), and the photocurrent (J_{ph}), the diode can more generally be written as:[3]

$$J = \frac{R_P}{R_S+R_P}\left\{J_0\left[exp\left(\frac{q(V-JR_S)}{n_{id}k_BT}\right) - 1\right] + \frac{V}{R_P}\right\} - J_{ph} \tag{1.3}$$

Such an equation is useful in analyzing the current-voltage (J-V) characteristics of a variety of photovoltaic devices to understand limitations in the design and mechanism of enhancement/deterioration in performance.

1.1.2 Molecular bonding in organic semiconductors

The HOMO and LUMO of organic semiconductors are just two of many MOs in a given molecule. MOs are formed from the combination of pure and hybridized atomic orbitals that overlap to form bonds. Hybridization of atomic orbitals explains the formation of energetically

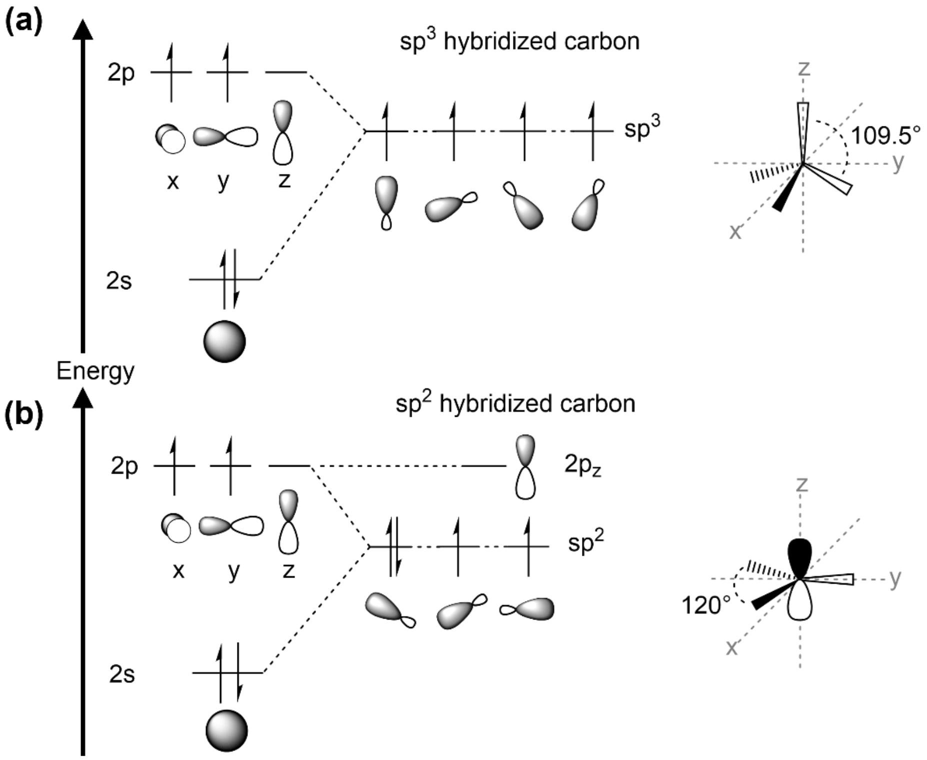

Figure 1.3. Hybridization of atomic orbitals. Carbon valence atomic orbitals undergo hybridization to form either **(a)** four sp^3 hybridized orbitals or **(b)** three sp^2 orbitals.

degenerate orbitals and bonds, such as in the case of the four sigma bonds present in methane. Each hydrogen atom has a half filled 1s atomic orbital, while the carbon atom would normally have a valence shell consisting of a filled 2s orbital and three half-filled 2p orbitals ($2p_x$, $2p_y$, and $2p_z$), which are shown in Figure 1.3a. There is no energetic difference between the four C-H methane bonds, and so the four valence orbitals of carbon must reconfigure into four energetically degenerate hybridized orbitals, called sp^3 orbitals because they are made from an s orbital and three p orbitals. The number and energy of the resulting orbitals must be conserved during hybridization so that four orbitals are created and have ¾ p character and ¼ s character, and the MO energies are drawn in Figure 1.3a as approximately ¾ of the p orbital energy level. Carbon can also hybridize into the sp^2 and sp configurations, the former is shown in Figure 1.3b, and results in three and two degenerate orbitals, respectively, while one and two p orbitals would remain in each case. Each hybridization case results in a distinct set of orbitals in energy and orientation, sp^3 orbitals are separated by 109.5°, sp^2 orbitals are planar when empty (electrons occupying the sp^2 and p orbital would cause the sp^2 orbitals to angle away from the p orbital due to electron-electron repulsion) and separated by 120°, while the sp orbitals lie along the same axis and are separated by 180°.

Molecular orbitals are complex, especially in systems with more than a handful of atoms. However, the basics can be simplified to explain the formation of MOs, and how different atomic orbitals might interact. There are three determining factors for how strongly atomic orbitals will interact, or "see" each other, to form MOs. First, the orbitals must be similar in energy. The 1s and 3d orbitals on neighboring carbons will have little to no interaction because of how dissimilar the energies are, even though they are in relative proximity and have a combined two electrons between them. Second, the strength of atomic orbital interaction is affected by the physical distance between the orbitals. Half-filled sp^3 carbon orbitals on neighboring carbon atoms will have a stronger interaction and subsequent influence on the shape (electron density) of the resulting MO than will the same orbitals on carbons separated by several atoms. Lastly, the spatial alignment of orbitals is critical to their interaction. Lone p orbitals on carbon atoms that are all oriented in the same direction can form MOs that span many atoms and allow for greater electron mobility (also known as conjugation).

A simplified example of MO formation is shown in Figure 1.4 for the HOMO and LUMO of ethene, which can be thought of as two CH_3 fragments joining together along an interatomic line between the carbons. A sigma bonding orbital (σ) is created by the overlap of the remaining sp^2 orbitals on each carbon and filled with two electrons to create a sigma bond, with the vast majority of the electron density existing between the two carbon atoms (the shaded regions

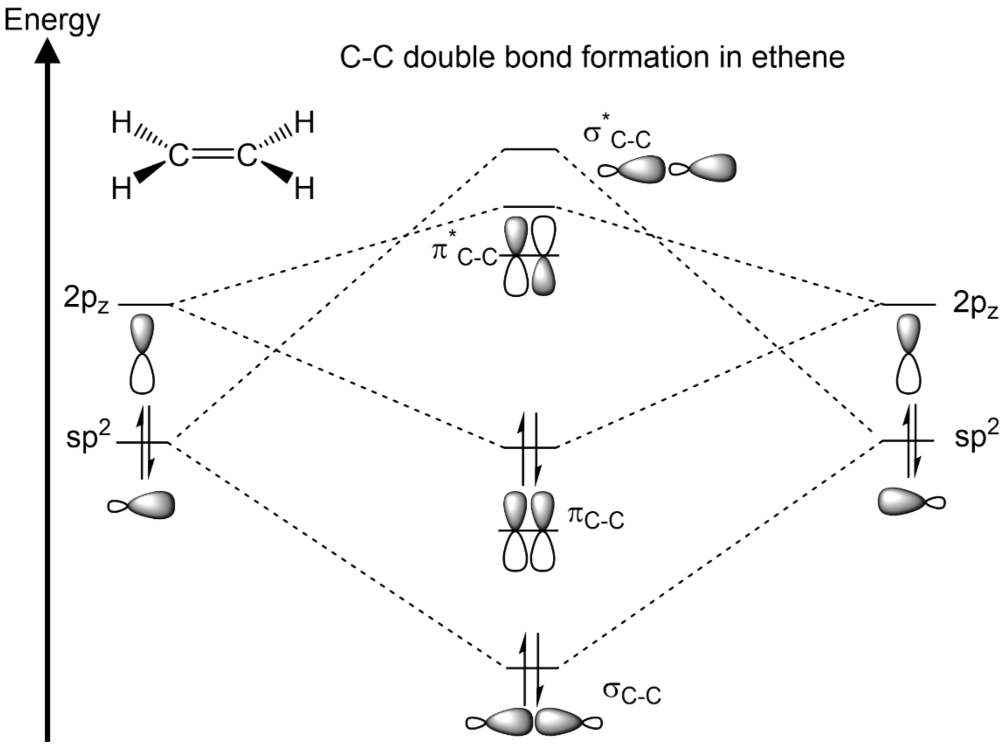

Figure 1.4. Formation of the ethene double bond. A simplified schematic of how the hybridized and unhybridized orbitals of two carbon atoms interact to form a double bond consisting of filled sigma and pi bonding orbitals and empty sigma and pi anti-bonding orbitals.

overlapping), indicating that both electrons will spend most of their time in that location. Since the electron density is firmly held between the two positively charged nuclei, the σ bond is a strong bond. For orbital conservation, a second MO must be formed, this time with unfavorable alignment of the orbital lobes (illustrated by the shaded and unshaded region overlapping) to produce an antibonding sigma orbital (σ^*). The energy lowering produced by the favorable alignment of orbital lobes for σ is offset by the energy raising unfavorable alignment of σ^* so energy is conserved. A second weaker bonding orbital is created by the favorable alignment of the p orbitals on both carbons to produce a pi bonding orbital (π), which when filled creates a pi bond with electron density located above or below the interatomic axis and a node along the axis itself. The electron density is further away from the nuclei and there is less overlap between p orbitals than the sp^2 orbitals, so the electrons are less tightly held and the π bond is higher in energy than the σ bond.

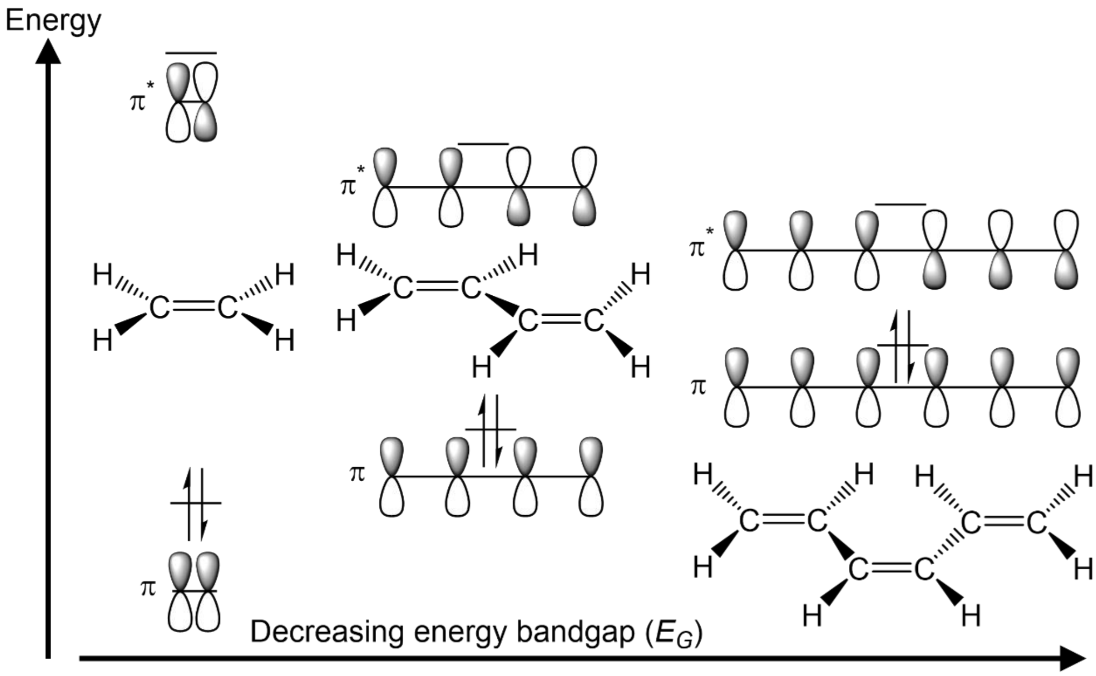

Figure 1.5. Reduction of the bandgap through an extended pi-conjugated network. An example of how alignment of p orbitals (and π bonds) on consecutive atoms creates a smaller bandgap as the number of aligned orbitals increases.

An anti-bonding pi orbital (π^*) is created by the opposing interaction of p orbitals and since the orbital overlap is weaker, the unfavorable interaction is weakened and the π^* orbital sits lower in energy than the σ^* orbital. The C-C π bond is the HOMO of ethene, while the π^* orbital is the LUMO, and the energy difference between π and π^* is the E_G for ethene. In reality, there will be some interaction between the C-C and C-H MOs, as they are not too different energetically and are located on neighboring atoms, although the MO alignment for the C-H bonds is not favorable for donation into the C-C bonds.

Aligned p-orbitals on atoms can form alternating π bonds to produce conjugated networks. The nature of the double bond assures some planarity in the molecules which allows the p-orbitals to be well aligned for electron movement from one MO to another. Extending the conjugated network creates more closely spaced MOs and therefore lowers E_G, a generalized example of this process is shown in Figure 1.5. Organic semiconductors have highly tunable bandgaps because the

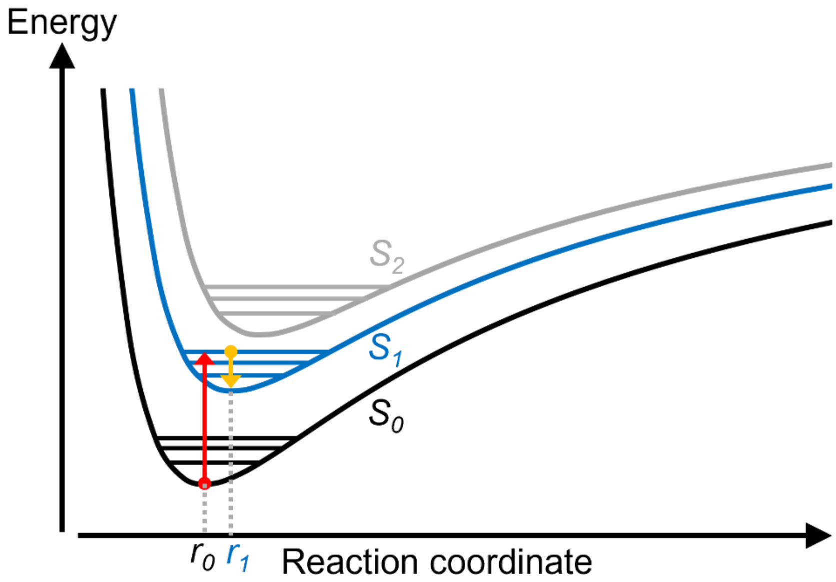

Figure 1.6. Potential energy curves. Potential energy curves for the electronic ground state (S_0) and first two excited states (S_1 and S_2) with several vibrational states (horizontal lines) shown for each electronic state. Electron excitation is shown to illustrate photoexcitation from ground state equilibrium (r_0, red arrow) and vibrational relaxation (orange arrow) to the S_1 state at a new equilibrium position (r_1).

π-conjugated network can be shortened or extended. When processed into neat thin films, favorable stacking of organic semiconductors can lead to alignment of the π-conjugated networks between molecules and a more crystalline (ordered) system with better electronic properties for OPVs.

MOs are the discrete electronic states of molecular semiconductors and electronic transitions from the HOMO (ground state, S_0) to LUMO (first excited state, S_1) occur when an electron is given enough energy to move between them. Within each electronic state are vibrational states (v = 0, 1, 2…n) associated with vibrational motion of the atoms in a molecule. A ground state electron occupies the S_0, v=0 state, and upon absorption of a photon with energy greater than E_G, the electron moves into the S_1 state (Figure 1.6, red arrow) and a given excited state vibrational level (v') before relaxing down to the lowest available vibrational state (v' = 0) by giving off thermal energy (Figure 1.6, orange arrow). As the electron moves into a new electronic state, the

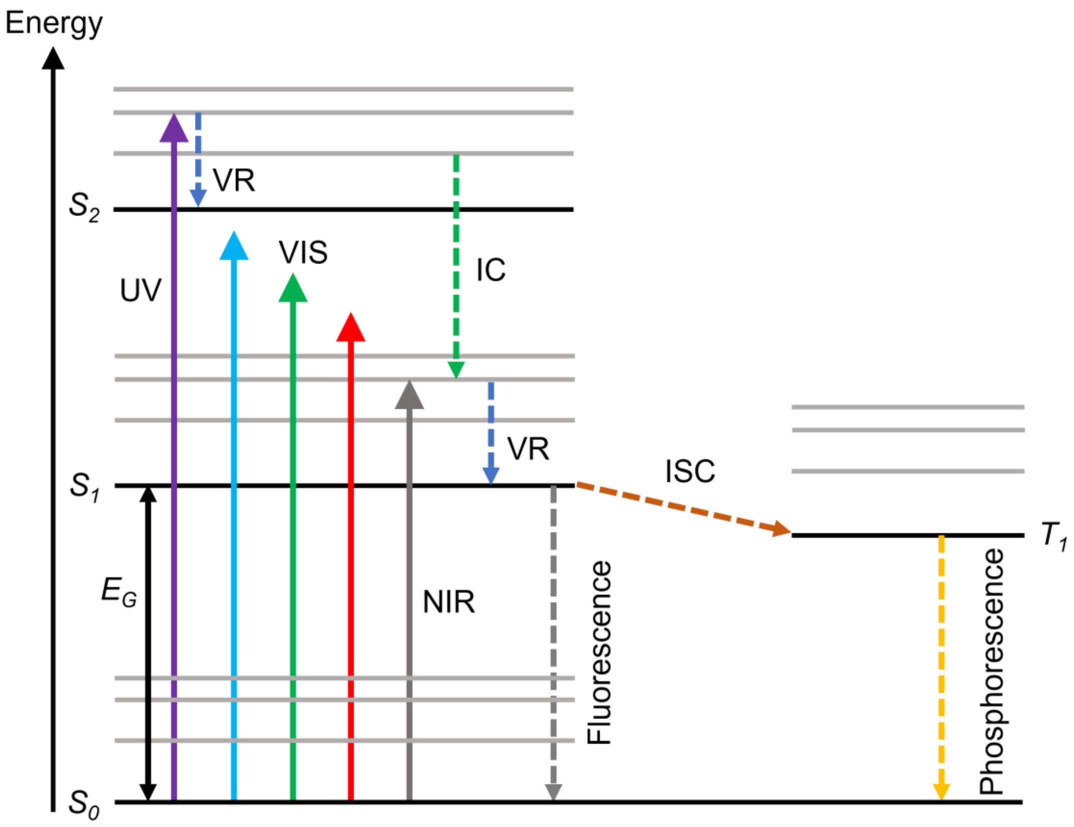

Figure 1.7. Jablonski diagram. A Jablonski diagram highlighting the different processes occurring upon photoexcitation of an electron in an organic semiconductor. Ultraviolet (UV, purple solid arrow) and near-infrared (NIR, gray solid arrow) light is absorbed. Visible light (VIS, blue, green, and red solid arrows) is not absorbed because of the optical gap. Vibrational relaxation within an electronic state (VR, blue dashed arrow) and internal conversion (IC, green dashed arrow) are nonradiative forms of relaxation. Intersystem crossing (ISC, dark orange dashed arrow) involves an excited state singlet electron changing spins to a triplet state. Fluorescence (gray dash arrow) and phosphorescence (orange dashed arrow) are forms of radiative relaxation from a singlet or triplet excited state to the ground state, respectively.

equilibrium position about which the involved nuclei oscillate lengthens to account for the reduced attractive electron-nuclei forces, increasing the bond length and often causing a change in MO shapes. This gives rise to the offset potential energy curves shown in Figure 1.6 for the S_0, S_1, and S_2 states, where excited states exhibit 1) higher energy and 2) a greater interatomic distance. A Jablonski diagram (Figure 1.7) details the different processes involved after photoexcitation. Absorption of light leads to excitation of an electron into a higher singlet state (gray and purple solid arrows), at which point the electron can go through several different processes. An electron can undergo vibrational relaxation (VR) within an electronic state (blue dashed arrow) or internal conversion (IC, green dashed arrow) between two electronic states. VR and IC are nonradiative processes and give off energy thermally as phonons. Alternatively, the excited state electron can relax back to the ground state via fluorescence (gray dashed arrow), releasing a photon. Last, the excited state electron can undergo a spin change in a process known as intersystem crossing (ISC, dark orange dashed arrow). In the ground state of a filled orbital, the electrons possess opposite spins of ½ and -½ to satisfy the Pauli exclusion principle and give a spin multiplicity ($2S + 1$, where S is the sum of the spins) of one so that they are singlet electrons. Upon excitation, the spin pairing remains as the excited state electron is spin paired with the ground state electron. A spin change for the excited state electron leaves the electron pair with parallel spins so that the spin multiplicity is now three, a triplet state. The singlet to triplet transition is spin forbidden but can be allowed through spin orbit coupling where the total angular momentum is maintained by equal and opposite changes in spin angular momentum and orbital angular momentum. The rate of ISC can be increased by overlapping excited vibrational states and is enhanced in molecules with significant spin-orbit coupling. After ISC, the electron can undergo recombination and release a photon (phosphorescence, orange dashed arrow) or a phonon. Phosphorescence is slower than fluorescence by an order of magnitude or more, and the associated excited state lifetime of the electron is much longer.

For many optoelectronic and optical applications, the quantum yield (Φ) is critical to the success of an organic semiconductor. This includes fluorescent bioimaging, where higher Φ improves diagnostic capabilities, and in PVs, where exciton diffusion efficiencies (discussed in section 1.2.5) and photon recycling generally improve with increased Φ. Conceptually, Φ is the ratio of emitted photons ($n_{ph\ emitted}$) to absorbed photons ($n_{ph\ abs}$) or the ratio of radiative (k_r) to k_r

and nonradiative (k_{nr}) recombination rates.[4]

$$\Phi = \frac{n_{ph\,emitted}}{n_{ph\,absorbed}} = \frac{k_r}{k_r + k_{nr}} \tag{1.4}$$

1.2 Introduction to organic photovoltaics

The discrete energies occupied by MOs and the sub-level vibrational states create one of the key differences between most inorganic semiconductors, which have a continuous density of states above E_G, and organic semiconductors, which possess optical gaps. This is illustrated in Figure 1.7, where ultra-violet (UV, purple solid arrow) light is absorbed and causes an electron to be excited to the S_2 electronic state, while near-infrared (NIR, gray solid arrow) is absorbed and causes electronic excitation to the S_1 state. In this illustration, the locations of S_0, S_1 and S_2 allows visible (VIS, blue, green, and red solid arrows) light to pass through the material, even though the photon energy is greater than E_G. As discussed above, the bandgap of organic semiconductors can be controlled through the π-conjugated network to allow the frontier molecular orbitals (S_0 to S_1 transition) to sit in the UV, VIS, or NIR region of the light spectrum.

1.2.1 Organic photovoltaic architecture

The p-n junction discussed in section 1.1.1, hereafter referred to as the heterojunction (HJ) between the donor and acceptor, is a key element of organic photovoltaics (OPVs) since its first introduction by Tang in 1987.[5] Previous OPVs were typically fabricated with a single organic active layer as a Schottky diode. The energetic offset between the donor and acceptor at the heterojunction is required in almost all cases because excitons are generated upon photoexcitation in organic semiconductors instead of free charge carriers, a process that will be examined in depth in section 1.2.5. In a traditional architecture single junction OPV shown in Figure 1.8a, the donor and acceptor, frequently referred to as the active materials or photoactive materials, are sandwiched between a top and bottom electrode. Supporting hole and electron transport layers

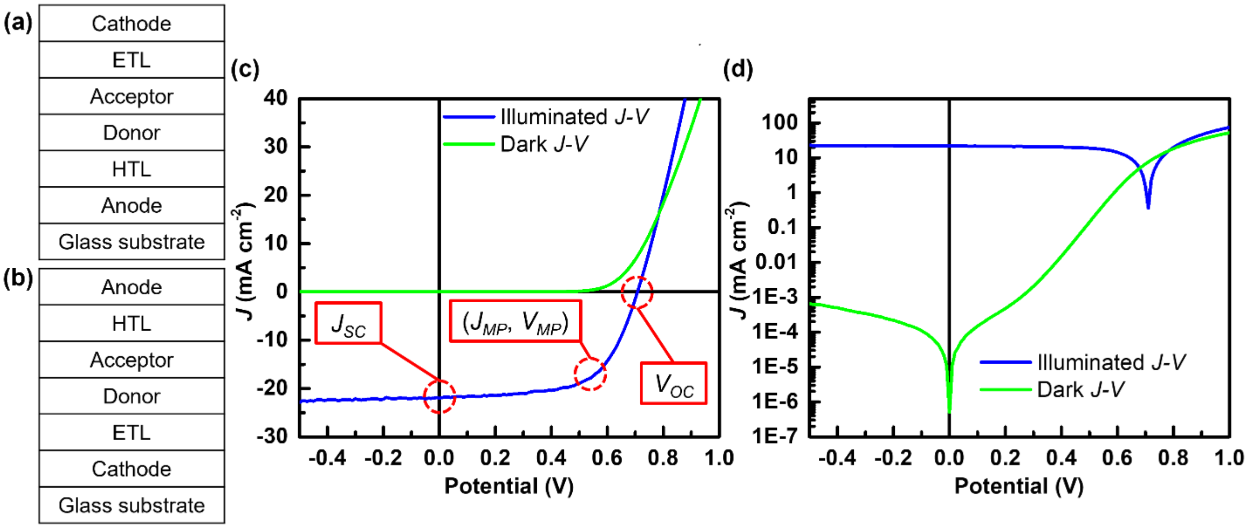

Figure 1.8. Device architectures and example *J*-*V* curve. Device stacks for **(a)** traditional and **(b)** inverted organic photovoltaics. **(c)** Example illuminated (blue) and dark (green) *J*-*V* curves with key parameters labeled. The dark *J*-*V* curve is the absolute value of the measured dark current. **(d)** Absolute value of example curves from **(c)** on a semi-log plot.

(HTL and ETL) are inserted between the electrodes and active layers to reduce recombination and facilitate single carrier transfer as well as to optimize absorption via complex optical interference. In an inverted architecture, electrons are collected through the donor and holes through the acceptor, and the HTL and ETL exchange places within the device stack (Figure 1.8b).

1.2.2 Active layer architectures

There are several common approaches to forming the donor-acceptor HJ in OPVs. The simplest is to sequentially deposit or grow the donor and acceptor as pure neat films, referred to as a bilayer or planar bilayer architecture (Figure 1.9a). There is essentially no intermixing between the two films and the roughness of the donor film is a key factor in the size of the interfacial area between donor and acceptor. A planar mixed HJ (Figure 1.9b) is a device structure with two mostly pure layers and a mixed region between them. It is typically formed from one of two methods, 1) sequential deposition of pure films where the mixed region forms naturally as a result of the processing technique, or 2) deposition of a donor neat film, followed by co-deposition of a mixed layer and then finished with a pure film of the acceptor. The co-deposition parameters determine

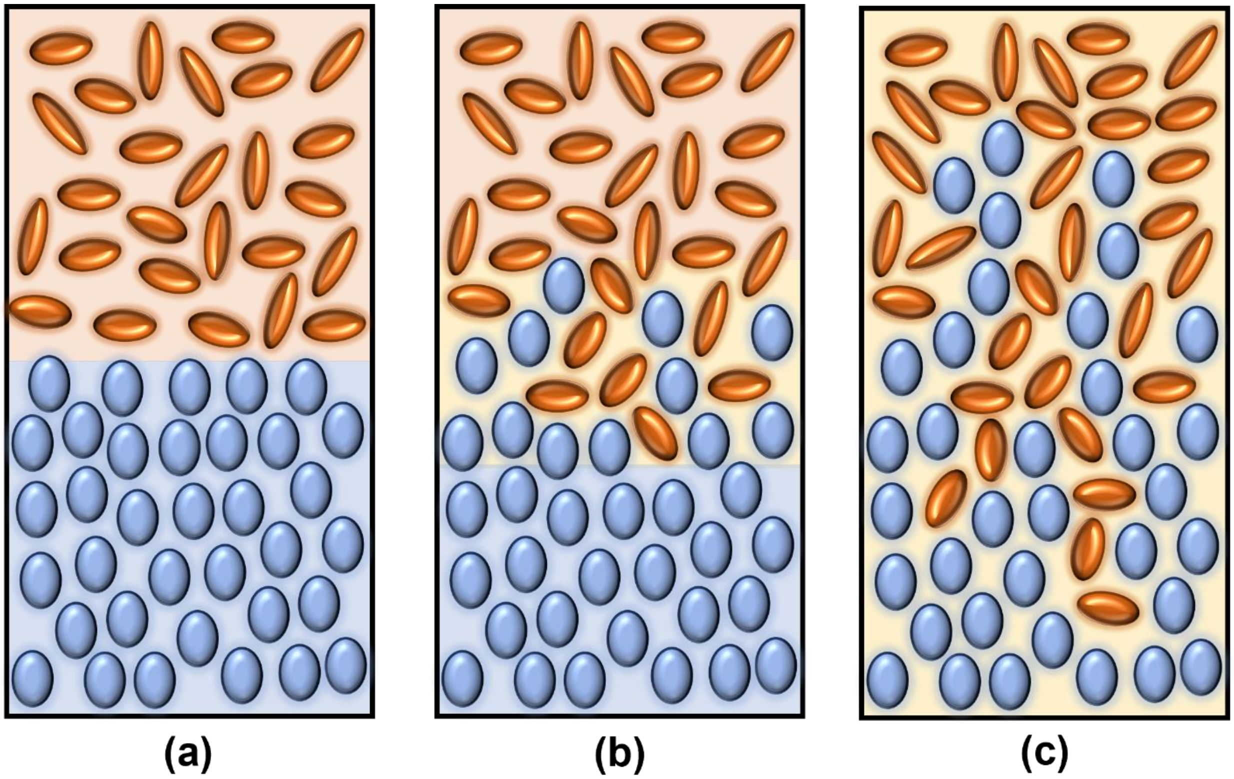

Figure 1.9. Active layer architectures. (a) Bilayer architecture composed of two neat films. **(b)** A planar mixed heterojunction architecture consisting of two neat films separated by a mixed region. **(c)** A bulk-heterojunction architecture made of a single film with two or more domains.

the thickness and chemical composition of the mixed region. This approach results in a donor-acceptor interface that is larger than in a bilayer but smaller than a bulk heterojunction (BHJ). One of the most common approaches in recent OPVs is to create BHJ active layers where the donor and acceptor are deposited simultaneously (Figure 1.9c). In most recent cases this is achieved via a solution-processing methods, but co-evaporation has also been demonstrated. The resulting active layer is considered a single film with usually two or more domains that possess a majority of one material. The ratio of the two materials is critical in a BHJ to determining the resulting morphology of the active layer, including the relative purity and size of the domains. The BHJ approach generally yields the largest donor-acceptor interfacial area, an important factor in device performance. Poor morphology control can result in excessive mixing where a single domain is formed. This is problematic for current production and will be discussed in section 1.1.6. The

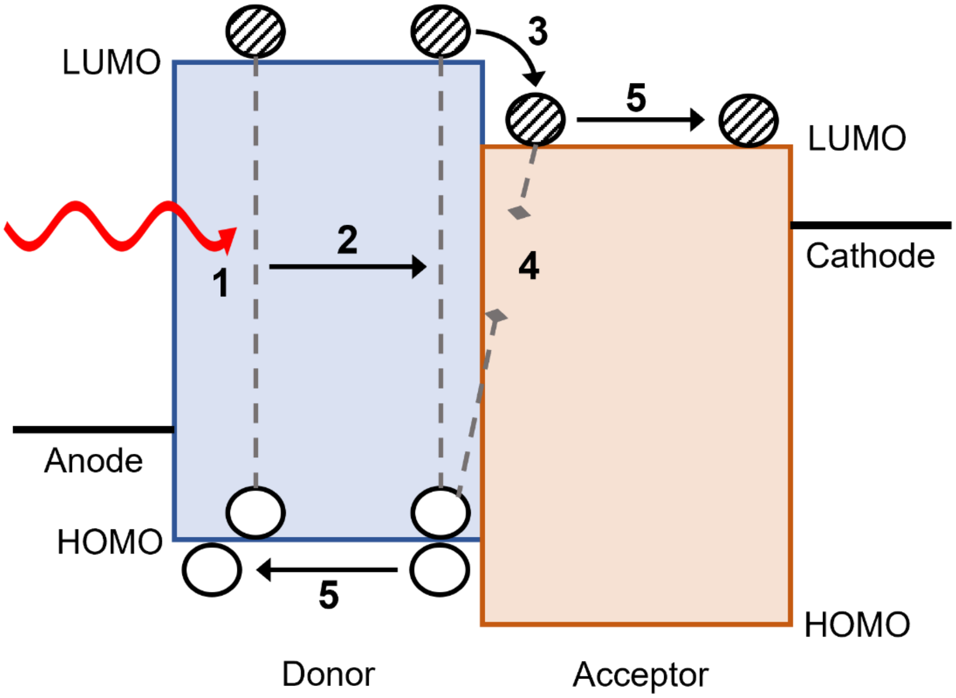

Figure 1.10. Current generation in OPVs. A schematic for current generation in a bilayer active layer traditional OPV with **(1)** absorption, **(2)** exciton diffusion, **(3)** charge transfer, **(4)** exciton dissociation, and **(5)** charge collection processes labeled. Additional transport layers are omitted for simplicity. Electrons and holes are drawn as patterned and un-patterned circles, respectively.

thermodynamic stability of a BHJ and of the mixed region in planar mixed HJs is important for the long-term stability of the OPVs. While BHJs have shown the highest efficiencies to date for OPVs and TPVs, there is some concern about commercial scability due to the complex nature of the morphologies formed.

1.2.3 Current-voltage and external quantum efficiency measurements

OPVs are primarily characterized electrically with two techniques, 1) measurement of the characteristic current-voltage (*J*-*V*) curves and 2) the external quantum efficiency (*EQE*) at each wavelength. *J*-*V* curves are measured by sweeping the applied voltage under simulated AM1.5G 1-sun illumination to capture the fourth-quadrant characteristic *J*-*V* behavior (power generating quadrant) of the device. *EQE* measures the ratio of ratio of electrons generated from the device (n_{e^-}) to photons incident on the device (n_{ph}) at each wavelength. An example *J*-*V* curve is shown in Figure 1.8c with key *J-V* parameters labeled. The power conversion efficiency (*PCE*) of any PV is calculated from the *J-V* parameters using Equation 1.5, where J_{SC} is the short-circuit photocurrent, V_{OC} is the open-circuit voltage, *FF* is the fill factor, P_0 is the input power, and *M* is the spectral mismatch factor.[6]

$$PCE = \frac{J_{SC}V_{OC}FF}{P_0 M} \tag{1.5}$$

The *FF* is calculated from Equation 1.6 from the J_{SC}, V_{OC}, and the current and voltage at the maximum power point, J_{MP} and V_{MP}, respectively:

$$FF = \frac{J_{MP}V_{MP}}{J_{SC}V_{OC}} \tag{1.6}$$

The *EQE* can be integrated to give the J_{SC} through Equation 1.7, an important consistency check in all PV fields.

$$J_{SC} = q\int_{\lambda_1}^{\lambda_2} EQE(\lambda)S(\lambda)d\lambda \tag{1.7}$$

Conceptually, the *EQE* describes the overall efficiency of the current generation process at each wavelength. Current generation for a traditional architecture single junction OPV is illustrated in Figure 1.10. Light of sufficient energy to excite an electron from S_0 to S_1 or S_2 is absorbed by an active material (step 1). The exciton formed upon absorption must diffuse to the donor-acceptor interface (step 2) where the energy difference is sufficient to allow the excited state electron to transfer to the acceptor in a process referred to as charge transfer (step 3). If the exciton is formed in the acceptor, the ground state hole will transfer over to the donor and the excited state electron will remain in the acceptor. The interfacial energy difference overcomes the coulombic binding energy of the exciton (E_B) and generates free charge carriers, referred to as exciton dissociation (step 4). In the last step involving the active materials, the free charge carriers move through the active layers (electrons through the acceptor, holes through the donor) to be collected at electrode layers on either side of the active layer (step 5). The product of the efficiencies describing each step in the current generation process at a given wavelength is related to the EQE by Equation 1.8,

$$EQE = \frac{n_{e^-}}{n_{ph}} = \eta_A \eta_{ED} \eta_{CT} \eta_{DS} \eta_{CC} = IQE \cdot \eta_A \tag{1.8}$$

with the component efficiencies represented as η_A (absorption), η_{ED} (exciton diffusion), η_{CT} (charge transfer), η_{DS} (exciton dissociation), and η_{CC} (charge collection). The last four efficiencies are often combined into the internal quantum efficiency (IQE), where IQE is the efficiency of converting absorbed photons into electrons and $IQE \leq EQE$ at every wavelength.

1.2.4 Absorption in organic photovoltaics

Absorption in OPVs generally comes in two forms, 1) absorption by the active materials for photocurrent generation, and 2) absorption by the electrodes and interlayers, termed parasitic absorption. Parasitic absorption in opaque OPVs is detrimental to device performance because it can reduce absorption in the active layers and lower the current produced. It is equally or even more important in transparent photovoltaics (TPVs) as it impacts *PCE* and optical performance, which will be discussed in Chapter 2. Active layer absorption efficiency at a given location within a layer is determined by the molecular extinction coefficient (α) and the strength of the electric field at that position. The total absorption efficiency is determined by the spatially resolved absorption and the overall active layer thickness, d. In comparison to inorganic semiconductors, organic semiconductors often possess much higher values of α, facilitating the production of thin film OPVs with active layers typically less than 100 nm thick. Due to complex optical interference effects that dominate absorption in OPVs, the overall thickness of the device determines the strength of the electric field at specific locations and adjusting the individual thickness of any one layer can therefore impact the absorption efficiency elsewhere in the device. The strength of optical interference effects are such that engineering design of non-active layer thicknesses is often more impactful to active layer absorption than the active layer thickness.

1.2.5 Excitons and exciton diffusion

Absorption of light by an organic semiconductor to move an electron into the excited state results in the formation of an exciton, a coulombically bound electron-hole pair, while electronic excitation in inorganic semiconductors often results in the generation of free charge carriers. This distinction is defined by the exciton binding energy (E_B), which is small enough in many inorganic semiconductors to be overcome at room temperature. The exciton binding energy can be estimated with the Bohr model for a hydrogen atom with a single electron given in Equation 1.9, where m_e is the effective mass of the electron, ε_0 is the permittivity of free space, ε_r is the dielectric constant of the semiconductor, and $\hbar$ is the reduced Planck constant ($h/2\pi$).[7]

$$E_B = \frac{q^4 m_e}{2\varepsilon_0^2 \varepsilon_r^2 \hbar^2} \tag{1.9}$$

The E_B is inversely proportional to the squared dielectric constant of the material, which is generally larger for inorganic materials (11.7 for silicon) than for many organics (~2 to 4). The energy available at room temperature (T = 300 K) is k_BT = 25.7 meV, more than enough to overcome E_B in silicon of 14.7 meV and produce free charge carriers. Even the largest dielectric constant organic materials still possess an E_B of ~100 meV, much larger than k_BT. For this reason, organic semiconductors do not typically generate substantial free charge carriers without a built-in potential difference large enough to overcome the E_B. This is why HJs are needed in OPVs to facilitate the dissociation of excitons into free charge carriers. A direct result of the low dielectric constant in organic semiconductors is the critical importance of exciton diffusion to an interface at which the electron-hole pair can be separated. The exciton diffusion efficiency is related to the exciton diffusion length (L_{ED}), the mean path length traveled by an exciton before recombination or dissociation, by Equation 1.10.[3] For many organic semiconductors, L_{ED} is in the range of 10-20 nm so that the key limiting factor in OPV performance is η_{ED} and the selected active layer morphology is critical to overcoming this limitation.[8]

$$\eta_{ED} = e^{(-d/L_{ED})} \tag{1.10}$$

Exciton diffusion occurs via three primary mechanisms, Förster resonant energy transfer (FRET), Dexter energy transfer, and trivial (radiative) energy transfer. The most likely mode of energy transfer can in part be determined by the type of exciton created and the spin-state of the exciton. Excitons in organic semiconductors have a large E_B, and therefore the electron will be tightly held to the hole and the exciton Bohr radii (r_E, Equation 1.11) will be small. This results in the hole and electron existing on the same molecule in what is called a Frenkel exciton.[7]

$$r_E = \frac{\hbar^2 \varepsilon_0 \varepsilon_r}{m_e q^2} \tag{1.11}$$

For an intermediate dielectric constant, a charge-transfer exciton is formed wherein the excited state electron and hole exist on different but adjacent molecules. Lastly, for very large r_E often found in inorganic semiconductors, Wannier-Mott excitons are created where the electron and hole can be separated by many atoms and the exciton Bohr radii is larger than the lattice constant of the material. Excitons are also designated as either singlet or triplet in much the same way as electrons discussed in section 1.1.2, where the excited state electron is either spin paired or has parallel spin with the ground state electron while also being bound to the hole.

Singlet exciton diffusion is possible through FRET, Dexter energy transfer, and trivial energy transfer. Exciton diffusion via FRET occurs through dipole-dipole coupling when the energy of the excited state electron is passed to an electron on a neighboring molecule, so that the electron on the donor relaxes from an excited state to S_0 and the acceptor electron moves from S_0 to an excited state (Figure 1.11a). The rate of energy transfer (k_F) for FRET is described by Equation 1.12, with the nearest neighbor distance (d_0), the Förster radius (R_0), and the exciton lifetime (τ_e). The Förster radius is the distance at which the efficiency for energy transfer is 50%.

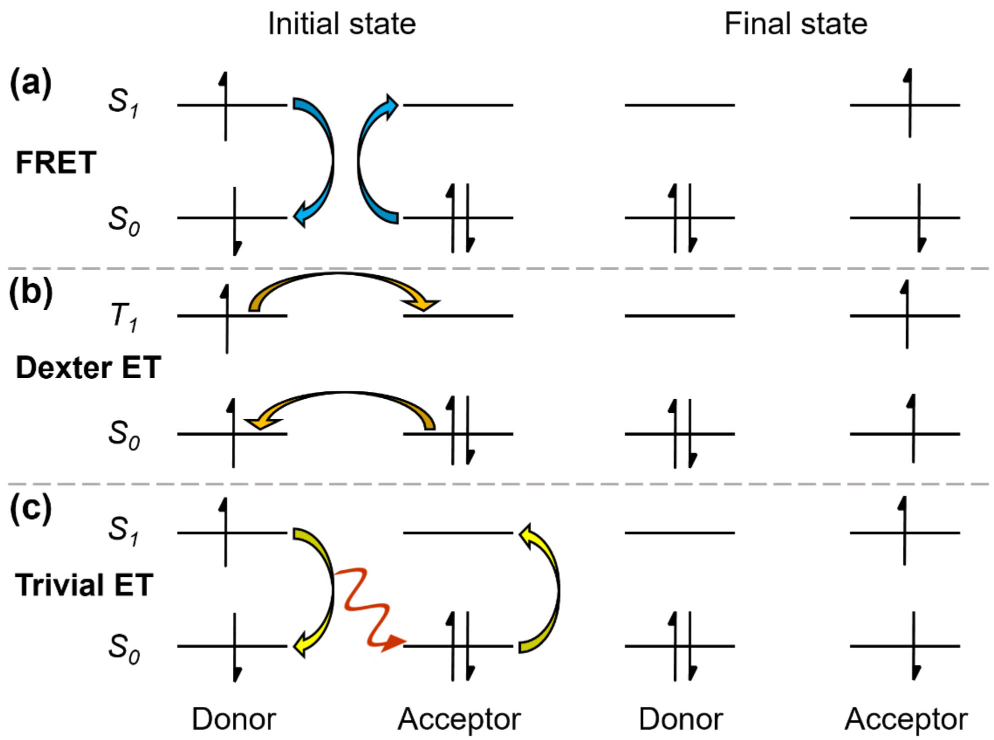

Figure 1.11. Modes of exciton diffusion. Schematic representation of the process for **(a)** Förster resonant energy transfer (FRET), **(b)** Dexter (triplet) energy transfer (Dexter ET), and **(c)** trivial energy transfer (Trivial ET).

Substituting the definition of R_0, Equation 1.12 can be expressed in measurable quantities such as the fluorescence quantum yield of the donor (Φ_F) and overlap integral of the donor emission and acceptor absorption (σ_{DA}), as well as the index of refraction (n) at maximum σ_{DA} and the transition dipole orientation factor (κ, equal to $0.845\sqrt{2/3}$ for amorphous films).[8]

$$k_F = \left(\frac{R_0}{d_0}\right)^6 \frac{1}{\tau_e} = \frac{1}{\tau_e d_0^6}\left(\frac{3}{4\pi}\frac{\kappa^2 \Phi_F}{n^4}\sigma_{DA}\right) \tag{1.12}$$

The overlap integral, σ_{DA}, is calculated from Equation 1.13, where $PL(\lambda)$ is the photoluminescence emission spectra for the donor, and $\alpha(\lambda)$ is the molar extinction coefficient of the acceptor.[9]

$$\sigma_{DA} = \frac{\int PL(\lambda)\alpha(\lambda)\lambda^4 d\lambda}{\int PL(\lambda) d\lambda} \tag{1.13}$$

In the case of exciton diffusion in a single component amorphous film, homogeneous FRET rate is optimized for closely packed molecules (small d_0) with a fast radiative recombination rate (low

τ_e, high Φ_F) and strong overlap between the emission and absorption profiles (large σ_{DA}). The L_{ED} for FRET is calculated from Equation 1.14, and similar to the FRET rate shows a strong dependence on d_0.[8]

$$L_{ED} = \frac{1}{\sqrt{6}} \frac{R_0^3}{d_0^2} \tag{1.14}$$

Dexter energy transfer for exciton diffusion occurs via electron exchange or hopping, shown in Figure 1.11b, where the excited state electron moves to the acceptor molecule and a ground state electron moves to the donor molecule. Dexter energy transfer is most common for triplet excitons, although it is also possible for singlet excitons, albeit with smaller rates. The rate of dexter energy transfer (k_D) is described in Equation 1.15, with the normalized overlap integral of donor emission and acceptor absorption (σ^*_{DA}), normalization constant (K), and the effective orbital radius of the final and initial electronic states (χ):[8]

$$k_D = \frac{2\pi}{h} \frac{K}{d_0^2} e^{(-2d_0/\chi)} \sigma^*_{DA} \tag{1.15}$$

The L_{ED} for Dexter energy transfer is given in Equation 1.16, and demonstrates a strong exponential decay dependence on the intermolecular distance (hopping distance) and a linear weaker dependence on the normalized overlap integral than the L_{ED} for FRET.[8]

$$L_{ED} = \sqrt{\frac{\tau K \sigma^*_{DA}}{3h}} e^{(d_0/\chi)} \tag{1.16}$$

With trivial energy transfer, the exciton relaxes back to the ground state and emits a photon that is absorbed by another molecule to excite another exciton, thus transferring the energy (Figure 1.11c). The rate of trivial energy transfer is strongly dependent on a high Φ and a relatively small α so that the emitted photon travels farther before reabsorption. Crucially, the rate and L_{ED} (Equation 1.17) are independent of the intermolecular distance.[10]

$$L_{ED} = \sqrt{\left(\frac{1}{6\alpha^2}\right)\left(\frac{\Phi}{1-\Phi}\right)} \tag{1.17}$$

In section 1.2.2, the donor-acceptor interfaces were compared for several common OPV active layer architectures. The η_{ED} can be greatly enhanced with a large interfacial area so that excitons have a much shorter path to travel to a dissociating interface. This is one of the keys to enabling excellent OPV performance in planar mixed HJs and BHJs. However, designing OPVs with longer LED can lead to similarly high efficiencies with much simpler processing.

1.2.6 Charge transfer and exciton dissociation

The charge transfer and exciton dissociation efficiencies are dependent on the energetics of the donor-acceptor interface, and at times are considered a single step in the current generation process. The LUMO-LUMO offset between the donor and acceptor is needed to overcome the exciton binding energy (Figure 1.10) and create free charge carriers. As discussed in section 1.2.5, E_B can be quite large in organic semiconductors owing to the low dielectric constants. Conceptually, the bandgap of the donor material could simply be raised until a sufficient offset is achieved. However, the V_{OC} of the OPV is determined by the smallest bandgap in the cell, which is the interface gap between the HOMO of the donor and the LUMO of the acceptor. The *PCE* is proportional to the voltage, so the balance between the interface gap and the LUMO-LUMO offset is crucial to generating photocurrent while maintaining the V_{OC}. The location and size of the bandgap therefore, are key design factors for organic semiconductors, and the donor-acceptor pair must be well chosen to optimize an OPV.

1.2.7 Charge collection

The final step in current generation in an OPV is the transfer of free charge carriers from the donor-acceptor interface to the supporting layers, and subsequently the electrodes. The η_{CC} is calculated from Equation 1.18 with the mean path length for charge collection, L_{CC} as:[3]

$$\eta_{CC} = \left(\frac{L_{CC}}{d}\right)\left(1 - e^{(-d/L_{CC})}\right) \tag{1.18}$$

There are two primary modes of carrier transport in organic semiconductor thin films, 1) carrier diffusion driven by a concentration gradient, or 2) carrier drift driven by the intrinsic electric field within the device. The carrier diffusion length, L_{Diff}, is related to the carrier mobility, μ, and carrier lifetime, τ, by Equation 1.19, where Z is the dimensionality factor equal to six for three-dimensional diffusion.

$$L_{Diff} = \sqrt{\frac{Zk_BT\mu\tau}{q}} \tag{1.19}$$

Carrier transport via carrier drift is described by Equation 1.20, where V_{BI} is the built-in electric field in the device and w is the depletion width.[11]

$$L_{Drift} = \frac{\mu\tau V_{BI}}{w} \tag{1.20}$$

The depletion width is a region around the donor-acceptor heterojunction devoid of free charge carriers so that carriers generated at the donor-acceptor interface experience a linearly decreasing voltage that moves the carriers away from the interface. The size of the depletion width is strongly correlated to the amount of band-bending at the donor-acceptor junction. Band-bending causes the V_{OC} to be strongly dependent on the thickness of the active layers. The depletion width size is difficult to measure, but has been shown to be quite small in organic semiconductors such that diffusion is usually the controlling mode of charge transfer.[12] Charge collection requires a continuous path for carriers to travel from the donor-acceptor interface to the electrodes. A perfectly mixed layer, or an overly well mixed BHJ creates an energetically torturous path for carriers to travel, greatly inhibiting charge collection.

1.3 Theoretical and experimental limits of organic photovoltaics

The fundamental theoretical limits of single-junction OPVs are now considered, along with the practical limitations of these devices. The theoretical Shockley-Queissar (SQ) limit for *PCE* of a single junction opaque PV is 33.1%.[3] The theoretical SQ limit can be increased by stacking multiple devices together to create a tandem PV device with *PCE* limits of 43% and 48% for two- and three-cell tandems, respectively.[3] The single junction SQ limit is derived with several key assumptions, 1) the PV is illuminated by an AM1.5G spectrum with 1-sun intensity, 2) the *EQE* is 100% at every wavelength above the bandgap and zero at every wavelength below the bandgap, 3) each photon absorbed creates only one exciton, and subsequently one electron with the remaining energy of the incident photon given off as heat by nonradiative relaxation, and 4) only radiative recombination exists in the PV cell. Given the above assumptions, the limiting factor in PV performance is the offset between current generation (*EQE* to the bandgap) and voltage (limited by the size of the bandgap) where a larger bandgap will increase the voltage and a smaller bandgap increases the current. The ideal bandgap for an organic semiconductor from the SQ limit is approximately 1.34 eV.[3] To understand the realistic limit, we first consider that the voltage in a single-junction OPV is actually limited by the interface gap, which must inherently be equal to or smaller than the bandgap of any material in the device. Thermal losses in the voltage will further reduce V_{OC} relative to the smallest material bandgap. From the discussion presented in section 1.2, it is clear that the assumption of 100% *EQE* above the bandgap is unlikely because of optical losses from electrode reflections and parasitic absorption. In OPVs, the active layer thicknesses must be optimized to achieve the best balance of absorption, exciton diffusion, and charge collection.

1.4 Current OPV state of the art performance metrics

The first single junction OPV by Tang demonstrated a *PCE* of 0.95% with a copper phthalocyanine and perylene derivative bilayer.[5] Pairing fullerene derivatives with polymers in bilayer OPVs increased *PCE*s to as high as 10.8% and 11.2% for binary and ternary (two polymers) devices.[13,14] The *PCE* of opaque OPVs has increased significantly in recent years, coinciding with the introduction of non-fullerene acceptors (NFAs) and their deployment in primarily BHJ architectures with donor polymers. NFAs are an exceptional class of discrete organic small molecules with strong extinction coefficients and electronic properties. Li et al. demonstrated 18.1% *PCE* in binary polymer-NFA BHJs with *FF* = 0.802, V_{OC} = 0.853 V, and J_{SC} = 26.5 mA cm^{-2}.[15] In some cases, two or three NIR absorbing NFAs are utilized in a single BHJ layer along with a visibly absorbing polymer in ternary or quaternary devices, which have achieved up to 19.3% *PCE* with J_{SC} = 26.6 mA cm^{-2}, V_{OC} = 0.896, and *FF* = 0.811.[16] These devices demonstrated 85-90% *EQE* from 500 to 800 nm.[16] All-small-molecule and all-polymer devices have also seen a rise in efficiency, although they still trail polymer-NFA BHJs. Qin et al. achieved 17.0% *PCE* with an all-small-molecule ternary OPV,[17] while Zhang et al. reached 16.5% *PCE* with a ternary all-polymer OPV.[18] In addition to BHJ approaches, sequential deposition techniques have quite recently led to high efficiency opaque OPVs with a planar mixed HJ architecture. Binary sequentially deposited OPVs have reached 18.2% *PCE* with J_{SC} = 26.8 mA cm^{-2}, V_{OC} = 0.860, and *FF* = 0.788.[19]

1.5 Summary

Organic semiconductors are highly adaptable materials that are good semiconductors for a range of electronic applications. They possess tunable selective absorption due to their discrete electronic states, and the bandgap of many organic semiconductors can be altered by extending or reducing conjugated networks in the molecule. OPVs are fundamentally limited by the tradeoff between photocurrent and voltage, both dependent on the bandgaps of the selected materials. Within the photocurrent, exciton diffusion is the primary limiting factor due to short exciton diffusion lengths, creating a tradeoff between absorption and exciton diffusion dependent on the active layer thickness. The development of BHJ and mixed planar HJ OPVs consisting of polymers and NFAs has reduced exciton diffusion limitations. BHJs have achieved efficiencies over 19%

PCE, and several different approaches and material combinations have achieved over 16% *PCE*. This demonstrates the effectiveness of organic semiconductors integrated into photovoltaics as light harvesting materials.

Chapter 2 – Transparent Photovoltaics

2.1 Introduction to transparent photovoltaics

Traditional opaque PVs deployed as building-integrated PVs (BIPVs) on the rooftops of existing infrastructure in the U.S. is one route to increase renewable energy production. This approach has the potential to generate up to 1400 TWh per year, almost 40% of the total electricity generation in the U.S.[20] However, many non-rooftop surfaces of existing infrastructure are not suitable for integration with traditional BIPVs because of the supporting infrastructure required or the need for transparency to visible light. TPVs offer an additional route to addressing the global energy demand as a complementary source of renewable energy to opaque PVs. Utilizing only the invisible portions of the solar spectrum, they are capable of transforming a wide variety of transparent and semitransparent surfaces into energy sources. Windows, greenhouses, cars, cellphones, and agricultural spaces are unavailable for integration with traditional PVs because of the required transparency. TPVs can be integrated with these surfaces without impacting the aesthetic appeal or altering their functionality. Furthermore, TPVs installed as BIPVs generate electricity near to the utilization site, reducing storage and distribution costs. In this chapter, we introduce key optical and electronic metrics for TPVs, different approaches to TPVs, and the fundamental and realistic limits arising from the need for aesthetic quality and high performance.

2.2 Optical and electronic evaluation of TPVs

A key fundamental difference between OPVs discussed in Chapter 1 and TPVs discussed here is the importance of the aesthetics and optical performance of TPVs. Achieving key thresholds in optical quality is of equal or even greater importance to the commercial deployment of TPVs than the power generation capabilities. To facilitate discussion of different types of TPVs and their limitations we introduce here four key figures of merit for evaluating TPVs.

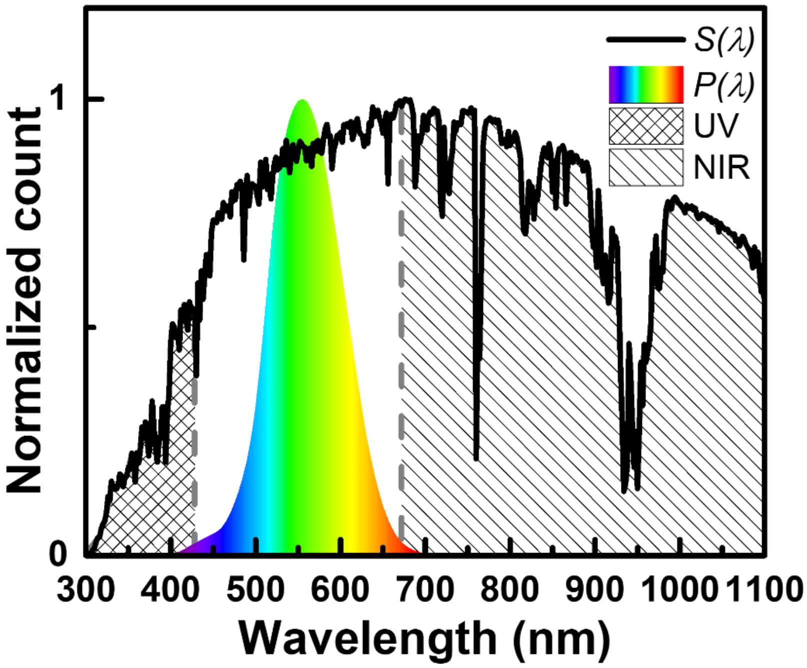

Figure 2.1. AM1.5G solar spectrum and photopic response. The AM1.5G solar spectrum for photon flux (black line) and the photopic response of the human eye (rainbow pattern). The ultraviolet (UV, cross-hatched pattern) and near-infrared (NIR, diagonal pattern) regions are marked on either side of the visible region (area between vertical dashed lines).

2.2.1 Average visible transmittance

The average visible transmittance (*AVT*) describes the overall transparency of a TPV weighted by the human eye photopic response, $P(\lambda)$ (Figure 2.1). This is expressed in Equation 2.1, where $T(\lambda)$ is the wavelength dependent transmittance of light through the device.[21,22]

$$AVT = \frac{\int T(\lambda)P(\lambda)S(\lambda)d\lambda}{\int P(\lambda)S(\lambda)d\lambda} \tag{2.1}$$

Important thresholds to achieve for commercial deployment of TPVs are around 50%-90% *AVT*.[22] If the *AVT* is below 50%, TPVs tend to be either highly colored, dark, or very reflective.[23] TPVs with *AVT* above 70% may still possess a color tint but will generally be clear or see-through. To contextualize TPV *AVT* performance, a quartz glass sheet has an *AVT* of approximately 92% due to ~4% reflection loss at each glass-air interface, and a standard double-pane window has an *AVT* near 80%.[22] Figure 2.2 shows the required *PCE* and *AVT* for various PV applications, highlighting

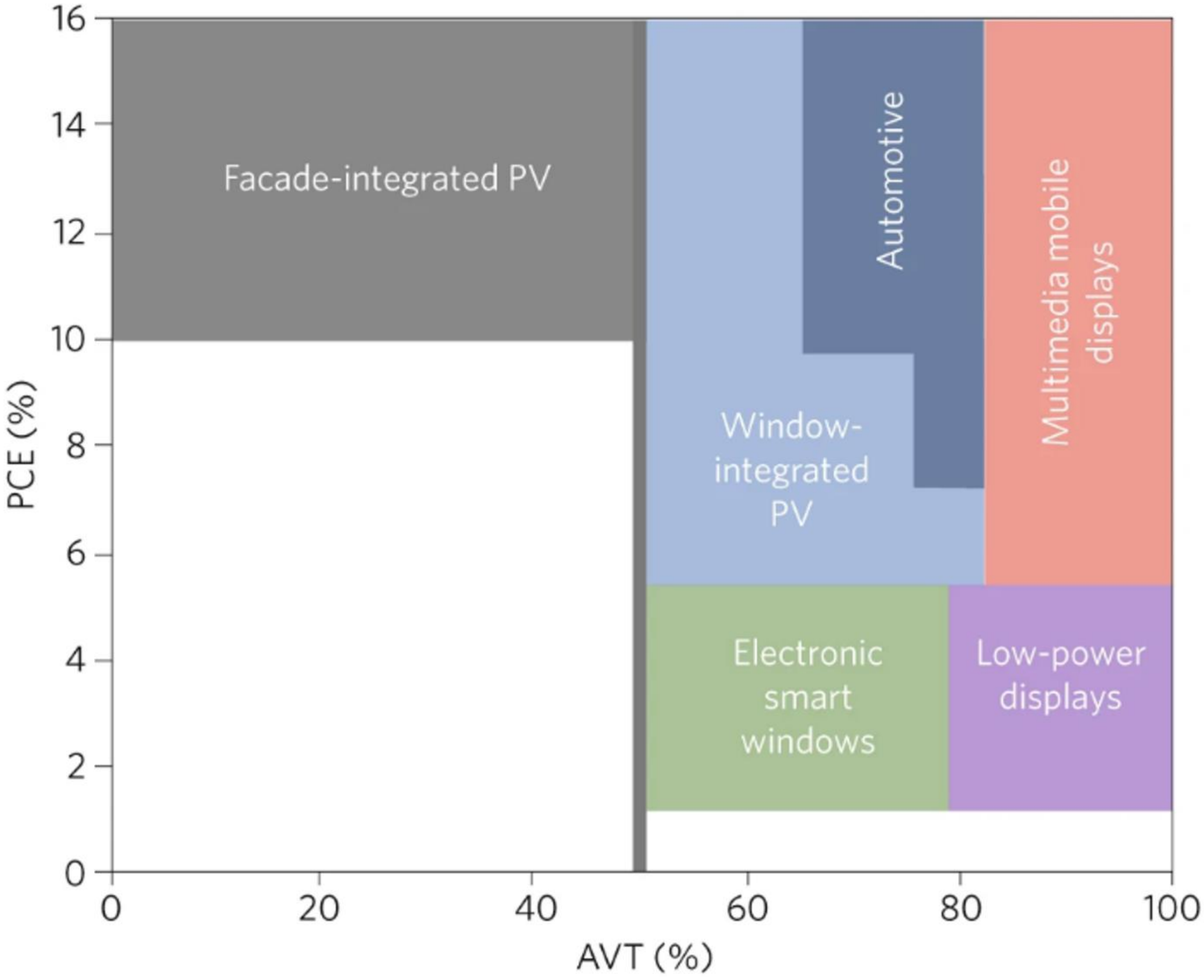

Figure 2.2. ***PCE* and *AVT* requirements for different PV applications.** The required power conversion efficiency (*PCE*) and average visible transmittance (*AVT*) for deployment of photovoltaics (PVs) based on the application. Figure reused with permission from ref. [22].

the importance of the *AVT*, and optical performance in general. While a relatively low *PCE* of 6% is required for window-integrated PVs, the minimum *AVT* is over 50%.

2.2.2 Light utilization efficiency

The light utilization efficiency (*LUE*), defined by Equation 2.2, captures the electronic and optical performance of a TPV in a single metric for comparison of devices with differing *AVT* and is limited by the SQ PCE limit (*AVT* = 100%).

$$LUE = PCE\ x\ AVT \tag{2.2}$$

It is a useful metric for evaluating the general quality of TPVs and an *LUE* ≥ 3.5% currently places

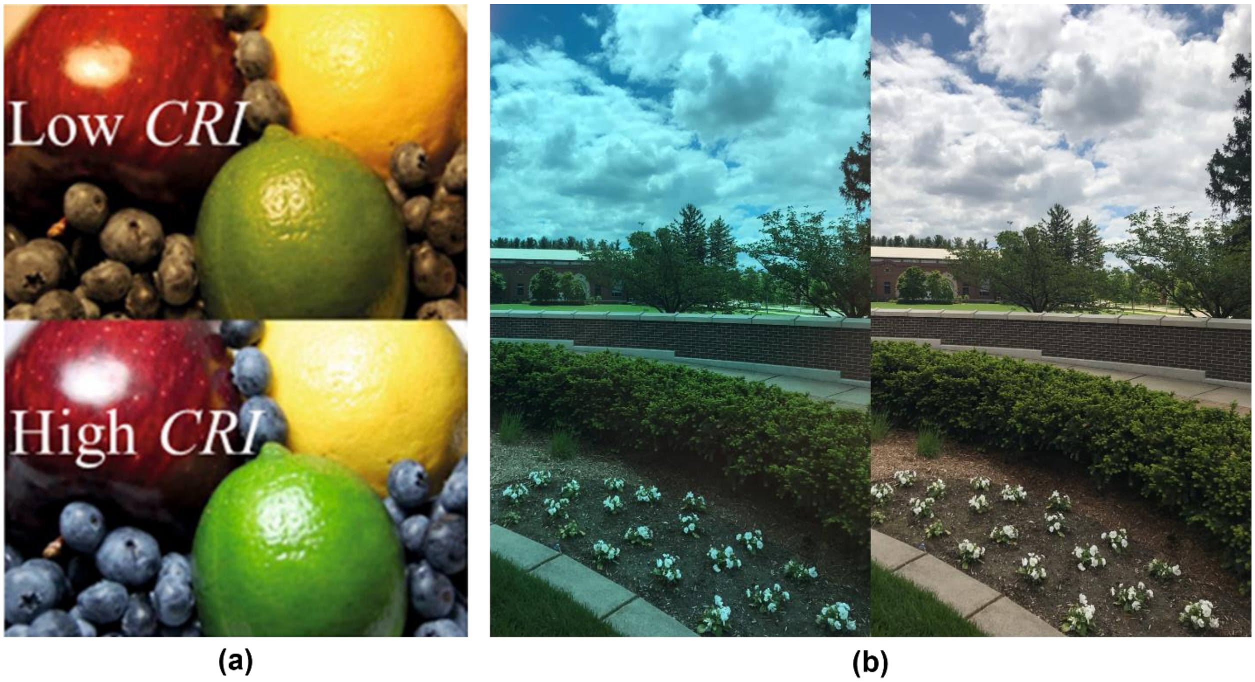

Figure 2.3. Examples of low and high *CRI*. (a) An example of low and high color rendering.[6] **(b)** A comparison of looking through a blue tinted TPV with a color rendering index of 65 and an average visible transmittance of 41% (left) and the same photo with the TPV removed (right).

among the best TPVs demonstrated. It is noted that the *LUE* does not convey a sense of the color tint of a TPV, which is also an important consideration for real-world applications.

2.2.3 Color rendering index and CIELab color coordinates

Two important metrics that quantify the color of a TPV are the color rendering index (*CRI*) and CIELab color coordinates (a^*, b^*). Both metrics are frequently used in the glass and window industries. The *CRI* describes how accurately a TPV renders the true color of an object when observed through the TPV, where the true color is based on unfiltered illumination of the object with the AM1.5G spectrum. *CRI* thresholds for commercial applications are 75 for acceptable quality, and 85 and above for excellent quality.[21,24] Two examples of low *CRI* (< 75) are shown in Figure 2.3 in comparison to reference images, with yellow (Figure 2.3a) and blue (Figure 2.3b) tints, respectively.[6] An unfiltered illumination of an object with the AM1.5G reference spectrum yields a *CRI* of 100, and importantly so will a neutral filter, as there will be no difference between the true color and the rendered color, just a decrease in overall light intensity. For this reason, *CRI* alone does not fully quantify the aesthetic performance. The CIELab color coordinates ($a*$, $b*$) quantify the specific color tint of the TPV and are commonly used in the window industry to assess the viability of a product for different applications. For tinted products in the glass and glazing industries, $-15 < a* < 1$ and $-15 < b* < 15$ are acceptable ranges. Mass-market architectural glass products use narrower ranges of $-7 < a* < 0$ and $-3 < b* < 7$.[25,26] It is important for TPVs to fall within the ranges listed here, however certain color tints (neutral or blue and green, as in Figure 2.3b) are generally preferable to others (yellow and red) for glazing and tinted glass applications.

2.2.4 Photon balance check

The photon balance check (Equation 2.3) is a crucial verification step for confirming a realistic reported *PCE* (from the J_{SC} via the *EQE*) and *AVT*.

$$A(\lambda) + T(\lambda) + R(\lambda) \leq 1 \tag{2.3}$$

The transmittance, $T(\lambda)$, and reflectance, $R(\lambda)$, of a TPV are measurable quantities (discussed in Chapter 3), while the absorption, $A(\lambda)$, is more difficult to assess. In TPVs without multi-exciton generation, the *EQE* is constrained by η_A where $EQE \leq \eta_A$ at every wavelength. Assuming an $IQE = 1$ for all wavelengths, *EQE* can be used as the upper-limit for $A(\lambda)$ through Equation 1.8. Substituting this in yields Equation 2.4, which can readily be evaluated for any TPV to confirm that the reported performance is within reason and that neither the *PCE* (*EQE*) nor *AVT* ($T(\lambda)$) have been overestimated.

$$EQE(\lambda) + T(\lambda) + R(\lambda) \leq 1 \tag{2.4}$$

2.3 Categorization of transparent photovoltaics

There are two primary branches of TPVs in terms of functionality, 1) PV devices with some level of transparency through the device, and 2) transparent luminescent solar concentrators

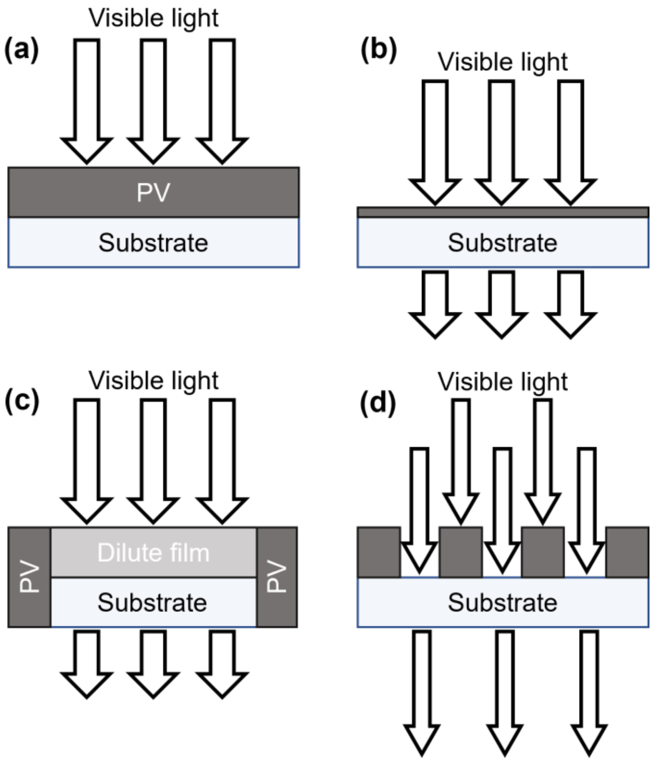

Figure 2.4. Non-wavelength selective approaches to TPVs. Schematic representation of **(a)** a fully opaque PV, **(b)** a non-wavelength selective thin TPV, **(c)** a non-wavelength selective dilute TLSC, and **(d)** a non-wavelength selective segmented TPV and how they interact with visible light. The PV cell is shown in gray mounted on a transparent substrate.

(TLSCs) which are optical devices with edge mounted PVs.[22] The active material in TLSCs functions as an absorber and emitter, with reemitted light waveguided to the side-mounted PV. TPVs and TLSCs each possess relative strengths and weaknesses. TPVs have typically demonstrated higher *PCE* but require two transparent conductive electrodes and are more complex structurally with a greater number of interlayers. For TLSCs to achieve high *PCE*, and J_{SC} specifically, the key challenge is overcoming the difficulty in achieving high NIR Φ with small overlap. Last, TPVs suffer from reduced visible transparency due to parasitic absorption and reflection from electrodes and supporting layers, and from neat semiconductor films, as opposed to the dilute doped active layer in TLSCs.

TPVs are broadly categorized based on the approach used to achieve transparency as either

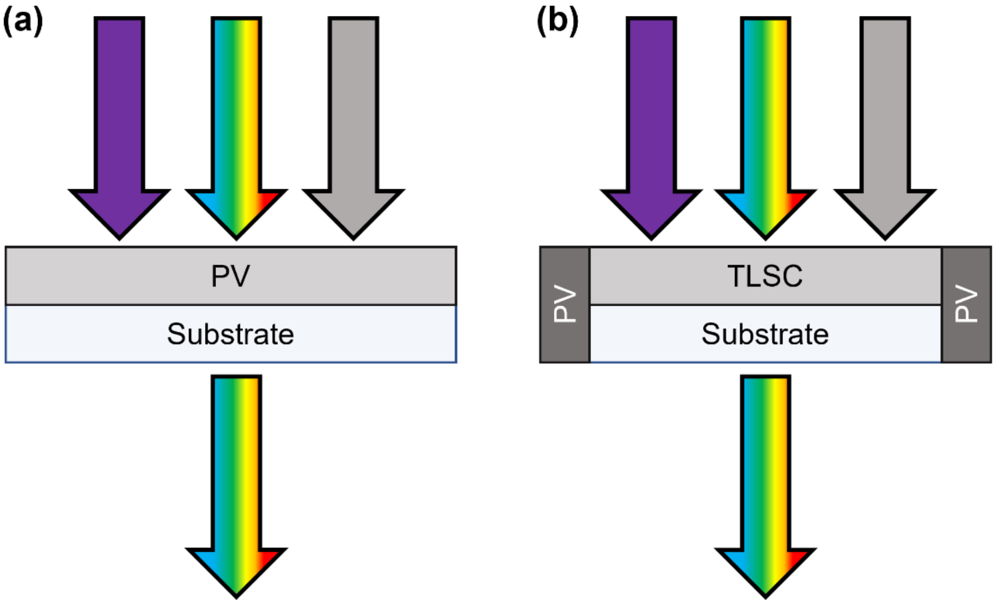

Figure 2.5. Wavelength selective approaches to TPVs. Schematic representation of **(a)** a wavelength selective traditional TPV and **(b)** a wavelength selective TLSC. Both examples of wavelength selective devices selectively absorb ultraviolet (purple arrow) and near-infrared (gray arrow) light while letting visible light (colored arrow) pass through.

non-wavelength selective or wavelength selective TPVs.[22] This is an important distinction as the fundamental transparency and theoretical efficiency limits are different for each approach.[21] Non-wavelength selective TPVs absorb across the solar spectrum and transparency is introduced through one of two methods, 1) taking an opaque PV (Figure 2.4a) and making the visibly absorbing layer(s) thin (Figure 2.4b) or dilute (Figure 2.4c) so that some visible light passes through, or 2) spatially segmenting opaque PVs so that certain regions have 100% transparency to visible light and others have no transparency to visible light (Figure 2.4d). There is a direct trade-off between *PCE* and the *AVT* in non-wavelength selective TPVs because transparency is achieved by removing photoactive material. Non-wavelength selective TPVs are generally limited to 50% or less *AVT* to maintain a reasonable *PCE*. At an *AVT* of ~80%, *PCE*s typically approach 0% due to reflection and optical losses.

Wavelength selective traditional TPV approaches offer a route to higher transparency and optical performance by utilizing semiconductors that absorb only invisible wavelengths of light in

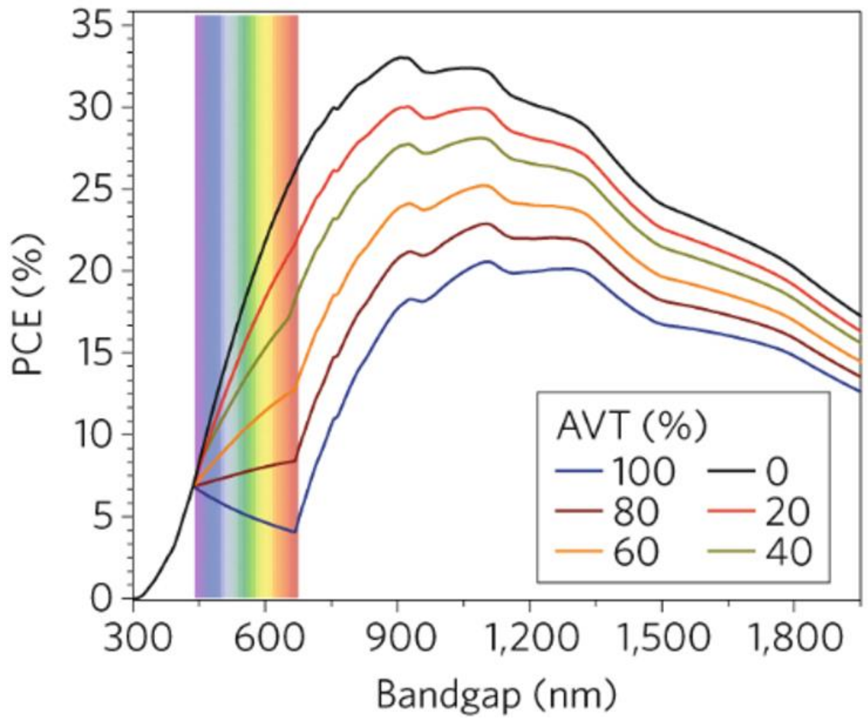

Figure 2.6. ***PCE*** **limit for TPVs as a function of bandgap and** ***AVT*****.** The power conversion efficiency (*PCE*) as a function of the active material bandgap for different levels of average visible transmittance (*AVT*). Figure reused with permission from ref. [22]. Data originally from ref. [21].

the UV and NIR (Figure 2.5a and b). Wavelength selective TPVs have a much smaller trade-off between *PCE* and *AVT* due to the photocurrent coming from UV and NIR light. Organic semiconductors are ideal candidates for a wavelength selective approach, as the optical gap that arises from a discontinuous density of states above the bandgap can be placed in the visible portion of the solar spectrum by design. This allows visible light to pass through the material while UV and NIR light is harvested for power production. From a power generation perspective, wavelength selective TPVs are able to access the most abundant portion of the solar spectrum for photon flux (Figure 2.1). The NIR contains 73.5% of the total photon flux of the solar spectrum, with 22.6% in the VIS and 3.9% in the UV.[21]

2.4 Limits for transparent photovoltaics

From a similar analysis of the SQ thermodynamic limit for PVs discussed in section 1.3, fully transparent (100% *AVT*) wavelength selective single junction TPVs have a theoretical limit of 20.6% *PCE* (or *LUE*) (Figure 2.6).[21] This is reduced from 33.1% for opaque single junction PVs primarily as a result of the decreased photocurrent without visible light absorption. Similar to opaque OPVs, E_G is the controlling factor of the voltage and current in TPVs in that it sets the smallest material bandgap in the TPV and the wavelength cutoff for light harvesting. The ideal bandgap for an active material in single junction wavelength selective TPVs is 1.12 eV (~1100 nm), smaller than the 1.34 eV ideal bandgap for the analogous opaque devices.[21] Practically, there is an expected 5-20% loss in *AVT* due to parasitic absorption and reflection from the electrodes and supporting layers. Limiting these optical losses is key to developing high *PCE* and *AVT* TPVs. Additionally, the underlying assumptions of 100% *EQE* at wavelengths above E_G (not including visible wavelengths) pertains to the theoretical limit here as well, so that a more practical limit of 11% *PCE* with ~80% *AVT* is estimated.[21] TPVs require organic semiconductors with the same properties that make them excellent candidates for OPVs, with the added requirement of selective absorption in the NIR and UV. Just as it is for OPVs, the exciton diffusion length of the active materials is a key factor for the *PCE* in TPVs.

2.5 Summary

Visibly transparent photovoltaics are an emerging technology that has complementary applications to existing traditional PVs and can further increase production of renewable energy. Crucially, TPVs can be readily integrated into existing infrastructure and have the potential to power buildings and charge electronics at the source of power generation without visibly affecting the aesthetic appeal or functionality. Wavelength selective TPVs take advantage of the significant photon flux in the invisible portions of the solar spectrum (> 75% of the total flux) to produce power while transmitting visible light. TPVs are characterized optically with the *AVT*, *CRI*, and CIELab color coordinates (a^*, b^*), and optoelectronically with the *LUE*. Key to the development of TPVs is the balance of power generation and aesthetic performance, which require active materials with excellent exciton diffusion and charge collection capabilities in tandem with selective NIR and UV absorption. Additionally, reducing optical losses from electrodes and supporting layers will enable better optically performing TPVs.

Chapter 3 – Cyanine-based Organic Salt Photovoltaics Review

This chapter was published as a review paper in *Sustainable Energy & Fuels* as "Organic Salt Photovoltaics".[27]

3.1 Introduction

Organic salts are ionic compounds comprised of a cation and anion with at least one organic molecule in the pair (Figure 3.1). The ionic character is similar to that of inorganic salts (e.g. NaCl, KCl etc.) but more closely related to ionic liquids in both composition and ordering. Indeed, while many semiconducting organic salts have extended conjugation to generate more interesting bandgaps, this typically increases melting points past decomposition limits. Common photoactive cations include cyanine dyes of varying conjugation length, polymethines, hemicyanines, ionic polymers, cyanine dyads, pyrylium dyes, chalcogenopyrylium monomethine, azapyrenes, and non-photoactive tetrabutylammonium, among others.[28–43] Anions used in organic salt PVs are generally non-photoactive and include halides, perchlorate, phosphates, antimonates, borates, carboranes, and even photoactive cyanine sulfonates.[44,45] Many of these counterions are weakly coordinating anions (WCAs), which is in part why organic salt OPVs, introduced in the 1970s, were not consistently investigated until a greater range of WCAs emerged.[46] Figure 3.2 depicts many of the cationic cyanines and counterions discussed in this review (cations are referenced by number as they are mentioned). Organic salts have been used historically in a wide range of applications including medical imaging, photographic emulsions, chemical sensors, 'click' bioconjugation, solar concentrators, and recording media.[3,47–64] Photovoltaic devices utilizing organic salts in the active layer are generally considered small molecule based organic solar cells, however the unique properties and tunability that organic salts provide warrants consideration as a new class of OPV donors and acceptors. Organic salts have many properties that make them

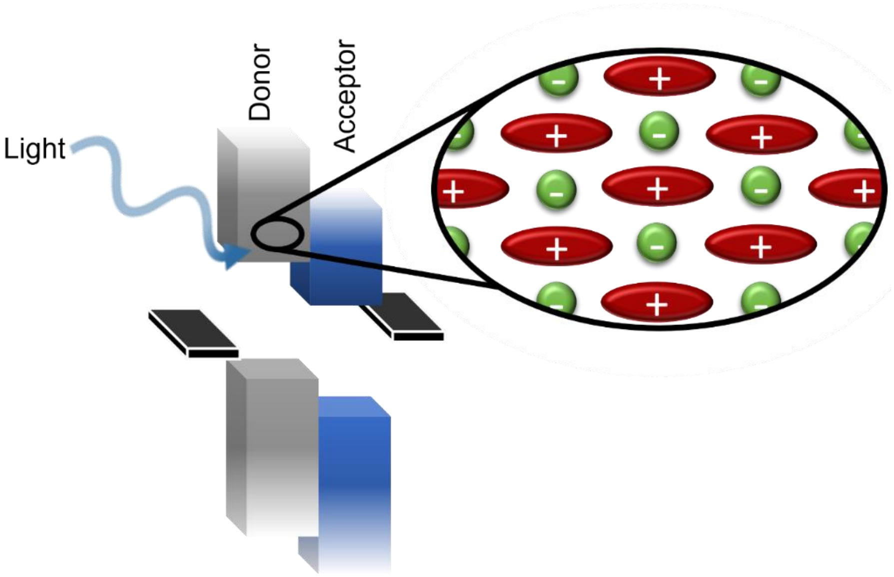

Figure 3.1. Schematic of an organic salt-based PV. A simplified schematic of an organic photovoltaic device showing light absorption by the active layers, one or both of which consist of the organic salt shown in the expanded view.

suitable materials for OPVs, including strong absorption demonstrated by high extinction coefficients, tunable absorption in the visible and near-infrared (Figure 3.3), precisely defined molecular weights, and are solution processable. Furthermore, the very notion of using organic salts conjures the image of table salt dissolving in water, thus implying the potential for a high sensitivity to moisture and a low likelihood for success in electronic applications. However, many of the demonstrated salts to date are sparingly soluble in water and actually show very good application in optoelectronics devices. The widespread use of these salts and their exceptional properties for OPV applications make them exciting materials for further research.

This review is outlined as follows: we first detail the historical integration of organic salts into solar cells before summarizing the properties of weakly coordinating anions. We then review topics unique to organic salt PVs, including the role of the counterion in these devices and ion mobility in the active layer. We then examine detailed photovoltaic processes in organic salt PVs, focusing on exciton diffusion and charge carrier generation, transport, and collection. We conclude by highlighting the capabilities organic salts enable in transparent photovoltaics, as well as the

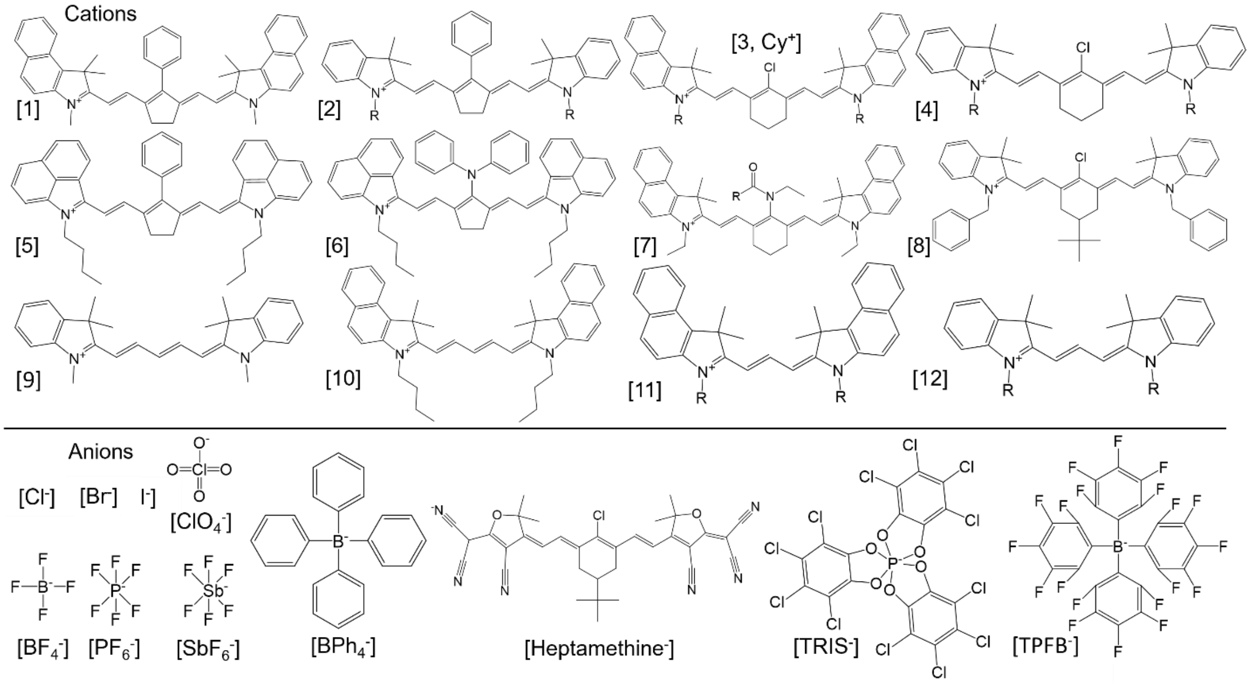

Figure 3.2. Various cationic cyanines and common counterions. Organic cationic cyanine dyes (top), including heptamethines (1-8), pentamethines (9-10), and trimethines (11-12). Common counterions (bottom) paired with cationic cyanines in organic salts.

stability of these devices, followed by a summary of important knowledge gaps in this emerging field.

3.2 Historical development of organic salt-based photovoltaics

We start by reviewing the development of organic salt based organic photovoltaics (OPVs), focusing on device and molecular structure, key photovoltaic parameters, and quantum efficiencies. For context, other single junction small-molecule and polymer based OPVs have been extensively reviewed and have achieved over 9% and 10% efficiencies, respectively, with multijunctions over 11% for polymer and small molecule devices.[64–66] *PCE*s for organic salt devices, in contrast, have risen from 0.3% to 3.7%, and parameters such as J_{SC}, V_{OC}, and *FF* have similarly increased. External quantum efficiencies (*EQE*s) have seen massive gains in magnitude and in breadth, reaching as high as 80% and harvesting light in the NIR, and recently extending out as far as 1600 nm.

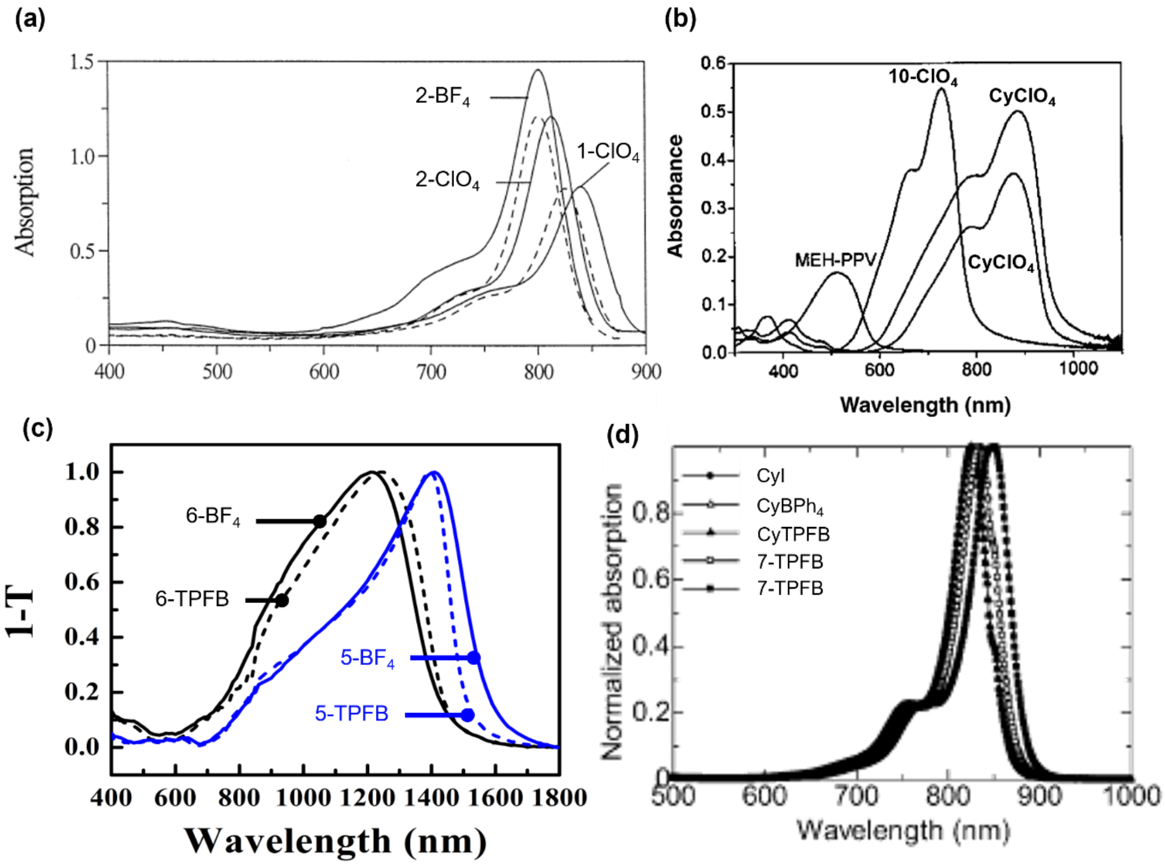

Figure 3.3. Absorption spectra of various organic salts. (a) Organic salt absorption in polyurethane acrylate (solid) and ethanol (dashed),[36] **(b)** organic salt thin films with NIR absorption,[76] **(c)** salt thin films demonstrating deep NIR absorption out to 1600 nm,[95] **(d)** thin films showing NIR absorption.[37]

Ghosh was among the first to propose the use of organic salts as active layers in 1978 in a U.S. patent for photovoltaic devices using an organic layer between two electrodes.[67] Ghosh put forth several different organic materials, including cyanines and hemicyanines, even though the organic salt variations of these materials were not reported among the data. One of the first reports of functioning organic salt PVs came from Stepanova et al., who used pyrylium dye cations with ClO_4^- counterions as an acceptor material for OPVs in the late 1970s.[68] Thin film preparation techniques noted by Whorle et al. in 1991 included vacuum deposition, spin coating, chemical vapor deposition, and plasma polymerization.[69] Stepanova's solar cells were fabricated with indium tin oxide (ITO) as the anode followed by vacuum deposited copper pthalocyanine, spin coated organic salt, and an indium cathode. This device demonstrated PCE = 0.43%, V_{OC} = 0.45 V, and J_{SC} = 1.6 mA cm^{-2} under 70 mW cm^{-2} irradiation. Early devices struggled to achieve high PCEs without the metallophthalocyanine donor Simon used.

Although organic salt based OPVs were first used in the 1970s and 1980s, consistent development of such devices did not start in earnest until the early 2000s.[70] In 2003, Meng et al. used a trimethine (cation 12)$^+$/ClO$_4^-$ organic salt as an acceptor and donor layer in OPVs.[71] An organic salt donor paired with a fullerene acceptor layer demonstrated efficiency = 0.0038%, with FF = 0.20, V_{OC} = 0.25 V, and J_{SC} = 0.11 mA cm^{-2}. The band gap of the organic salt was 2.1 eV, an order of magnitude higher than the V_{oc}. The high bandgap salt limits spectral harvesting to photons with equivalent or greater energy, leading to the low J_{SC}. With this organic salt as the acceptor, paired with a polymer donor layer, the device demonstrated PCE = 0.0082%, V_{OC} = 1.28 V, J_{SC} = 0.05 mA cm^{-2}, and FF = 0.20. A peak EQE from the organic salt of 4% was demonstrated at 575 nm. Other work showed the use of organic salts as acceptors and donors in bulk heterojunction devices (BHJ) with a thin film of two organic salts on a gold substrate.[72] Both organic salts utilized anionic trimethines and exhibited a 2% peak EQE at 650 nm. The reported PCE was 0.05%, with a 0.19 V V_{OC} and 0.007 mA cm^{-2} J_{SC}.

Despite improvements, early investigations of organic salt PVs suffered from particularly low PCEs. In 2005 Nuesch et al introduced a PEDOT:PSS interlayer between the ITO anode and trimethine (12)$^+$/ClO$_4^-$ donor paired with fullerene.[73] Devices with PEDOT:PSS had V_{OC} = 0.43 V and J_{SC} = 0.13 mA cm^{-2} while those without demonstrated V_{OC} = 0.28 V and 0.1 mA cm^{-2} J_{SC}. PEDOT:PSS improved the hole extraction into ITO, improving V_{OC} by over 50%. Improving on this initial PEDOT:PSS interfacial layer, Nuesch et al. demonstrated modest PCE = 0.09% at 31 mW cm^{-2} illumination, which decreased to 0.02% at 310 mW cm^{-2}.[74] At higher intensity, the fill

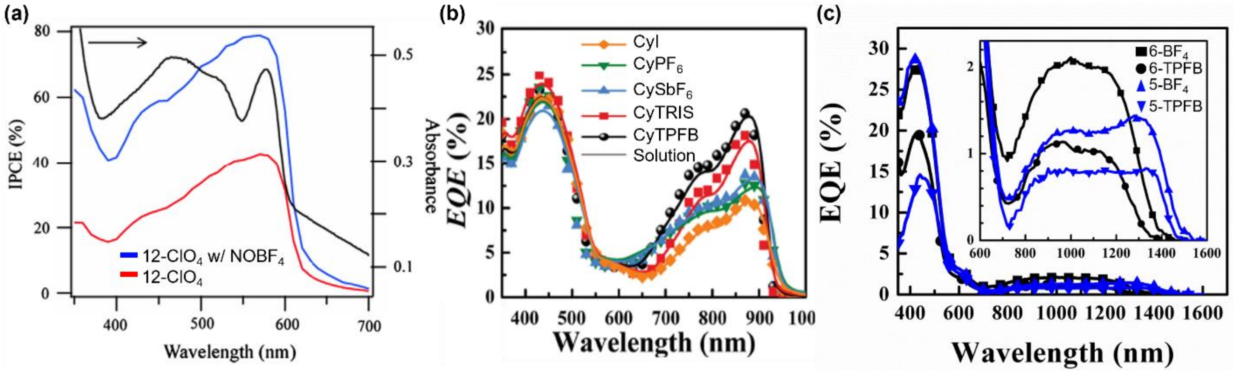

Figure 3.4. External quantum efficiency of organic salt-based PVs. (a) Demonstration of 80% peak incident photon conversion efficiency (*IPCE*, also known as external quantum efficiency, *EQE*) after addition of dopant NOBF$_4$.[78] **(b)** *EQE* of various anions paired with the same cation.[94] **(c)** *EQE* of organic salt devices demonstrating deep NIR (1600 nm) photoresponse.[95]

factor was notably low at 0.16 (any value less than 0.25 shows inverted curvature in the *J-V* and indicates high resistances). In 2005, Meng et al. synthesized fullerene – organic salt dyads, wherein the trimethine cation of the trimethine$^+$/ClO$_4^-$ organic salt was covalently bonded to fullerene, paired with an additional fullerene acceptor layer.[75] Devices demonstrated 6% peak *EQE* at 540 nm with *PCE* = 0.041% at 310 mW cm^{-2} illumination, a 0.33 V V_{OC}, and 1.2 mA cm^{-2} J_{SC}. Castro et al. created devices utilizing a polymer/organic salt blend.[76] Three organic salts were mixed with the polymer, MEH-PPV, one with a pentamethine (10) cation, the others with a heptamethine (Cy$^+$) cation, all with a ClO$_4^-$ counterion. Figure 3.3b shows the absorption spectra for this system. The pentamethine (band gap of 1.5 eV) demonstrated a V_{OC} = 0.63 V, whereas the heptamethine (band gap of 1.13 eV) showed, surprisingly, a higher V_{OC} = 0.79 V. However, the J_{SC} was small, on the order of 1 µA cm^{-2} or less for all three devices, which limited the efficiency.

In 2008, Fan et al. investigated the doping of organic salt PVs by ambient air, water, and oxygen, with and without irradiation.[77] Fresh devices with a trimethine (12)$^+$/ClO$_4^-$ salt demonstrated *PCE* = 0.14%, with V_{OC} = 0.47 V, J_{SC} = 0.46 mA cm^{-2}, and 0.189 *FF*. After three hours of exposure to ambient atmosphere and irradiation at 5 mW cm^{-2} solar cells obtained a 1.2% PCE, 0.73 V V_{OC}, 1.83 mA cm^{-2} J_{SC}, and 0.274 *FF*. Doping with humid nitrogen or oxygen without irradiation saw little increase in performance indicating that oxygen exposure paired with irradiation improved devices. Fan et al. followed up that work in 2010 by doping bilayer trimethine (12)$^+$/ClO$_4^-$ salt (band gap of 1.7 eV) PVs with the nitrosonium salt NOBF$_4$, which has been used previously as an oxidizing agent.[78] At full sun irradiation and a concentration of 0.02 wt.% NOBF$_4$, a PCE = 2.0% was demonstrated with V_{OC} = 0.72 V, J_{SC} = 8.3 mA cm^{-2}, and FF = 0.34. The peak EQE of the devices, shown in Figure 3.4a, increased to 80% at 580 nm. In achieving such a high surprisingly high EQE there two primary possibilities. It is unlikely that the dopant improved the exciton diffusion length or bulk dissociation. Rather, it is more likely that the trimethine salt, already possessing an inherently high exciton diffusion length, showed enhancement from the lowering of charge collection barrier and/or improved charge collection. Alternatively, it is possible that the nitrosonium dopant promoted C$_{60}$ diffusion into the trimethine layer, potentially forming a bulk heterojunction structure and increasing the exciton dissociation efficiency. While the mechanism is still unclear, the utilization of PEDOT:PSS and Alq$_3$ interfacial layers, along with NOBF$_4$ as a dopant in trimethine salts resulted in remarkable performance in both PCE and EQE for a planar architecture.

The use of longer conjugated polymethines in OPVs was limited until Bouit et al. used heptamethines in 2009.[79] BHJ devices with a 1:2 PCBM and heptamethine (8)$^+$/heptamethine$^-$ salt layer demonstrated PCE = 0.4%, with J_{SC} = 3.78 mA cm^{-2}, V_{OC} = 0.37 V, and 11% peak EQE at 785 nm. This is one of the first instances of organic salt OPVs efficiently harvesting NIR light, and although the peak was lower than Fan's doped devices, it was red shifted over 200 nm. Absorbing NIR photons became a key ability of the organic salts and opened opportunities for deep NIR harvesting and transparent devices. In 2010, Fan et al. utilized PANI:DBS instead of PEDOT:PSS as an interfacial layer in trimethine (12)$^+$/PF$_6^-$ salt (1.8 eV band gap) PVs, demonstrating an *EQE* above 40% from 400 to 600 nm.[80] A *PCE* = 3% was attained, with *FF* = 0.61, J_{OC} = 6.92 mA cm^{-2}, and a 0.72 V V_{OC}. To better understand interfacial layers, Berner et al. investigated the effects of the anode buffer layer, TiO_X, smoothness on inverted device performance in 2013, utilizing the organic salt from Fan's work in 2010.[81] Sol-gel processed TiO_X demonstrated the best performance with *PCE* = 3.7%, V_{OC} = 0.88 V, J_{SC} = 6.2 mA cm^{-2}, and *FF* = 0.678. A TiO_X sputtered device achieved *PCE* = 2.9%, V_{OC} = 0.84 V, J_{SC} = 5.4 mA cm^{-2}, and *FF* = 0.63. The sol-gel processed and sputter deposited TiO_X results indicate the importance of a smooth, low resistance interfacial layer. Similarly, Malinkiewicz et al. studied the differences between PEDOT:PSS and MoO_3 interfacial layers in bilayer polymethine$^+$/anion$^-$ organic salt PVs.[82] Four salts were used, trimethine (12)$^+$/ClO_4^-, two other trimethine cations (11) with PF_6^-, and pentamethine (9)$^+$/PF_6^-. Organic salts with the PF_6^- counterion demonstrated improved *J-V* characteristics without the S-shaped curve seen with trimethine$^+$/ClO_4^- salts that implies a high bulk or interface resistance and which improved the *FF*. The role of the bulkier counterion PF_6^- is likely related to ion mobility in the active layer and is discussed in a later section. Replacing PEDOT:PSS with MoO_3 as the interfacial layer improved *J-V* characteristics even though the peak *EQE* from the organic salts decreased from 45% to 30%. The best device utilized a 23 nm layer of trimethine (11)$^+$/PF_6^- organic salt (1.9 eV band gap) and MoO_3, demonstrating a *PCE* = 2.9% with a V_{OC} = 0.92 V, J_{SC} = 5.1 mA cm^{-2}, and *FF* = 0.62. Malinkiewicz also observed changes in device performance based on interfacial layer and counterion selection, demonstrating improved *J-V* characteristics attributed to changes in either material.

Much of the development in organic salt PVs utilized layers of organic salt or a bulk layer of salt paired with fullerene, however, some work has been done in using organic salts as light harvesting dopants in polymer OPVs. In 2010, Yap et al. fabricated MEHPPV:PCBM heterojunction organic solar cells doped with tetrabutylammonium hexafluorophosphate ($TBAPF_6$), an organic salt.[83] The organic salt increased the J_{SC} from 0.54 µA cm^{-2} to 6.41 µA cm^{-2}, V_{OC} from 0.24 to 0.50 V, and fill factor from 0.16 to 0.18 compared to undoped devices. Due to the low *FF* and J_{SC} the *PCE* was $5.77x10^{-4}$%. Three years later, Sabri et al. investigated the concentration effect of $TBAPF_6$ doped MEH:PPV devices, demonstrating a 0.15% *PCE*, 0.53 V V_{OC}, 1.06 mA cm^{-2} J_{SC}, and 0.27 *FF* for 20 wt.% $TBAPF_6$.[84] J_{SC} and V_{OC} increased from 10 to 20 wt.% $TBAPF_6$ and decreased at 30 and 40 wt.%. Optimization of organic salt doping increased performance but such devices were still an order of magnitude lower in efficiency than organic salt PVs at the time. Most work with organic salts to this point had focused on relatively small inorganic anions, such as I^-, ClO_4^- and PF_6^-, but some work had been done with larger counterions, including polymeric counterions. In 2014, Wang et al. fabricated organic solar cells using a sulfoethyl methacrylate/methacrylate anion and trimethine (12) cation for an organic salt.[85] A 4.9 nm trimethine $(12)^+$/polymer$^-$ layer demonstrated *PCE* = 0.93% with V_{OC} = 0.63 V, J_{SC} = 2.3 mA cm^{-2}, and *FF* = 0.64. The best devices had *EQE*s between 6 and 10% from 400 to 700 nm. Limited progress has been made working with polymeric anions in the organic salt, although other bulky anions have recently received greater attention.

The anionic polymer discussed in the work of Wang et al. was one of the first organic counterions used and one of the first other than I^-, ClO_4^- and PF_6^-. A bulkier weakly coordinating organic anion, Δ-tris (tetrachloro-1,2 benzenediolato) phosphate(V) ($TRISPHAT^-$ or $TRIS^-$), that was used in several recent reports was introduced by Veron et al. to organic salt bilayer solar cells in 2014.[86] Devices with heptamethine $(4)^+$/$TRIS^-$ (1.17 eV band gap) salt demonstrated *PCE* = 2.2%, V_{OC} = 0.63 V, J_{SC} = 6.4 mA cm^{-2}, and *FF* = 0.648. Similar devices with PF_6^- showed *PCE* = 0.9%, V_{OC} = 0.38 V, J_{SC} = 3.6 mA cm^{-2}, and *FF* = 0.54. PF_6^- devices demonstrated a wider absorption profile paired with decreased current, indicating that a lower fraction of generated excitons diffused to the acceptor/donor interface and separated to create current. The counterion's role in lowering or increasing this charge generation efficiency however was not well understood.

Previous work doping organic salt PVs with oxygen or $NOBF_4$ led to significant improvements in efficiency, and in 2015, Jenatsch et al. utilized a p-type dopant in organic solar cells to investigate the effect of concentration and active layer thickness device performance.[87] A heptamethine $(4)^+/PF_6^-$ salt doped with a Co(III) complex and paired with fullerene was explored. Undoped devices demonstrated a decrease in FF and J_{SC} as the organic salt thickness increased while V_{OC} initially increased before decreasing for larger thicknesses. Undoped device efficiency increased from 1.20% at 10 nm thickness to 1.23% at 20 nm before declining to 0.95% for 45 nm thick salt layers. Doped devices demonstrated slight gains and losses in FF and V_{OC}, respectively, as the salt thickness increased. Doped PVs had decreased V_{OC} and J_{SC} relative to undoped devices at the same thickness due to higher recombination losses and exciton quenching, respectively. Undoped devices were more efficient at low thicknesses, although 10 and 20 nm salt layers were the most efficient and doped cells were not fabricated at those thicknesses. Jenatsch' work with doped PVs highlights some of the difficulties of optimizing V_{OC}, J_{SC}, FF, and EQE via material selection and implementation. While 20 nm undoped organic salt PVs demonstrated the best efficiency, other configurations showed higher V_{OC} or J_{SC}, indicating that better efficiencies are achievable with the right materials and optimization.

Dye-sensitized solar cells, a subset of organic PVs, have demonstrated efficiencies up to 7.3% and peak EQEs at almost 90%.[88] Recent progress in utilizing organic salts in DSSCs has been limited and such devices have struggled relative to other DSSCs, such as those utilizing squaraine dyes (8.9% PCE) or a combination of squaraine and other polymethine dyes (7.6%).[89,90]

Furthermore, all organic salt DSSCs have trailed DSSCs utilizing Ru-complex sensitizers.[90] For these reasons, organic salt DSSCs will not be discussed in depth, however, reviews of DSSC progress can be found elsewhere.[90–93]

While the anion was previously thought to have minimal impact on the organic salt PV, a key discovery was the systematic understanding of the importance and role of the counterion in the organic salt. Suddard et al. were the first to systematically investigate the effect of a range of counterions in organic salt based PVs as shown in Figure 3.4b and Figure 3.5a.[94] Device architecture incorporated a heptamethine (Cy^+)/anion$^-$ salt paired with fullerene and explored a series of anions including I^-, PF_6^-, SbF_6^-, TRIS$^-$, and tetrakis(pentafluorophenyl)borate (TPFB$^-$). Devices with TPFB$^-$ showed the highest efficiency, demonstrating a 2.0% PCE, 0.71 V V_{OC}, J_{SC} = 4.7 mA cm^{-2}, and FF = 0.60. Figure 3.5a demonstrates the drop from TPFB$^-$ to TRIS$^-$ devices in V_{OC} from 0.71 to 0.63 V, leading to PCE = 1.7% for CyTRIS. Short circuit current decreased to 4.4 mA cm^{-2} and FF increased to 0.62. The EQE peak for TPFB$^-$ devices were over 20% at 870 nm, as shown in Figure 3.4b, and increased with thickness from 9 nm to 12 nm before declining. The 0.71 V V_{OC} of the TPFB$^-$ device was near the predicted excitonic voltage limit for OPVs at that optical excitonic gap, demonstrating the potential of counterions to maximize the open circuit voltage by specifically modulating the frontier orbital level which led to an increase in the junction interface gap (reducing interface recombination). The full implications of the counterion in device performance are discussed in greater detail below.

In 2016, Young et al. used organic salts with benzene and phenylaniline groups anchored to a heptamethine backbone with a benzo[cd]indole end group in OPVs. In that work, they demonstrated the ability to harvest energy from the deep NIR spectrum up to 1600 nm, an unprecedented range for any photoactive organic materials and a result of ultra-low 0.8 eV

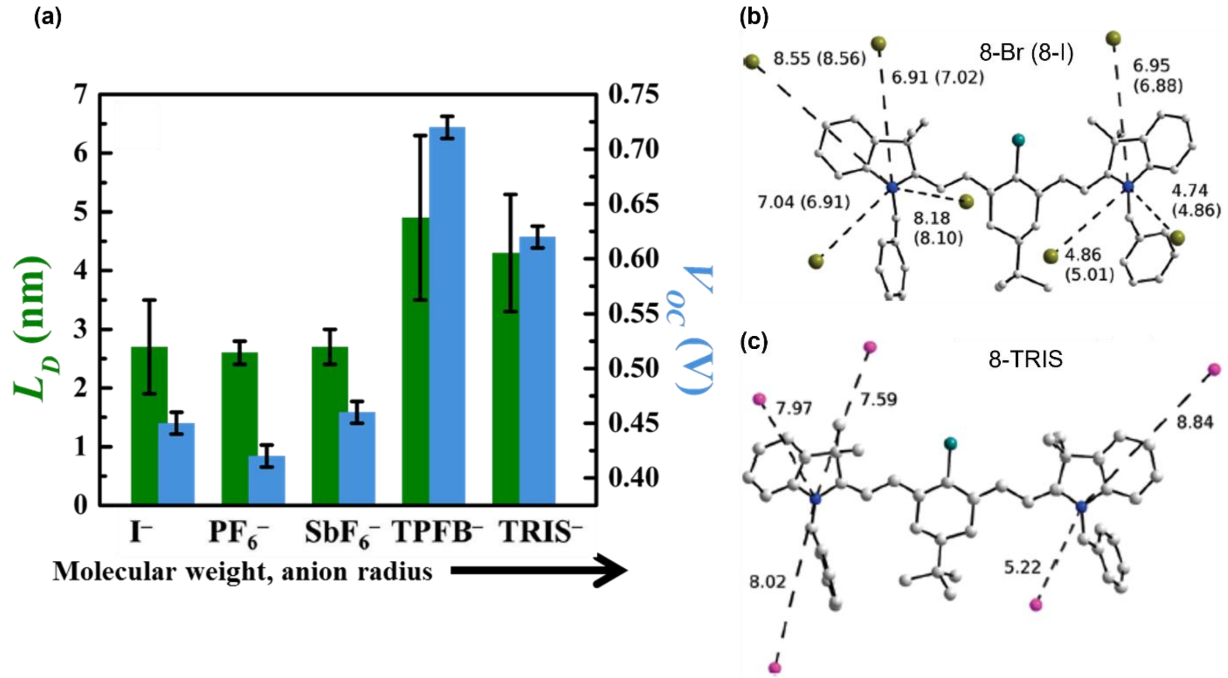

Figure 3.5. Impact of the counterion on organic salt-based PVs. (a) Exciton diffusion length (L_{ED}) and V_{OC} of organic salt PVs with cation 3 and a range of anions, demonstrating the variation caused by anion selection.[94] Position and distances of the nearest anion neighbours for **(b)** small counterions Br^- (I^-) and **(c)** large counterion $TRIS^-$ demonstrating bond length alteration due to cation/anion pairing.[99]

bandgaps as shown in Figure 3.4c.[95] Four different combinations of two heptamethine cations (5 and 6) paired with BF_4^- or $TPFB^-$ counterions demonstrated NIR photon harvesting and conversion to current with peak NIR *EQE*s reaching 2.1% at or past 1000 nm. Device efficiencies were limited by low V_{OC} (max of 0.33 V) and *EQEs*, but nonetheless demonstrated a route to deep harvesting that is important for the highest efficiency multijunction cells and photodetectors.

3.3 Weakly coordinating anions

Many counterions used in organic salt OPVs are classified as WCAs, or non-coordinating anions, and their unique properties are important for understanding why organic salts are such an interesting and exciting class of molecules for OPVs. WCAs are used in ionic liquids, batteries, fuel cells, electrochemistry, and ion catalyzed organic reactions, among other applications.[46] WCAs only weakly interact with cations, are unlikely to bind to many metal centers and thus can stabilize cations against oxidation. Some WCAs include BF_4^-, SbF_6^-, PF_6^- $Sb_3F_{16}^-$, $B(CF_3)_4^-$, $B(ArCF_3)_4^-$, $CHB_{11}Me_5Br_6^-$, and $B_{12}Cl_{11}NMe_3^-$.[96] Common starting materials for WCAs include strong cationic oxidants, Bronsted acids, or metal cations. WCAs have a negative charge spread over many electronegative atoms and often exhibit larger molecular radii, allowing them to weakly interact with and stabilize reactive, unstable, and electrophilic cations.[97] Superacids have been demonstrated by WCAs with hydrogen counter ions, and can protonate alkanes to produce carbocations.[46,96]19, 70 WCAs are exciting materials for organic salt based OPVs because of their strong stabilizing properties, allowing for the facile use of a range of cations and imparting additional tunability.

3.4 Role of the counterion in organic salt photovoltaics

Early work in organic salt PVs assumed the role of the counterion was less important relative to the cation. Several studies investigated counterions and demonstrate that they actually have large effects in such devices. The first evidence for a relevant role of the counterion was found by Demchuk et al., who examined excited state relaxation times for organic salts in different media through time resolved absorption spectroscopy.[98] Polar media, such as ethanol, demonstrated no sensitivity to the counterion, however, weakly polar solvents like dichloroethane demonstrated relaxation times ranging from 100 to 50 ps depending on the anion. A clear trend in anion nucleophilicity, size, etc., was not observed. Bouit et al. demonstrated that the anion could impact the structural state (ranging from asymmetric to symmetric) of the cation.[99] Figure 3.5b demonstrates that small anions such as Br^- or I^- polarized the cation and caused it to take on an asymmetric dipolar structure, whereas bulkier $TRIS^-$ ions caused the heptamethine to adopt a symmetric ideal polymethine state as shown in Figure 3.5c. Thus it was demonstrated that bond length alteration was impacted by counterion selection, an interesting mechanism with potential for altering optoelectronic properties. Bouit et al. concluded that counterion effects could be important and warranted further investigation.

Bulavko et al. examined BHJ polymer solar cells with organic salt dopants and the effect that the anion had on photovoltaic processes.[100] Counterions with low oxidation potentials contributed to the process of electron-hole generation, dissociation, and recombination through ion pairs formed by the organic salt wherein photoinduced electron transfer between the anion and cation can occur, forming radical species involved in the generation of current.

Suddard et al. systematically investigated the role of the counterion and demonstrated that anion selection led to widely varied performances in solar cells, with TPFB$^-$ achieving $V_{OC} = 0.71$ V, while devices with I$^-$ showed $V_{OC} = 0.45$ V (Figure 3.5a and Figure 3.6).[94] However, V_{OC} improvement was not proportional to anion molecular weight or radius directly but suggested it was tied to the degree of halogenation and the electronegativity of the halogens. Previous work had suggested that anions played no role in the redox potentials measured in solution by cyclic voltammetry.[76] However, using photoemission spectroscopy on solid films, Suddard showed that changes in V_{OC} stemmed from the suppression of recombination losses at the interface, a direct result of anion controlled adjustment of the highest molecular orbital by up to 1 eV. Figure 3.6a, c, and e show that the energy levels in these salt systems could be finely tuned (~0.01eV) by chemically alloying various anions, simultaneously enabling the enhancement of V_{OC} and EQE. This tuning approach can be exploited to optimize energy level alignment for arbitrary donor-acceptor pairings with novel and ultra-low bandgap organic salts, and was extended to several new molecules with V_{OC} near the theoretical limit (for their bandgap) and photoresponse from 950 nm out past 1600 nm. Traverse et al. recently investigated a range of counterions paired with Cy$^+$ and the effect of the counterion on properties such as the HOMO energy level, solubility, surface

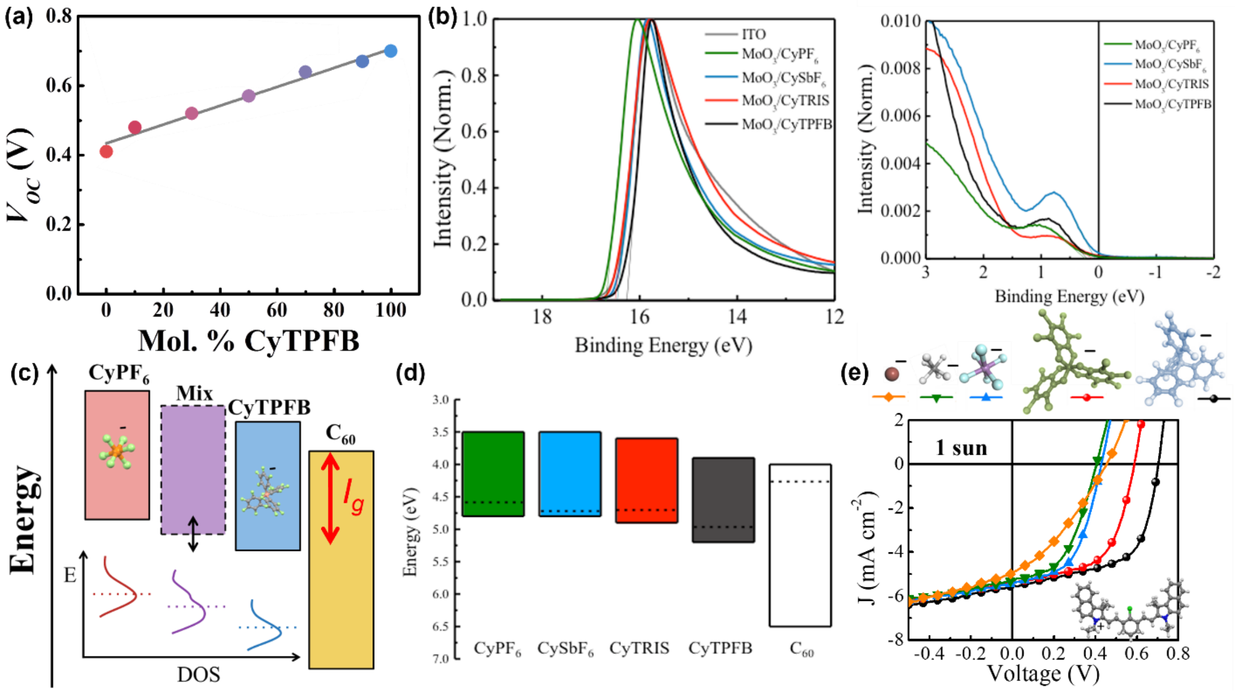

Figure 3.6. Impact of the counterion on V_{OC} and energy levels. (a) V_{OC} of organic salt thin films with varying compositions of counterions TPFB$^-$ and PF$_6^-$.[94] **(b)** Ultraviolet photoelectron spectroscopy data for cation Cy$^+$ paired with different anions.[94] **(c)** Schematic demonstrating improved energy alignment between the organic salt and adjacent C$_{60}$ layer via counterion selection or blending.[94] **(d)** Schematic showing energy levels for cation Cy$^+$ paired with various counterions.[94] **(e)** *J-V* curves demonstrating the alteration of V_{OC} for cation Cy$^+$ paired with various counterions.[94]

energy, and lifetime of devices.[101,102] Similar to the work done by Suddard et al., Traverse et al. showed the dependence of the V_{OC} and HOMO on the counterion.[101] Additionally, proper counterion selection was shown to increase the device lifetime to seven years.[102] Unlike with the tuning of the HOMO energy level, device lifetime was not correlated to the degree or nature of halogenation. Instead, device lifetime showed an exponential relationship with the water contact angle of the organic salt, with larger water contact angles corresponding to longer device lifetimes. Their work suggests that increased hydrophobicity of the organic salt film caused by the counterion reduces degradation of the organic salt.

The counterion clearly plays a significant role in organic salt PV performance. Indeed, organic salts are now a powerful approach to modulate the frontier orbital energy level alignment via anion exchange and blending, demonstrated in Figure 3.6c and 6d, creating an independent chemical tuning parameter to adjust the electronic properties without fundamentally altering the cation bandgap. This tunability can help to bypass the recombination/electron-transfer tradeoff which previously hindered the smallest bandgap molecule-based photovoltaics and limited photoresponse in these materials to <1200 nm and further aid in the optimization for salts throughout the solar spectrum.

3.5 Ion mobility

A unique aspect of organic salt PVs is the presence of ions in the active layer, and the mobility of such ions has been an important field of research. Nuesch et al. compared devices with separate cations and anions to those with covalently bonded anions and cations to observe ion mobility effects.[74] Absorption profiles were similar for both devices, but the C_{60} contribution to *EQE* in the ultra-violet was much larger for mobile counterion devices. Nuesch et al. attributes the greater UV *EQE* to electric field changes in the fullerene layer, and noted that mobile ions can lead to space charge buildup in the active layer.

Benmansour et al. demonstrated that mobile ion generated space charge build up impacts photovoltaic processes.[103] Application of a negative bias caused fullerene, normally an acceptor in organic salt PVs, to act as an electron donor due to the migration of Cl^- counterions into the fullerene layer, demonstrating the potential of ion mobility to alter organic salt PV processes and performance. Lenes et al. used applied biases to determine the ionic space charge effect on device efficiency, demonstrating that negative biases create space charge that enhances efficiency for trimethine $(12)^+/PF_6^-$ and trimethine $(11)^+/ClO_4^-$ devices (Figure 3.7a and 7b).[104] The *FF* and J_{SC} were largely unchanged by biasing, whereas V_{OC} decreased for positive bias and increased for negative bias. Positive biasing caused cations to accumulate at the donor/acceptor interface, raising

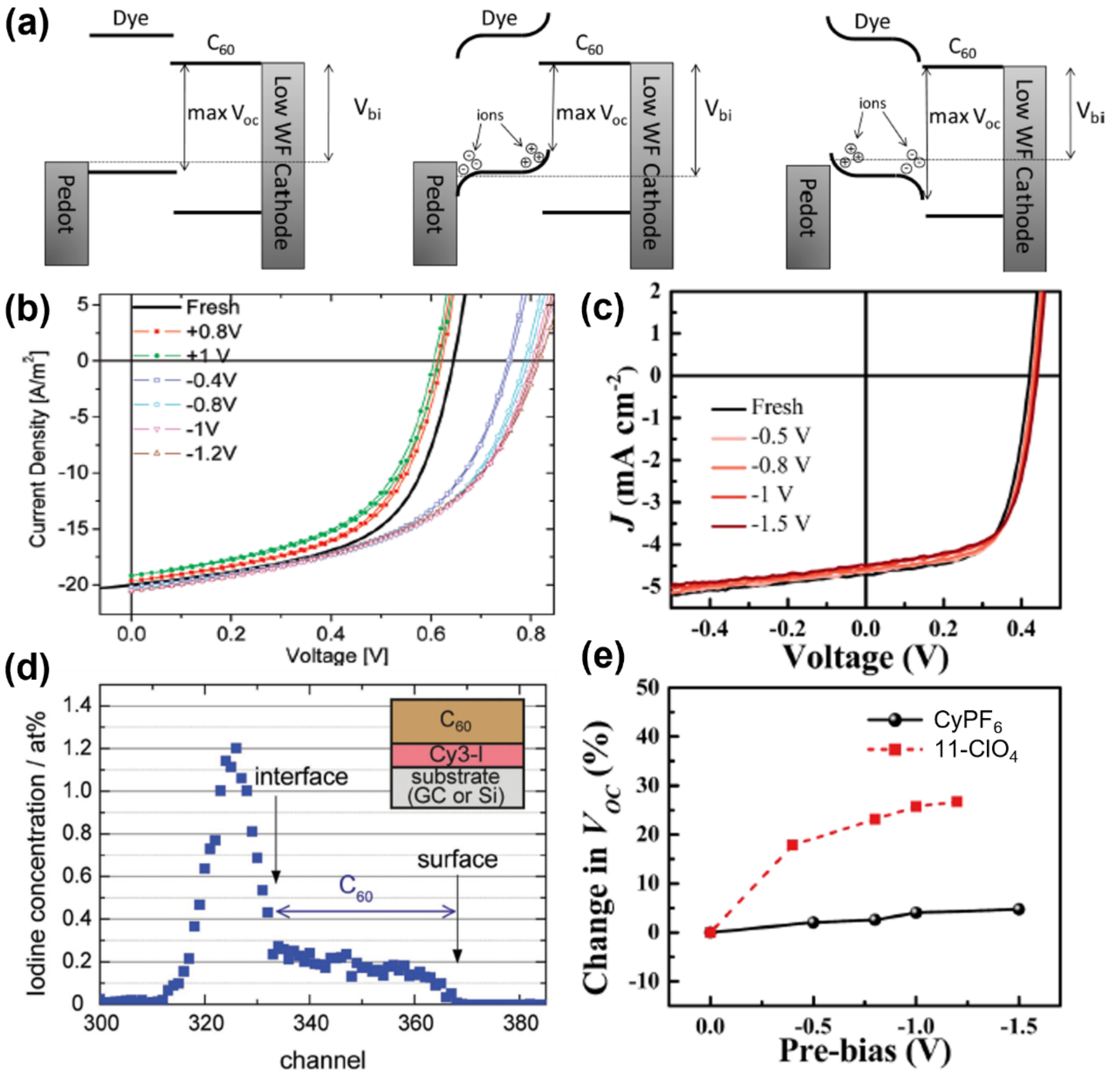

Figure 3.7. Impact of ion presence in organic salt-based PVs. (a) Schematic demonstrating ionic space charge build-up and its impact on V_{OC} for particular cation/anion pairings.[104] **(b)** Data demonstrating the change in V_{OC} for organic salt 11-ClO_4 under different biasing conditions, which can create ionic space charge build-up.[104] **(c)** V_{OC} data for $CyPF_6$ under different biasing conditions, demonstrating no significant ion mobility.[94] **(d)** Rutherford backscattering spectroscopy data for 12-I demonstrating the I^- counterion diffusing through the donor layer and C_{60} acceptor layer.[105] **(e)** Comparison of V_{OC} data under biasing conditions for 11-ClO_4 and $CyPF_6$.[94]

the donor HOMO level and decreasing V_{OC}, while negative biasing moved counterions towards the active layer interface, lowering the donor HOMO level and increasing V_{OC}. Lenes et al. noted that ion mobility could enhance device performance and proposed future work take advantage of this unique ability in organic salt PVs. Similarly, Suddard et al. negatively biased devices out to -

1.5 V and demonstrated no change in V_{OC} for heptamethine (Cy^+)/PF_6^- or heptamethine (Cy^+)/$TPFB^-$ salts, as shown in Figure 3.7c, suggesting that ion mobility was not a factor in devices with larger conjugated cations paired with bulkier anions. Figure 3.7e compares the two salts, where the bulkier salt demonstrates no ion mobility effects.[94] Decreased ion mobility is potentially beneficial for stable device performance, although the effect of the larger cation is not yet fully understood.

Jenatsch et al., provided recent evidence of ion migration through an organic salt PV device and monitored the potential through the fullerene layer as ions migrated.[105] Figure 3.7d shows a profile of the counterion, I^-, in regular and inverted structure devices obtained via Rutherford backscattering spectroscopy. Jenatsch et al. demonstrated significant ion diffusion into the fullerene layer in both structures, although regular architecture showed higher levels of I^- in fullerene. A sharp drop off in I^- occurs at the donor/acceptor interface. Jenatsch et al. provided the first data directly showing ion migration from the donor layer into the acceptor of an organic salt PV device.

Demonstrating the process and effects of ion migration and space charge buildup are important for understanding one of the fundamental differences between organic salt PVs and other small molecule organic solar cells. Ion migration has most commonly been observed with the smallest anions (e.g. I^-), but is also sensitive to the cation structure. The ability to both enhance and suppress such migration may be a critical factor moving forward, and it appears that such control is at hand.

3.6 Exciton diffusion and charge carriers

The photovoltaic process in bilayer and BHJ organic salt solar cells can be divided into five steps, (1) photon absorption and exciton generation by the active material, (2) exciton diffusion to the donor/acceptor interface, (3) charge transfer of electrons from the donor material and holes from the acceptor, (4) dissociation of electron and hole pairs into free charge carriers, and (5) the transfer of hole and electrons to electrodes and collection of the charge. We discuss these fundamental processes as it is key to optimizing devices and creating high efficiency organic salt PVs.

3.6.1 Exciton diffusion

Higgins et al. used near-field scanning optical microscopy (NSOM) to demonstrate that exciton diffusion lengths (L_{ED}) were less than 50 nm in psuedoisocyanine organic salts.[106] Other groups, including Suddard et al., have since reported exciton diffusion lengths for organic salt PVs on the order of 5 to 10 nm, shown in Figure 3.5a, similar to many other small molecule exciton diffusion lengths.[8] They demonstrated the L_{ED} was dependent on the anion, increasing from 2.5 nm for CyI, CyPF$_6$, and CySbF$_6$ to 5 nm, for CyTRIS and CyTPFB observed alongside a concomitant increase in the optimum salt thickness for the maximum quantum efficiency.[94] One possible mechanism for exciton diffusion is via long range Förster transfer, wherein the exciton diffusion length is proportional to R_0^3, the cubed Förster radius and inversely proportional to d^2, the lattice constant of the salt.[8] While increasing the average hopping distance by increasing the anion size, it is possible to counterbalance this effect by the reduction in the non-radiative rate for exciton quenching so that there can be a sensitive optimum.[107] A second mechanism is short range (nearest neighbor hopping) Dexter energy transfer, where L_{ED} exhibits an exponential decay with separation distance and quickly becomes negligible for non-nearest neighbor interactions. Förster transfer could only explain half of the change in L_{ED} due to changes in n and the lack of photoluminescence (PL) makes Förster transfer a questionable primary exciton diffusion mechanism. Dexter transfer is also improbable due to the larger nearest neighbor distances in heptamethine$^+$/TPFB$^-$ or TRIS$^-$ compared to I$^-$ or PF_6^- salts, meaning that L_{ED} should generally decrease, not increase. Thus, understanding the mechanism of exciton diffusion remains a key unanswered question in organic salts.

Given the relatively small exciton diffusion lengths reported so far, the use of BHJ structures with blended donor-acceptors will be a key approach to avoid exciton diffusion limitations in organic salt photovoltaics.[94] Such devices would require shorter exciton diffusion to a donor/interface, increasing the number of excitons that successfully dissociate into charge carriers. Research into BHJ devices with organic salts has been limited, but warrants further investigation to understand how to control phase separation and morphology in these systems.[76,79,81–83] It is likely that the thermodynamic processes that drive bulk heterojunction formation will be strongly influenced by both the anion selection and the general ionic character of the organic salts.

3.6.2 Charge injection

The transport and collection of free charge carriers has been improved by the introduction of interlayers and understanding of interfacial interactions. Nuesch et al. introduced a PEDOT layer that limited the injection of electrons from the organic salt donor into ITO, and subsequent generation of photocurrent, via a 1.3 eV energy barrier at that interface.[73] Elimination of this loss mechanism improved current generation. Jenatsch et al. observed a hole trapping mechanism at the MoO_3/organic salt interface resulting from a thin solvent layer solubilizing part of the salt and lowering charge carrier mobility.[108] Trapped hole lifetimes were greater than 200 µs, making them easily distinguishable from free holes. The mechanism was only present when a polar fluorinated alcohol solvent was used, and was absent when a less polar solvent such as chlorobenzene was used. Layer interfaces and trap states for exciton dissociation and free charge carrier collection is an important design consideration for organic salt PVs.

3.6.3 Electron transfer

Risse et al. used femtosecond pump-probe experiments to examine the photoinduced electron transfer process, observing a picosecond scale process for cyanine borate organic salt.[109] The excited state charge transfer process occurs on the femtosecond timescale when the organic salt is blended with PCBM, typically an acceptor material, and charge is transferred into the PCBM. The kinetics of organic salt to PCBM electron transfer compared to intra-molecular electron transfer are important for understanding BHJ charge transfer mechanisms and rates. Devizis et al. monitored the process of free charge carrier generation and identified exciton dissociation as the rate-limiting step using ultrafast transient Stark shift spectroscopy.[110] Bilayer trimethine $(12)^+/PF_6^-$ and fullerene thin films were subjected to an electric field and electromodulated differential absorption on a pump-probe spectrometer was used to monitor the generation and transport of free charge carriers. Non-overlapping electroabsorption (EA) spectra of the organic salt and fullerene allowed for independent observation of electron and hole movement in each layer. Fullerene EA bands decreased with time while organic salt EA bands remained constant, indicating that electron motion in fullerene was responsible for decay in the electric field during the nanosecond probing period. Devizis et al. confirmed the orders of magnitude difference of electron mobility in pure C_{60} (not fullerene as an acceptor in organic salt PVs), and hole mobility in the organic salt reported by Jenatsch et al. Furthermore, Devizis et al. determined the rate limiting step in the photovoltaics process of organic salt PVs to be the escape of the electron from the Coulomb potential at the donor-acceptor interface, which lasts for hundreds of picoseconds, and potentially longer given that the applied electric field likely lowered the barrier for the electron.

The exciton binding energy (E_B) is another key parameter as it defines the excess potential required at the interface to promote electron transfer and exciton dissociation. Young et al. used the tunability of the frontier energy levels with anion blending to extract the exciton binding energies of very small bandgap salts.[95] By finding the energy level at which there was a sharp *EQE* cutoff as the HOMO was reduced, the excess energy needed to enable efficient electron transfer was estimated. Binding energies were found to vary significantly both with changes in cation structure and bandgap, where E_B = 0.55 eV for heptamethine (6) with a bandgap of 0.9 eV, and E_B = 0.40eV for heptamethine (5) with a bandgap of 0.8 eV. The changes correlated with changes in the index of refraction, which were suggestive of changes in the dielectric constant. In this case, the binding energies limited the V_{OC} to roughly half the interface bandgap to maintain efficient dissociation (*EQE*). Understanding routes to modulate the binding energy, particularly at these very small bandgaps, is a key area of exploration.

3.6.4 Charge carrier mobilities

Jenatsch et al. used photogenerated charge extraction by linearly increasing voltage to determine hole mobility in a trimethine $(12)^+/PF_6^-$ layer.[108] A light pulse generated charge carriers in the photovoltaic device, and a voltage ramp extracted the carriers. The delay time between carrier generation and the voltage ramp allows for investigation of the charge carrier recombination kinetics. Conventional methods for determining mobilities requires micron thick layers, such that organic salt-based PVs cannot typically be used due to solubility limits. The calculated mobility was attributed to the organic salt because fullerene calculations saw an unreasonable order of magnitude increase in mobility for a similar increase in C_{60} thickness. The mobility was demonstrated to be 4 x 10^{-5} $cm^2\ V^{-1}\ s^{-1}$ and was assigned to hole transport because electron mobility in C_{60} and PCBM in previously reported work was on the order of 1 $cm^2\ V^{-1}\ s^{-1}$.[111,112] Tennakone et al. estimated electron mobilities of 8 x 10^{-2} cm^2 V^{-1} s^{-1} in rhodamine B thiocyanate films on a copper thiocyanate surface using the Mott-Gurney equation with measured space-charge saturated current.[113] To obtain the space-charge saturated current, the organic salt, rhodamine B thiocyanate was vacuum dried and pressed into a pellet between two steel electrodes with an applied DC current yielding the current density and applied voltage needed for the Mott-Gurney equation. Pitigala et al. utilized the same method to estimate hole mobility in a $pentamethine^+/SCN^-$ salt at 7.2 x 10^{-3} cm^2 V^{-1} s^{-1}, two orders of magnitude higher than the mobility Jenatsch et al. reported in organic salt PVs.[108,114] From both reports however, the hole mobility was low, and Jenatsch et al. demonstrated the effect of such limited hole mobility in organic salt PVs with active layer thickness dependent performance testing.[61] Photovoltaic performance declined with thick (>30 nm) active layers, owing to either exciton diffusion or hole mobility limitations.

Organic salts have also demonstrated usefulness as electron transport layers (ETLs) in organic PVs.[115] While organic salt ETLs do not possess the same function as organic salt active layers, this demonstration highlights the capable electron transport properties in such materials and suggests that there are at least modest electron mobilities in organic salts. To date, however, the mobility of electrons in organic salt PVs have not been well characterized, and few works have reported hole mobility in such devices. Considering the performance of salts in the PVs described above is similar in electrical performance (series resistance, fill factors), hole mobilities are likely to be similar (at least) to other amorphous small molecule semiconductors (~10^{-5} - 10^{-3} cm^2 V^{-1} s^{-1}). Given the impact that the anion can play in the frontier energy levels, work function, charge transfer efficiency, and exciton diffusion length, as shown in Figure 3.5 and Figure 3.6, it is then expected that the anion could play a similarly important and interesting role in the carrier transport properties. Another key factor in the magnitude of electronic properties is the well-known impact

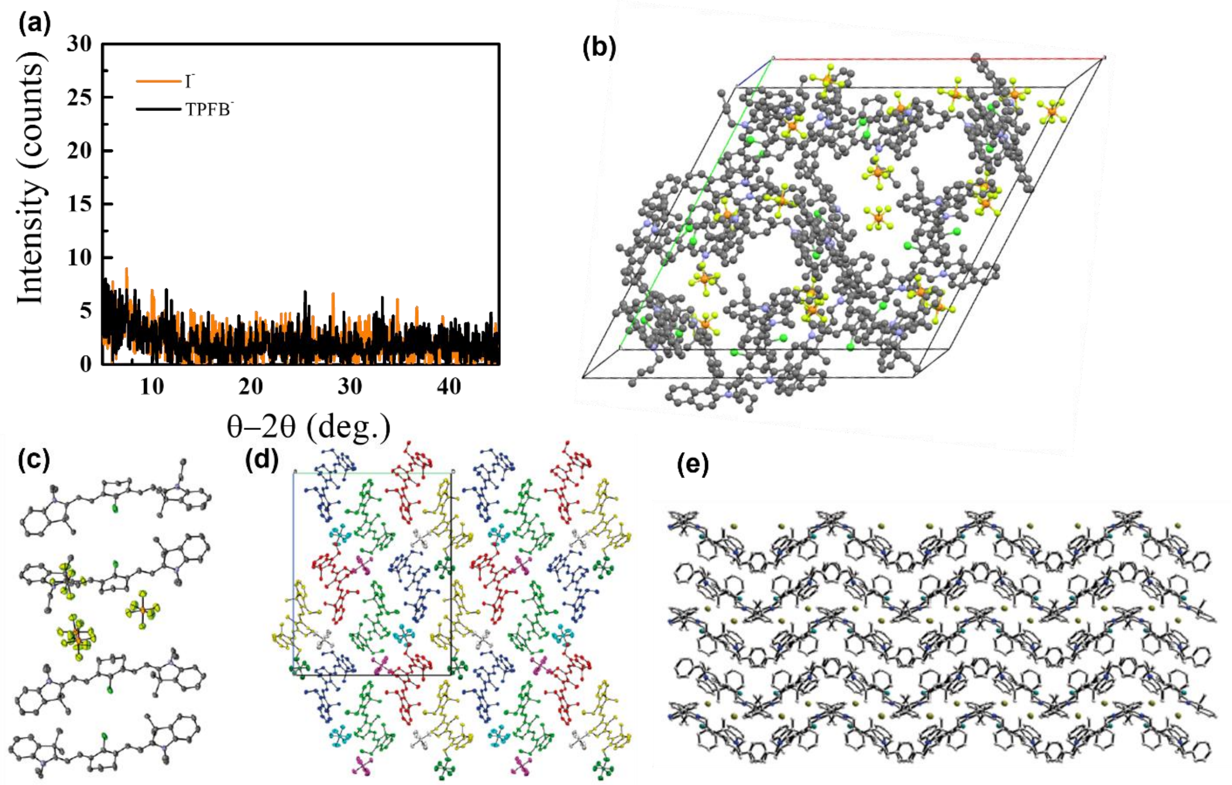

Figure 3.8. Crystallinity of organic salt thin films. (a) Representative XRD data for CyI and CyTPFB demonstrating amorphous thin-film structures.[94] Solved crystal structures for **(b)** $CyPF_6$,[94] **(c)** the asymmetrical structure of 4-PF_6,[86] **(d)** 4-PF_6 where colors represent equivalent symmetry,[81] and **(e)** 8-Br.[99]

of crystalline order.[116,117] Among all of the reports of organic salts used in thin films PVs there has been little evidence for any crystalline nature of thin films. Figure 3.8a demonstrates two of the organic salts that we have explored, for example, have been shown to be amorphous glasses. However, we and others have reported several crystal structures from slow-solution growth, as shown in Figure 3.8b-e, so that it is possible that tuning the crystalline content in films could be used to further enhance electronic properties and efficiencies.[44,86,94,99,118]

3.7 Organic salt transparent photovoltaics

Perhaps the most promising and exciting application of organic salts is in transparent photovoltaics (TPVs), which have emerged recently as a new class of photovoltaic devices.[21,119] Due to the outstanding capabilities of organic salts to absorb selectively in the NIR spectrum, both

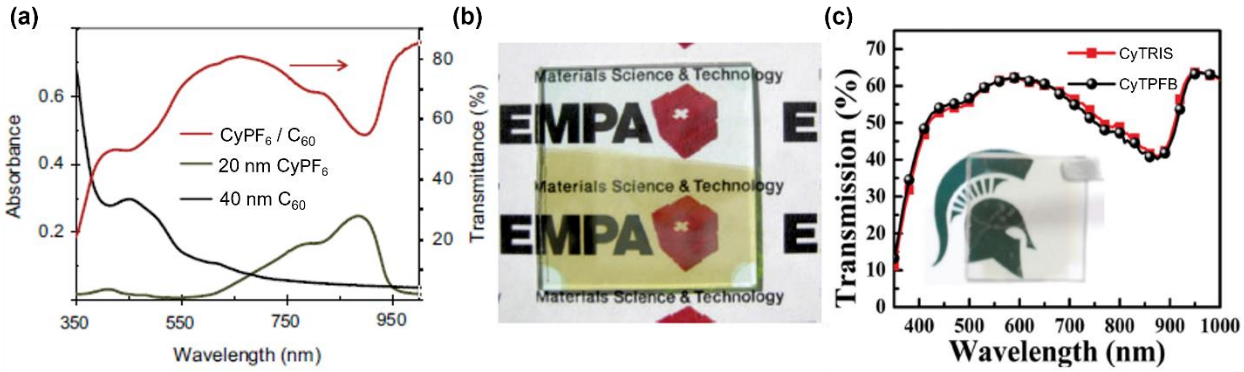

Figure 3.9. Organic salt-based transparent photovoltaics. (a) Absorption and transmission spectra for transparent photovoltaic devices utilizing organic salt $CyPF_6$.[120] **(b)** Picture of a transparent device represented in **(a)**.[120] **(c)** Transmission spectra for CyTPFB and CyTRIS based devices with a picture shown in the inset.[94]

in absorption breadth and *EQE*, TPVs with organic salts have demonstrated average visible transmittance (*AVT*) as high as 70% and device efficiencies greater than 2% as shown in Figure 3.9. This is approaching the highest efficiencies and transparencies reported for non-salt TPVs of 4-5%. Nonetheless, the salts have demonstrated the deepest photoresponse of any organic semiconductors and therefore could also play a role in transparent multijunction cells.[22]

Zhang et al. reported heptamethine $(3)^+/PF_6^-$ organic salt PVs with *AVT* for 450 – 670 nm of up to 67%, and observed that *AVT* was a strong function of cathode thickness and composition (Figure 3.9a and b).[120] A 1.5% efficient device with a non-transparent 100 nm Ag cathode was tested for cathodes of different thicknesses and Ag/Alq_3 compositions. *AVT* increased from 42.8% (8 nm) to 47.9% (12 nm), and decreased to 39.2% (16 nm) and 31.0% (20 nm) for Ag cathodes. A 12/60 nm Ag/Alq_3 cathode demonstrated the best *AVT* = 67.2% with *PCE* = 0.7%, V_{OC} = 0.39 V, J_{SC} = 3.8 mA cm^{-2}, and *FF* = 0.496. Figure 3.9a and b show the absorption and transmission curves with an image of the transparent device. Simulations performed by Zhang calculated the optical field strength (E^2) in the cathode layer to understand how Alq_3 influenced the *AVT*, which depends greatly on E^2 exiting the cathode and is similar to TPV work.[71] Simulated 60 nm Alq_3 had 81% transmittance of 568 nm light, compared to 79.8% experimentally. *AVT* was calculated from optical modeling data and demonstrated the highest transmittance for 12 nm Ag/60 nm Alq_3 at 69.6%, in good agreement with experimental work. Minimal changes in *AVT* and *PCE* were observed for varying active layer thicknesses. Veron et al. fabricated semitransparent OPVs with a heptamethine $(4)^+$/TRIS$^-$ salt (1.4 eV bandgap).[86] Using a Ag/Alq_3 cathode, devices were demonstrated with maximum AVT = 66% from 450 to 670 nm, PCE = 2.2%, J_{SC} = 6.4 mA cm^{-2}, V_{OC} = 0.63 V, and FF = 0.54, a significant improvement from the 0.7% *PCE* for the heptamethine$^+$/PF_6^- salt.

Suddard et al. subsequently created heptamethine (Cy$^+$)/TPFB$^-$ organic salt (1.34 eV band gap) TPVs with a 2nm Ag interfacial metal layer, 100 nm MoO_3 and a 100 nm ITO cathode, demonstrating average device PCE = 0.8%, J_{SC} = 2.5 mA cm^{-2}, V_{OC} = 0.69 V, FF = 0.53 and AVT = 60.4%, but which had a voltage nearing the theoretical excitonic limit for OPVs. Figure 3.9c demonstrates the transmission curve with an image of the device.[94] Development of high efficiency TPVs requires energy harvesting deep into the NIR. Young et al. demonstrated organic salts with selective NIR absorption edges out to 1600 nm and NIR peak *EQE*s as high as 2.1%, shown in Figure 3.4c.[95] Absorption and photocurrent generation this deep had not been seen previously in any organic semiconductor and was thus a significant advancement in organic salt TPVs.[121]

3.8 Stability of organic salt photovoltaic devices

The longevity and stability of organic salt PVs are important factors in determining the potential and commercial viability of such devices. Wicht et al. studied the stability of bilayer organic salt and fullerene solar cells with both normal and inverted structures.[122] Regular devices stored in the dark under N_2 demonstrated a 10-20% drop off in J_{SC} and FF over 100 days, and a similar drop off in V_{OC} if an Al cathode was used instead of Ag, which is less reactive because of the self-passivating nature of Al. Devices with PEDOT:PSS showed more degradation than those with MoO_3 because PEDOT:PSS lowered the pH of the adjacent ITO layer, causing corrosion and allowing indium atoms to diffuse into the device. Ambient air testing demonstrated higher stability for inverted structures due to the increased protection provided for fullerene against O_2, which can be reactive with fullerene but must first diffuse through the organic salt in the inverted structure. Organic salt thin films demonstrated a constant absorption spectra upon exposure to ambient conditions, showing photostability. Stress testing under heat and light demonstrated 30 to 60% degradation of V_{OC}, FF, and J_{SC} in 17 days, while PCE stabilized at 15% of fresh devices. The T_{80} after a 5-day burn-in was 72 hours, compared to 10 hours for fresh devices.

In addition to developing organic salt TPVs, Zhang et al. examined the stability of their heptamethine (Cy^+)/PF_6^- based devices.[120] A device with a 50 nm Ag cathode demonstrated the best protection against degradation for V_{OC}, J_{SC}, and FF in the dark under N_2. Devices with a 50 nm Ag cathode layer under 1 sun and N_2 showed a 20% decrease in FF and J_{SC}, a slight drop off in V_{OC}, and an overall 40% degradation in PCE in 100 hours, with a T_{80} of 30 hours. Wicht et al. demonstrated that illumination can cause rapid degradation for particular cation/anion organic salt PVs, and mechanisms for this photodegradation were evaluated by Zhang et al.[122,123] Trimethine $(12)^+$/PF_6^- films showed no changes in absorption, confirming the photostability of organic salts noted by Wicht et al. MoO_3 and C_{60} degradations were isolated via layer by layer 24 hour stress testing in devices and MoO_3/C_{60} bilayer selective excitation. MoO_3 photodegradation to Mo^{5+} accounted for the V_{OC} decline and half of the J_{SC} decrease within 24 hours. Upon degradation to Mo^{5+} the work function changes from 5.6 eV to 5.3 eV, altering the energetics and hole extraction efficiency at the salt/MoO_3 interface.

As mentioned in the discussion on the impact of the counterion, Traverse et al. measured the device performance of a variety of CyX salts under continuous AM1.5G 1-sun illumination.[102] Extrapolated lifetimes on the order of years were observed with little change in quantum efficiency. The counterion was found to tune the hydrophobicity of the organic salt film, which produced a seven-year lifetime for CyTPFB. Nonetheless, the stability of organic salts as active layers remains an important criterion to enable organic salt PVs to become commercially viable.

3.9 Conclusions

Organic salts are an emerging class of active layers for organic photovoltaics and have demonstrated outstanding tunability in the structural, optical, and electronic properties. We have reviewed the historical development of such devices and discussed the exciting features organic salts bring to organic photovoltaics, including transparent devices, long lifetimes, ultra-deep NIR harvesting, and facile adjustment of energy levels. Most of the previous research in this field has focused on planar devices. Understanding thermodynamically-driven phase separations in organic salt donor-acceptor blends will be an important area of future investigation to enable the fabrication of high efficiency bulk heterojunction architectures. Future research should also focus on understanding the mechanisms of energy transport, the limitations of the binding energies, what role the ionic character has in exciton dissociation and migration, and how deep organic salts can absorb into the NIR. The development of solution processable organic salts with highly tunable properties can ultimately enable opportunities to approach the excitonic efficiency limit for OPVs while opening up new prospects for low-cost transparent solar cells, photodetectors, and multijunction cells.

Chapter 4 – Experimental Techniques

This chapter presents an overview and key concepts for experimental techniques used in the ensuing chapters to synthesize or characterize materials and devices related to OPVs, TPVs, and PDT. Specific experimental details of how a given technique was implemented for each project are included in the respective chapter.

4.1 Synthesis

4.1.1 Organic salt ion exchange reaction and purification

Organic salt synthesis is achieved through ion exchange reactions that replace the base counterion of a chromophore for another desired counterion. Ion exchange reactions are carried out in solvent systems that utilize solvent orthogonality between precursors and products so that the desired product compound precipitates out of solution after the ion exchange occurs. Ion exchange from the base counterion (typically a small, hard ion) to larger counterions is favorable and results in a lower polarity product. Excess of the desired counterion is added to drive the reaction forward. The precipitate is collected via vacuum filtration and solvent washing, which functions as an initial purification step. With ideal solvent orthogonality, any remaining precursors and side product are dissolved during the solvent wash. Realistically however, there will be some side product or unreacted precursor in the crude product, necessitating an additional purification step.

Silica gel chromatography is used to purify the crude product and remove unwanted product and unreacted precursors. For small batches of product (150 mg or less) a silica gel plug is used (Figure 4.1). Silica gel chromatography separates compounds based on their polarity, which determines the residence time for each chemical in the plug (or column). The eluent (solvent) will also affect the residence time. The product compound is recognized by its color and collected.

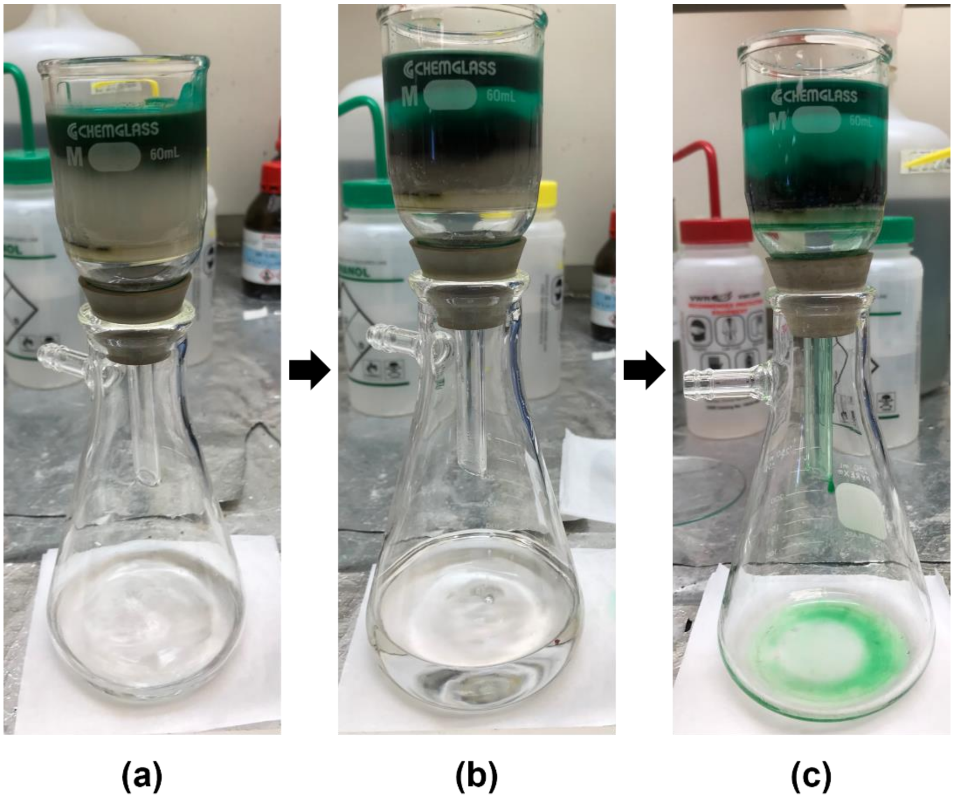

Figure 4.1. Ion exchange reaction purification. Silica gel purification process with **(a)** the silica gel plug with crude product added, **(b)** colored product band moving through the plug, and **(c)** collection of the purified organic salt product.

Large scale (1 g or more of purified product) organic salt synthesis is achieved in a similar manner to small scale reactions, however the silica gel purification is done via a silica gel column instead of a plug (Figure 4.2).

4.1.2 Mass spectrometry

Purity of synthesized organic salts is assessed using ultra-high performance liquid chromatography mass spectrometry (UHPLC-MS). Two dilution sets are made of organic salts and their precursors. UHPLC-MS is run in both positive and negative mode to capture data for both ions of the salts (Figure 4.3), and the chromatographic peaks are integrated at each concentration for the m/z corresponding to the four ions involved in an organic salt ion exchange reaction. The integrated data for the parent compound is used to create a calibration curve for each

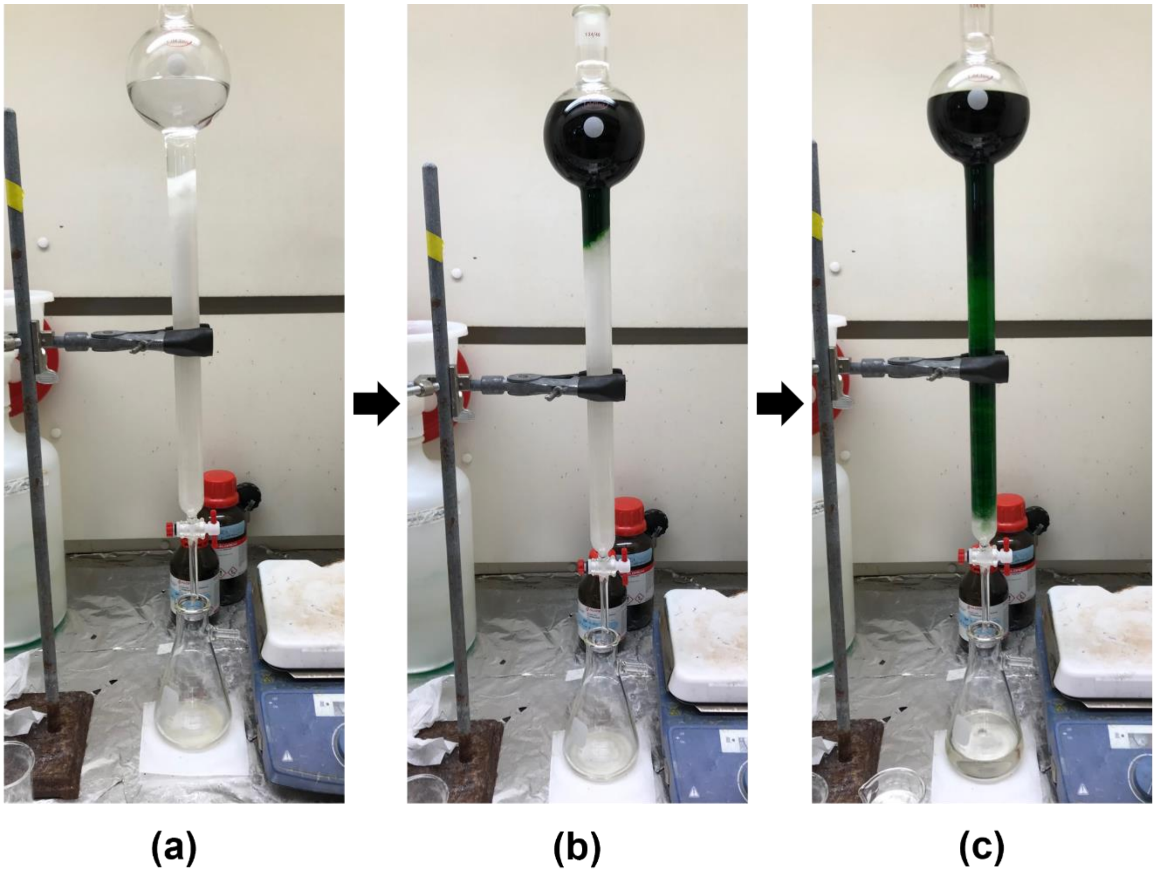

Figure 4.2. Large scale synthesis purification. Silica gel purification process with **(a)** the prepared column, **(b)** crude product dissolved in DCM and added to the column, and **(c)** product moving through the column just before collection with eluent DCM added every few minutes.

species, and the purity of the product compound is calculated based on the integrated signal for the product relative to the calibration curve. In other cases, such as for verifying the synthesis of molybdenum containing nanoclusters or for identifying product compounds resulting from organic salt degradation, the same general procedure is followed albeit without a full purity calculation. Instead, the linearity of the m/z signal of the compound of interest combined with the absence of precursor signals is taken as a sufficiently pure product.

4.1.3 Nanoparticle formation

Nanoparticles of the organic salts were formed for use as active agents in PDT and fluorescent bioimaging in order to capture the electronic shift of the HOMO energy level observed in solid-state films.[94,101] Organic salts are first dissolved into dimethyl sulfoxide (DMSO), a

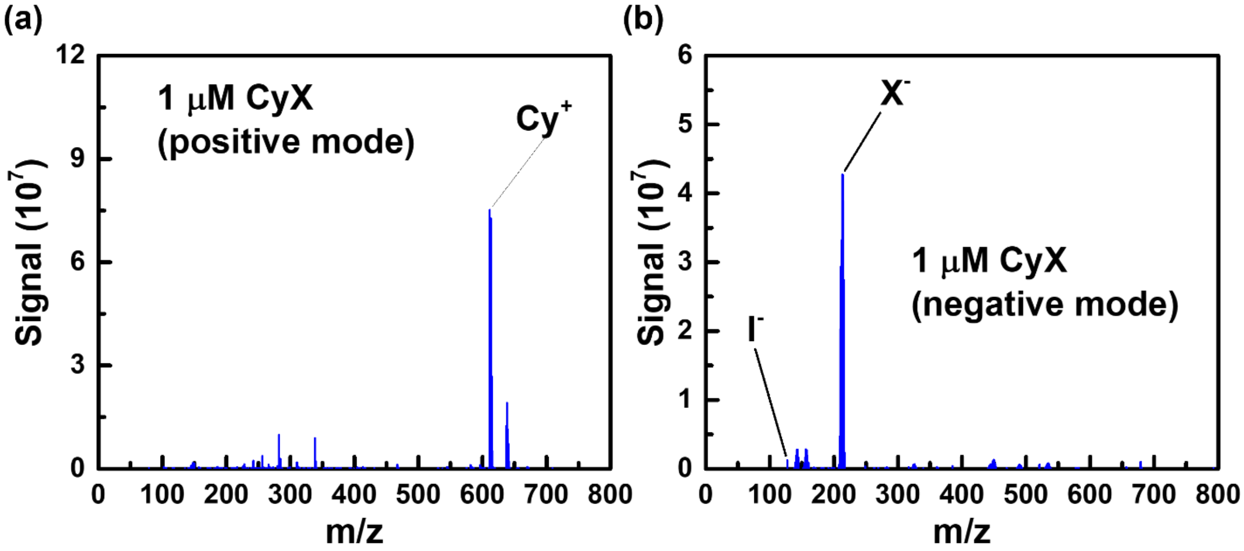

Figure 4.3. Example mass spectrometry data for CyX compounds. (a) Example positive mode ultra-high performance liquid chromatography mass spectrometry (UHPLC-MS) data for high purity (> 95%) organic salts following ion exchange using precursors CyI and CsX. Cs^+ signal is at least four orders of magnitude lower than the Cy^+ signal and does not register on the scan. **(b)** Example negative mode UHPLC-MS data for the same sample shown in **(a)**. The original counterion I^- presents a signal more than an order of magnitude smaller than the new counterion, X^-.

solvent in which all organic salts used in this work possess high solubility (>10 mg mL^{-1}). At this point, the salts are individual molecules and the ions are dissociated. To form nanoparticles in solution, the organic salt-DMSO solutions are added into deionized water (DI-H_2O) to induce flash nanoprecipitation. The salts are largely insoluble in DI-H_2O and aggregate into fully dissolved solubilized nanoparticles as a result. The use of a non-solvent (DI-H_2O) to induce organic salt aggregation into nanoparticles is similar to the process of flash nanoprecipitation (FNP).[124] In FNP, the addition of a non-solvent causes aggregation of the active material and adsorption of an amphiphilic polymer to coat the newly formed nanoparticle. Unlike in FNP however, the organic salt nanoparticles synthesized here are not coated with a polymer to induce aqueous solubility and cellular uptake.

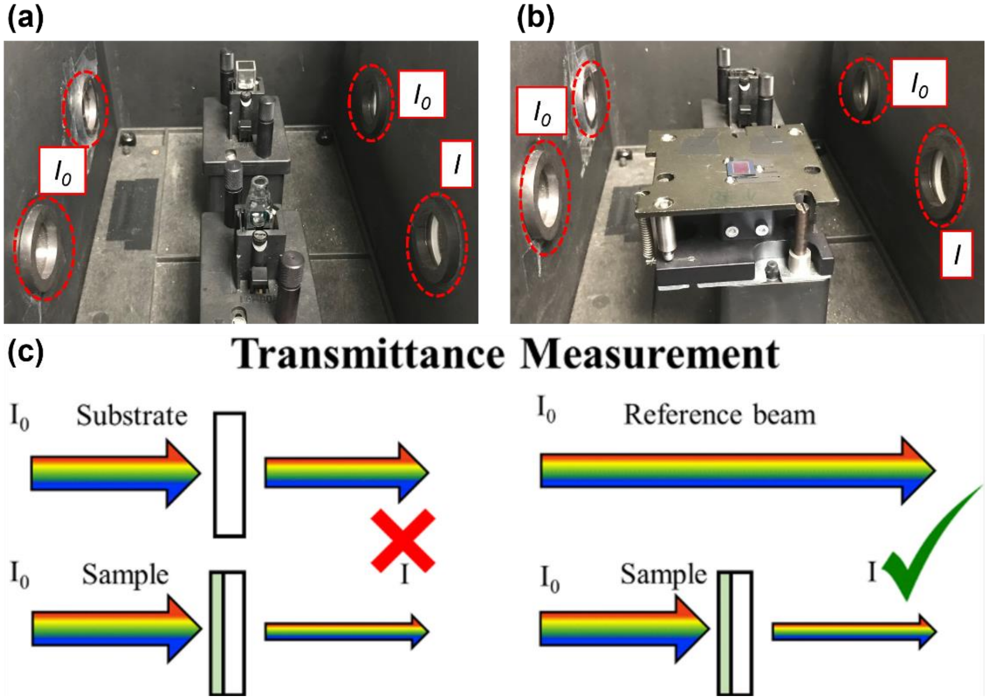

Figure 4.4. Ultraviolet visible near-infrared spectroscopy. Setup for ultraviolet visible near-infrared spectroscopy for **(a)** solution transmittance measurements and **(b)** thin film reflectance measurements. The proper setup for thin film transmittance measurements **(c)** with the reference slot empty and all light passing through the thin film sample.[6] Monochromated light enters through the circled ports on the left and passes through either the reference slot (back) or sample slot (front) before leaving the testing chamber to the right. The input light intensity I_0 and exit light intensity I is labeled for each setup.

4.2 Material characterization

4.2.1 Ultraviolet-visible and near-infrared light spectroscopy

Measurements of transmission, reflection, and absorption are critical to understanding how materials can function in PVs and PDT/fluorescent imaging, and to characterizing the performance of TPVs. Transmission (solutions and films) and reflection (films) measurements were made using a Perkin Elmer Lambda 900 UV/VIS/NIR Spectrometer in transmission mode. For solution measurements, the sample solution was loaded into a borosilicate glass cuvette and placed in the sample slot, and a second cuvette was filled with the solvent system and placed in the reference slot to isolate the material of interest (Figure 4.4a). Transmission measurements were made where the intensity of monochromated light transmitted through the sample, I, is compared to the

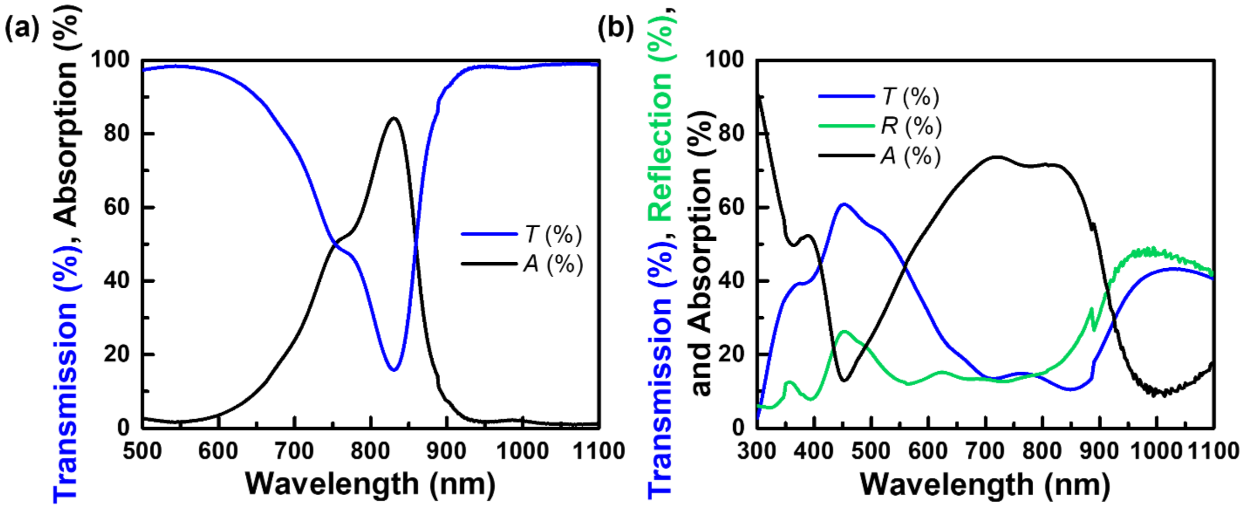

Figure 4.5. Ultraviolet visible near-infrared spectroscopy example data. (a) Example ultraviolet visible near-infrared (UV-VIS NIR) spectroscopy data for an organic salt dissolved in dimethyl sulfoxide. Absorption (*A*(%), black line) is calculated as 100 – *T*(%) from the measured transmission data (*T*(%), blue line). **(b)** Example UV-VIS NIR spectroscopy data for a thin film. Absorption (*A*(%), blank line) is calculated as 100 – *T*(%) – *R*(%) from the measured transmission and reflection data (blank and blank lines, respectively).

intensity of light passing through the reference slot, I_0, and used to calculate the transmission, *T(%)* with Equation 4.1.

$$T(\%) = 100\%\ x\ \frac{I}{I_0} \tag{4.1}$$

From Equation 4.1, the molecular extinction coefficient, α, can be calculated with Beer's law (Equation 4.2), where l is the path length (cuvette width) and C is the concentration. The extinction coefficient, k, is calculated from Equation 4.3.

$$\log_{10}\frac{I_0}{I} = \frac{100}{T(\%)} = \alpha l C \tag{4.2}$$

$$\alpha = \frac{4\pi k}{\lambda} \tag{4.3}$$

The absorption is calculated as 100-*T(%)* since the reflection is subtracted out by placing an identical cuvette with pure solvent in the reference slot (Figure 4.5). Solid-state measurements are more complicated because the reflection cannot be subtracted out with a reference sample. For example, reflections off of a reference sample such as glass will be different than reflections off of an experimental thin film on a glass substrate. Therefore, in order to calculate the absorption of a film, the reflection must also be measured since they cannot be as simply subtracted as in the case of solution measurements due to complex optical interference. Reflection measurements of thin films were made with a 6° specular accessory installed on the sample beam side (Figure 4.4b). The system is then calibrated to a control sample of aluminum to give 100% reflectance. A borosilicate glass sample was measured after calibration and compared with a known reflectance to give a correction factor for experimental samples. For all solid state measurements, the reference slot was kept empty (Figure 4.4c).[6] In many cases the sample substrate was smaller than the slot in the spectrometer so windows of the same size were created in the sample and reference slots to ensure that all light passed through the sample. For TPVs the transmission data was used to calculate the optical figures of merit discussed in Chapter 2.

4.2.2 Photoluminescence and quantum yield

Photoluminescence (PL) and quantum yield (Φ) measurements were made with a Photon Technology International Fluorometer using emission scans. In most cases, monochromated light is generated and illuminates a cuvette/substrate with either the organic salt in a solvent system (experimental sample) or the solvent system (reference sample) and the PL is captured by a detector measuring the intensity at a particular emission wavelength. For PL measurements, the cuvette/substrate sits in the spectrofluorometer testing chamber and light is emitted in all directions with the detector capturing only the light that escapes the chamber to the detector (Figure 4.6a). To measure the Φ, the ratio of emitted photons to absorbed photons (Equation 1.4), an integrating sphere is placed over the cuvette/substrate to ensure that as many emitted photons as possible are captured (Figure 4.6b). The integrating sphere has a white, highly reflective surface so that emitted photons will reflect until they are uniformly distributed around the sphere and a small opening of

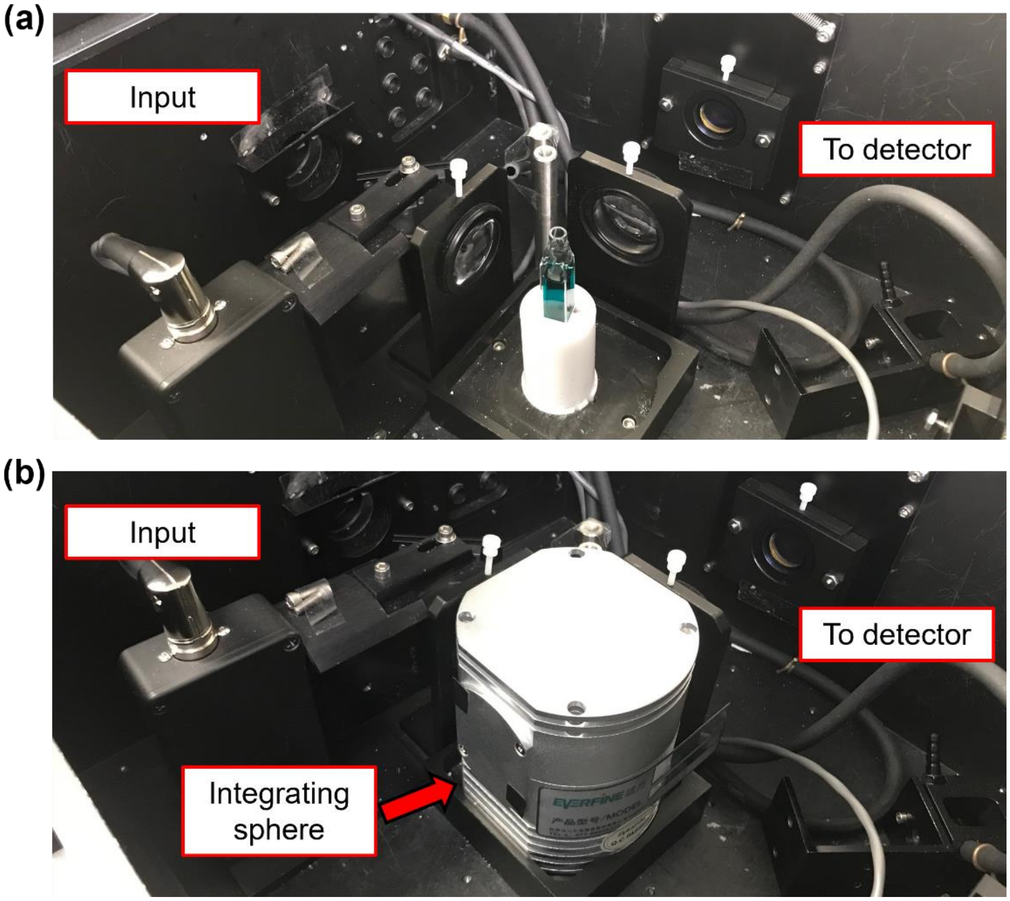

Figure 4.6. Photoluminescence and quantum yield setup. (a) Testing setup for photoluminescence measurements and **(b)** testing setup for quantum yield measurements with the integrating sphere. Monochromated light of the excitation wavelength enters from the top left port labeled input and excites the sample in the cuvette (center) with emitted photons passing through the port in the top right to the detector.

the integrating sphere allows a small portion of this light to exit into a detector. To calculate Φ, the excitation and emission peaks were measured for the reference and sample (Figure 4.7). The difference in integrated intensity between the reference (PL_R) and sample (PL_S) (Equation 4.4) for the excitation peak (λ_1 to λ_2) gives the absorbed photons (Figure 4.7, square pattern) and for the emission peak (λ_3 to λ_4) gives the photons emitted (Figure 4.7, diagonal pattern). The ratio of emitted photons to absorbed photons is the quantum yield, Φ.

$$\Phi = \frac{n_{ph\,emitted}}{n_{ph\,absorbed}} = \frac{\int_{\lambda_3}^{\lambda_4} PL_S d\lambda - \int_{\lambda_3}^{\lambda_4} PL_R d\lambda}{\int_{\lambda_1}^{\lambda_2} PL_R d\lambda - \int_{\lambda_1}^{\lambda_2} PL_S d\lambda} \tag{4.4}$$

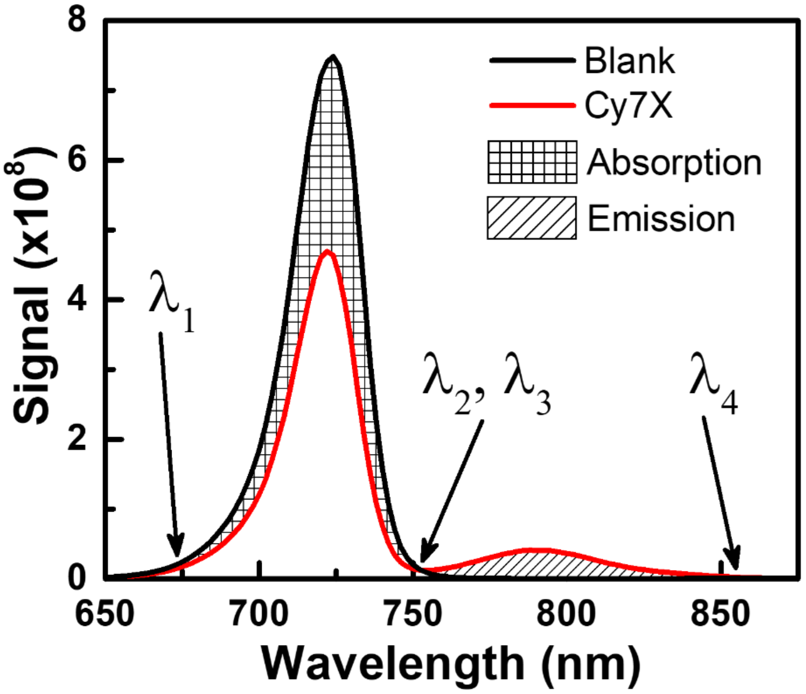

Figure 4.7. Quantum yield example data. Emission curves for pure dimethyl sulfoxide (Blank, black line) and organic salt (Cy7X, red line). The integrated difference between the two curves for the excitation peak (725 nm) gives the total number of photons absorbed by Cy7X (square pattern, absorption). The integrated difference between the two curves for the emission peak (800 nm) yields the total number of photons emitted by Cy7X (diagonal pattern, emission). The ratio of emitted photons to absorbed photons is the quantum yield. For this example, the calculated quantum yield is 26%.

4.2.3 Scanning electron microscopy

Scanning electron microscopy (SEM) is an imaging technique where an electron beam is used to scan a surface and generate a surface image, and can give information about morphology and composition. The electron beam comprised of high energy electrons interacts with the surface and results in 1) scattering of the incident electrons, 2) absorption of high energy electrons leading to emission of secondary electrons from the sample, or 3) absorption of incident electrons and photon emission after electron relaxation. Detectors can collect each of the resulting particles for analysis. Surface imaging is achieved by mapping the relative intensity of secondary electrons emitted from each location on the surface. Electron emission can create ions, creating a charging current that builds over time to greatly reduce the surface image quality. Growing the film of

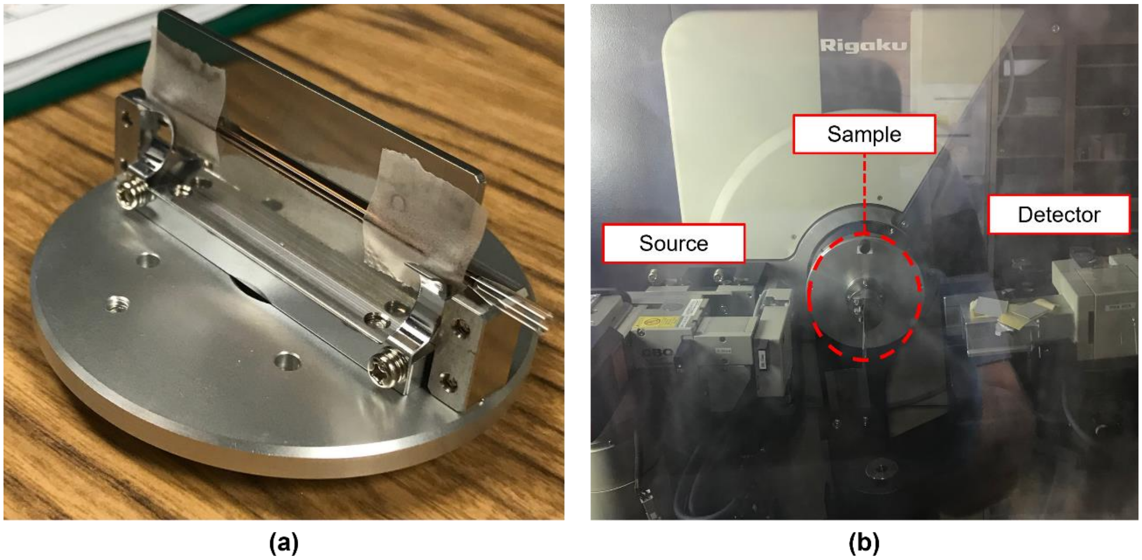

Figure 4.8. Small angle x-ray scattering setup. Setup of the glass capillary filled with PbS quantum dots for small angle x-ray scattering (SAXS) in **(a)** the SAXS sample stage, and **(b)** the diffractometer.

interest on a conductive substrate or creating a conductive pathway between the film and the substrate stage can partially or fully offset the effect of a charging current.

4.2.4 Small-angle x-ray scattering

Small-angle X-ray scattering (SAXS) measures the scattering of x-rays passing through a sample at small angles, typically less than 10°, to give information about the particle size distribution of nanomaterials or the size and shape of larger molecules. For nanoparticle size distribution measurements, solutions were loaded into boron-rich glass capillaries with 1.5 mm outside diameter (Charles Supper Company, Figure 4.8a). Parallel beam and SAXS alignment procedures were performed to prepare the diffractometer (Figure 4.8b) for measurements. Care must be taken when filling and mounting the glass capillaries to fill the entire capillary and remove air bubbles while not breaking the capillary.

4.2.5 Atomic force microscopy

Atomic force microscopy (AFM) is a scanning probe technique that can be used to give information about a film or surface, including film thickness, surface roughness, and surface

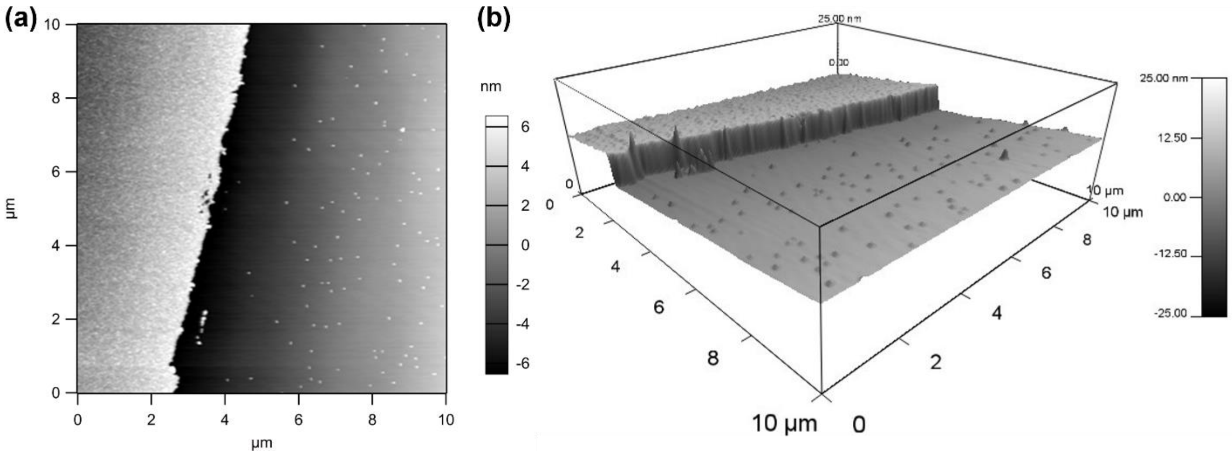

Figure 4.9. Example atomic force microscopy data for Ag thickness measurement. An example of atomic force microscopy images for a 12 nm silver (Ag) film on a silicon substrate. **(a)** A 2-dimensional image of the edge of the Ag film (left) and silicon substrate (right). **(b)** A 3-D representation of the image in **(a)**.

morphology. In tapping mode AFM, a laser is focused on the tip of a cantilever, which moves across the surface of interest while oscillating at a constant amplitude and frequency. Intermittent contact with the surface causes the tip to deflect, and the deviation in tip position maps the surface.

4.2.6 Differential pulse voltammetry

Differential pulse voltammetry (DPV) is a voltametric technique related to linear or cyclic voltammetry in which small voltage pulses are made as the voltage is swept. The current is measured before and after the pulse with the difference plotted as a function of the potential. DPV is a useful technique for studying sensitive or dilute analytes because the charging current, the movement of charges in response to the larger voltage change, is subtracted for each measurement. This leaves only the faradaic current, that which corresponds to the redox event of interest. A standard three electrode setup is used for DPV, in which the redox event to be studied occurs at the working electrode as a function of the applied potential. A reference electrode is used to measure and control the potential, and itself remains at constant potential via an internal electrochemical reaction. Current generated by the redox event at the working electrode flows

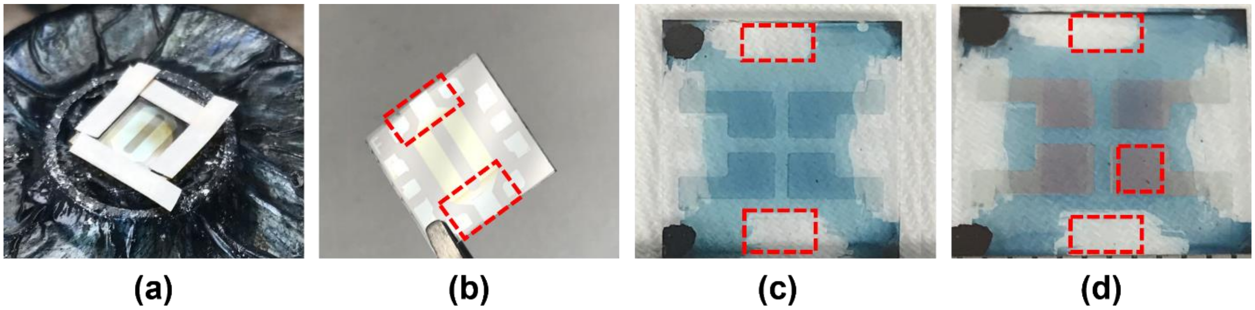

Figure 4.10. Transparent device processing. Pictures of transparent photovoltaic (TPV) processing **(a)** before spin-coating ZnO, **(b)** after spin-coating ZnO, and **(c, d)** after device processing is finished with the ITO pads exposed. Black dots on the corner of the substrate differentiates between substrates of the same device stack during testing. The cleared ITO pads at the top and bottom of the device are outlined in red. The side ITO pads have also been kept clear in **(b)**. One device active area is outlined in red in **(d)**.

through the counter electrode, which must be larger in active area so that the working electrode is the limiting factor for current production. DPV can be used to measure oxidation and reduction potentials, and the former has previously been correlated to changes in the HOMO level of the analyte.[125]

4.3 Device fabrication

All devices were fabricated on glass substrates with patterned ITO as the bottom contact. Substrates were cleaned via sonication and plasma cleaning to remove dust and prepare the ITO for a clean electrical contact to the next layer. Subsequent layers after the ITO were grown either via spin-coating, a solution process, or high vacuum thermal vapor deposition, a solid-state processing technique. Both techniques will be covered in detail in the following sections. In order to maximize PV performance, ITO contacts on the top, bottom, and sides of the substrate were covered during film growth, either with tape (Figure 4.10a and b) for spin-coating or a substrate mask for vapor deposition. For certain layers grown via spin-coating in the glovebox, a razorblade was used to scrape off the material from the edges of the substrate to expose the ITO contacts after film growth. The top and bottom ITO contacts could be cleared off after device fabrication was complete, while the side ITO pads were cleared in the glovebox prior to the next film growth. An

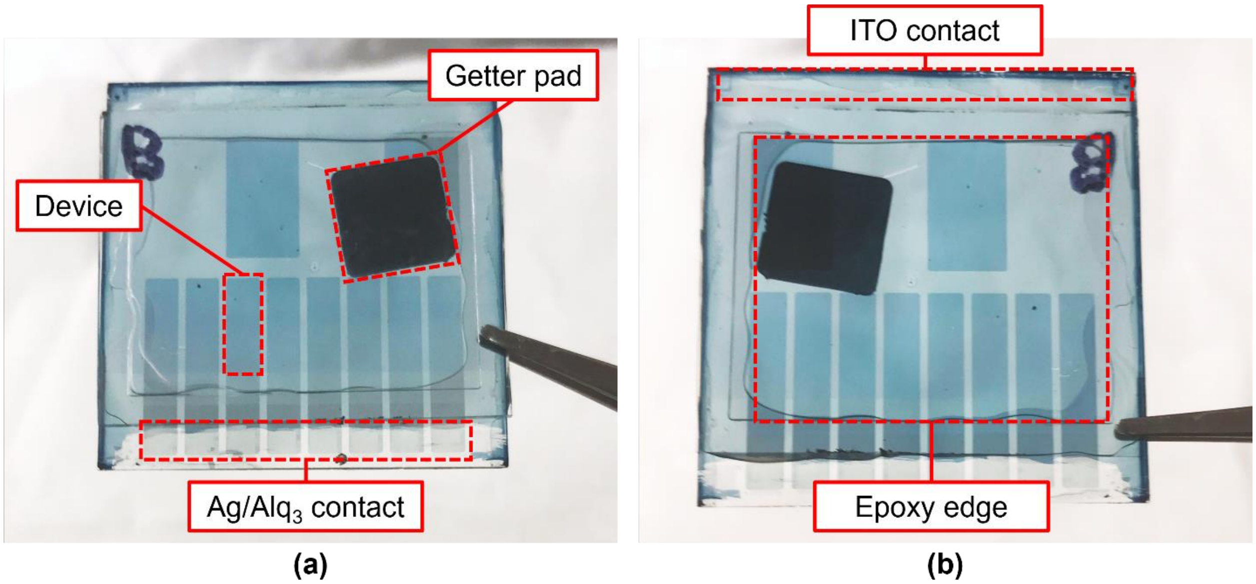

Figure 4.11. Encapsulated large area devices for lifetime testing. Large area transparent photovoltaic device from the **(a)** front and **(b)** back. Devices are encapsulated by applying a UV-curable epoxy (DELO) around the edge outlined in **(b)**. Cavity glass with a getter pad is placed on top of the device and the epoxy is cured in an oxygen and moisture free environment to form a seal around the devices. The top contact (Ag/Alq_3) and ITO contact are exposed outside of the epoxy and cavity glass seal in **(a)** and **(b)**, respectively, to allow for testing.

example of this is shown in Figure 4.10c and d, where the blue film is the layer formed via spin-coating and removed via razorblade.

Large area devices, typically for lifetime assessment, were fabricated on 1.5” x 1.5” substrates with prepatterned ITO. The procedures for exposing the ITO contacts were repeated as described above. Lifetime devices were encapsulated with cavity glass sealed around the outside of the device area with a UV curable epoxy (Figure 4.11). The epoxy seal provides a barrier against oxygen, water, and other contaminants that could cause device degradation. A getter pad was placed on the cavity glass so that it is inside the sealed device. Oxygen or moisture entering the sealed cavity will be captured via adsorption onto the getter pad, further protecting the device. It is important that the getter pad be placed so as not to block the device area(s), and that the epoxy does not spread to cover the exposed ITO contacts (Figure 4.11).

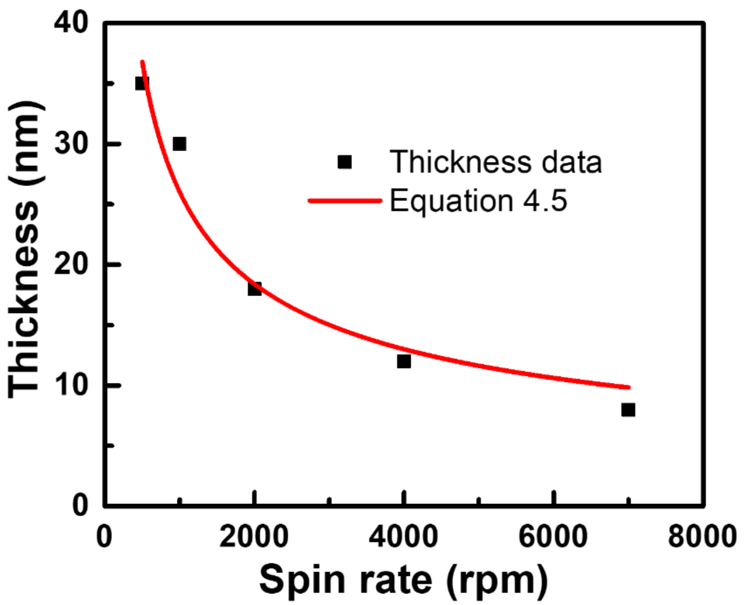

Figure 4.12. Thin film thickness versus spin-coating rate. Thickness of an organic salt film as a function of spin rate (black squares) with a fitted model of Equation 4.5 (red line). Data was fitted with a proportionality constant.

4.3.1 Spin-coating

Spin-coating is a solution processing method used in all four of the projects presented here that can yield films of thicknesses ranging from a few nanometers to microns. Key variables in the resulting thickness and quality (uniformity, roughness, coverage) of the film are related to the solvent, solute, and processing conditions. The vapor pressure and viscosity of the solvent are tied directly to the spin-rate and spin duration needed to grow quality films. High vapor-pressure solvents such as acetone can be difficult to spin-uniform films with because the timescale of solvent evaporation is smaller than that of spin-coating. High boiling point solvents such as DMSO or DMF can place limitations on the maximum thickness grown because they may require high spin-rates to remove the solvent. The film thickness, d, is related to the spin rate, ω, by Equation 4.5. An example of spin rate dependent film thickness is shown in Figure 4.12.

$$d \propto \frac{1}{\sqrt{\omega}} \tag{4.5}$$

For the solute, the size and molecular weight can impact the viscosity of the resulting solution. Polymers such as PTB7-Th yield more viscous solutions than IEICO-4F, and accordingly need a larger volume to completely cover the substrate and generally yield thicker films at the same concentration. The solubility and chosen concentration of the solute are critical to determining the maximum thickness of a spin-coated layer and which solvents are viable for spin-coating. Solubility is also impactful as a low solubility may necessitate solution stirring and/or heating. Spin-coating from a heated solution (or onto a heated substrate) will change the film thickness and the solution volume required to completely cover the substrate and can be challenging to replicate. In this work, solute concentration is used as the variable to alter film thickness in most cases because it gives a strongly linear correlation to thickness and offers a broader range of resulting thicknesses than varying the spin-rate. Lastly, solvent orthogonality is key for solution processing because previously grown layers can be redissolved when the next solution is applied, leading to partial or full layer removal, or layer blending.

Processing conditions, including substrate and solution temperature, can play a key role in spin-coating films. As mentioned, the spin-rate directly ties to the film thickness, and the acceleration used is similarly impactful. Rapid acceleration to the desired spin-rate provides the most consistent film thickness batch to batch. Multiple spin-rates can also be used as in the case of PTB7-Th, where an initial rate sets the thickness and a secondary, higher spin-rate step is used to ensure that all of the solvent has been removed. Films spun in this work were all done with static spin-coating, where the solution is pipetted onto the substrate and spreads to cover the substrate before the spin-coating process starts. It is important for substrate-to-substrate reproducibility that the time between pipetting and spin-coating is as consistent as possible. An alternative to static spin-coating is dynamic spin-coating, where the substrate is spins and the solution is pipetted after the substrate reaches a steady-state spin-rate. Dynamic spin-coating is more useful for certain

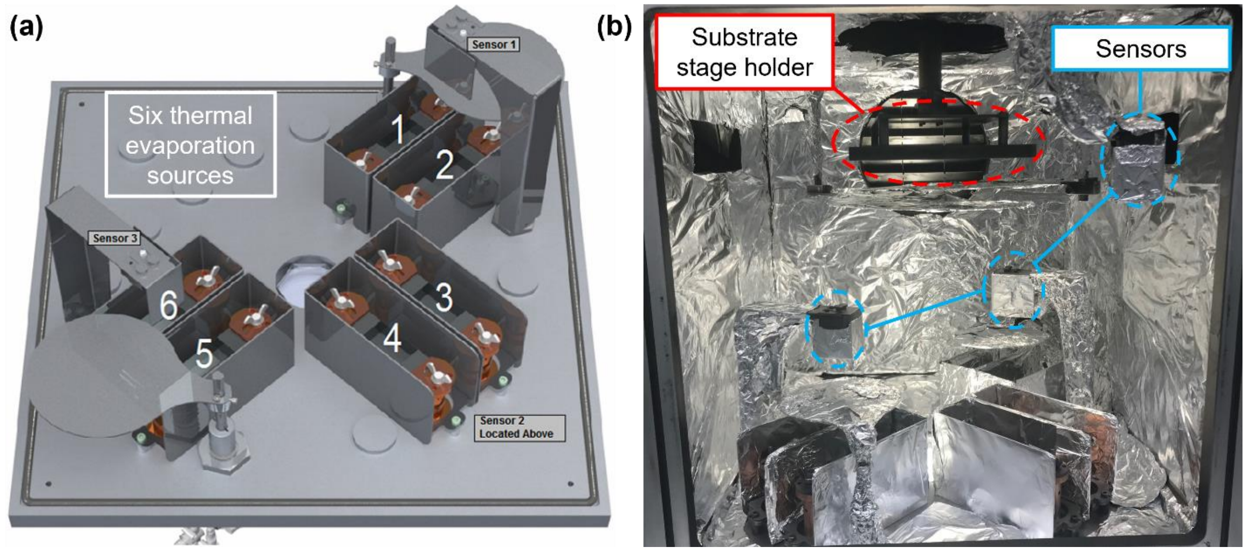

Figure 4.13. High vacuum thermal vapor deposition system. (a) Schematic of the high vacuum thermal vapor deposition AMOD system detailing the six thermal evaporation boats, three sensors, and two substrate shutters. **(b)** Picture of the cleaned and re-foiled AMOD chamber. The three sensor positions are outlined in blue, and the substrate stage holder, where devices are held during thin film growth, is outlined in red.

solvents, but it can be difficult to achieve full substrate coverage or acquire adequately thick films, and can require more solution volume.

Solution processing via spin-coating is an important technique for thin film processing of materials that are not compatible with thermal or high vacuum techniques due to their more fragile bonds or high molecular weight and subsequently high sublimation temperature relative to their decomposition temperature. Spin-coating is limited in the uniformity that can be achieved with larger substrates. In this thesis, the largest substrates used were 1.5” x 1.5”, and even smaller substrates show visible edge effects (thicker films at substrate edges due to boundary conditions). Spin-coating also wastes the majority of the material, as most of the solute is thrown off the film during spinning, and the solvent is either thrown off or evaporated. The amount of material needed and wasted for spin-coating are limiting for of scale-up. However, for lab-scale device fabrication, especially of organic semiconductors, it is excellent because of the uniformity, thickness range, and reproducibility.

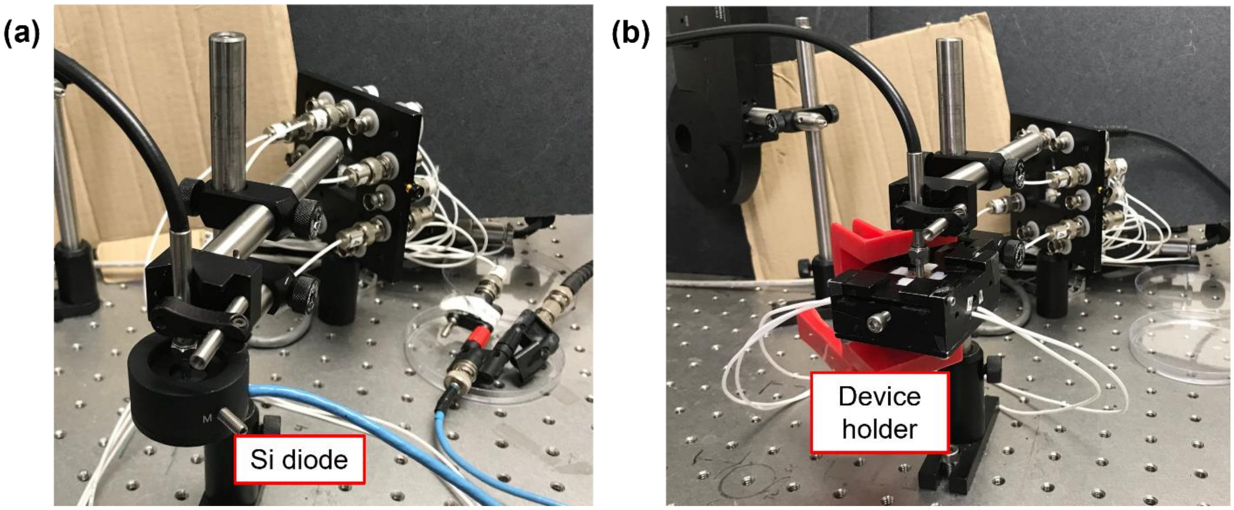

Figure 4.14. External quantum efficiency calibration and testing. (a) Setup for external quantum efficiency (*EQE*) calibration with the silicon diode and **(b)** *EQE* testing setup for photovoltaic devices.

4.3.2 High vacuum thermal vapor deposition

Thin films grown via thermal vapor deposition in this work were done at high vacuum with a base pressure of $3\text{x}10^{-6}$ torr. Materials were loaded into resistive baffled or dimpled tungsten boats or crucibles clamped between copper posts (Figure 4.13). A voltage applied across the posts heats the tungsten, sublimating the selected material which deposits onto the substrates above the boat as a thin film. Ag, BCP, and Alq_3 were loaded as needed the day before device fabrication, while MoO_3 and C_{60} were loaded fresh for each device set. Angstrom engineering deposition software in concert with a PID controller was used to control the power and growth rate, which were measured by quartz crystal monitors (QCM) calibrated to measure the thickness at the substrate location via a tooling factor. Film thicknesses for recalculating the tooling factor were measured with VASE or AFM and the nominal and experimental thicknesses were used to calculate a new tooling factor with Equation 4.6.

$$tf_{new} = \left(\frac{d_{meas}}{d_{QCM}}\right) tf_{old} \tag{4.6}$$

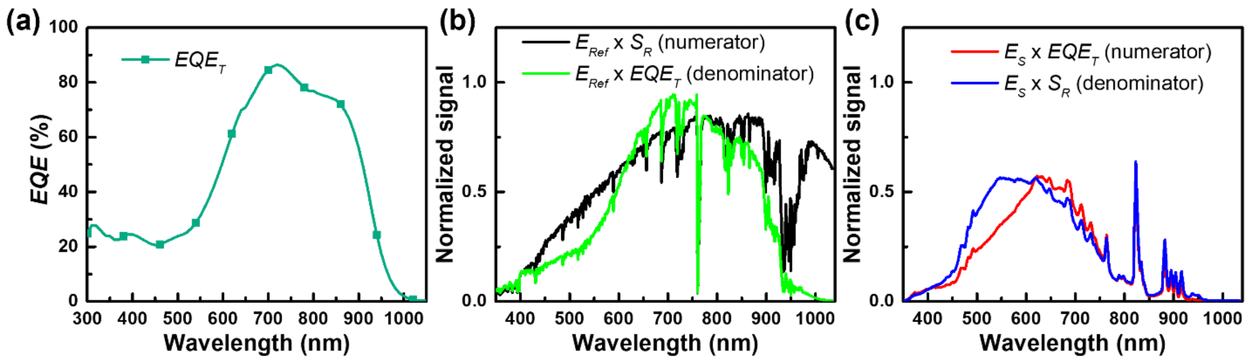

Figure 4.15. Mismatch factor calculation. (a) Experimental device *EQE* used in this example mismatch factor calculation. **(b-c)** Mismatch factor integrands used to calculate the spectral mismatch factor (*M*) of approximately 1.2 with Equation 4.7. All data sets are normalized for the calculation. **(b)** The product of the AM1.5G spectra (E_{Ref}) and the silicon diode response (S_R) (black curve), and E_{Ref} and the device *EQE* (EQE_T) (green curve). **(c)** The product of the *J-V* lamp spectra (E_S) and EQE_T (red curve), and E_S and S_R (blue curve).

4.4 Device characterization

4.4.1 Current-voltage characteristics

To measure the current-voltage characteristics of the devices, each device is loaded into the device holder and placed a set distance from a xenon arc lamp. The distance and intensity of the lamp are calibrated with a NREL-calibrated Si reference cell with KG5 filter so that the device experiences 1-sun intensity (100 mW/mm^2). The voltage applied across the device is swept to capture the characteristic J-V curve. A minimum of 5 devices were tested for *J-V* at each condition. Light intensity dependent *J-V* scans are taken using a filter wheel, which puts a neutral density filter between the lamp and the device, and the *J-V* characteristics are measured at the new lower intensity. Dark current-voltage scans are run with the lamp closed or blocked off, and all other lights off or blocked. The device is loaded into the device holder and covered with a box to further prevent any irradiation of the device and the *J-V* curve is taken.

4.4.2 External quantum efficiency

External quantum efficiency (*EQE*) measurements were made with monochromated light from a tungsten halogen lamp chopped at 200 Hz. A Newport-calibrated Si diode was used to calibrate the system prior to taking *EQE* measurements (Figure 4.14a). After calibration, devices are loaded into the substrate holder and positioned as close as possible to the optical fiber, shown in Figure 4.14b. The monochromated light exiting the optical fiber should be entirely contained within the device active area to provide an accurate *EQE*. Additionally, all other light sources must be covered or turned off so that no background illumination of the calibration diode or device is present. The current generated at each wavelength is measured with a picoammeter and background signal is removed via a lock-in amplifier.

As mentioned above, the overall lamp intensity for *J-V* measurements is calibrated with a silicon reference cell. However, the shape of the spectrum or relative intensity at each wavelength may not match the AM1.5G spectrum. To correct for this, the spectral mismatch factor (*M*) is calculated from the device *EQE* (EQE_T), the Si calibration diode responsivity (S_R), and the AM1.5G (E_{Ref}) and *J-V* lamp (E_S) spectra with Equation 4.7. The four integrands of Equation 4.7 are plotted in Figure 4.15 to provide a visual representation of the spectral mismatch.

$$M = \frac{\int_{\lambda_1}^{\lambda_2} E_{Ref}(\lambda) S_R(\lambda) d\lambda}{\int_{\lambda_1}^{\lambda_2} E_{Ref}(\lambda) EQE_T(\lambda) d\lambda} \frac{\int_{\lambda_1}^{\lambda_2} E_S(\lambda) EQE_T(\lambda) d\lambda}{\int_{\lambda_1}^{\lambda_2} E_S(\lambda) S_R(\lambda) d\lambda} \tag{4.7}$$

The lamp spectra is measured periodically with an Ocean Optics Spectrometer. The device *EQE*, diode responsivity, and lamp spectra were all normalized prior to calculating the mismatch factor. Additionally, mismatch factors were also calculated for the filtered lamp spectra used for light intensity dependent measurements. Mismatch should be calculated and reported for each cell with different *EQE*. Typically, the *EQE* is measured first, then the mismatch (*M*) calculated and then the lamp intensity can be set to 1 sun for that test cell for *J-V* measurement. Alternatively (and often), we set an approximate 1 sun and then correct the *PCE* and actual lamp intensity afterwards. Mismatch should be calculated for differing intensities (especially if neutral density filters are used to lower the light intensity) because the solar simulator spectra will shift.

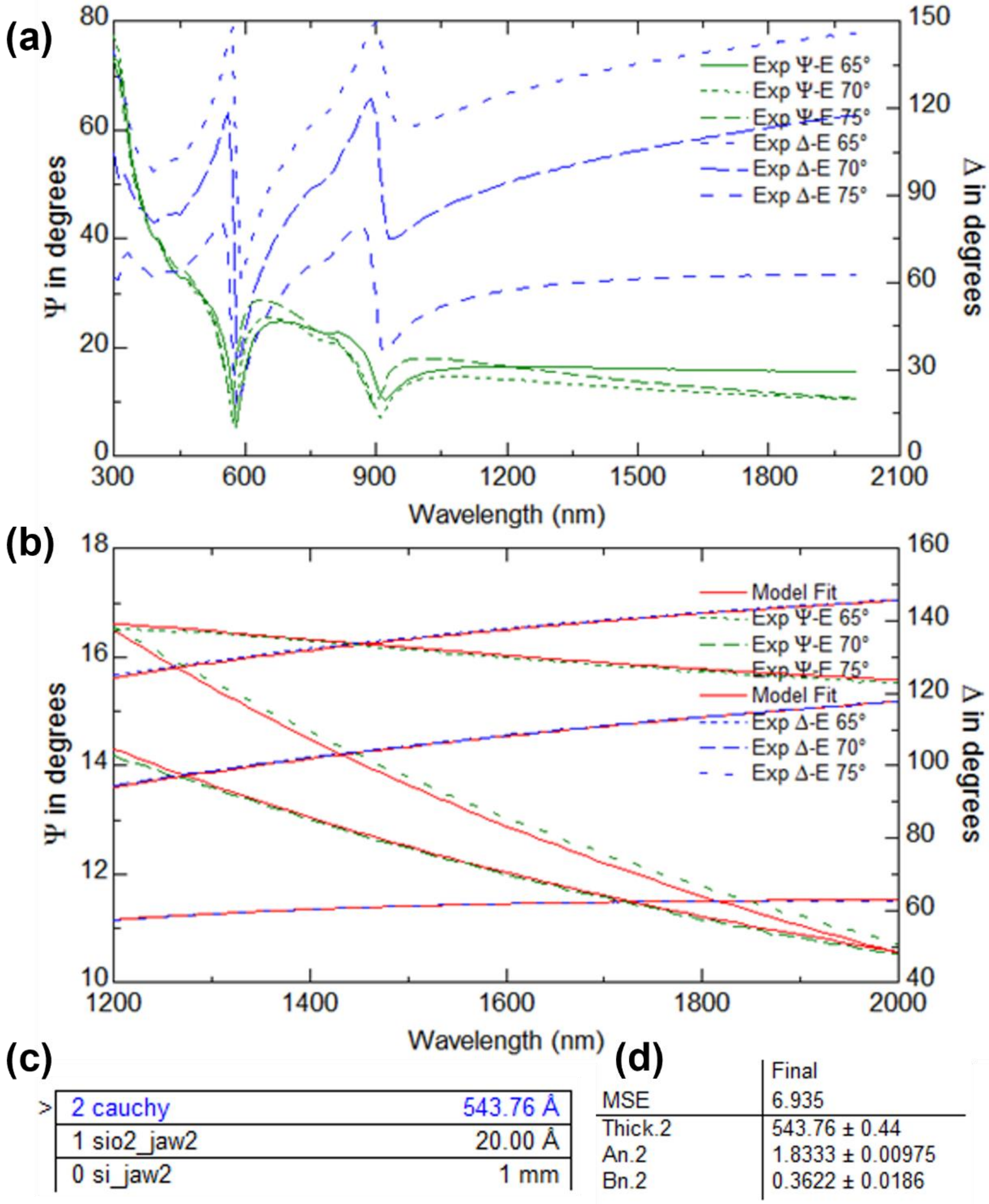

>	2 cauchy	543.76 Å
	1 sio2_jaw2	20.00 Å
	0 si_jaw2	1 mm

	Final
MSE	6.935
Thick.2	543.76 ± 0.44
An.2	1.8333 ± 0.00975
Bn.2	0.3622 ± 0.0186

Figure 4.16. VASE thickness fitting. (a) Raw ellipsometry data output for an organic salt thin film. **(b)** Model generated fit in the transparent region of the film (1200 to 2000 nm) to obtain the organic salt film thickness. **(c)** The model used to fit the data consisting of the silicon (Si) substrate, silicon dioxide layer (SiO_2), and the Cauchy layer used to model the organic salt film. **(d)** The fit results from a two-parameter fit (An.2 and Bn.2) for the thickness (54 nm).

4.4.3 Variable angle spectroscopic ellipsometry

Thin film thicknesses were measured with a Woollam Ellipsometer using VASE. Films were spun or deposited onto silicon wafers with approximately 20 Å of SiO_2 on top. VASE

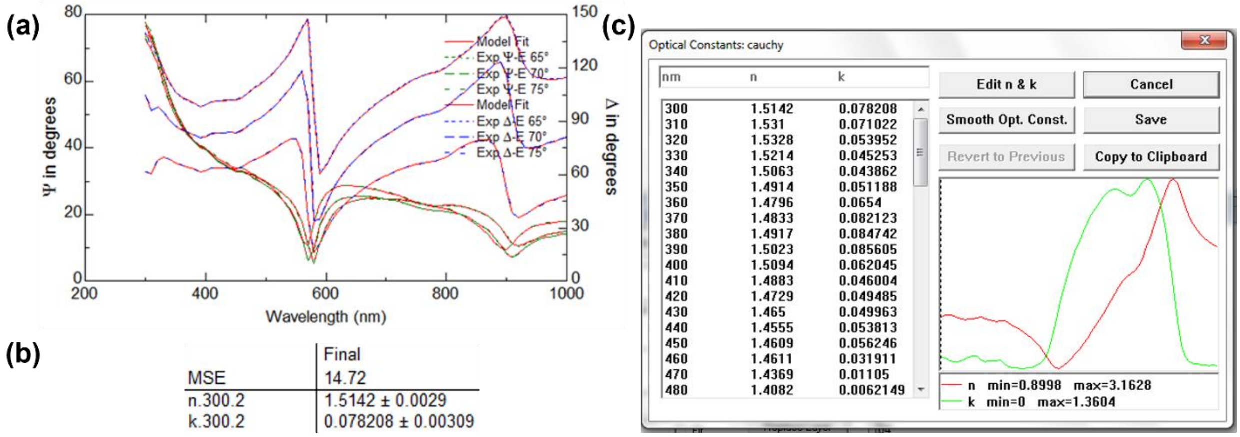

	Final
MSE	14.72
n.300.2	1.5142 ± 0.0029
k.300.2	0.078208 ± 0.00309

nm	n	k
300	1.5142	0.078208
310	1.531	0.071022
320	1.5328	0.053952
330	1.5214	0.045253
340	1.5063	0.043862
350	1.4914	0.051188
360	1.4796	0.0654
370	1.4833	0.082123
380	1.4917	0.084742
390	1.5023	0.085605
400	1.5094	0.062045
410	1.4883	0.046004
420	1.4729	0.049485
430	1.465	0.049963
440	1.4555	0.053813
450	1.4609	0.056246
460	1.4611	0.031911
470	1.4369	0.01105
480	1.4082	0.0062149

n min=0.8998 max=3.1628
k min=0 max=1.3604

Figure 4.17. VASE optical constant fitting. (a) Point-by-point fit of ellipsometry data for the optical constants in the region of organic salt absorption. **(b)** End result of the fit when starting at the long wavelength end (1000 nm) and going to the short wavelength end (300 nm). **(c)** Output window showing the fitted optical constants n and k over the selected wavelength range.

measures the changes to polarized light caused by reflections in the sample. Light from a xenon lamp is monochromated and passed through a polarizer to produce polarized light that is either parallel or perpendicular to the plane of incidence. A continuously rotating polarizer (called the analyzer) collects the reflected light and measures changes to the amplitude (Ψ) and phase (Δ) of the polarized light (Figure 4.16a), which are related to the Fresnel reflection coefficients for polarized light, r_p (parallel) and r_s (perpendicular), and the ratio of the two, ρ, as shown in Equation 4.8.[126]

$$\tan(\Psi)e^{i\Delta} = \rho = \frac{r_p}{r_s} \tag{4.8}$$

A Cauchy fit (Equation 4.9) is employed to fit the ellipsometric data for thickness, d, and the optical constants that constitute the complex index of refraction, n and k.

$$n(\lambda) = A + \frac{B}{\lambda^2} + \frac{C}{\lambda^2} \tag{4.9}$$

A transparent region of the film is selected (1200 to 2000 nm for many materials in this work, for which k = 0 in this range), and the experimental data is fitted with typically two (A and B from Equation 4.9) and in some cases three (A, B, and C) parameters to ensure a good fit and an accurate thickness measurement, which is quantified by the mean squared error (Figure 4.16b-d). If the optical constants were needed, the non-transparent region of the film was selected, and the fitting parameters and thickness were held constant while a point by point fit of *n* and *k* was carried out (Figure 4.17). A general fit was then performed to ensure Kramers-Kronig consistency.

4.4.4 Hole mobility measurements

Single carrier hole only devices were created with a thick layer of the active material sandwiched between layers of MoO_3, which possesses a deep HOMO level to prevent electron injection. Standard ITO and Ag bottom and top contacts complete the device. *J-V* testing was performed in the dark by sweeping the voltage from -3.5 to 3.5 V. Device data was fit with the Mott-Gurney equation (Equation 4.10) for space charge limited current (SCLC) to extract the hole mobility after confirming symmetric *J-V* behavior (single carrier device and not a diode) in both positive and negative sweeps.

$$J = \frac{9}{8}\varepsilon\mu\frac{V^2}{d^3} \tag{4.10}$$

The SCLC regime was identified by the linear region described by J vs V^2, where ε is the dielectric constant of the organic salt approximated by the product of the permittivity of free space and the squared index of refraction of the organic salt, and d is the thickness of the organic salt film.

4.4.5 Transient photovoltage measurements

Transient photovoltage measurements were made to assess carrier lifetime[127,128] by exciting devices with a Stradus 785 nm laser pulsed for 1 µs with a 500 µs period by an Agilent 80MHz Function/Arbitrary Waveform Generator. Devices were biased with a white light so that V_0, the baseline potential, was equal to the V_{OC} of each device (Figure 4.18). The open-circuit condition prevents charge carrier extraction from the device. Upon excitation with the pulsed laser, excited state electrons are generated, causing a small perturbation in the measured voltage. As time

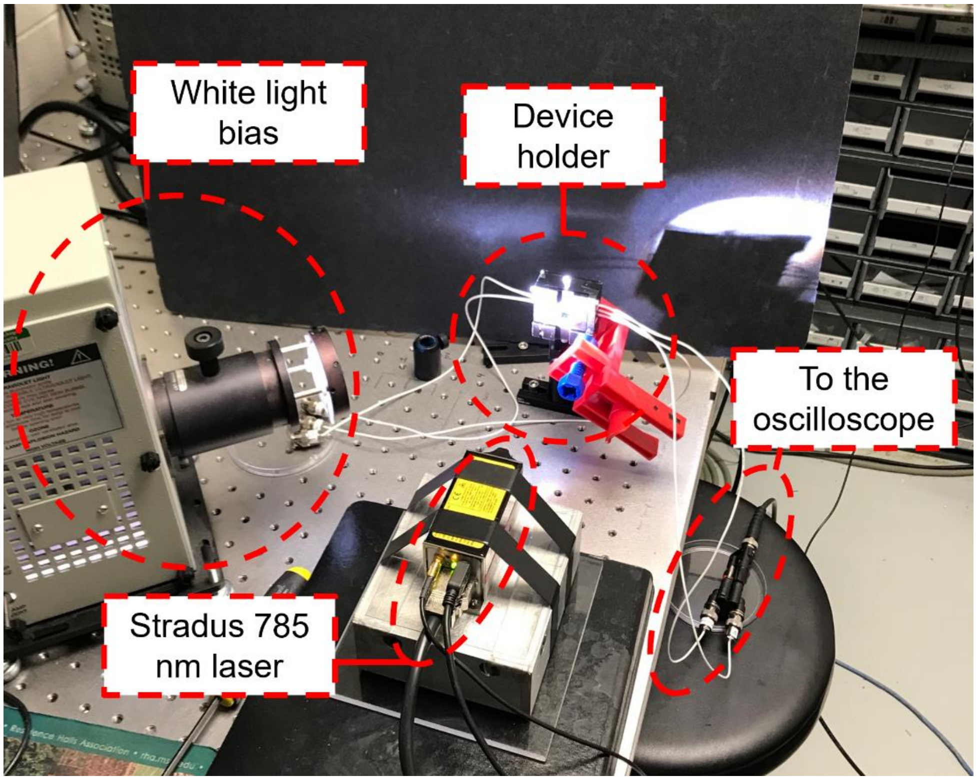

Figure 4.18. Transient photovoltage setup. Setup of the device, laser, and white light bias for transient photovoltage measurements.

passes, excited state carriers recombine and the potential perturbation decays. The voltage decay was measured with an Agilent DSO-X 3032A Oscilloscope at 1 MΩ impedance and fitted with an exponential decay equation (Equation 4.11), where V is the measured potential, t is the time, A is the pulse amplitude, and τ_h is the carrier lifetime.

$$V = A\ exp\left(\frac{-t}{\tau_h}\right) + V_0 \tag{4.11}$$

4.5 Transfer matrix optical modeling and *EQE* fitting

Transfer matrix optical modeling is a common approach used to model the propagation of light through a stack of thin-film materials constituting a PV device.[95,129,130] As discussed in section 1.2.4, absorption in OPVs is dominated by complex optical interference effects rather than the Beer-Lambert law. This phenomenon is due to the thickness of the layers being on a similar order of magnitude (or smaller) as the wavelengths of light incident on the device. For each layer,

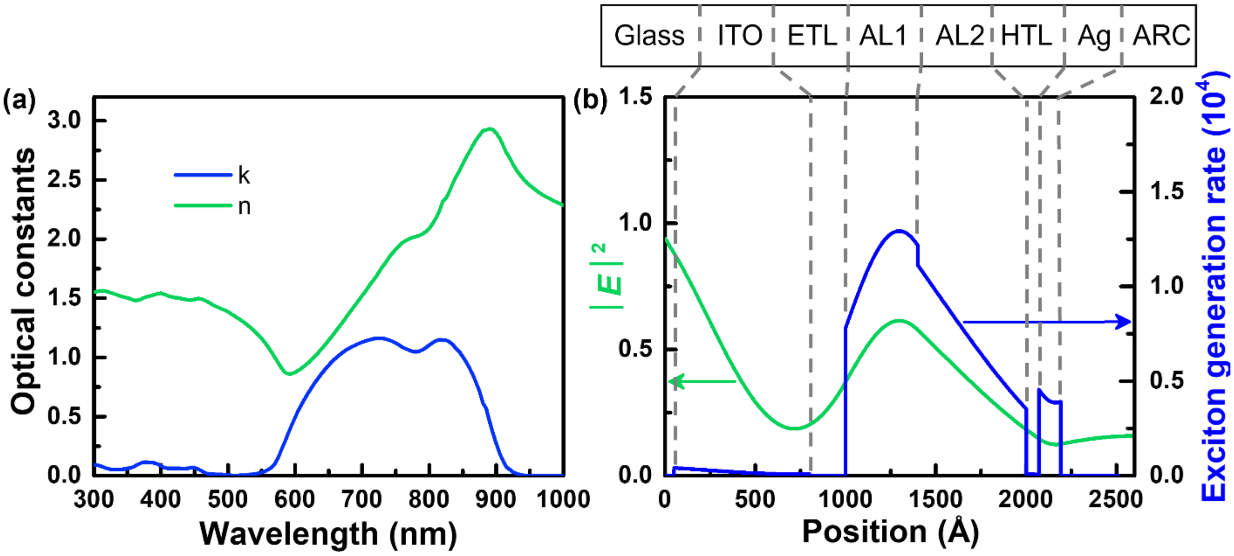

Figure 4.19. Optical constants, electric field, and exciton generation rate. (a) Example optical constants obtained from ellipsometry used in the optical modeling. **(b)** Example electric field ($|E|^2$)and exciton generation rate calculated from the transfer matrix optical modeling code for a representative TPV device with active layers AL1 and AL2 and an antireflection coating (ARC). The device architecture is presented at the top, with the donor material (AL1) located from 1000 to 1400 Å and the acceptor (AL2) from 1400 to 2000 Å so that the donor-acceptor interface is at 1400 Å.

j, of thickness d_j, optical constants (n_j and k_j) are extracted from VASE fits. These constants make up the complex index of refraction, $\tilde{n}_j$ (Equation 4.12) and are used to write matrices that describe the interaction of the electric field at every interface and in each layer of a device stack. Example optical constant profiles are shown in Figure 4.19a.[129,130]

$$\tilde{n}_j = n_j + ik_j \tag{4.12}$$

The propagation of light through layer j of thickness d_j is described by Equation 4.13,[130]

$$L_j = \begin{bmatrix} e^{-i\xi_j d_j} & 0 \\ 0 & e^{i\xi_j d_j} \end{bmatrix} \tag{4.13}$$

Where ξ_j is given in Equation 4.14:[130]

$$\xi_j = \frac{2\pi}{\lambda}\tilde{n}_j \tag{4.14}$$

For adjacent layers j and k, the Fresnel coefficients for transmission (t_{jk}) and reflection (r_{jk}) are written Equations 4.15 and 4.16.[130]

$$t_{jk} = \frac{2\tilde{n}_j}{\tilde{n}_j + \tilde{n}_k} \tag{4.15}$$

$$r_{jk} = \frac{\tilde{n}_j - \tilde{n}_k}{\tilde{n}_j + \tilde{n}_k} \tag{4.16}$$

Utilizing the Fresnel coefficients, an equation describing the propagation of the electric field incident on (E_j) and leaving (E_k) an interface between layers j and k is given in Equation 4.17. The plus and minus symbols are used to denote the electric field propagating in the forward (+) and reverse (-) directions.[129,130]

$$\begin{bmatrix} E_j^+ \\ E_j^- \end{bmatrix} = I_{jk} \begin{bmatrix} E_k^+ \\ E_k^- \end{bmatrix} = \begin{bmatrix} \frac{1}{t_{jk}} & \frac{r_{jk}}{t_{jk}} \\ \frac{r_{jk}}{t_{jk}} & \frac{1}{t_{jk}} \end{bmatrix} \begin{bmatrix} E_k^+ \\ E_k^- \end{bmatrix} \tag{4.17}$$

The transfer matrix, S_T, for the device stack consisting of m layers is calculated from L_j and I_{jk} using Equation 4.18.

$$S_T = \begin{bmatrix} S_{11} & S_{12} \\ S_{21} & S_{22} \end{bmatrix} = \left(\prod_{n=1}^{m} I_{(n-1)n} L_n \right) I_{m(m+1)} \tag{4.18}$$

Similar to Equation 4.17, where I_j describes the transformation of the electric field entering and leaving an interface between two layers, the transformation of the incident electric field entering and leaving the device, $E_0^{+/-}$ and $E_{m+1}^{+/-}$ is described by S_T in Equation 4.19.

$$\begin{bmatrix} E_0^+ \\ E_0^- \end{bmatrix} = S_T \begin{bmatrix} E_{m+1}^+ \\ E_{m+1}^- \end{bmatrix} \tag{4.19}$$

The electric field at a given position x within layer j is described by Equation 4.20.

$$E_j(x) = E_j^+ + E_j^- = \left(t_j^+ e^{i\xi_j x} + t_j^- e^{-i\xi_j x}\right) E_0^+ \tag{4.20}$$

Using Equation 4.20, the exciton generation rate (G_j) at position x is written in Equation 4.21, where Q_j is the time averaged absorbed power at x, and c is the speed of light.[130]

$$G_j(x) = \frac{\lambda}{hc} Q_j(x) = \left(\frac{\lambda}{hc}\right) \left(\frac{4\pi c \varepsilon_0 k_j n_j}{2\lambda}\right) \left|E_j(x)\right|^2 = \frac{2\pi \varepsilon_0 k_j n_j}{h} \left|E_j(x)\right|^2 \tag{4.21}$$

Example exciton generation rate and electric field profiles are shown in Figure 4.19b. A 1-D steady state exciton diffusion equation can be written including the generation rate from Equation 4.21, where *p* is the exciton density at position *x*, τ_j is the exciton lifetime in layer *j*, and $L_{ED}{}^{j}$ is the exciton diffusion length of layer *j* defined in Equation 4.23 with the exciton diffusivity, D_j, and dimensionality factor, *Z*.

$$L_{ED}^{j}{}^{2}\frac{\partial^2 p(x)}{\partial^2 x} - p(x) + \tau_j G_j = 0 \tag{4.22}$$

$$L_{ED}^{j}{}^{2} = \sqrt{Z D_j \tau_j} \tag{4.23}$$

Equation 4.22 can be solved for the current produced by each exciton generating layer with the boundary condition *p*(*x*) = 0 at $x = x_{DA}$, where x_{DA} is the donor-acceptor interface location.[130]

$$J_j = q\frac{L_{ED}^{j}{}^{2}}{\tau_j}\left|\frac{\partial p}{\partial x}\right|_{x=x_{DA}} \tag{4.24}$$

Equation 4.24 holds for other interfaces, however interfaces between active materials and metals or supporting layers (ETL/HTL) will generally be unable to dissociate excitons to produce current, and instead will non-radiatively quench excitons. Equation 4.24 assumes that the efficiency of charge collection, η_{CC}, charge transfer, η_{CT}, and exciton dissociation, η_{DS} are equal to 1. For a sufficient LUMO-LUMO offset between donor and acceptor materials, this is a valid assumption for η_{CT} and η_{DS}. In the case that these assumptions hold, the current depends only on the exciton diffusion efficiency, captured by $L_{ED}{}^{j}$, and the absorption efficiency, which is a determining factor in the solution to *p*(*x*). Normalizing the current generated at the dissociating interface by the incident photon flux yields Equation 4.25 describing the *EQE* from layer *j* given the above assumptions.

$$EQE_j = \frac{J_j}{\frac{1}{2}qc\varepsilon_0|E_0^+|^2} \tag{4.25}$$

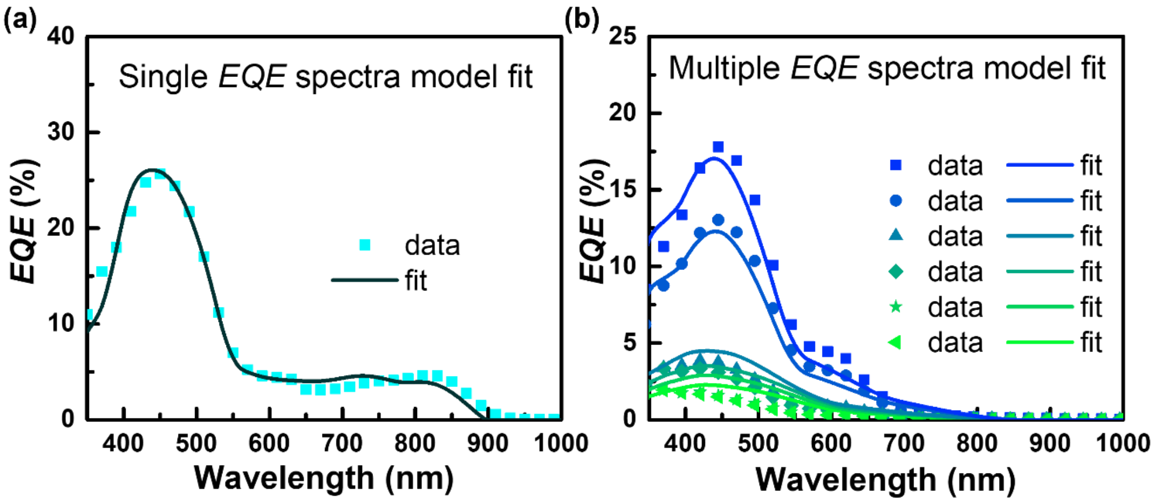

Figure 4.20. Transfer matrix modeling and *EQE* fitting. (a) A single *EQE* dataset fit for characteristic diffusion lengths from the original *EQE* modeling code and **(b)** the simultaneous fit of several *EQE* datasets with increasing donor thickness (blue to green) for diffusion and charge collection lengths from the modified *EQE* modeling code.

With an exciton diffusion length, the transfer matrix optical model is capable of generating an expected *EQE* profile for an OPV device based on the optical constants for all layers of the device, the exciton diffusion lengths of the donor and acceptor, and the incident light spectra (1-sun intensity AM1.5G solar spectrum). A more accurate model for systems where L_{CC} is not significantly larger than L_{ED} can be generated by including the charge collection efficiency equation (Equation 1.18) where d is the entire film thickness.[3] The L_{ED} and L_{CC} are supplied by the user to the model either as a set/fixed value or as a guest that can be iterated to fit the predicted *EQE* to one or more experimentally measured *EQE* spectra. An example of a single fitted *EQE* curve and several fitted *EQE* datasets are shown in Figure 4.20a and b. Alternatively, the transfer matrix optical model can be used to predict electronic (J_{SC}) and optical (*A* for opaque devices, *AVT* for TPVs) device performance. For opaque devices, this is a powerful tool for determining the device thickness needed to position the electric field at its strongest near the donor-acceptor interface to enhance exciton diffusion efficiency. For TPVs, the model is useful for predicting the transparency of hypothetical device structures, including for finding the optimal thickness of a

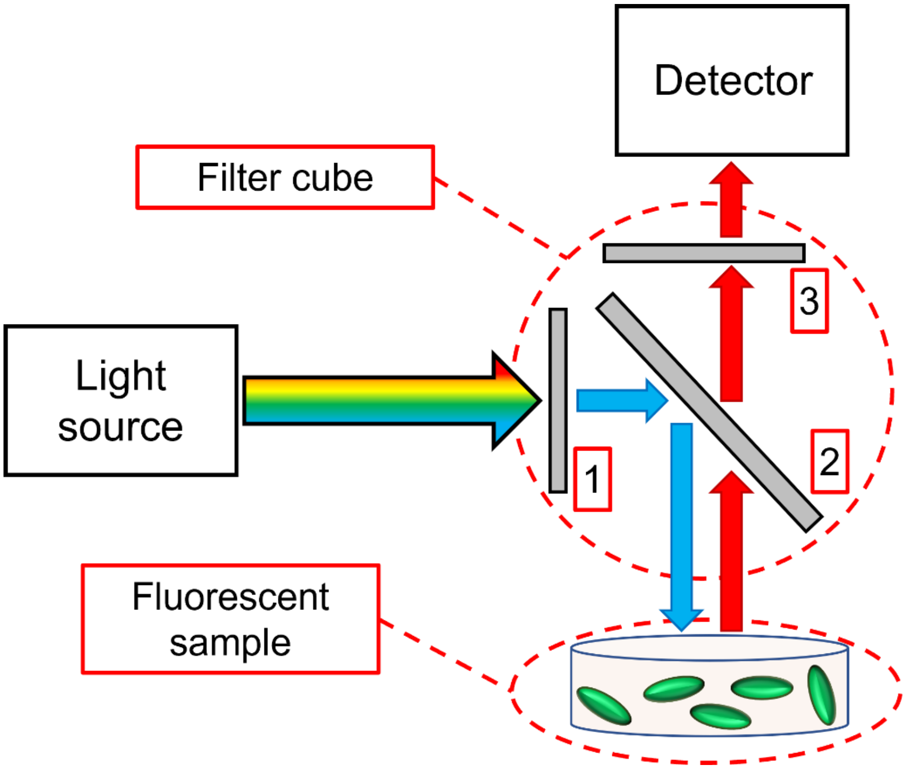

Figure 4.21. Fluorescent imaging operating principles. A general schematic detailing the operating principles of fluorescent microscopy with the excitation light (rainbow patterned arrow), filtered excitation light (blue arrow), and emission light (fluorescence, red arrow) The components of the filter cube are (1) the excitation filter, which removes unwanted excitation wavelengths, (2) the dichroic mirror that reflects the excitation wavelength and transmits the emission wavelengths, and (3) the emission filter, which removes unwanted fluorescence from other fluorophores in the sample.

given layer to maximize *AVT* without using the time and materials to make the optimization device sets.

4.6 Fluorescent imaging

Fluorescent imaging is a powerful microscopy technique in which a fluorophore is excited with a certain wavelength of light and re-emitted light at a new wavelength is captured by a detector to create an image. The separation between the absorption peak and emission peak of the fluorophore is the Stokes shift, which plays a role in determining the setup required for fluorescence imaging. The fluorescence intensity of the material of interest will be much weaker than the exciting light, so that the key to capturing the fluorescence is preventing the excitation light from being reflected or scattered into the detector. To this end, a central component of a fluorescence microscope is the filter cube (Figure 4.21), which can consist of three parts, 1) an excitation filter to allow only the desired exciting wavelength to reach the sample, 2) a dichroic mirror, which reflects the exciting wavelength while transmitting the fluorescence wavelength, and 3) an emission filter to remove undesired fluorescence if there are multiple fluorophores present. The excitation filter is needed primarily if the exciting light is from a broad-spectrum light source versus a narrow-spectrum light source that only features the wavelength of interest. If the light source contains wavelengths of light of the expected fluorescence, this light must be filtered out.

To generate a fluorescent image, exciting light from the light source is incident on the dichroic mirror and is reflected towards the sample. The exciting light passes through the excitation filter, removing unwanted wavelengths before illuminating the sample. Light is absorbed and remitted at wavelengths determined by the Stokes shift and with an efficiency based on the fluorescence quantum yield, $\Phi_{F.}$ Emitted light and reflected excitation light reaches the dichroic mirror, which reflects the excitation light and transmits the fluorescence. The fluorescence is then collected by the detector to produce an image. If there are multiple fluorophores in the system, the filter cube could be designed to reflect the shorter fluorescence wavelengths (transmitting longer fluorescent wavelengths). However, if the desired fluorescence is of a shorter wavelength than unwanted fluorescence, a short-pass emission filter could be added to the filter cube to selectively block the deeper emission.

Chapter 5 – Charge Transfer in Organic Salt Photovoltaics

This chapter was published in *Journal of Applied Physics* as "Impact of charge character on anionic cyanine-based organic salt photovoltaics".[131]

5.1 Introduction

Organic small molecules are highly suitable in electronics, imaging, optoelectronics, and therapeutics due to their strong molecular extinction coefficients, processability, tunable absorption bands, and high fluorescence quantum yields. In optoelectronics, organic small molecules have given rise to organic photovoltaics (OPVs) and transparent photovoltaics (TPVs) in non-fullerene all-small molecule devices[132,17,133,134] or paired with polymeric[135] donors in bulk heterojunction solar cells. All-small molecule OPVs recently achieved over 17% power conversion efficiency (*PCE*),[17] and offer yet unrealized potential for industrial scale TPVs. Organic salts are a class of organic small molecules composed of an ionic chromophore and a counterion, and have been employed in a wide range of applications including photodetectors,[27,58] OPVs,[86,94,95,101,102,136–142] transparent luminescent solar concentrators,[9] TPVs,[86,94] fluorescent imaging, and photodynamic therapy.[143,144] A common chromophore within organic salts is a cyanine dye, categorized in part by the length of the conjugated bridge, most commonly three (trimethine), five (pentamethine), or seven (heptamethine) atoms long. The bridge length and additional conjugation on the ends of the cyanine determine the location of the main absorption band, which can be tuned through the visible spectrum to deep into the near-infrared (NIR). To date, most demonstrations of organic salts in OPVs and TPVs have focused on a cationic chromophore paired with various counterions, which were long thought to have minimal impact on the device performance. Recent work has shown a range of counterion effects, including that counterion exchange can tune the highest occupied molecular orbital (HOMO) by over 1 eV,[94] increase exciton diffusion lengths,[94,101] extend device lifetimes to greater than seven years under standard illumination,[102] and increase molecular order in a neat film to improve device performance.[86,138,141] The best organic salt devices to date have achieved 4.3% power conversion efficiency (*PCE*) in tandem OPVs[142] and 2.2% in single-junction TPVs,[86] well below the realistic limit for TPVs.[21] Devices were restricted by short exciton diffusion lengths (<10 nm) that limit devices to thin layers of organic salt, and a general inability to form a stable bulk heterojunction (BHJ), as only two have been shown to date, achieving less than 0.4% *PCE*.[79,139] Exciton diffusion has only recently been studied in organic salt PVs,[94,101] while charge transport has been studied in other electronic devices, including dye-sensitized solar cells,[145] inorganic PVs,[146] photodetectors,[147] and phthalocyanine-fullerene PVs.[11,148] Charge transport in organic salts has only been explored in the form of long excited-state lifetimes and hole mobilities for cationic chromophores.[140] Anionic cyanines in organic salts have been studied for light-based applications,[149–152] but have seen very little use in OPVs and TPVs. Kawasaki fabricated simplified dye-sensitized solar cells with anionic trimethine cyanines that demonstrated 1-2% external quantum efficiency (*EQE*) at the peak salt absorption wavelength.[72] Bouit et al. synthesized an organic salt consisting of two cyanine dyes, one cationic and one anionic, and deployed the salt as the donor material in a BHJ OPV with 0.37% *PCE* and 11% peak *EQE* from the organic salt.[79] Control devices with an anionic heptamethine based organic salt achieved 0.07% *PCE* and approximately 1% peak *EQE* from the salt. To explore organic salt OPVs from a new perspective, we fabricated devices from four new salts comprised of an anionic heptamethine cyanine chromophore and sodium cation(s). This selection of materials allowed us to independently study the effects of increased conjugation and charge character in the chromophore on device performance and underlying processes such as exciton diffusion and charge transfer.

Pairing the organic salts with fullerene, we created devices with two isolated absorption regimes and distinct thickness dependent performance decay trends that allowed us to independently study and quantify exciton diffusion and charge transfer for each salt. We utilized transfer matrix optical modeling to fit our thickness-dependent data for characteristic lengths of exciton diffusion and charge collection, and demonstrated the impact that charge character on the chromophore has on each process. We then characterized carrier mobility and lifetime of the organic salts to elucidate the origin of improved charge transfer. Our work offers insight into the nature of fundamental charge transfer processes in these exciting materials and a platform from which to characterize exciton diffusion and charge transfer from a single device.

5.2 Methods

5.2.1 Experimental methods

PV device fabrication began with pre-patterned ITO coated glass substrates cleaned via sequential sonication for 10 minutes in deionized water, acetone, and isopropanol. Substrates were dried on a hotplate at 100°C for one minute before plasma cleaning for 10 minutes. Cleaned substrates were loaded into an Angstrom Engineering thermal vapor deposition chamber and 10 nm of MoO_3 was deposited at a base pressure of $3x10^{-6}$ torr. Organic salts were dissolved in methanol at concentrations of 1-10 mg/mL and neat films were spun on MoO_3 at 2000 rpm to yield films with thicknesses ranging from 3 to 70 nm as measured by VASE on Si substrates. Substrates with organic salt and MoO_3 films were loaded into the deposition chamber where 40 nm of C_{60}, 7.5 nm BCP, and 80 nm Ag were deposited to complete the device stack. A special mask was used for Ag deposition to define an active area of 4.43 mm^2.

Devices were characterized with current-voltage (*J*-*V*) curves acquired under illumination from a Xe arc lamp with intensity calibrated to 1-sun with a NREL-calibrated Si reference cell with KG5 filter. *EQE* measurements were made with monochromated light from a tungsten halogen lamp chopped at 200 Hz. A Newport-calibrated Si diode was used to calibrate the system prior to taking *EQE* measurements. A spectral mismatch factor of ~1.05 was calculated for the *J*-*V* measurements. A minimum of five devices were measured for each condition.

Hole only devices were fabricated on the same ITO coated glass substrates used for devices. 30 nm MoO_3 was grown on the substrates at $3x10^{-6}$ torr after sonication and plasma cleaning. 10 mg/mL of each organic salt in methanol was spun at 2000 rpm to form 45-55 nm films. 30 nm MoO_3 was grown on top of the organic salt and finally 80 nm Ag was grown using a mask to define the active area of 4.43 mm^2. *J*-*V* testing was performed in the dark by sweeping the voltage from -3.5 to 3.5 V. Device data was fit with the Mott-Gurney equation (Equation 4.8) for SCLC to extract the hole mobility after confirming symmetric *J*-*V* behavior (single carrier device and not a diode) in both positive and negative sweeps. The SCLC regime was identified by the linear region described by J vs V^2.

Transient photovoltage measurements were made to assess carrier lifetime[127,128] by exciting devices with a Stradus 785 nm laser pulsed for 1 µs with a 500 µs period by an Agilent 80MHz Function/Arbitrary Waveform Generator. The voltage decay was measured with an Agilent DSO-X 3032A Oscilloscope at 1 MΩ impedance and fitted with an exponential decay equation (Equation 4.9). Devices were biased with a white light so that V_0 was equal to the open circuit voltage and no net current flowed through the devices.

Thin film transmission data was collected for organic salt films spun from 10 mg/mL solutions onto cleaned unpatterned ITO coated glass substrates. A PerkinElmer UV-Vis spectrometer was used to make transmission measurements of the films. The reference slot was empty for solid-state thin film measurements. For solution measurements, organic salts at 10 µM in methanol were loaded into a borosilicate glass cuvette and placed in the sample slot of the spectrometer. Pure methanol in a second cuvette was placed in the reference slot. Transmission data was collected to obtain the absorption as 100-T(%). Photoluminescence measurements were made with a Photon Technology International fluorometer on 10 µM solutions of each salt. Error bars represent the standard error calculated from experimental uncertainty in measurement techniques and variation in measured variables.

The mass and charge of each of the four anionic heptamethines were verified with a high mass resolution ultra high-performance liquid chromatography mass spectrometry (UHPLC-MS) system, the Waters Xevo G2-XS QTof. Salts were dissolved in MeOH at 1 µM. An injection volume of 10 µL was used with pure MeOH as the eluent. Background scans with MeOH were run before and after each organic salt sample. Peak signals from the chromatography column were observed at approximately two minutes, and were integrated to yield the mass-to-charge signals.

5.2.2 Computational methods

EQE can be broken into five component efficiencies shown in Equation 1.8. To model PV devices, η_{CT} and η_{DS} are assumed to equal unity for a donor-acceptor interface with sufficient energetic offset to transfer charge and dissociate excitons into free charge carriers. Transfer matrix optical modeling[95] was used to calculate the electric field and absorption profile (η_A) in PV devices based on measured optical indices of refraction. The charge collection efficiency equation[3] (Equation 1.18) was used to describe charge collection losses in the organic salt and C_{60} layers. The exciton diffusion length ($L_{ED,D}$) for each organic salt were calculated with a nonlinear regression fit of the squared standard error for the difference between measured and calculated *EQE*. Devices with the thinnest organic salt layer were fitted for $L_{ED,D}$ and the exciton diffusion length of C_{60} ($L_{ED,A}$) with a C_{60} charge collection length ($L_{CC,A}$) of 100 nm. Charge

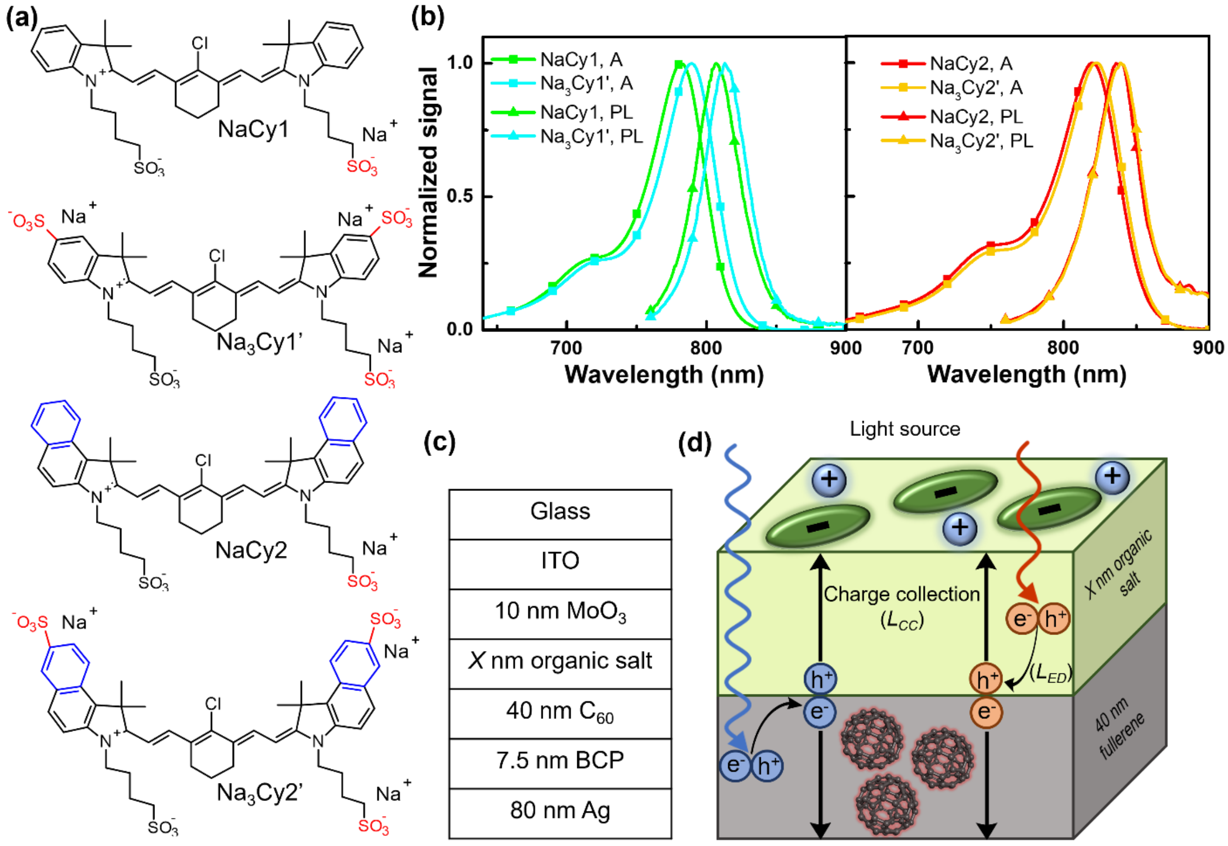

Figure 5.1. Anionic heptamethines used as donor compounds in photovoltaics. (a) Anionic heptamethines used in this study which vary in charge (-1 or -3) or conjugation. **(b)** Absorption (A) and photoluminescence (PL) data for the four chromophores. **(c)** Solar cell architecture with variable organic salt thickness and fixed acceptor (C_{60}) thickness. **(d)** Schematic of the current generation process in organic salt photovoltaics.

collection losses from the organic salt layer were not included in this initial model as $L_{CC} >> L_{ED}$ for most organic materials. All other devices were fit with a fixed $L_{ED,A}$ and $L_{CC,A}$, and a variable $L_{ED,D}$ to prevent artificial shortening of $L_{ED,A}$ as a result of organic salt charge collection losses in the C_{60} absorption regime.

The calculated external quantum efficiency, $EQE_{fixed\ L_{ED,A}}$, was used to modify Equation 1.18 to form Equation 5.1 and fit the experimental EQE at 440 nm for the organic salt charge collection length ($L_{CC,D}$) as a function of organic salt thickness. This wavelength was selected as the peak C_{60} EQE with minimal organic salt absorption.

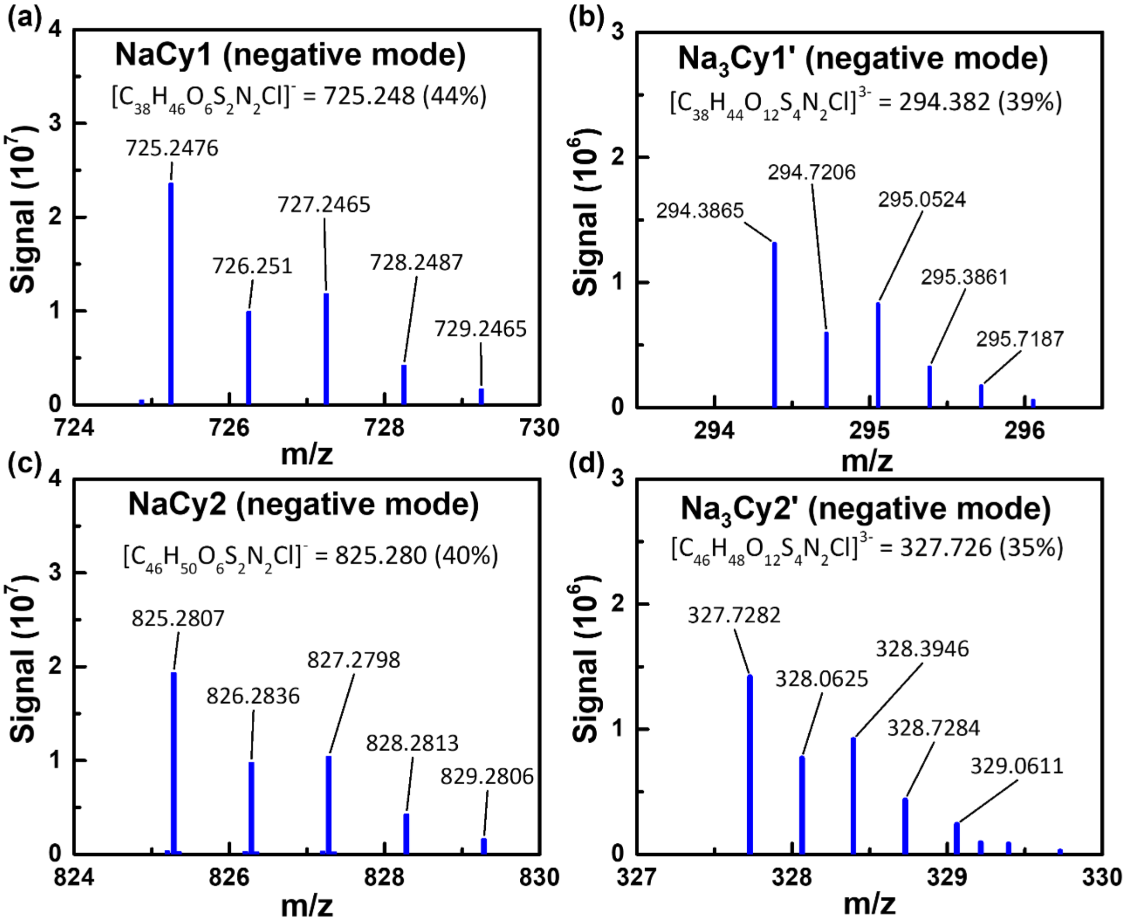

Figure 5.2. Mass spectrometry signals for anionic heptamethines. (a-d) Ultra high-performance liquid chromatography mass spectrometry (UHPLC-MS) isotope peaks for each of the four anionic heptamethines featured in this work. The expected signal for the primary peak is given on each plot along with the relative abundance. Salts were dissolved at 1 µM in methanol.

$$EQE = EQE_{fixed\ L_{ED,A}} \left(\frac{L_{CC}}{d}\right)\left(1 - exp\left(\frac{-d}{L_{CC}}\right)\right) \qquad (5.1)$$

5.3 Results and discussion

5.3.1 Device characterization

Four organic salts consisting of an anionic heptamethine chromophore paired with sodium counterions were selected for this study (Figure 5.1a). All four salts absorb and emit light selectively in the NIR (Figure 5.1b), and are labeled as NaCy1, Na_3Cy1’, NaCy2, and NaCy2’, with the prime designation indicating two additional sulfonate groups on the chromophore. The

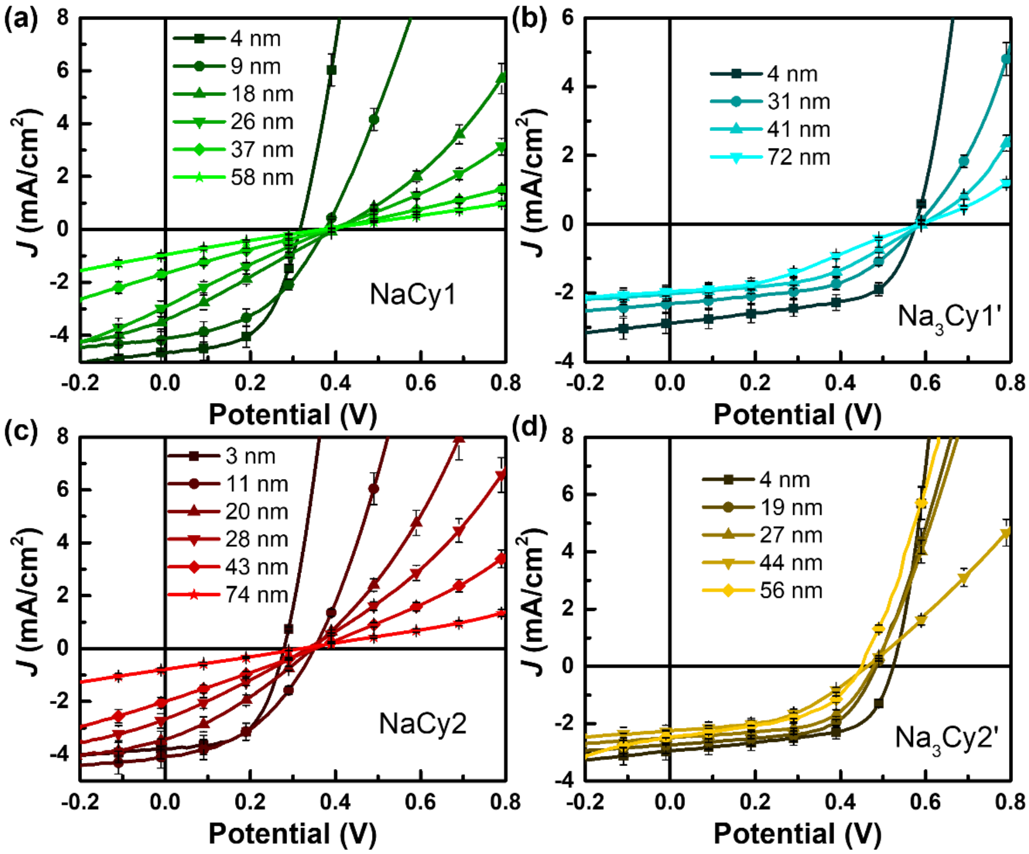

Figure 5.3. Thickness dependent current-voltage (*J*-*V*) data. (a-d) *J*-*V* data for photovoltaic devices as a function of organic salt thickness. Singly charged chromophores **(a, c)** demonstrate significant loss in J_{SC} as organic salt thickness increases while triply charged salts **(b, d)** demonstrate little decline in J_{SC}.

salts vary in either 1) end group conjugation (benzyl vs. naphthyl), NaCy1 to NaCy2 and Na_3Cy1' to Na_3Cy2', or 2) total charge character on the chromophore (-1 with 1 paired cation vs. -3 with 3 paired cations for every anion), NaCy1 to Na_3Cy1' and NaCy2 to Na_3Cy2', which allows for the effects of these physical characteristics to be isolated. Single heterojunction bilayer devices were fabricated with each donor salt at various thicknesses paired with 40 nm C_{60} as the acceptor (Figure 5.1c). The mass and net charge of the salts were verified with UHPLC-MS (Figure 5.2a-d). The selective absorption of the salts in the NIR and C_{60} in the UV and short VIS (<600 nm) creates two distinct regions for photocurrent generation. This process is illustrated in Figure 5.1d, where NIR light absorbed by the salts creates an excited state electron-hole pair (exciton) that diffuses to the

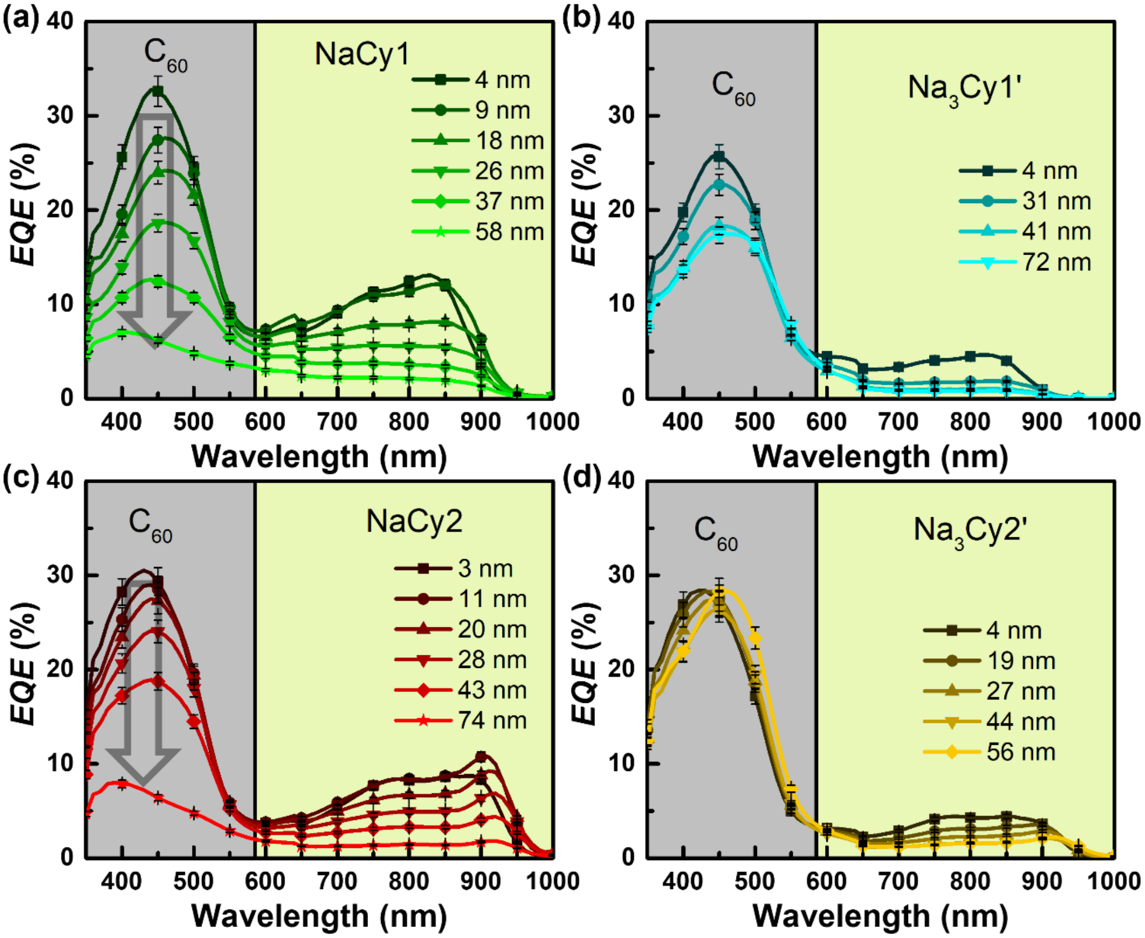

Figure 5.4. Thickness dependent *EQE* data. (a-d) *EQE* data for photovoltaic devices as a function of organic salt thickness, divided into regions of C_{60} (gray) and organic salt (yellow) absorption. Singly charged salts **(a, c)** show large drop-off in both regions as the donor thickness is increased while triply charged salts **(b, d)** demonstrate only slight drops in the C_{60} region but severe loss in the organic salt absorption regime.

salt-C_{60} interface. The electron transfers to C_{60} and the energetic offset between the lowest unoccupied molecular orbital (LUMO) of the salt and C_{60} overcomes the exciton binding energy to produce two free charge carriers, which move through the C_{60} (electron) or organic salt (hole) to the electrodes. Photocurrent generation from C_{60} undergoes an analogous process with UV-VIS light, where the dissociated exciton from C_{60} creates a hole that must transport similarly through the donor salt layer. We studied these processes in PV devices via thickness-dependent *J-V* curves (Figure 5.3a-d) and *EQE* data (Figure 5.4a-d) for each salt. The open circuit voltage (V_{OC}) of the

Table 5.1. Organic salt photovoltaic device parameters. Key parameters from *J-V* characteristic curves for each device. J_{SC} and *PCE* values calculated from the integrated *EQE* are included in parentheses.

Compound	*d* [nm]	J_{SC} [mA cm^{-2}] (Int. J_{SC})	V_{OC} [V]	*FF*	*PCE* [%] (w/ Int. J_{SC})
NaCy1	4	4.6 ± 0.4 (4.5)	0.32 ± 0.01	0.55 ± 0.06	0.81 ± 0.07 (0.79)
	9	4.1 ± 0.4 (4.3)	0.38 ± 0.01	0.44 ± 0.04	0.68 ± 0.07 (0.72)
	18	3.4 ± 0.3 (3.6)	0.40 ± 0.01	0.26 ± 0.03	0.35 ± 0.03 (0.37)
	26	2.9 ± 0.3 (2.8)	0.39 ± 0.01	0.23 ± 0.02	0.26 ± 0.03 (0.25)
	37	1.7 ± 0.2 (1.9)	0.38 ± 0.01	0.24 ± 0.02	0.16 ± 0.02 (0.17)
	58	1.0 ± 0.1 (1.1)	0.37 ± 0.01	0.24 ± 0.02	0.09 ± 0.01 (0.097)
Na_3Cy1’	4	2.9 ± 0.3 (2.7)	0.58 ± 0.02	0.58 ± 0.06	1.0 ± 0.1 (0.91)
	31	2.3 ± 0.2 (2.2)	0.58 ± 0.02	0.50 ± 0.05	0.67 ± 0.06 (0.64)
	41	2.0 ± 0.2 (1.8)	0.59 ± 0.01	0.45 ± 0.05	0.53 ± 0.05 (0.48)
	72	2.0 ± 0.2 (1.8)	0.59 ± 0.02	0.36 ± 0.03	0.42 ± 0.04 (0.38)
NaCy2	3	3.8 ± 0.4 (3.6)	0.28 ± 0.01	0.57 ± 0.06	0.60 ± 0.07 (0.57)
	11	4.1 ± 0.4 (3.7)	0.35 ± 0.01	0.43 ± 0.04	0.62 ± 0.06 (0.56)
	20	3.4 ± 0.4 (3.3)	0.35 ± 0.01	0.31 ± 0.03	0.37 ± 0.04 (0.36)
	28	2.7 ± 0.3 (2.8)	0.33 ± 0.02	0.27 ± 0.03	0.24 ± 0.03 (0.25)
	43	2.0 ± 0.2 (2.2)	0.35 ± 0.01	0.26 ± 0.03	0.18 ± 0.02 (0.20)
	74	0.78 ± 0.08 (0.9)	0.32 ± 0.02	0.26 ± 0.03	0.065 ± 0.008 (0.075)
Na_3Cy2’	4	2.9 ± 0.3 (2.7)	0.52 ± 0.02	0.59 ± 0.05	0.9 ± 0.1 (0.83)
	19	2.7 ± 0.3 (2.6)	0.48 ± 0.02	0.59 ± 0.05	0.76 ± 0.09 (0.74)
	27	2.5 ± 0.2 (2.4)	0.48 ± 0.01	0.58 ± 0.06	0.70 ± 0.06 (0.67)
	44	2.2 ± 0.2 (2.3)	0.46 ± 0.02	0.46 ± 0.05	0.46 ± 0.05 (0.49)
	56	2.5 ± 0.2 (2.6)	0.45 ± 0.02	0.49 ± 0.05	0.55 ± 0.05 (0.57)

devices is controlled by the interface gap between the salt HOMO and C_{60} LUMO and is independent of donor thickness with the exception of devices with less than 5 nm of organic salt. This suggests interface energetics between the salt and C_{60} are essentially constant (no band bending). Thickness independent interface energetics indicates a consistent LUMO-LUMO offset for carrier generation. The voltage increases with increased charge character on the chromophore, from 0.4 V to 0.6 V for NaCy1 to Na_3Cy1’ and 0.35 V to 0.5 V for NaCy2 to Na_3Cy2’ (Table 5.1). This is notable, as minimal changes in the optical bandgap are observed with increased charge character either in the solution state (Figure 5.1b) or the solid state (Figure 5.5) and suggests that

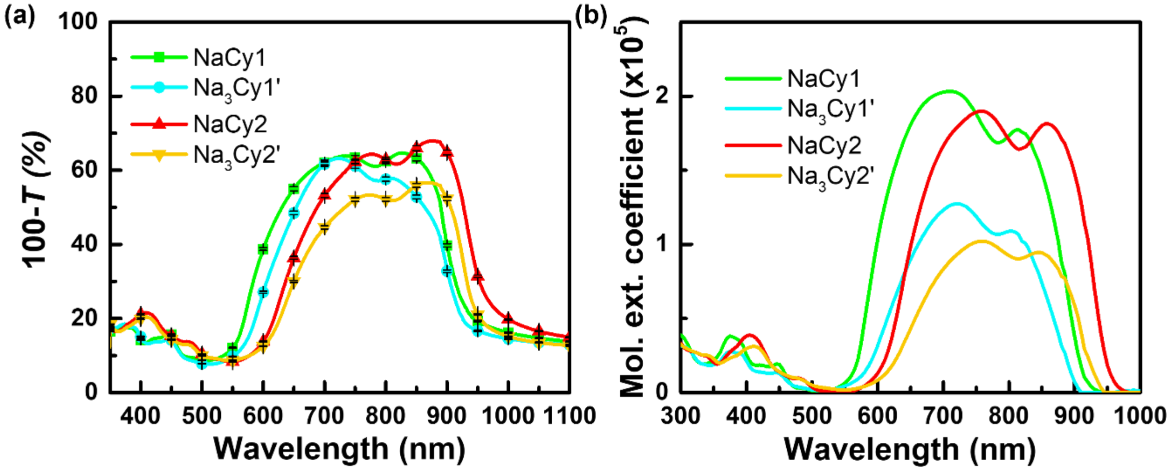

Figure 5.5. Thin film absorption profiles for organic salts. (a) 100-Transmission(%) of organic salt films spun from 10 mg/mL solutions onto ITO covered glass substrates. **(b)** Molecular extinction coefficients calculated with optical constants from variable angle spectroscopic ellipsometry measurements.

either the bandgap is shifted down to create a larger interface gap between the organic salt HOMO and C_{60} LUMO, or there are fewer energetic losses. The voltage decreases with increased conjugation from Cy1 to Cy2 (0.4 to 0.35 V and 0.6 to 0.5 V). This is expected, as extra conjugation narrows the bandgap, likely raising the HOMO and decreasing the interface gap. Another key trend is seen in the forward *J-V* curve where the resistance (inverse of the curve slope) increases with organic salt thickness for singly charged chromophores NaCy1 and NaCy2, but only slightly for Na_3Cy1' and Na_3Cy2', suggesting charge character on the chromophore improves conductivity in the bulk organic salt film. A similar phenomenon is observed in the short circuit current (J_{SC}), which drops consistently as the NaCy1 and NaCy2 films become thicker, while remaining constant for triply charged chromophores. The J_{SC} consists of photoelectric contributions from both active compounds, and the observed trends strongly suggest charge transfer limitations for NaCy1 and NaCy2, but not for Na_3Cy1' and Na_3Cy2'. We investigated further by studying the organic salt thickness dependent *EQE* for each salt (Figure 5.4a-d), which is related to the J_{SC} with Equation 1.7. In general, J_{SC} values measured from *J-V* align well with integrated J_{SC} from *EQE*, validating

Table 5.2. Characteristic parameters for anionic heptamethine based organic salts. Bandgap estimated from thin film absorption cutoffs for each salt. Exciton diffusion lengths extracted from transfer matrix optical modeling and a regression fit of *EQE* data. Charge collection lengths extracted from a fit of organic salt thickness dependent *EQE* data at 440 nm using a modified charge collection efficiency equation. Hole mobilities from Mott-Gurney fitted *J-V* data collected from hole only devices. Hole lifetimes from transient photovoltage decay fits. Calculated charge diffusion length (L_{diff}).

Compound	E_g [eV]	$L_{ED,D}$ [nm]	$L_{CC,D}$ [nm]	μ_h [cm^2 V^{-1}s^{-1}]	τ_h [μs]	L_{Diff} [nm]
NaCy1	1.34	5 ± 1	20 ± 3	$2.0 \pm 0.3 \cdot 10^{-6}$	6.5 ± 0.4	14 ± 3
Na_3Cy1’	1.34	3 ± 1	90 ± 20	$2.8 \pm 0.2 \cdot 10^{-5}$	4.6 ± 0.5	45 ± 4
NaCy2	1.29	7 ± 1	40 ± 8	$4.0 \pm 0.3 \cdot 10^{-6}$	7.1 ± 0.4	21 ± 2
Na_3Cy2’	1.31	4 ± 1	900 ± 300	$6.5 \pm 0.5 \cdot 10^{-5}$	12.7 ± 0.9	113 ± 8

the trends observed for the four organic salts. The separate absorption domains of C_{60} (UV and short VIS) and organic salt (NIR) are marked in Figure 5.4 to delineate the origin of photon absorption and exciton formation. Examining the organic salt region, singly charged chromophores demonstrate higher peak *EQEs* (at low thicknesses) than salts with increased charge character on the chromophore at similar thicknesses. Molecular extinction coefficients are slightly stronger for organic salts with singly charged chromophores (Figure 5.5b), and a combination of increased absorption and larger exciton diffusion length explains the higher NIR *EQE*. All four salts demonstrate significant roll-off in the NIR with increased thickness, indicating overarching limitations from exciton diffusion, charge collection, or both. Turning to the C_{60} domain, we observe two starkly different trends between the singly and triply charged anions. NaCy1 and NaCy2 demonstrate significant drop off in C_{60} *EQE* as the donor salt thickness increases while Na_3Cy1’ and Na_3Cy2’ show little change in the C_{60} *EQE*. Given the constant C_{60} thickness, the lone variable from Equation 1.8 changing with organic salt thickness is the charge collection of the hole moving through the salt layer, described by Equation 1.18. The sharp decay in photocurrent generated from C_{60} suggests that organic salts with singly charged chromophores possess much shorter charge collection lengths than those with a -3 net charge. The *EQE* in the

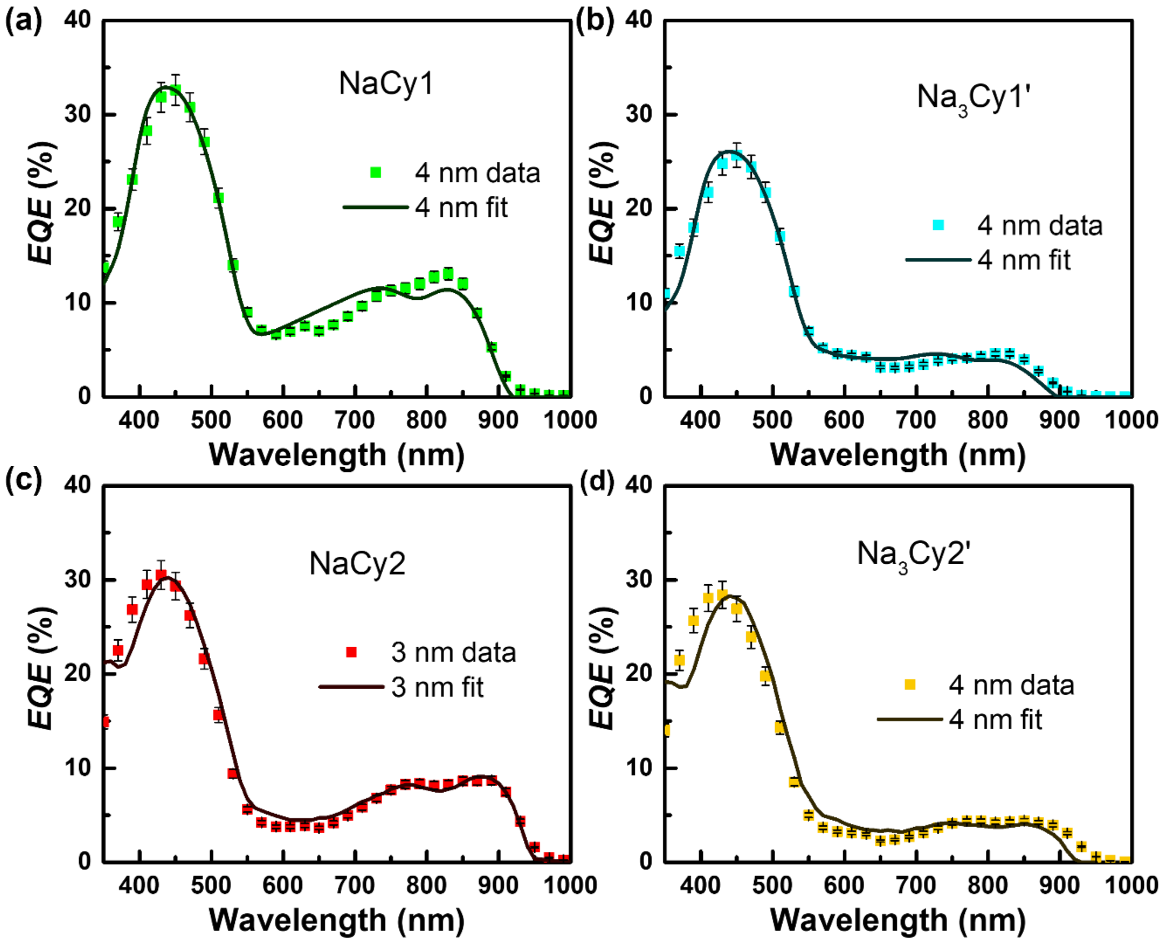

Figure 5.6. Exciton diffusion fitting of fullerene and the organic salts. (a-d) Fitted *EQE* data for the thinnest organic salt layer devices based on transfer matrix optical modeling.

C_{60} region for Na_3Cy1' and Na_3Cy2' shows high relative efficiencies at salt thickness greater than 50 nm, which is in good agreement with the J_{SC} values discussed earlier.

5.3.2 Charge transfer analysis

To further understand the charge transfer capabilities of the four organic salts, transfer matrix optical modeling[95] was used to first extract exciton diffusion lengths ($L_{ED,D}$ and $L_{ED,A}$) and then charge collection lengths for each salt ($L_{CC,D}$), which are included in Table 5.2. Initial fits for exciton diffusion lengths are shown in Figure 5.6, where the model is in excellent agreement with experimental *EQE* data. Increased charge character on the chromophore leads to decreased exciton diffusion lengths as expected from analysis of the NIR region *EQE* discussed above. *EQE*

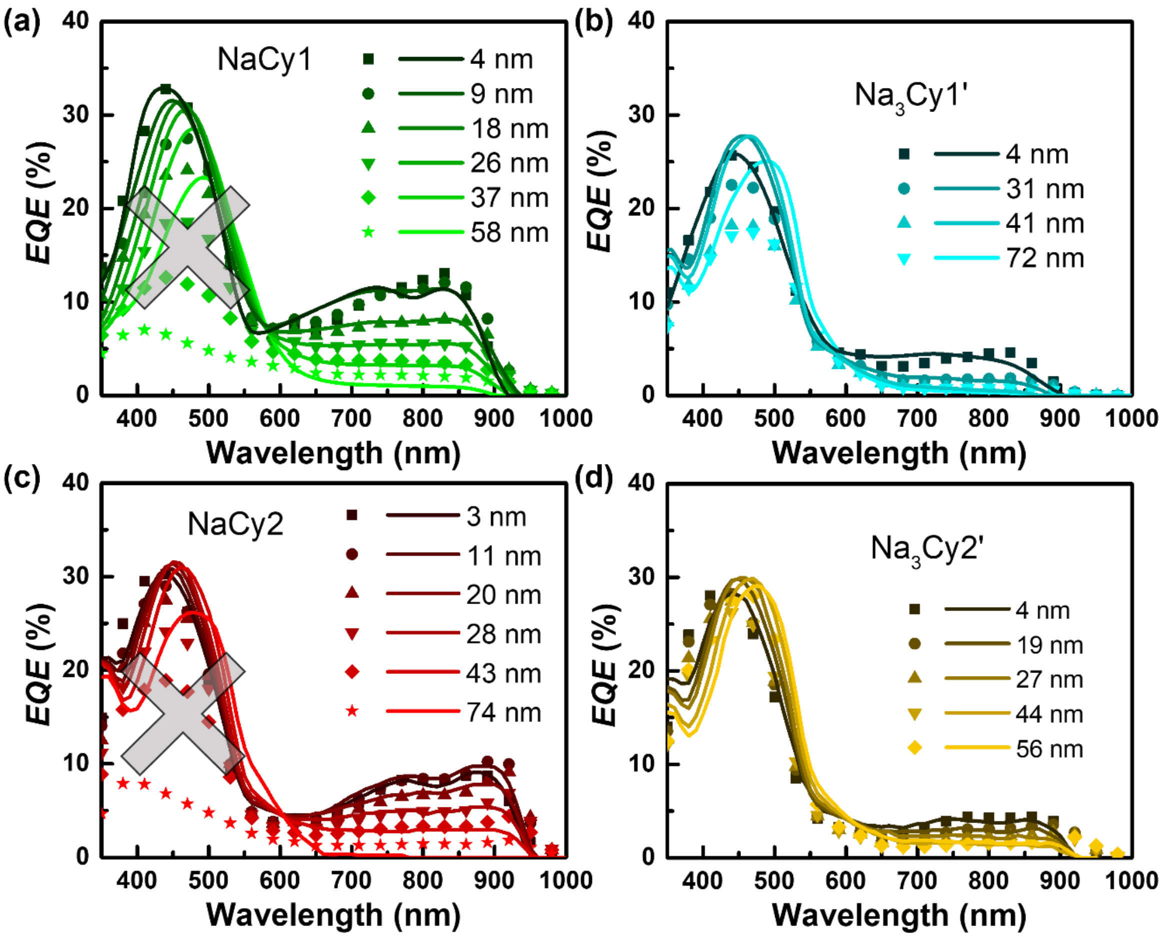

Figure 5.7. Fitted *EQE* data with a fixed fullerene diffusion length. (a-d) Organic salt thickness dependent *EQE* data fitted with a fixed fullerene (C_{60}) diffusion length. Calculated *EQE* (smooth lines) at 440 nm were used as the pre-factor to modify the charge collection equation for charge collection length fitting.

modeling with a fixed $L_{ED,A}$ shows a clear difference between singly and triply charged anionic cyanines (Figure 5.7). Devices with minimal charge collection losses are fitted well by the model, as exciton diffusion is the primary limitation. This is the case for Na_3Cy1' and Na_3Cy2', shown in Figure 5.7b and d, and as the dashed lines in Figure 5.8b and d, where the model accurately captures the experimental *EQE* thickness dependent trends. For NaCy1 and NaCy2, large charge collection losses cause the C_{60} region *EQE* to drop off with organic salt thickness and the model cannot account for the losses with a fixed $L_{ED,A}$ (Figure 5.7a and c, and dashed lines in Figure 5.8a and c).

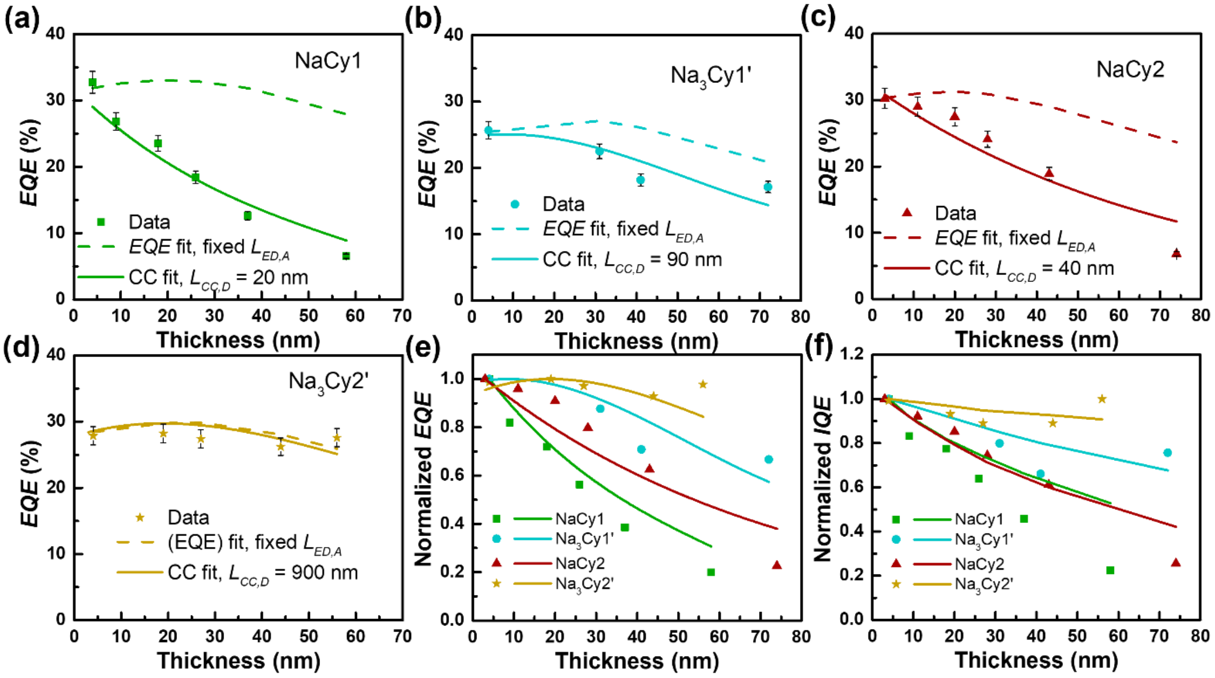

Figure 5.8. Isolating hole collection losses in organic salt photovoltaics. (a-d) *EQE* at 440 nm (peak C_{60} response) as a function of organic salt thickness (data points). Data fitted with fixed acceptor diffusion length but no organic salt charge collection losses (dashed line). Data fitted with a fixed $L_{ED,A}$ and a charge collection model (solid line). **(e, f)** Normalized *EQE* **(e)** and *IQE* **(f)** at 440 nm as a function of organic salt thickness with the charge collection model.

Equation 5.1 was used to fit experimental *EQE* at 440 nm for organic salt charge collection lengths, and the resulting fits are shown as the solid line in Figure 5.8a-d. As expected from analysis of the *J-V* and *EQE* data, organic salts with increased charge character possess significantly longer charge collection lengths (Table 5.2). To examine the trends from a different perspective, normalized *EQE* and *IQE* (calculated with Equation 1.8 from modeled absorption) data and fits are shown in Figure 5.8e and f. The triply charged anionic cyanines still demonstrate surprisingly distinct charge transfer behavior, which is especially evident for the thicker organic salt devices.

5.3.3 Charge collection length analysis

Charge collection lengths were determined by the carrier mobility and lifetime for carriers moving through the organic salt films. In the donor, hole transfer is driven by two mechanisms,

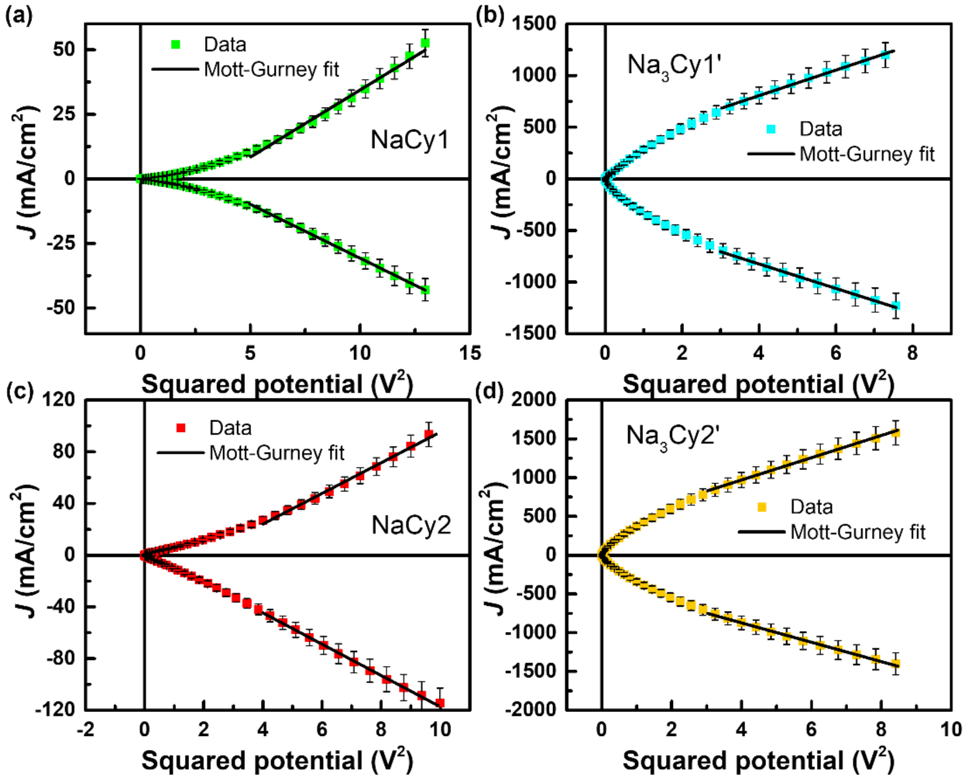

Figure 5.9. Hole mobility data and Mott-Gurney fit. (a-d) Current density (J) as a function of the squared potential (V^2) from hole only devices for each organic salt fitted with the Mott-Gurney equation for space charge limited current. Curves are fit where J is linearly related to V^2.

diffusion of holes due to the concentration gradient from the organic salt-C_{60} interface where excitons are dissociated to the MoO_3-organic salt interface where holes are extracted to the electrodes, and by carrier drift due to the built-in electric field present in the device. Carrier drift lengths are inversely proportional to the depletion width,[11] the size of which is associated with the amount of band bending at the donor-acceptor interface. Significant band bending indicates a large region of linearly decreasing (or increasing) voltage across the donor-acceptor heterojunction and results in the V_{OC} varying strongly with layer thickness. As we note above, the V_{OC} for all four salts is largely independent of organic salt thickness for $d > 5$ nm, indicating that the depletion widths are likely small (similar to other reports[12]) and charge transport is carrier diffusion limited. Carrier diffusion lengths (L_{Diff}) are related to the carrier mobility and lifetime by Equation 1.19 with the dimensionality factor, Z, equal to 6 for three-dimensional diffusion.

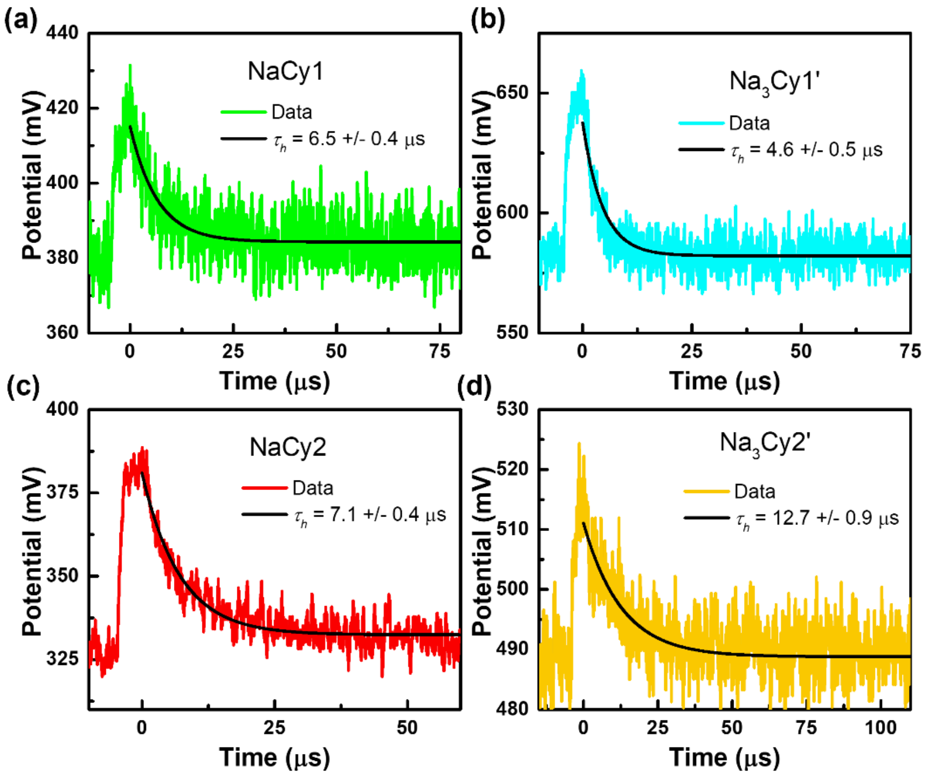

Figure 5.10. Transient photovoltage measurements of organic salt photovoltaics. (a-d) Photovoltage decay (data) as a function of time for each organic salt device fitted with an exponential decay function (black line) to extract the hole carrier lifetime.

Hole only devices, verified as single carrier devices by the symmetric *J-V* curves which do not show a built-in potential ($V_{OC} \neq 0$) or diode formation (unsymmetrical *J-V* properties for forward and reverse bias), fitted with the Mott-Gurney equation (Equation 4.10) for SCLC (Figure 5.9a-d) allow for μ_h to be calculated from the slope of the region where $J \alpha V^2$. Current generated at low potentials are likely ohmic in nature where $J \alpha V$, indicating that a space charge region has not yet been formed. Hole mobilities (Table 5.2) increase by over an order of magnitude from NaCy1 to Na$_3$Cy1' and NaCy2 to Na$_3$Cy2', suggesting that increased negative charge character on the cyanine improves charge transfer through organic salt films. The hole mobility trends are in good agreement with the calculated L_{CC} and device performance in *EQE*.

To complete the charge collection characterization of the organic salts, transient photovoltage measurements were made for each salt under V_{OC} to assess the carrier lifetime.[127,128]

Data fitted with an exponential decay function is shown in Figure 5.10 and the extracted hole lifetimes, τ_h, are reported in Figure 5.10. No clear correlation is found in carrier lifetimes related to charge character or conjugation, so that the L_{CC} is largely dictated by changes in the mobility. However, Na_3Cy2' possesses the largest τ_h, which combined with the highest mobility explains the stable C_{60} *EQE* past 50 nm and the large L_{CC}. L_{Diff} calculated from the measured mobility and lifetime is reported in Table 5.2. In comparison to L_{CC}, L_{Diff} shows excellent agreement with the overall trend between organic salts in regard to the increased charge character improving charge transfer. Conceptually, enhanced hole transfer could occur via the anionic chromophores, where increased negative charge character stabilizes the positively charged hole. Alternatively, the increased presence of cationic counterions could provide a pathway of static positive charges that accelerate hole movement via charge repulsion. Our analysis of the charge collection lengths shows improved carrier mobility drives efficient charge transfer in organic salt films comprised of triply charged anionic heptamethines.

5.4 Conclusions

We demonstrated a series of anionic salt donor OPVs. Through fabrication and analysis of organic salt thickness dependent devices with four anionic heptamethines we showed a surprising change in charge transport based on the charge character of the salt that is consistent with variation in conjugation. Triply charged chromophores possess orders of magnitude higher carrier mobilities than singly charged chromophores yielding excellent charge collection for thick (> 50 nm) organic salt films, while coming at the cost of reducing the exciton diffusion length slightly. Improved mobility leads to devices with sustained acceptor and donor *EQE* for thicker salt layers, higher photocurrent, and better device performance. This fundamental understanding of how to improve charge transport is critical to realizing organic salts as high efficiency TPV materials. The key limiting factor for organic salts moving forward is the short exciton diffusion lengths, which previous work has suggested can be enhanced by counterion selection and will be the focus for future work. Additionally, this work suggests that there could be similarly interesting effects of total charge in cationic cyanines. Ultimately, a combination of charge transfer optimization via chromophore charge character and counterion selection for optimizing exciton diffusion length and orbital energy levels could produce exciting new organic salts for a variety of photovoltaic and optoelectronic applications.

Chapter 6 – High Efficiency Transparent Photovoltaics

The work presented in this chapter was submitted for publication and is in review.

6.1 Introduction

Transparent photovoltaics (TPVs) are a rapidly emerging field of research and industrial production that possess the power to meet the energy demand via integration with existing infrastructure and new avenues of deployment.[21,22] TPVs are an excellent complement to traditional photovoltaics (PVs) as they can be deployed on windows, greenhouses, farmland, cars, cellphones, and any other surface that is unavailable for integration with opaque PVs. Unlike traditional solar technologies which often require new infrastructure or a repurposing of space to make solar energy fields, TPVs can be installed seamlessly into existing surfaces to minimize costs and environmental impact. TPVs are commonly classified as either non-wavelength selective (spatially dispersed or thin opaque PVs) or wavelength selective.[22] This distinction is important as these types of TPVs have different theoretical limits as a function of average visible transmittances (*AVT*). Wavelength selective TPVs offer a route to the highest possible combination of power conversion efficiency (*PCE*) and *AVT* by selectively harvesting ultra-violet (UV) and near-infrared (NIR) light. This is captured in the light utilization efficiency (*LUE = PCE x AVT*), which is a good metric for tracking progress in the field. Traditional TPVs have achieved excellent *PCE*s but are typically limited to *AVTs* less than 70%, and more often less than 50% due to parasitic absorption of supporting layers and visible absorption of most donor materials.[153–157] To date, the best wavelength selective TPV has achieved an *LUE* of 5.35% using a bulk-heterojunction (BHJ) blended active layer consisting of an NIR absorbing polymer and non-fullerene acceptor (NFA).[158] Most demonstrations of high efficiency (*PCE* > 5%) wavelength selective TPVs have utilized a BHJ structure.[153–155] Although BHJ architectures often result in the best organic photovoltaic (OPV) performance, scaleup of such structures (large area consistency and yield) can be challenging. A critical parameter in BHJ architectures is the ratio of donor polymer to acceptor NFA, with the optimal ratio typically at 1:1.5 setting a minimum amount of polymer required and thus limiting the *AVT*. Recently, a new approach to high efficiency OPVs has been developed in which the donor and acceptor are sequentially deposited in a layer-by-layer (LBL) method.[19,159–161] Such devices have achieved *PCE*s comparable to the best BHJ OPVs,[16,19] but have seen limited usage in TPVs and only low *AVT*.[162,163] The LBL approach offers better control over the precise thickness of each active material without inherently compromising the morphology and device performance. Additionally, there have been few studies on the impact of polymer thickness in LBL devices on TPV performance and aesthetics. Xu et al. fabricated opaque photovoltaics with a visibly absorbing donor polymer D18.[163] Devices with 65 nm D18 yielded *PCE* = 12.6% and *AVT* = 22.8% for a 2.9% *LUE*. Song et al. demonstrated TPVs with 8.0% *PCE* and 23.0% *AVT* with *LUE* = 1.8%.[162] The polymer (PTB7-Th) was used as a donor and the thickness was varied independently of other parameters from 50 to 80 nm, although the best TPV utilized 45 nm. More critically, LBL TPVs have not yet demonstrated *AVT* above 25%.[162,163] In this work, we report NIR wavelength selective high efficiency LBL TPVs. We utilize a solution processed LBL approach to formulate a planar heterojunction (HJ) of an NIR absorbing polymer and NFA and demonstrate an excellent TPV with this approach. Often in BHJs the role of various materials as a donor or acceptor can be hidden, whereas these roles are clearly defined in LBL structures. Notably, we utilize the polymer as an electron accepting material and the NFA as an electron donor with an inverted structure. Polymer thickness is varied from 5 to 85 nm and its impact on the optical and electrical performance is thoroughly evaluated. After optimization, we demonstrate a LBL TPV with *PCE* of 8.8%, *AVT* of 40.9%, and an *LUE* of 3.6% comparable to the best TPVs

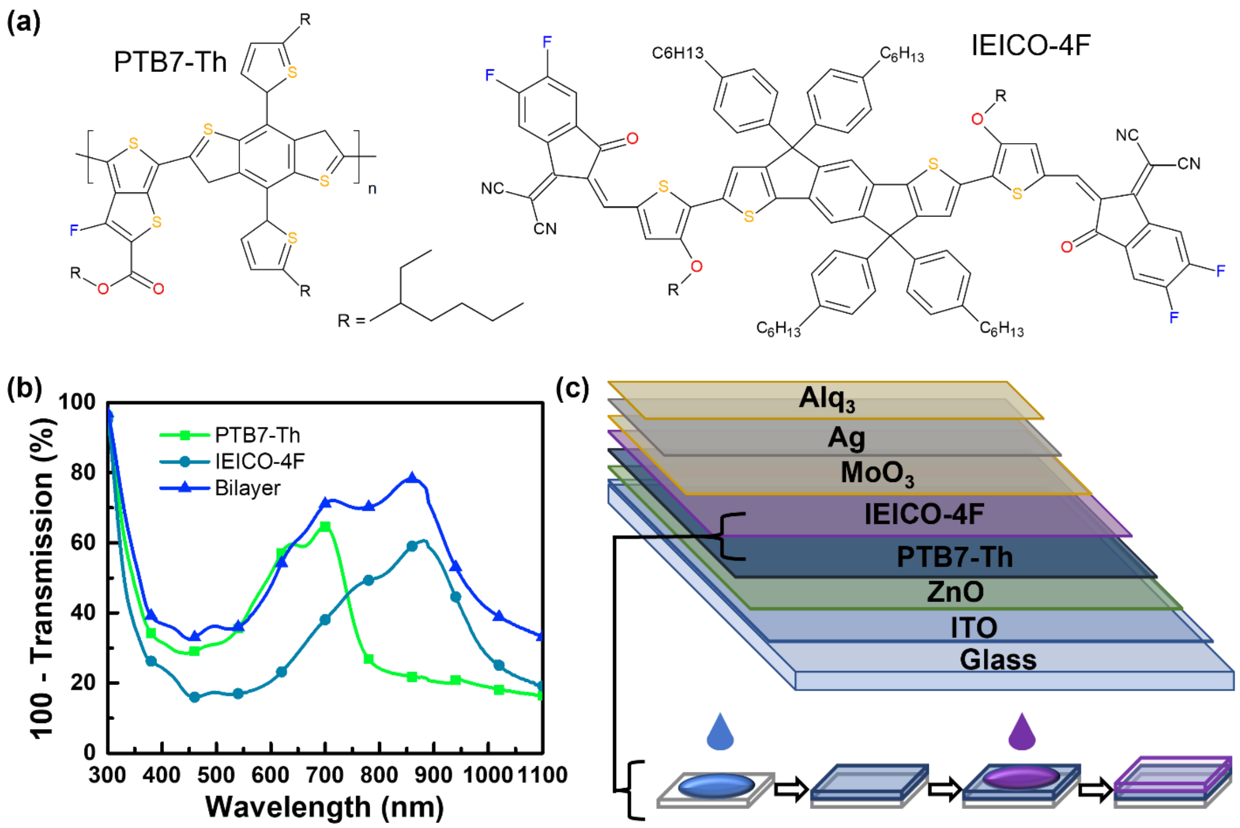

Figure 6.1. Active materials and architecture used for photovoltaic devices. (a) Chemical structures of PTB7-Th, polymer donor, and IEICO-4F, non-fullerene acceptor. **(b)** Transmission data through neat films of PTB7-Th (light green), IEICO-4F (dark green), and a sequentially deposited bilayer of PTB7-Th and IEICO-4F (blue) on zinc oxide and indium tin oxide covered glass substrates. **(c)** Inverted bilayer semitransparent device architecture and the sequentially spin-coated bilayer nature of the active layers.

reported to date. Transfer matrix optical modeling is enabled by the LBL approach and used to extract exciton diffusion lengths for PTB7-Th and IEICO-4F of 200 (±100) nm, and charge collection regimes defined by the polymer thickness.[95] Our work highlights the potential of LBL wavelength selective TPVs as an important and alternative approach to BHJs for future devices and points to exceptional excitonic and electronic properties of these materials.

6.2 Results

In this work, we fabricate inverted LBL TPVs with the near-infrared absorbing polymer PTB7-Th and NFA IEICO-4F as the electron accepting and donating materials,[162] respectively,

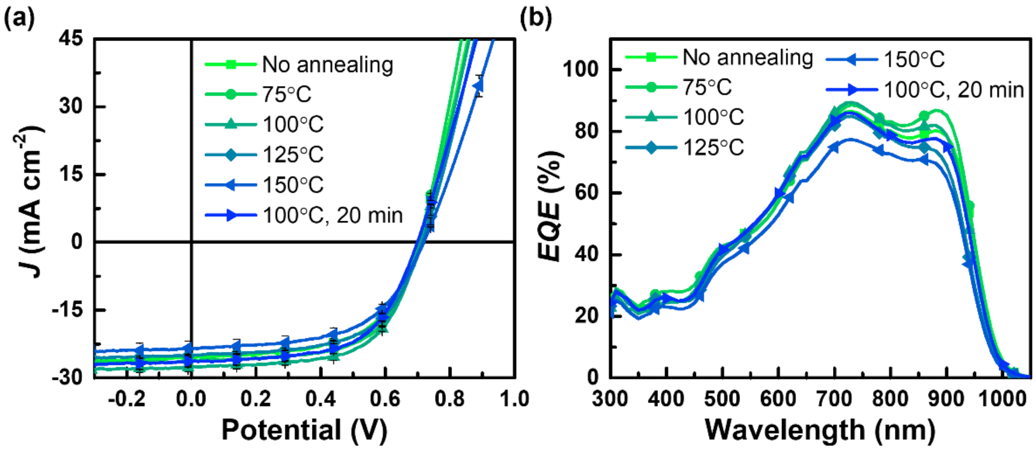

Figure 6.2. *J-V* and *EQE* curves for annealing temperature optimization. (a) Current-voltage characteristic curves for devices annealed at different temperatures and **(b)** corresponding *EQE* curves. Devices annealed for 10 minutes unless specified otherwise. IEICO-4F was dissolved in 73.5% o-xylene, 24.5% n-butanol, and 2% 1-chloronaphthalene. The device architecture was 120 nm ITO, 20 nm ZnO, 40 nm PTB7-Th, 55 nm IEICO-4F, 7 nm MoO_3, 80 nm Ag.

where the chemical structures of both are shown in Figure 6.1a. PTB7-Th and IEICO-4F provide complementary absorption of NIR light with individual thin film absorption (Figure 6.1b) peaks at 700 and ~900 nm, respectively, while the bilayer exhibits broad NIR absorption from 700 to 900 nm with a desirable transparent window in the visible spectrum. PTB7-Th contributes some visible light absorption with a strong absorptive shoulder at 625 nm. For the layer order for the inverted architecture (Figure 6.1c), we use a ZnO electron transport layer (20 nm), sequentially deposited active layers, a MoO_3 hole transport layer (7 nm), and a thin Ag top electrode (8-20 nm) with Alq_3 as an antireflection coating (0-50 nm). For reference, opaque devices were fabricated with a thick (80 nm) Ag electrode. The active layers are formed by sequential spin-coating of neat

Table 6.1. *J-V* parameters for annealing temperature optimization.

Device	J_{SC}/M [mA cm^{-2}]	M	Int. J_{SC} [mA cm^{-2}]	V_{OC} [V]	FF	PCE [%] (Int. J_{SC})
Unannealed	21.9 ± 0.8	1.16	22.8	0.700 ± 0.004	0.57 ± 0.03	8.7 ± 0.6 (9.0)
75C	22.8 ± 0.7	1.14	23.4	0.699 ± 0.005	0.61 ± 0.02	9.7 ± 0.5 (10.0)
100C	23.5 ± 0.9	1.16	23.1	0.704 ± 0.004	0.62 ± 0.01	10.3 ± 0.4 (10.2)
125C	21.3 ± 0.9	1.18	21.9	0.708 ± 0.004	0.59 ± 0.01	8.9 ± 0.4 (9.1)
150C	21 ± 1	1.17	20.1	0.711 ± 0.004	0.55 ± 0.03	8.2 ± 0.7 (7.9)
110C, 20 min	23 ± 1	1.17	22.5	0.703 ± 0.005	0.59 ± 0.02	9.5 ± 0.5 (9.3)

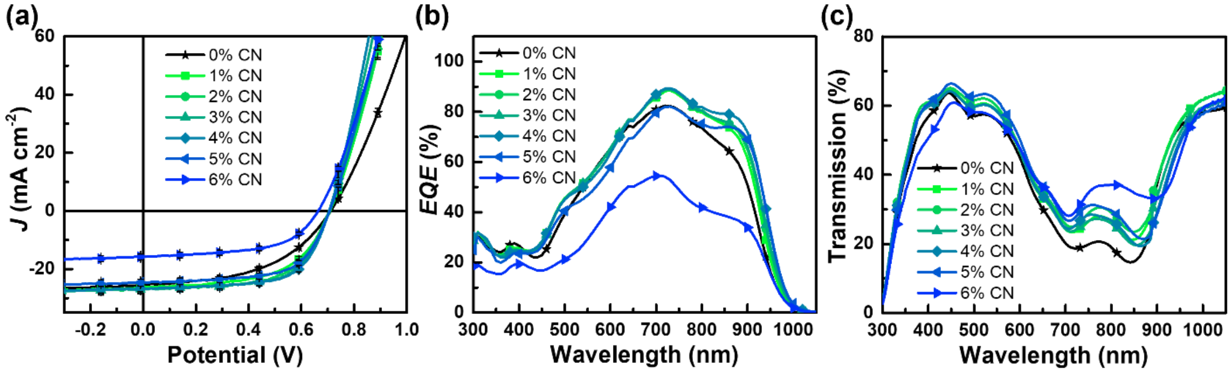

Figure 6.3. Solvent additive optimization. (a) Characteristic current-voltage (J-V) curves and **(b)** external quantum efficiencies (EQE) for opaque devices (OPVs) with different 1-chloronaphthalene doping in the IEICO-4F solution. **(c)** Transmission data for the device stack up to the active layers for the opaque devices (ITO, ZnO, PTB7-Th, and IEICO-4F).

films of PTB7-Th and IEICO-4F utilizing solvent orthogonality.[162] O-xylene readily dissolves IEICO-4F, whereas PTB7-Th is soluble only with stirring and heat. In contrast, the polymer is insoluble in n-butanol which is added at 24% v/v to the IEICO-4F solution to minimize redissolving of the PTB7-Th neat film during IEICO-4F spin-coating. The solvent additive 1-chloronaphthalene (CN) was added to the IEICO-4F solution at 0-6% v/v. Concentrations of the active layer solutions were used to individually determine the resulting film thicknesses, a key difference in experimental control compared to BHJs which use the donor-to-acceptor ratio to control the resulting morphology.

TPV electrical and optical performance was optimized by consideration of key variables affecting the active layers (annealing temperature, solvent additive level, and PTB7-Th thickness)

Table 6.2. Solvent additive optimization device parameters.

Device	J_{SC}/M [mA cm^{-2}]	M	Int. J_{SC} [mA cm^{-2}]	V_{OC} [V]	FF	PCE [%] (Int. J_{SC})
0% CN	20 ± 1	1.26	20.9	0.711 ± 0.003	0.49 ± 0.01	7.0 ± 0.3 (7.3)
1% CN	22 ± 1	1.23	22.6	0.711 ± 0.002	0.57 ± 0.01	8.9 ± 0.5 (9.1)
2% CN	22 ± 1	1.22	22.8	0.701 ± 0.003	0.61 ± 0.01	9.4 ± 0.6 (9.7)
3% CN	22 ± 1	1.22	22.9	0.707 ± 0.003	0.63 ± 0.01	9.8 ± 0.6 (10.2)
4% CN	23 ± 1	1.20	23.2	0.707 ± 0.003	0.64 ± 0.02	10.4 ± 0.5 (10.4)
5% CN	21 ± 1	1.18	21.4	0.708 ± 0.003	0.63 ± 0.01	9.4 ± 0.5 (9.5)
6% CN	12.7 ± 0.8	1.25	13.2	0.665 ± 0.008	0.58 ± 0.02	4.9 ± 0.3 (5.1)

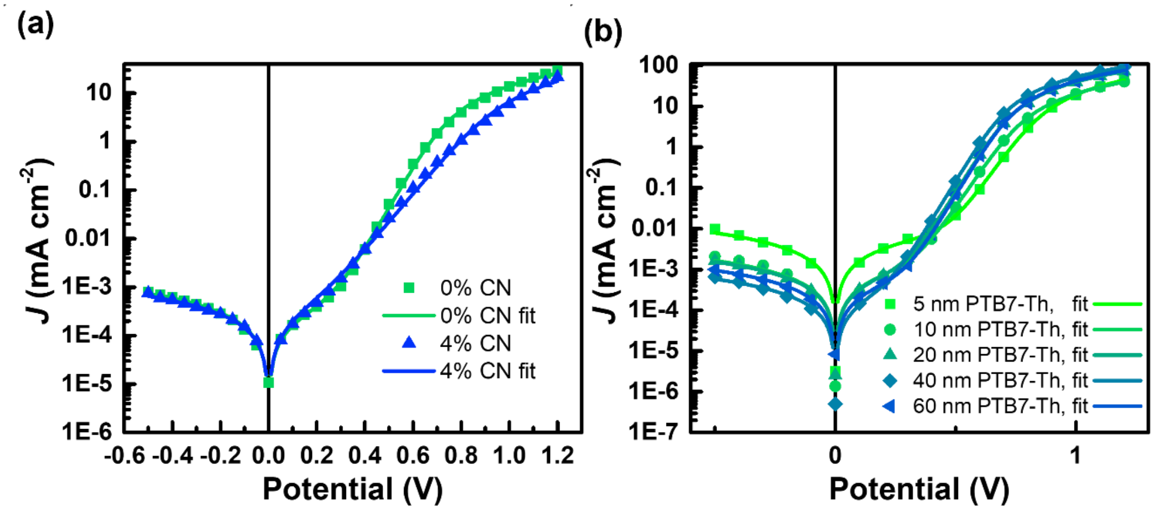

Figure 6.4. Dark *J*-*V* for 1-chloronaphthalene and polymer thickness optimized devices. (a) Dark current for devices made with 0% and 4% 1-chloronaphthalene. **(b)** Dark current for devices with different PTB7-Th thickness.

and the top contact (Ag and Alq_3 thickness). Current-voltage (*J*-*V*) characteristic curves and external quantum efficiencies (*EQE*) for thermal annealing of the active layers in opaque devices are given in Figure 6.2 with corresponding device parameters, including the spectral mismatch factor (*M*), in Table 6.1. For opaque devices without thermal annealing, LBL opaque devices achieved a *PCE* of 8.7%. With optimal annealing at 100 °C for 10 minutes, the *PCE* reached 10.3%. The improvement in device performance comes from equal gains in the short circuit photocurrent (J_{SC}) and fill factor (*FF*). Solvent additives such as 1,8-diiodoctane and CN have been thoroughly characterized and shown to improve morphology in polymer-NFA LBL PVs by increasing aggregation in the NFA resulting in improved *FF* and decreased recombination.[19,160,164–168] Interestingly, while solvent additives in pre-mixed BHJ solutions are present with both active layer materials, LBL approaches generally feature solvent additive only in the NFA solution. In our work, optimization of CN additive levels in the IEICO-4F solution finds significant improvement in opaque device electronic performance, evidenced in the *J*-*V* curves (Figure 6.3a) and device parameters (Table 6.2), including J_{SC} corrected with *M* for each

Table 6.3. Dark *J-V* fit parameters for 1-chloronaphthalene and polymer thickness optimized devices.

Device	R_P [MΩ cm^2]	R_S [Ω cm^2]	n_{id}	J_0 [A cm^{-2}]
0% CN	0.68	14.87	1.95	2.16e-9
4% CN	0.80	11.64	2.86	2.48e-8
5 nm PTB7-Th	0.063	6.27	2.01	8.73e-10
10 nm PTB7-Th	0.30	8.70	1.94	1.53e-9
20 nm PTB7-Th	0.32	5.36	1.78	1.47e-9
40 nm PTB7-Th	0.86	4.48	1.74	2.17e-9
60 nm PTB7-Th	0.52	5.09	1.72	8.72e-10

device. Devices without CN have a *FF* of just 0.49, while optimized devices with 4% CN in the IEICO-4F solution possess a *FF* of 0.64. CN optimization enhances J_{SC} to a lesser extent with a relative gain of 10% from 0 to 4% CN. We note that the J_{SC} improvement comes almost entirely with the first small addition of CN to IEICO-4F, while *FF* enhancement is incremental from 0% to 4%, albeit with the largest gain from 0 to 1% CN. The J_{SC} and *FF* decline rapidly at CN levels greater than 4%, as the photocurrent is reduced by nearly half at 6% CN and the *FF* to 0.58. The *EQE* (Figure 6.3b) for CN optimization reveals photocurrent improvement across the spectrum upon addition of 4% CN to the IEICO-4F, including in regions of PTB7-Th absorption. Transmission data (Figure 6.3c) for glass substrates with ITO, ZnO, PTB7-Th, and IEICO-4F indicate subtle changes in the absorption profile of the active layers. The absorption peak for IEICO-4F is slightly red shifted with the addition of CN suggesting CN influences aggregation or crystallite formation in IEICO-4F. To characterize the PV performance with and without CN doping of the IEICO-4F solution, we report dark *J-V* spectra for the 0% and 4% devices (Figure 6.4a) fitted with the ideal diode equation (Equation 1.3) and the extracted dark *J-V* parameters in Table 6.3.[94,169] There is a clear difference in the shape of the dark *J-V* curve under positive bias conditions and this is seen in the increase of the ideality factor (n_{id}) and the series resistance (R_S).

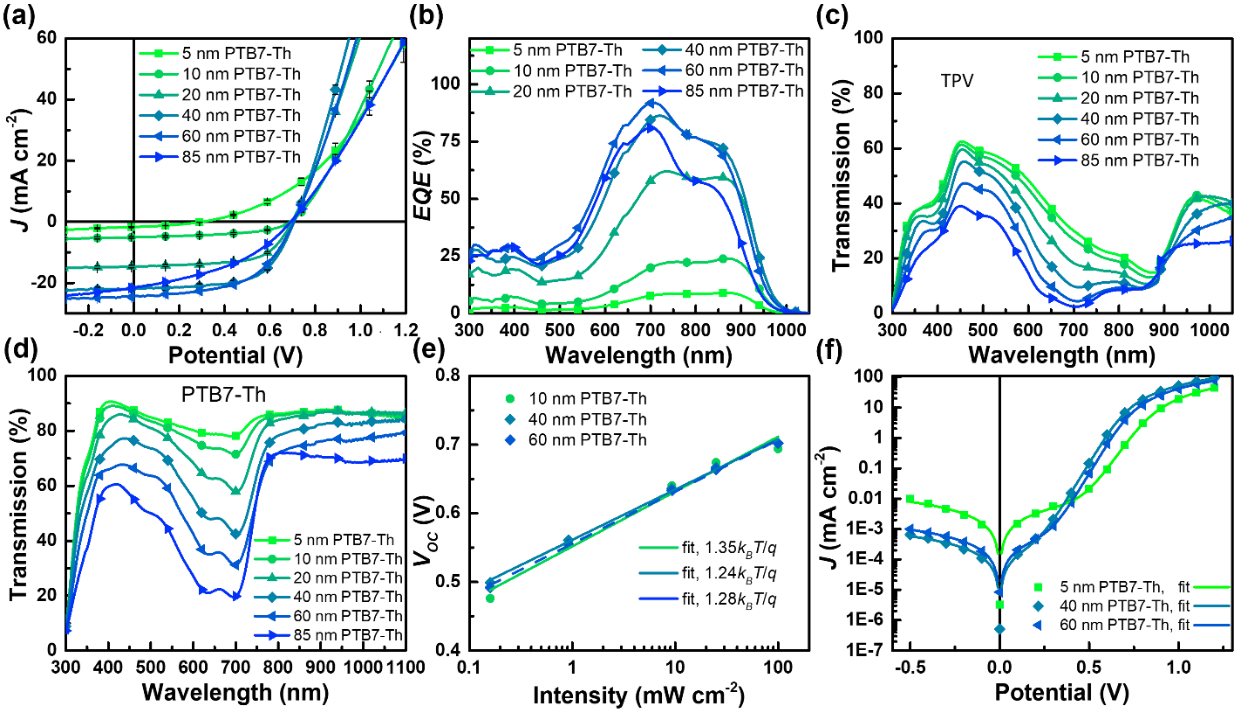

Figure 6.5. Polymer thickness optimization. (a) Characteristic current-voltage (*J*-*V*) curves, **(b)** external quantum efficiencies (*EQE*), and **(c)** transmission for transparent devices with different PTB7-Th thickness. **(d)** Transmission data for polymer films of varying thickness on glass substrates covered with ITO and ZnO. Dependence of **(e)** V_{OC} on light intensity (P_0) with linear fits of V_{OC} vs ln(P_0) and the slope proportional to k_BTq^{-1}. **(f)** Fitted dark *J-V* data for 5, 40, and 60 nm PTB7-Th.

Both devices possess $n_{id} > 1.5$, indicating relatively high levels of bimolecular recombination.[170] Considering the shape of the *J-V* curves and the *FF* improvement from 0% to 4% CN, it is clear that the combination of increased shunt resistance (R_P) and decreased R_S caused by the presence of CN during neat film formation is a critical factor for device improvement. The increased ratio of R_P to R_S could also improve the charge collection efficiency (η_{CC}) of holes through the IEICO-4F, causing improved *EQE* across the spectrum and a higher *FF*.

A key difference in device fabrication between BHJ and bilayer devices is the freedom to vary the individual thicknesses of the two active materials independently, enabling the ability to readily extract characteristic lengths through transfer matrix optical modeling. Here, we investigate the full range of polymer thickness from 5 nm to 85 nm in TPVs while fixing the IEICO-4F

Table 6.4. Polymer thickness optimization device parameters.

Device	J_{SC}/M [mA cm^{-2}]	M	Int. J_{SC} [mA cm^{-2}]	V_{OC} [V]	FF	PCE [%] (Int. J_{SC})	AVT [%]	LUE [%] (Int. J_{SC})
5 nm PTB7-Th	1.7 ± 0.2	0.95	1.9	0.29 ± 0.05	0.34 ± 0.02	0.17 ± 0.04 (0.19)	52.9	0.089 (0.10)
10 nm PTB7-Th	5.4 ± 0.3	0.95	5.1	0.694 ± 0.006	0.51 ± 0.02	1.9 ± 0.1 (1.8)	50.4	0.96 (0.91)
20 nm PBT7-Th	14.8 ± 0.4	1.01	14.1	0.701 ± 0.005	0.63 ± 0.01	6.5 ± 0.2 (6.2)	45.5	3.0 (2.8)
40 nm PTB7-Th	19.6 ± 0.7	1.12	19.7	0.702 ± 0.004	0.61 ± 0.01	8.4 ± 0.3 (8.4)	41.6	3.5 (3.5)
60 nm PTB7-Th	20.4 ± 0.8	1.21	21.2	0.702 ± 0.004	0.54 ± 0.01	7.7 ± 0.3 (8.1)	32.7	2.5 (2.6)
85 nm PTB7-Th	16.9 ± 0.8	1.27	17.6	0.696 ± 0.003	0.42 ± 0.01	4.9 ± 0.2 (5.1)	24.4	1.2 (1.3)

thickness. PTB7-Th thickness dependent *J*-*V* curves (Figure 6.5a) demonstrate interesting trends in J_{SC}, open circuit voltage (V_{OC}), and *FF* (Table 6.4). The V_{OC} is stable down to 10 nm of PTB7-Th before decreasing sharply at 5 nm. As expected, the J_{SC} decreases from 20 mA cm^{-2} for 40 nm PTB7-Th to less than 2 mA cm^{-2} for 5 nm PTB7-Th. Very thick polymer layers (85 nm) lead to reduced photocurrent, while the ideal range for *PCE* of 40 to 60 nm demonstrates stable J_{SC}. The *FF* reaches an optimum in TPVs with 20 nm PTB7-Th and declines quickly for polymer thicknesses less than 20 nm and greater than 40 nm. The *EQE* spectra shows a maximum integrated J_{SC} for 60 nm PTB7-Th, with 40 nm demonstrating a slightly diminished *EQE* at the PTB7-Th peak and into the visible portion of the spectrum. Decreasing polymer thickness below 40 nm

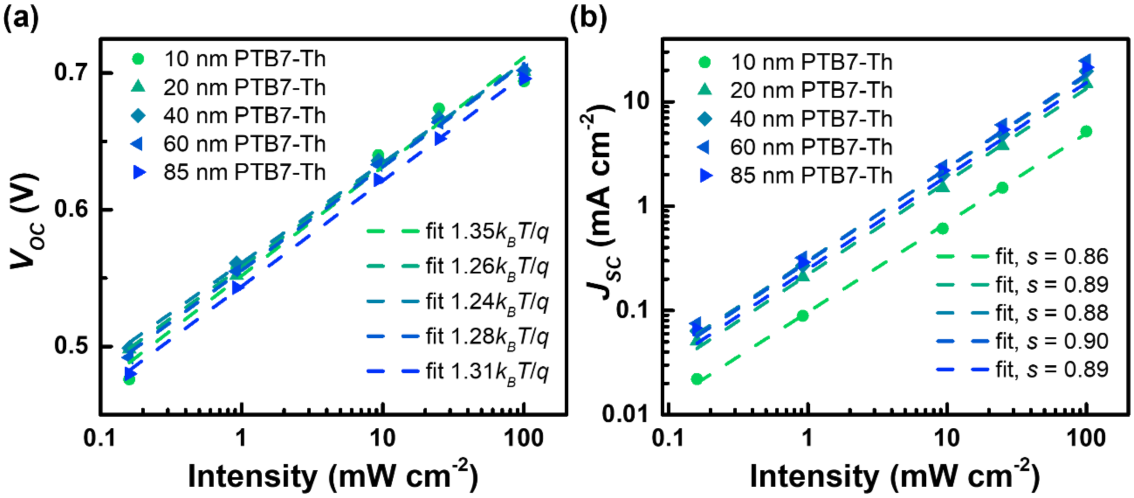

Figure 6.6. Light intensity dependent V_{OC} and J_{SC} for polymer thickness devices. Dependence of **(a)** V_{OC} on light intensity (P_0) with linear fits of V_{OC} vs ln(P_0) and the slope proportional to k_BTq^{-1}. Dependence of **(b)** J_{SC} on P_0 with power fits of $J_{SC}\ \alpha\ P_0^s$ plotted on log-log scale.

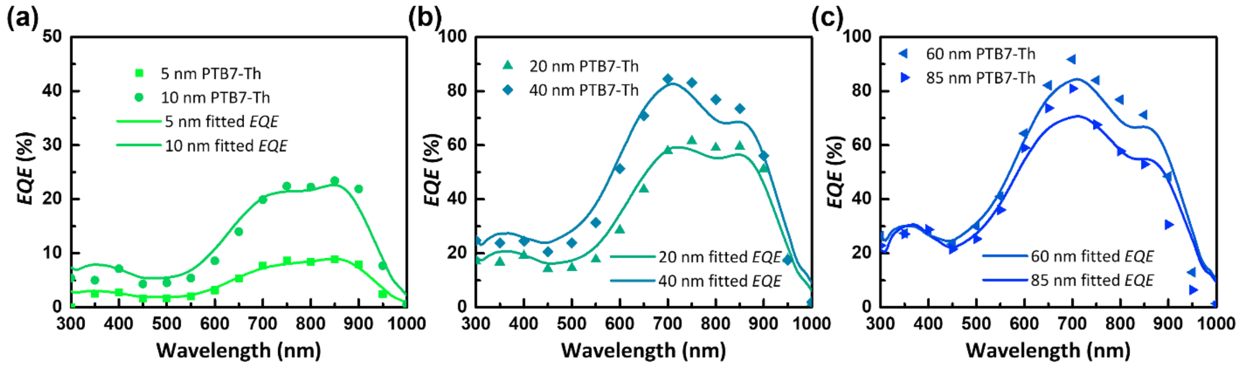

Figure 6.7. Transfer matrix optical modeling and *EQE* fitting. Measured external quantum efficiency (*EQE*) data (symbols) and the fitted *EQE* (solid lines) based on transfer matrix optical model and nonlinear regression fit for transparent photovoltaics with PTB7-Th thicknesses of **(a)** 5 and 10 nm, **(b)** 20 and 40 nm, and **(c)** 60 and 85 nm PTB7-Th.

reveals an unexpected trend where the *EQE* is reduced across the entire spectrum, including the deeper NIR region of pure IEICO-4F absorption. Light intensity (P_0) dependence of the V_{OC} (Figure 6.5e, Figure 6.6a) shows a meaningful increase in slope when the polymer thickness deviates from 40 nm. J_{SC} (Figure 6.6b) meanwhile does not show any strong dependence on P_0 as a function of PTB7-Th thickness.

Fitted dark *J*-*V* data as a function of polymer thickness (Figure 6.5f, Figure 6.4b, Table 6.3) reveals several trends. The reverse dark saturation current (J_0) is largely independent of polymer thickness, while n_{id}, R_S, and the shunt (parallel) resistance R_P all show a strong dependence on PTB7-Th thickness. R_S and R_P reach a minimum and maximum, respectively, at the optimal thickness of 40 nm in strong agreement with the combination of high J_{SC} and *FF*

Table 6.5. *EQE* modeling fit parameters for polymer thickness dependent devices.

Device	$L_{ED,A}$ [nm]	$L_{ED,D}$ [nm]	L_{CC} [nm]	Model J_{SC} [mA cm^{-2}]	Exp. J_{SC} [mA cm^{-2}]
5 nm PTB7-Th	200	200	7	2.0	1.9
10 nm PTB7-Th	200	200	20	5.3	5.1
20 nm PTB7-Th	200	200	115	14.7	14.1
40 nm PTB7-Th	200	200	1800	20.4	19.7
60 nm PTB7-Th	200	200	8560	21.1	21.2
85 nm PTB7-Th	200	200	265	18.1	17.6

Table 6.6. PTB7-Th, Ag, and Alq3 thickness dependent device optical parameters.

Device	*PCE* [%] (Int. J_{SC})	*AVT* [%]	*LUE* [%] (Int. J_{SC})	*CRI*	(*a**, *b**)
5 nm PTB7-Th	0.18 ± 0.04 (0.19)	52.9	0.095 (0.10)	84.9	(-7.9, -6.3)
10 nm PTB7-Th	1.9 ± 0.1 (1.8)	50.4	0.96 (0.91)	82.8	(-8.7, -7.6)
20 nm PBT7-Th	6.5 ± 0.2 (6.2)	45.5	3.0 (2.8)	75.2	(-12.2, -10.6)
40 nm PTB7-Th	8.4 ± 0.3 (8.4)	39.6	3.3 (3.3)	63.8	(-18.5, -12.6)
40 nm PTB7-Th (ARC)	8.4 ± 0.3 (8.4)	41.6	3.5 (3.5)	65.3	(-17.7, -12.7)
60 nm PTB7-Th	7.8 ± 0.3 (8.1)	32.7	2.6 (2.6)	53.1	(-23.4, -14.0)
85 nm PTB7-Th	4.9 ± 0.2 (5.1)	24.4	1.2 (1.3)	44.5	(-23.7, -17.6)
8 nm Ag	7.2 ± 0.2 (7.0)	37.8	2.7 (2.7)	66.6	(-14.1, -16.2)
10 nm Ag (ARC)	8.4 ± 0.3 (8.4)	41.6	3.5 (3.5)	65.3	(-17.7, -12.7)
12 nm Ag (ARC)	8.8 ± 0.4 (8.8)	40.9	3.6 (3.6)	63.1	(-17.7, -15.6)
16 nm Ag (ARC)	9.8 ± 0.4 (9.8)	36.0	3.5 (3.5)	52.8	(-21.6, -19.8)
20 nm Ag	10.0 ± 0.4 (10.1)	28.6	2.8 (2.9)	46.8	(-21.1, -24.0)
0 nm Alq_3	7.9 ± 0.6 (8.6)	29.7	2.4 (2.6)	60.9	(-15.0, -19.8)
20 nm Alq_3	8.2 ± 0.4 (8.6)	34.2	2.8 (2.9)	61.0	(-16.3, -19.3)
30 nm Alq_3	8.3 ± 0.4 (8.3)	39.5	3.3 (3.3)	63.7	(-16.4, -17.6)
40 nm Alq_3	8.3 ± 0.1 (8.5)	41.8	3.5 (3.6)	65.1	(-16.8, -16.0)
50 nm Alq_3	8.2 ± 0.1 (8.2)	43.0	3.5 (3.5)	69.1	(-15.9, -12.7)

observed in the *J*-*V* curves.

Transfer matrix optical modeling was used to model the PTB7-Th thickness dependent TPVs. Nonlinear regression fits of the measured *EQE* are shown in Figure 6.7 with the extracted characteristic lengths in Table 6.5. Optical parameters for each material are used to calculate the electric field strength within the device and the spatially resolved exciton generation rate in the active layers. The model fits the measured *EQE* with an exciton diffusion length (L_{ED}) for PTB7-Th and IEICO-4F, as well as the limiting charge collection length (L_{CC}), either hole or electron collection, whichever is limiting. This provides insight into the nature of exciton diffusion and charge collection as a function of PTB7-Th thickness.

In addition to the impact on electrical performance, polymer thickness is a key variable to

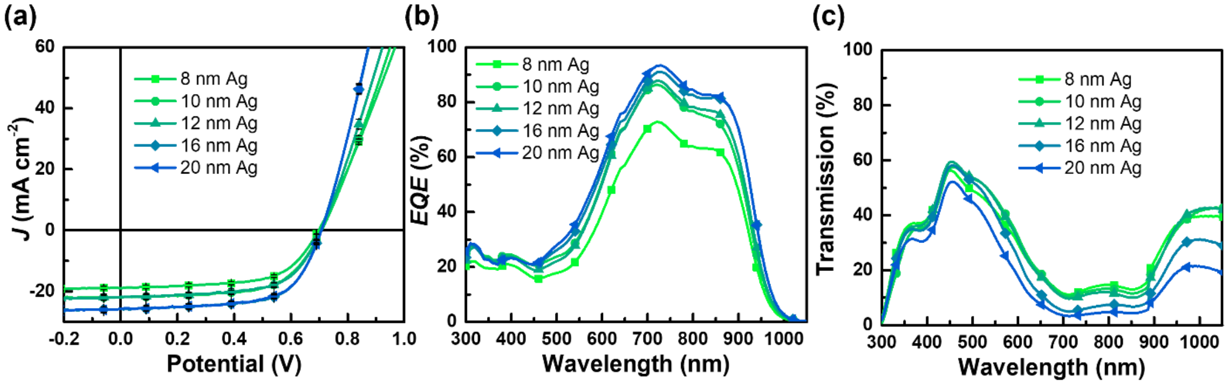

Figure 6.8. Ag thickness dependence on device performance. (a) Characteristic current-voltage (*J-V*) curves, **(b)** external quantum efficiencies (*EQE*), and **(c)** transmission for transparent devices with different Ag thickness. Transmission curves with 10, 12, and 16 nm Ag were measured with an index matched antireflection coating on the glass side.

optimize for its impact on the optical qualities of the TPVs. PTB7-Th accounts for most of the visible absorption in the device, and this is made clear from transmission measurements for the entire TPV device stack (Figure 6.5c) and for the device stack up to the PTB7-Th layer (Figure 6.5d). As expected, key optical figures of merit including the *AVT*, color rendering index (*CRI*), and the CIELAB color space coordinates (*a**, *b**) vary strongly with polymer thickness (Table 6.6). Over the full thickness range, *AVT* more than doubles and the *CRI* increases from 44.5 to 84.9. As a result, the *LUE* reaches a clear optimum at 40 nm PTB7-Th.

To fully optimize TPVs for electronic and optical performance, we look at the impact of thin-Ag thickness as the top transparent electrode (Figure 6.8 and Table 6.7) and the thickness of the antireflection layer Alq_3 (Figure 6.9 and Table 6.8). Ag thickness was varied from 8 to 20 nm, and all devices were made with a 40 nm Alq_3 capping layer. Small effects on the J_{SC} and *FF* were

Table 6.7. Ag thickness dependent device parameters.

Device	J_{SC}/M [mA cm^{-2}]	M	Int. J_{SC} [mA cm^{-2}]	V_{OC} [V]	*FF*	*PCE* [%] (Int. J_{SC})	*AVT* [%]	*LUE* [%] (Int. J_{SC})
8 nm Ag	16.8 ± 0.5	1.10	16.2	0.701 ± 0.004	0.62 ± 0.02	7.3 ± 0.2 (7.0)	37.8	2.8 (2.7)
10 nm Ag	19.6 ± 0.7	1.12	19.7	0.702 ± 0.004	0.61 ± 0.01	8.4 ± 0.3 (8.4)	41.6	3.5 (3.5)
12 nm Ag	19.8 ± 0.9	1.10	19.9	0.705 ± 0.005	0.63 ± 0.01	8.8 ± 0.4 (8.8)	40.9	3.6 (3.6)
16 nm Ag	21.5 ± 0.7	1.11	21.5	0.708 ± 0.004	0.64 ± 0.01	9.8 ± 0.4 (9.8)	36.0	3.5 (3.5)
20 nm Ag	21.8 ± 0.8	1.12	22.1	0.710 ± 0.003	0.64 ± 0.02	9.9 ± 0.4 (10.1)	28.6	2.8 (2.9)

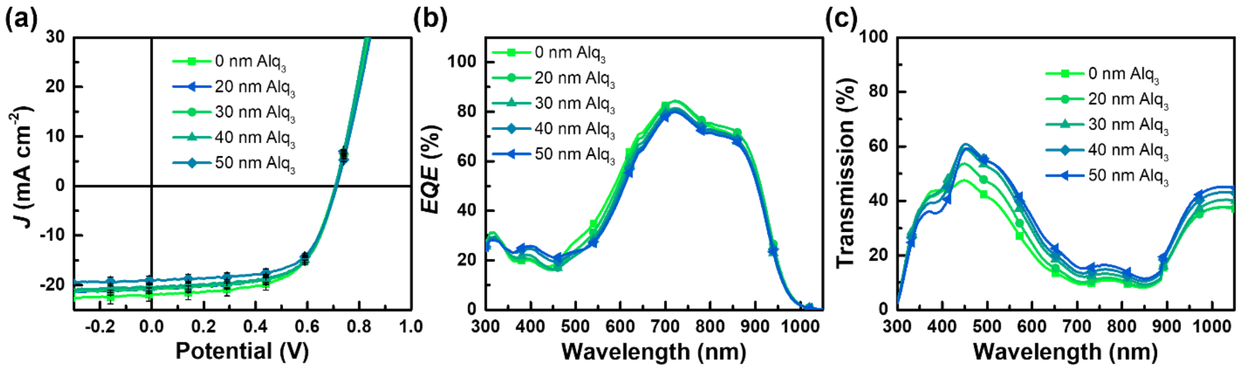

Figure 6.9. Alq$_3$ thickness dependence on device performance. (a) Characteristic current-voltage (*J*-*V*) curves, **(b)** external quantum efficiencies (*EQE*), and **(c)** transmission for transparent devices with different Alq$_3$ thickness. Transmission curves measured with an index matched antireflection coating on the glass side.

observed, likely due to enhanced charge carrier collection from improved conductivity of the electrode layer. Optically, an optimum Ag thickness was found at 10 nm for *AVT*, while the electronic and optical performances achieved a maximum at 12 nm yielding a *LUE* of 3.6%. Alq$_3$ thickness was evaluated on devices with 12 nm Ag and 35 nm PTB7-Th, and a strong effect on *AVT* was demonstrated, increasing from 29.7% without an Alq$_3$ layer to 43% with 50 nm Alq$_3$. The TPV *PCE* declines at 50 nm Alq$_3$ however, with an *LUE* of 3.5% compared to 3.6% at 40 nm. While only small improvements were made to the device performance through optimization of the Ag and Alq$_3$ layers, they are still important to reaching the overall efficiencies achieved in this work of *PCE* = 8.8%, *AVT* = 40.9%, and *LUE* = 3.6%, data for which is shown in Figure 6.10a-c and Table 6.9. A large-scale device is pictured in Figure 6.11a. We also examine the electrode impact on transparency using transfer matrix optical modeling and estimate that replacing the

Table 6.8. Alq$_3$ thickness dependent device parameters.

Device	J_{SC}/M [mA cm^{-2}]	M	Int. J_{SC} [mA cm^{-2}]	V_{OC} [V]	FF	PCE [%] (Int. J_{SC})	AVT [%]	LUE [%] (Int. J_{SC})
0 nm Alq$_3$	18 ± 1	1.17	19.7	0.710 ± 0.004	0.62 ± 0.01	7.9 ± 0.6 (8.6)	29.7	2.4 (2.6)
20 nm Alq$_3$	18.4 ± 0.8	1.13	19.5	0.709 ± 0.003	0.63 ± 0.01	8.2 ± 0.4 (8.6)	34.2	2.8 (2.9)
30 nm Alq$_3$	18.5 ± 0.8	1.13	18.7	0.710 ± 0.003	0.63 ± 0.01	8.3 ± 0.4 (8.3)	39.5	3.3 (3.3)
40 nm Alq$_3$	18.2 ± 0.8	1.12	18.7	0.711 ± 0.004	0.64 ± 0.01	8.3 ± 0.1 (8.5)	41.8	3.5 (3.6)
50 nm Alq$_3$	18.4 ± 0.8	1.05	18.4	0.707 ± 0.004	0.63 ± 0.01	8.2 ± 0.1 (8.2)	43.0	3.5 (3.5)

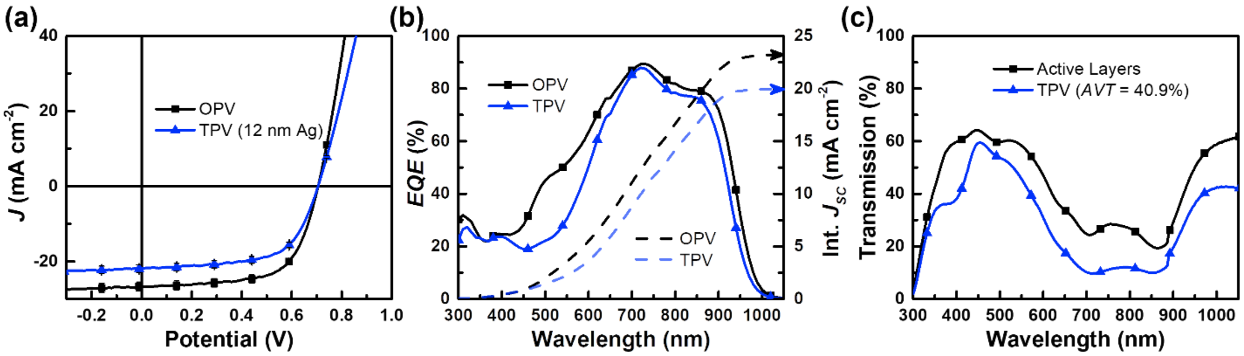

Figure 6.10. Optimized transparent photovoltaic device data. (a) Characteristic current-voltage (*J-V*) curves and **(b)** external quantum efficiencies (*EQE*) with integrated short circuit current (dashed lines) for fully optimized transparent photovoltaic (TPV) devices (blue) compared with the optimized opaque device (OPV, black). TPVs were fabricated with 7 nm MoO_3, 12 nm Ag, and 40 nm Alq_3 on top of the sequentially deposited active layers. **(c)** Transmission data for the complete TPV device stacks with an antireflection coating attached on the glass substrate side with index matching gel (blue), and for the device stack up to the active layers for the opaque devices (black).

Ag/Alq_3 top contact with sputtered ITO would likely increase the transparency by 10% or more (Figure 6.12), and lead to *AVT*s up to 60% for thin PTB7-Th layers.[95]

A critical component of verifying any transparent solar cell is the photon balance check (Equation 2.4), where the sum of reflection (*R(%)*), transmission (*T(%)*), and *EQE* (as a substitute for absorption with internal quantum efficiency = 100%) are less than or equal to 100 at every wavelength. We provide the photon balance for our fully optimized device in Figure 6.11b, and note that the balance check is satisfied and that we achieve internal quantum efficiencies (*IQEs*) at or above 90% for much of the NIR region. Furthermore, we provide photon balance checks for all TPVs made in this work in the Appendix. A second important verification is from the comparison of the measured J_{SC} with the integrated photocurrent from the *EQE*, which show excellent agreement for our devices. The impact of the ARC, observed in the low reflection achieved in Figure 6.11b is detailed in Figure 6.13 and Table 6.10, where the *R(%)* decreases and *T(%)* increases across the spectrum. Some of the light allowed into the device by the ARC will be absorbed on the initial pass through the device or reflected at the Ag electrode and absorbed in the

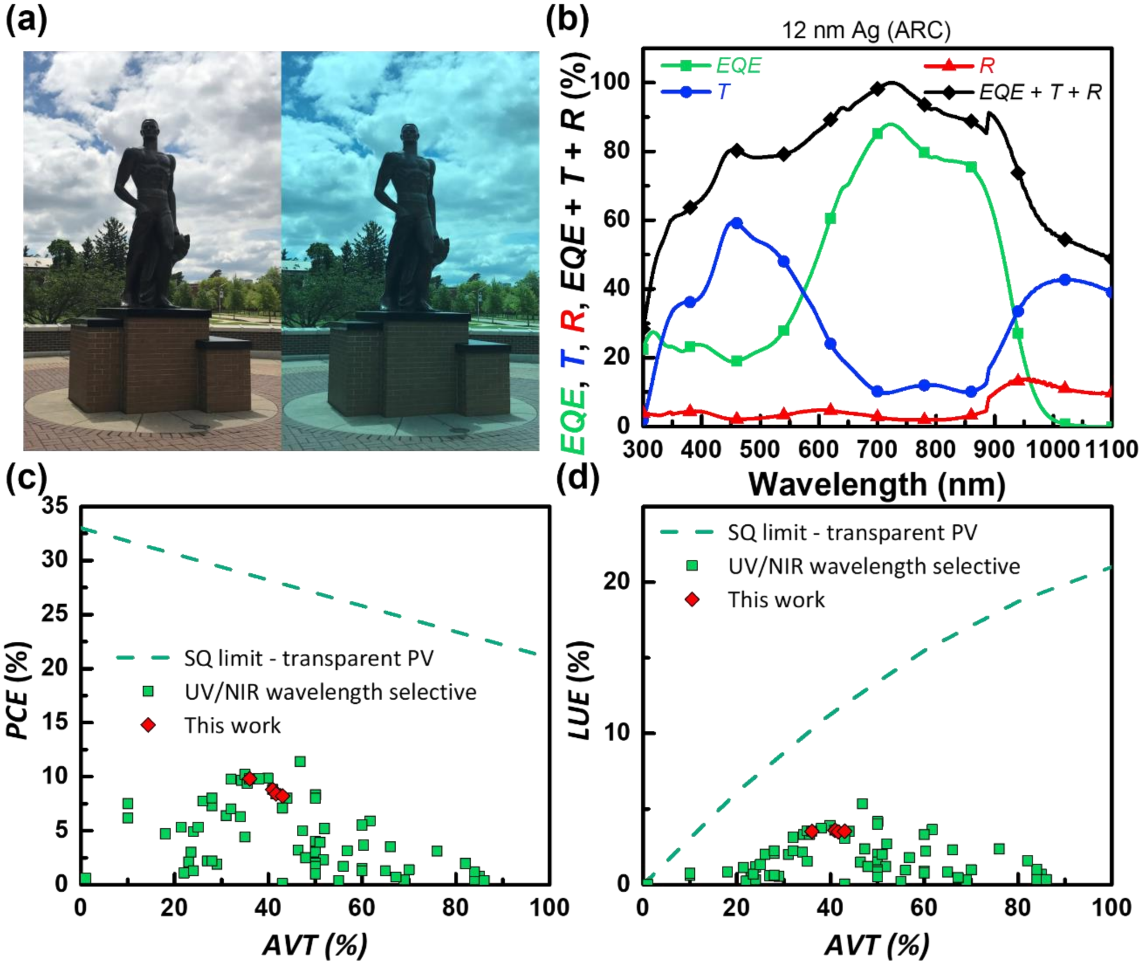

Figure 6.11. Aesthetic characterization of TPVs and literature comparison. (a) Image of a transparent photovoltaic (TPV) device with 35 nm PTB7-Th and 12 nm Ag. **(b)** Photon balance for the optimized TPV. A comparison of literature single-junction, ultraviolet or near-infrared wavelength selective TPV performances with devices prepared in this work for **(c)** *PCE* vs *AVT*, and **(d)** *LUE* vs *AVT* with the Shockley-Queisser limit for transparent single-junction PVs shown as a dashed line.

reduced double pass present in TPVs. Initial lifetime measurements are reported in Figure 6.14, and demonstrate that devices operate at ~67% of the initial *PCE* after 1000 hours.

6.3 Discussion

Optical and electronic performance are equally important in TPVs, and PTB7-Th thickness

Table 6.9. Optimized transparent photovoltaic device parameters.

Device	J_{SC}/M [mA cm^{-2}]	M	Int. J_{SC} [mA cm^{-2}]	V_{OC} [V]	FF	PCE [%]	AVT [%]	LUE [%]
OPV	23 ± 1	1.20	23.2	0.707 ± 0.003	0.64 ± 0.02	10.4 ± 0.5 (10.4)	-	-
TPV (12 nm Ag)	19.8 ± 0.9	1.10	19.9	0.705 ± 0.005	0.63 ± 0.01	8.8 ± 0.4 (8.8)	40.9	3.6 (3.6)

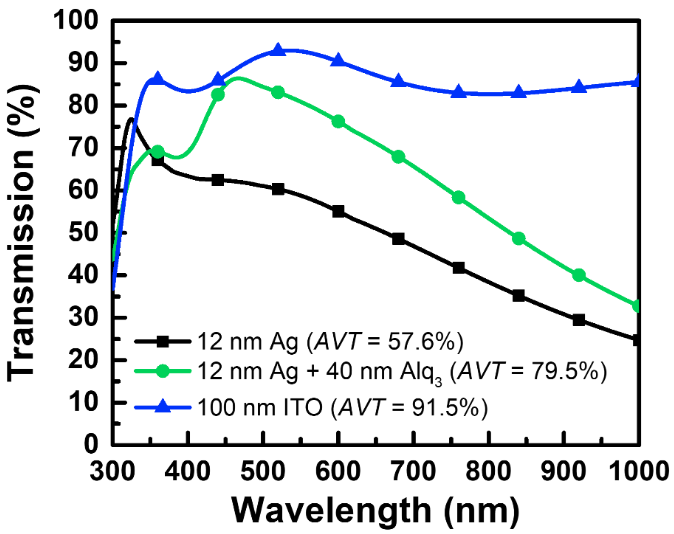

Figure 6.12. Calculated transmission through different top electrodes. Transparency through three different top electrodes on a glass substrate calculated with transfer matrix optical modeling.

was the most critical parameter studied in this work in its effect on the *LUE*. Two key trends from the PTB7-Th thickness dependent data were the sharp loss of V_{OC} at 5 nm, and the steep and uniform drop in *EQE* as polymer thickness decreased from 40 nm to 5 nm.

The sharp V_{OC} cutoff at 5 nm PTB7-Th indicates that ~10 nm is sufficient to form a neat layer that remains intact after spin-coating IEICO-4F. Lee et al. demonstrated via high-resolution cross-sectional tunneling electron microscopy that neat films can remain intact following sequential spin-coating,[171] and Wei et al. produced devices with *PCE* > 17% using a protective

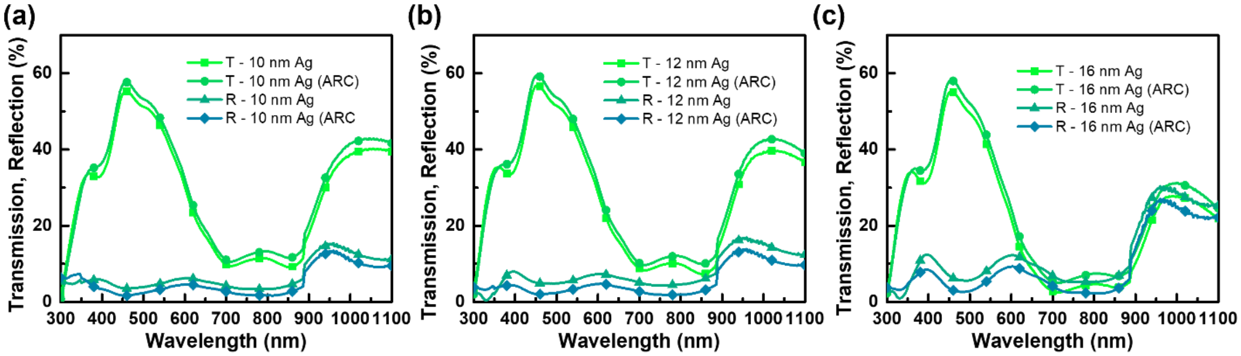

Figure 6.13. Impact of antireflection coating on optical performance. Transmission and reflection data for devices with and without an antireflection coating (ARC) on the glass side for transparent photovoltaics with **(a)** 10 nm, **(b)** 12 nm, and **(c)** 16 nm Ag electrode layers.

Table 6.10. Impact of antireflection coating on optical performance.

Device	*PCE* [%] (Int. J_{SC})	*AVT* [%]	*LUE* [%] (Int. J_{SC})	*CRI*	(*a**, *b**)
10 nm Ag	8.4 ± 0.3 (8.4)	39.6	3.3 (3.3)	63.8	(-18.5, -12.6)
10 nm Ag (ARC)	8.4 ± 0.3 (8.4)	41.6	3.5 (3.5)	65.3	(-17.7, -12.7)
12 nm Ag	8.8 ± 0.4 (8.8)	38.7	3.4 (3.4)	61.2	(-18.6, -15.5)
12 nm Ag (ARC)	8.8 ± 0.4 (8.8)	40.9	3.6 (3.6)	63.1	(-17.7, -15.5)
16 nm Ag	9.8 ± 0.4 (9.8)	33.5	3.3 (3.3)	48.8	(-23.2, -20.3)
16 nm Ag (ARC)	9.8 ± 0.4 (9.8)	36.0	3.5 (3.5)	52.8	(-21.6, -19.8)

solvent layer to reduce mixing and produce high purity domains, suggesting that high efficiency devices are possible with little to no mixed region.[172] Exciton diffusion lengths of NFAs, measured with *EQE* quenching and transient absorption spectroscopy of exciton annihilation, are sufficient to support a bilayer infrastructure with a thin (NFA < 50 nm) layer.[173] However, many LBL demonstrations have concluded that significant intermixing occurs via swelling of the polymer film during NFA deposition to form a mixed region of varying size within the planar heterojunction.[159–161,164–167,174,175] We explain the V_{OC} drop at 5 nm as the result of an incomplete

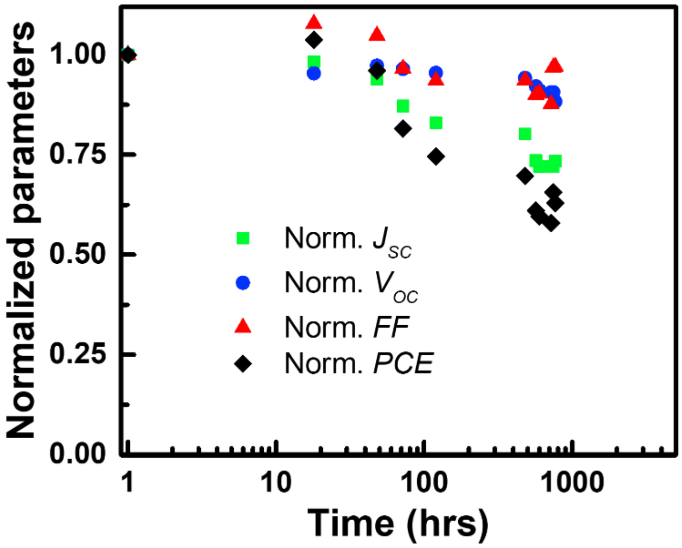

Figure 6.14. Shelf life of bilayer photovoltaic devices. Normalized device parameters for large area (A = 27 mm^2) transparent devices devices encapsulated with getter pads and stored in the dark in an oxygen and moisture free atmosphere between tests.

film of PTB7-Th allowing for a continuous path of IEICO-4F in parts of the structure from ZnO to MoO_3. The low J_{SC} produced from the 5 nm PTB7-Th device is the result of exciton dissociation likely from any remaining islands of PTB7-Th where a dissociating HJ still exists. Thus, the polymer thickness study suggests that up to 5 nm of PTB7-Th can be dissolved during the IEICO-4F deposition, which might result in the intermixed region of up to 5 nm between layers of PTB7-Th and IEICO-4F. Ideal diode parameters (Table 6.3) from fitted dark *J-V* curves as a function of PTB7-Th thickness (Figure 6.4 and Figure 6.5f) reveal decreased R_P, and increased R_S and n_{id} as polymer thickness decreases from 40 nm to 5 nm. Conceptually, decreased R_P causes increased shunting resulting in current loss and a voltage drop by creating an alternate pathway for current so that a partial junction and resistor are formed in parallel. Increased n_{id} above 1.5 indicates more bimolecular recombination. This conclusion is consistent with the P_0 dependence of the V_{OC} (Figure 6.5e, Figure 6.6a) and J_{SC} (Figure 6.6b). V_{OC} is related to P_0 by Equation 6.1.

$$V_{OC} \propto \frac{k_B T}{q} \ln(P_0) \tag{6.1}$$

The magnitude of the slope of V_{OC} vs $\ln(P_0)$ signifies the dominant mode of recombination in the device. A slope approaching k_BT/q indicates bimolecular recombination controls the process recombination process of charge carriers, and a slope of $2k_BT/q$ points towards increased monomolecular or trap-assisted recombination.[174,176] Relatively small changes are observed in the slope as polymer thickness changes from 10 to 85 nm, however a clear minimum is reached at 40 nm PTB7-Th. The magnitude of this shift in slope is comparable to that observed when CN is added,[162,164,167,174] indicating a similarly strong effect that we also observed in the *EQE*. Independent of PTB7-Th thickness, the slopes in Figure 6.6a are closer to k_BT/q than $2k_BT/q$ which indicates that bimolecular recombination is the dominant mode of recombination. The exponent of a power law relationship between J_{SC} and P_0 (Equation 6.2) describes the relative amount of bimolecular recombination in a device, with s approaching 1 indicative of less bimolecular recombination:

$$J_{SC} \propto {P_0}^s \tag{6.2}$$

No clear trend is observed in the value of *s* as polymer thickness changes, although 10 nm PTB7-Th yields the lowest measured *s* with the most bimolecular recombination. The *s* values calculated here are lower than others reported for LBL devices,[162,164,174] especially for 10 nm PTB7-Th, suggesting increased bimolecular recombination.

To provide a framework for our analysis of the PTB7-Th thickness dependent *EQE* trends, we describe the *EQE* in Equation 1.8 as the product of five component efficiencies for absorption (η_A), exciton diffusion (η_{ED}), charge transfer (η_{CT}), exciton dissociation (η_{DS},), and charge collection (η_{CC}). Decreased polymer absorption at 5 nm PTB7-Th explains the significant photocurrent loss in the short NIR, VIS, and UV regions, but not the loss of *EQE* from IEICO-4F. From Figure 6.5c, the *EQE* reduction is largely caused by an electronic effect rather than optical interference because the *EQE* loss is uniform across the spectrum from 300 to 900 nm in both PTB7-Th and IEICO-4F absorption ranges. For a HJ that is spatially uniform across the entire device, there is typically either a sufficient energetic offset between donor and acceptor to yield high η_{CT} and η_{DS} or there is not, and the device effectively turns off.[95] We do not observe this binary effect in our devices, as the photocurrent steadily drops from 40 nm to 20, 10 and 5 nm PTB7-Th.

Exciton diffusion is interface dependent parameter from the standpoint of 1) the location of exciton generation relative to the interface (optical interference related effects) and 2) the shape and overall area of the PTB7-Th:IEICO-4F interface (morphology effects). Reduced η_{ED} from IEICO-4F could explain the low photocurrent in the 800-1000 nm range. Charge collection is affected by the PTB7-Th:IEICO-4F interfacial area, as carriers with a longer path length from the interface to MoO_3 (holes) or ZnO (electrons) will have a lower η_{CC}.[3,11] Charge collection through PTB7-Th should theoretically become more efficient with a shorter path length.

To understand the *EQE* drop off from the 60 nm to 10 nm PTB7-Th, transfer matrix optical modeling was combined with a nonlinear regression fit of the measured *EQE* to extract characteristic lengths and assess the impact of optical interference.[95,131] The exciton diffusion lengths for PTB7-Th and IEICO-4F were extracted to be 200 nm (± 100 nm) to give the best *EQE* fit at 60 nm PTB7-Th. Exciton diffusion lengths greater than the active layer thickness do not necessarily represent the actual L_{ED} of a material. That is, the model becomes notably insensitive to the L_{ED} once the values start to exceed the largest thicknesses (hence the large uncertainty on the fits). Rather, these values indicate a highly efficient η_{ED} for these devices with L_{ED}s that are at least great than the total active layer thickness (e.g. 100 nm) and potentially as high as 200 nm.

The large fitted $L_{ED,A}$ and $L_{ED,D}$ reveal that the limiting factor on device performance is not exciton diffusion related. Each *EQE* spectra was fitted for the limiting charge collection length (L_{CC}), which could be attributed to either IEICO-4F or PTB7-Th, depending on the layer thickness. Three distinct regimes are observed in the reported L_{CC}. Low PTB7-Th thicknesses (< 40 nm) have L_{CC} smaller than or on the same magnitude as the active layer thickness. PTB7-Th layers between 40 and 60 nm possess a L_{CC} much greater than the active layer thickness, while at 85 nm L_{CC} drops off sharply to 265 nm. The 7 nm L_{CC} for 5 nm PTB7-Th agrees with the previous conclusion that the HJ is incomplete and results in an inability to separate excitons. The V_{OC} is similar between 10 nm and thicker PTB7-Th layers which suggests that the HJ is complete at 10 nm PTB7-Th. Decreasing R_P and increasing R_S indicate losses in carrier transport due to recombination through the PTB7-Th at thicknesses less than 40 nm. Similarly, the ideality factor increases from 40 nm

PTB7-Th to 10 nm PTB7-Th, also indicating increased recombination rates. The 10 and 20 nm PTB7-Th devices are limited by recombination, likely due to thinner polymer layers being more prone to leakage current such as pinholes. This leads to higher recombination rates of photogenerated carriers (generated across all wavelengths) with leakage current, and effectively lower L_{CC}, EQE, and J_{SC}. The 40 and 60 nm PTB7-Th devices have $L_{ED,A}$, $L_{ED,D}$, and L_{CC} much greater than the active layer thicknesses. The sharp drop-off in L_{CC} from 8560 nm at 60 nm polymer to 265 nm at 85 nm likely reveals a change in the limiting carrier type from hole limited (in the IEICO-4F donor) to electron limited (in the PTB7-Th acceptor) as the polymer thickness increases.

From the combination of experimental data and modeling, an ideal thickness range for electronic performance is found from 40 to 60 nm PTB7-Th. However, the LBL approach allows thinner polymer layers to be used without critically hampering the heterojunction, evidence by the high FF and $PCE > 6\%$ at 20 nm PTB7-Th. The benefit of a thin PTB7-Th layer is also important in the optical evaluation of the device.

Three critical parameters to evaluate for optical quality are the AVT, CRI, and (a^*, b^*). AVT describes the overall transparency of the device relative to human perception, with values less than 50% typically resulting in colored, dark, or strongly tinted TPVs. $AVT > 60\%$ will generally look clear and is considered acceptable for many transparent applications.[22] CRI captures how accurately the true color of an object observed through the device is rendered, with $CRI > 80$ considered acceptable.[21,22,24] The color chromaticity coordinates (a^*, b^*) define the specific color tint, with a desired range of $-15 < a^* < 1$ and $-15 < b^* < 15$ in glass and glazing industries for tinted products and $-7 < a^* < 0$ and $-3 < b^* < 7$ for mass-market architectural glass products. We note that TPVs with yellow or red tint (a^* and/or $b^* > 0$) are generally less appealing for glass products than those with a neutral or blue/green tint (negative values of a^* and b^*).[25,26] Aesthetically, PTB7-Th thickness is critical to the optical quality of the devices, where > 20 nm PTB7-Th results in low *AVT* (< 50%), and a *CRI* of 63 for the optimal device as well as (*a**,*b**) outside of the desired range. This is visually evident from the device picture in Figure 6.11a, where the relatively strong PTB7-Th absorption of 550 to 675 nm light gives the devices a strong blue color. Shifting the polymer thickness from 40 nm to 20 nm moves the TPVs into an acceptable range of color space coordinates for many window applications. The *CRI* and *AVT* reach 82.8 and 50.4%, clearing industry standards at 10 nm PTB7-Th. Utilizing 5 nm of PTB7-Th, the *CRI* and (*a**, *b**) approach the ideal ranges for glass products. The strong effect of polymer thickness on optical performance illustrates the utility of the LBL approach.

To provide context for the performance, we present a comparison of the device performance metrics in this work to other wavelength selective single heterojunction devices in Figure 6.11c and d. Our devices achieve good *PCE*, *AVT*, and *LUE* compared to the current state of the TPV field. Notably, while many TPVs have reached 7-10% *PCE* with moderate *AVT*, only a few have demonstrated *LUE* of 3 or higher, but mostly with notably poor *CRI*.[153,155,177,178] Looking forward, improving optical performance while maintaining electronic performance is a key area of focus. There are two primary routes to improving optical performance by 1) minimizing parasitic absorption from the electrodes with more transparent but equally conductive materials, such as with ITO replacing the Ag/Alq3 anode, and 2) altering the PTB7-Th polymer to reduce visible absorption. Chemical modification of the PTB7-Th monomer core to red shift the absorption is one route to achieving better optical performance while maintaining the structure of PTB7-Th:NFA devices. Alternatively, several polymers with deeper NIR absorption have been demonstrated,[179] including DPP2T which maintained an excellent V_{OC} of 0.75 V in a BHJ with IEICO-4F.[154] Reduced energetic losses will be required to maintain the V_{OC} with a narrower bandgap polymer, and less visible light harvesting will come at some cost of photocurrent that could potentially be offset with deeper NIR harvesting.

6.4 Conclusions

In this work we present high performance solution processed layer-by-layer deposited TPVs based on an uncommon donor-acceptor architecture. In addition, we demonstrate a detailed study of the impact of polymer (acceptor) thickness on power generation and aesthetic performance. We find that the LBL approach uncovers large exciton diffusion lengths for PTB7-Th and IEICO-4F with a L_{ED} and L_{CC} greater than the active layer thickness tested, highlighting the strength of the planar HJ formed as a result of sequential deposition processing. An optimized *PCE* and *AVT* of 8.8% and 40.9% is achieved, yielding an *LUE* of 3.6% comparable to the best TPV demonstrations to date. Optically, thinner layers of polymer move the devices from a less appealing optical regime to one that is acceptable for many applications with *AVT* > 50% and *CRI* > 80. Future work for LBL TPVs should focus on improving the optical performance of these devices to push the *AVT* and *CRI* to acceptable levels while maintaining *PCE > 8%*. Overall, these devices demonstrate the power of the LBL approach for transparent solar technologies via unique control over active layer thicknesses, architecture design, and optimization that could ultimately aid in the scaleup of these devices.

6.5 Methods

6.5.1 Active layer and ZnO solution preparation

PTB7-Th (1-Material) was dissolved in o-xylene (Sigma Aldrich) at 1-10 mg mL^{-1} and covered, stirred, and heated at 70°C overnight. IEICO-4F (1-Material) was dissolved in o-xylene:n-butanol:1-chloronaphthalene (Sigma Aldrich) at 75:25:0, 74.25:24.75:1, 73.5:24.5:2, 72.75:24.25:3, 72:24:4, 71.25:23.75:5, and 70.5:23.5:6 v/v ratios to yield 1-chloronaphthalene doping of 0 to 6%.[162] IEICO-4F solutions were then covered, stirred, and heated at 70°C overnight. ZnO solutions were prepared with 1 g zinc acetate dihydrate (Sigma Aldrich), 0.277 mL ethanolamine (Sigma Aldrich), and 10 mL 2-methoxyethanol (Sigma Aldrich), and covered and stirred rigorously overnight in a fumehood.[180]

6.5.2 Device fabrication

Pre-patterned ITO coated glass substrates were cleaned via sequential sonication for 10 minutes each in deionized water, acetone, and isopropanol. Substrates were dried on a hotplate at 135 °C for 1 minute and then plasma cleaned under light vacuum for 10 minutes. The ZnO layer was spin-coated onto the substrates immediately after plasma cleaning for 30 s at 4000 rpm (50 µL, 2000 rpm/s acceleration). ZnO covered substrates were annealed at 200 °C for 20 minutes in air prior to moving to a glovebox for active layer spin-coating. PTB7-Th films were spun using 65 µL at 1000 rpm for 15 s and 2000 rpm for 5 s to yield thicknesses ranging from 5-85 nm as measured by VASE. Films were spun on silicon wafers for VASE measurements. IEICO-4F films were spun at 1500 rpm for 45 s (60 µL solution) to yield films of approximately 55 nm. After sequential bilayer deposition, devices were annealed at temperatures ranging from room temperature to 150 °C for 10-20 minutes. Substrates were then loaded into a high vacuum thermal vapor deposition chamber (Angstrom Engineering) where 7 nm of MoO_3 was deposited at $3x10^{-6}$ torr. Finally, a top contact of Ag (opaque devices – 80 nm) or Ag and Alq_3 (TPVs) was deposited using a special mask to define an active area of 4.43 mm^2. For TPVs, Ag thickness (measured with AFM) ranged from 8 to 20 nm and Alq_3 thickness (VASE) from 0 to 50 nm.

6.5.3 Device testing

Current-voltage (*J*-*V*) characteristic curves were measured with a Keithley 2420 SourceMeter under illumination from a Xe Arc lamp calibrated to 1-sun intensity with a NREL-calibrated Si reference cell with KG5 filter. A minimum of 5 devices were tested for each condition. *EQE* measurements were made with monochromated light from a tungsten halogen lamp chopped at 200 Hz. A Newport-calibrated Si diode was used to calibrate the system prior to taking *EQE* measurements. For each structure with distinct *EQE*, the spectral mismatch factor, *M*, was calculated from Equation 4.5. Dark *J-V* curves were taken with the device holder covered and all light sources turned off. Light intensity (P_0) dependent *J-V* curves were taken with four different neutral density filters placed between the Xe Arc lamp and the device. Note that the mismatch was also corrected for each filter. Dark *J-V* fitting (photocurrent, $J_{ph} = 0$) of the ideal diode equation (Equation 1.3) was performed in MATLAB to extract device parameters.[3,94]

6.5.4 Optical performance assessment

Un-patterned ITO coated glass substrates were used to prepare device stacks for optical characterization. Optical devices were fabricated simultaneously with electronic PVs to ensure the same device conditions but without the patterned mask defining the top contact (Ag and Alq_3). A dual-beam Perkin Elmer Lambda 900 UV/VIS/NIR Spectrometer was used in transmission mode to measure the transmittance and reflectance of TPVs. The reference slot was kept empty for all thin film measurements and devices were placed so that all incident light passed through the sample. Reflectance measurements were made with a 6° specular accessory installed on the sample side. Optical figures of merit including *AVT*, *CRI*, and (a^*,b^*) were calculated from transmittance data using the available spreadsheet.[6] For 1-chloronapthalene doping level optimization, optical samples were complete after deposition of the PTB7-Th and IEICO-4F active layers. For PTB7-Th thickness optimization, optical samples for transmittance characterization of just the PTB7-Th layer were complete after depositing PTB7-Th on ZnO and ITO covered glass substrates. Full devices with various PTB7-Th thickness were prepared for determination of the optical figures of merit.

6.5.5 Shelf-life assessment

Large area devices (27 mm^2) were fabricated in the same manner as smaller devices for the optimal TPV (12 nm Ag, 40 nm PTB7-Th, 40 nm Alq_3 and 4% CN) and encapsulated with a getter pad using a UV-curable epoxy (DELO). Devices were stored in the dark in an oxygen and moisture free environment and were temporarily placed in atmospheric conditions for *J-V* testing under 1-sun illumination from a Xe Arc lamp. *J-V* data was normalized to the fresh device performance.

6.5.6 Optical modeling

Transfer matrix optical modeling and *EQE* fitting were performed similarly to previous works.[95,131] Exciton diffusion lengths were optimized to give the best fit for the 60 nm PTB7-Th *EQE* and were then held constant for the L_{CC} fit of each PTB7-Th thickness. The charge collection equation described in Equation 1.18 was used to extract L_{CC}.[3] The charge collection efficiency was calculated for both IEICO-4F and PTB7-Th at each L_{CC} in the fitting process using the respective layer thickness and the lowest η_{CC} was used as the limiting rate for current generation form both layers.

Chapter 7 – Graphene Nanoribbon Photovoltaics

The work presented in this chapter was submitted for publication and is in review.

7.1 Introduction

Graphene materials possess outstanding electrical and mechanical properties, including room temperature carrier mobilities greater than 15,000 cm^{2}V^{-1}s^{-1}, [181] a conductivity greater than silver, a Young's modulus of 1 TPa, and tensile strength of 50-60 GPa.[182,183] Given the exceptional properties, graphene is a natural choice for electronic and optoelectronic applications and has been integrated into photovoltaic devices (PVs) as a conductive layer and electrode in thin film, organic, polymer, and dye sensitized PVs.[184–188] Graphene is a 2-dimensional zero gap semiconductor or semi-metal, and as a result, has not been directly used as light harvesting or photoactive layers in PV cells. It is well known that a bandgap can be generated by confining graphene with a dimension lower than the Bohr radius. One dimensional graphitic materials have been synthesized with bandgaps ranging from 1 eV to 3.5 eV based on both top-down and bottom-up approaches.[189,190] Carbon nanotubes (CNTs) were among the first examples of one-dimensional carbon-based materials with bandgaps suitable for photovoltaics based on the nanoscale diameter of the CNT.[191–195] Graphene nanoribbons (GNRs) have emerged recently as a new class of one-dimensional carbon material synthesized from the bottom-up with a tunable bandgap controlled by the ribbon width and minimized edge defects. GNRs offer bandgaps suitable for charge separation and close to the ideal Shockley-Queisser (SQ) theoretical limit range between 1.1V and 1.4 eV.[3] Combined with low cost and low toxicity, this makes GNRs an exciting candidate for the next generation of thin film optoelectronic devices.

GNRs were initially realized using top-down approaches, including CNT unzipping,[196–201] graphene etching,[202] and graphene chemical vapor deposition.[203] GNRs synthesized from such approaches often have a wide distribution of thicknesses, shapes, and defects, and therefore widely vary in their electronic and optical properties. This variability makes PV device fabrication with top-down GNRs difficult if large diameter CNTs are unzipped to yield wide GNRs with shorting pathways. Top-down GNRs often have undesired oxide groups or other defects that negatively impact conductivity and solubility that impedes processing. Furthermore, the width of GNRs synthesized from graphene sheets or unzipping multi-walled CNTs were often too large (>10 nm) to produce a bandgap suitable for charge separation, limiting their use to non-optical applications.[196–199,201,202] Zheng et al. and others have demonstrated that thinner GNRs are possible when synthesized by unzipping single-walled CNTs, although challenges with uniformity and processability remain.[200] More recently, a range of new bottom-up approaches were used to synthesize GNRs with greater uniformity, improved solubility, and widths small enough to induce suitable bandgaps.[189,204–216] One bottom-up approach developed by Yang et al. using nonoxidative alkyne benzannulation yielded GNRs with widths less than 5 nm and an optical bandgap (~1 eV) on the edge of the ideal bandgap range (1.1-1.4 eV) for PVs from the SQ limit, allowing for photon absorption across the ultra-violet (UV), visible (VIS), and near-infrared (NIR) portions of the solar spectrum.[189] Bottom-up syntheses offer control over side groups attached at the ribbon edge that greatly improve solubility and lead to facile formation of thin films needed for PVs via spin-coating and other solution processed deposition methods.

GNRs have been used in a variety of applications, including field effect transistors (FETs),[196–198,203,217] sensors,[218,219] electrochemical catalysis,[220–222] batteries,[223] and PVs.[224–229] In PVs, GNRs have been utilized as transport layers and electrodes, including hole transport layers for polymer and perovskite PVs,[224,225] electron transport layers in perovskite devices,[226,227] and indium tin oxide replacement electrodes in polymer PVs.[228] GNRs were also demonstrated in Schottky solar cells as part of an electrode junction with silicon nanowires.[229] Several studies investigated the optoelectronic properties of GNRs and found or calculated exciton binding energies of 1.8 eV,[230] 1.6 eV,[231] and 0.7 eV for various GNRs.[232] Tries et al. also found an exciton lifetime of over 100 ps in solution-dispersed GNRs.[232] These studies collectively indicate strong excitonic effects in GNRs and the long exciton lifetime is particularly promising for optoelectronic applications, but GNR implementation into optoelectronic devices as a photoactive light harvesting material has not yet been realized. In this work, we demonstrate photovoltaic devices utilizing GNRs as a photoactive component. We find that GNRs function as electron donors when paired with fullerene (C_{60}) in bilayer graphitic devices and generate photocurrent across the solar spectrum to their bandgap. We utilize optical modeling to dissect device performance into individual components and identify charge transport and carrier mobility limitations stemming from out-of-plane resistance from bulk GNR films. In presenting GNR photoactive devices we open a new window for the utilization of graphitic materials in renewable energy technologies.

7.2 Results

7.2.1 Demonstration of photocurrent from graphene nanoribbons

Bilayer solar cells with an active layer comprised of GNR (donor) and C_{60} (acceptor) were fabricated to explore the photovoltaic effect of GNRs. A representation of GNR generated photoelectrons in the active layer is shown in Figure 7.1a, where GNRs absorb light to generate excitons, which diffuse to the donor-acceptor interface and separate so that GNR photoelectrons are transferred through the fullerene layer. The GNRs shown schematically in Figure 7.1b were synthesized using nonoxidative alkyne benzannulation (Figure 7.2).[189] They exhibit a bandgap of approximately 1.03 eV, harvesting photons across the UV, VIS, and NIR portions of the solar

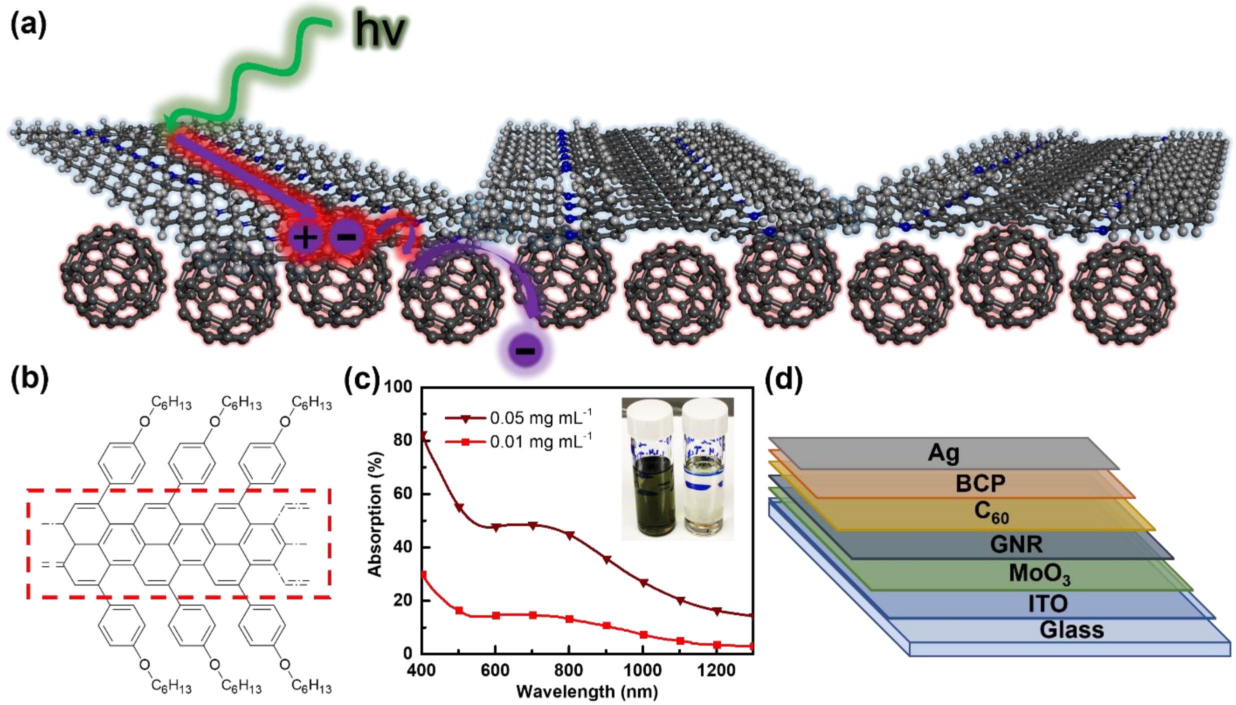

Figure 7.1. Photoelectric effect from GNR thin films in photovoltaic devices. (a) Schematic of the photoelectric effect in graphene nanoribbon (GNR) thin films as observed in photovoltaic devices utilizing a GNR-C_{60} bilayer active layer. **(b)** Two-dimensional drawing of the GNR used in this work with the graphitic core outlined.[182] **(c)** Absorption (100 - %Transmission) of the GNR in 1,2,4-trichlorobenzene at 0.01 mg mL^{-1} and 0.05 mg mL^{-1}, demonstrating light harvesting across the ultraviolet, visible, and near-infrared spectrums. **(d)** Photovoltaic device architecture. Devices were grown on indium tin oxide patterned glass substrates, with molybdenum trioxide (MoO_3) as a hole transport layer, the GNR-C_{60} active layer, bathocuproine (BCP) electron transport layer, and silver (Ag) top electrode.

spectrum. Solution absorption profiles of the GNR at 0.01 $mgmL^{-1}$ and 0.05 $mgmL^{-1}$ are shown in Figure 7.1c. At high concentrations, the GNR exhibits strong aggregation effects, resulting in scattering deep into the NIR spectrum. The current-voltage (J-V) characteristic curves of PVs with a bilayer architecture (Figure 7.1d) were measured with varying GNR thicknesses (Figure 7.3a). This data is compared to a C_{60}-only (Shockley diode) device for reference. The first and most obvious feature is the reduction in the open circuit voltage (V_{OC}) when the GNRs are added to the device. This is expected as the GNR bandgap is much smaller than that of the C_{60}. The short circuit photocurrent density (J_{SC}) increases with the GNR layer present at 3.0 and 3.5 nm thicknesses,

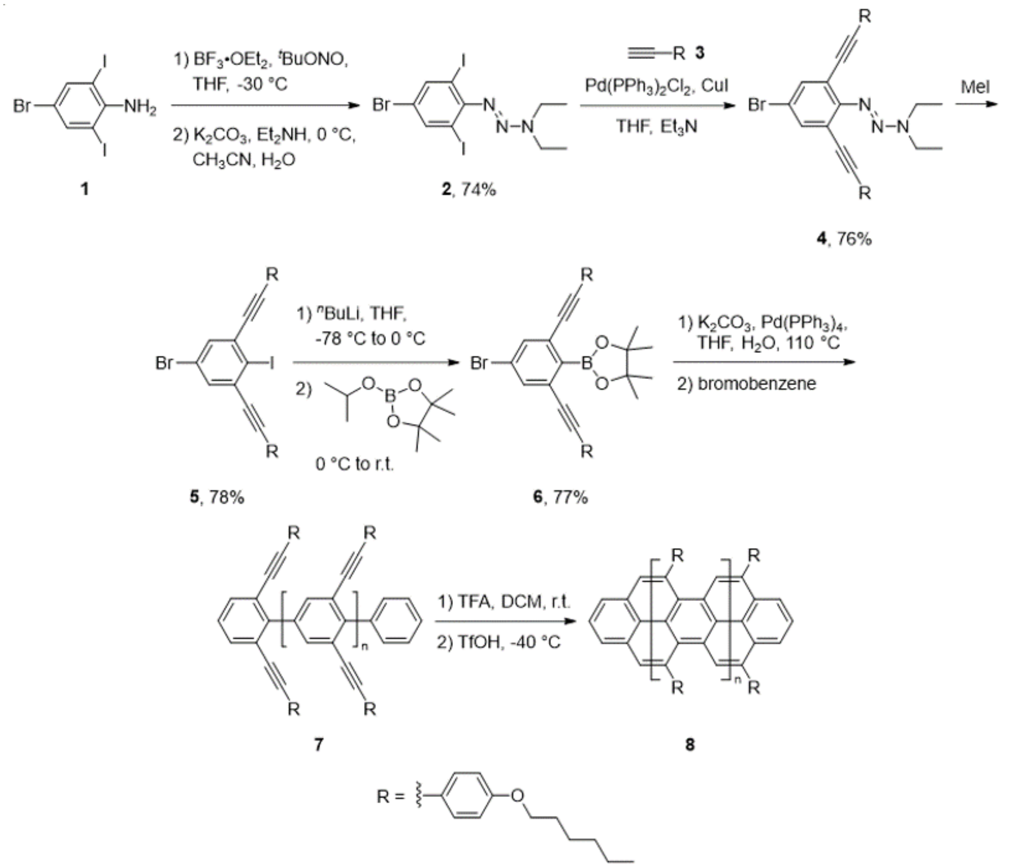

Figure 7.2. Summary of the synthesis pathway for graphene nanoribbons. A summary of key steps in the bottom-up synthesis of graphene nanoribbons.[182]

indicating GNR photocurrent contributions. External quantum efficiencies (*EQE*) were measured, and the 3.0 nm device is shown in comparison to the C_{60}-only device in Figure 7.3b. The GNR clearly contributes photocurrent to the device in the UV, VIS, and NIR regions, marking a key demonstration of GNRs as a functional active material in PVs. While C_{60} absorbs only into the middle of the visible region, the devices produce current to past 1000 nm into the NIR (Figure 7.3c). We estimate the actual current contribution of the GNR as the difference between the 3 nm and C_{60}-only devices, shown as the black line in Figure 7.3b. Peak *EQE* from the GNR is greater than 6% at 500 nm, an excellent achievement compared to the 2.3% *EQE* achieved by CNTs in their first photoactive optoelectronic demonstration.[191] *EQE* can be integrated with Equation 1.7 to calculate the J_{SC}. The estimated GNR contribution to the integrated J_{SC} is roughly half of the

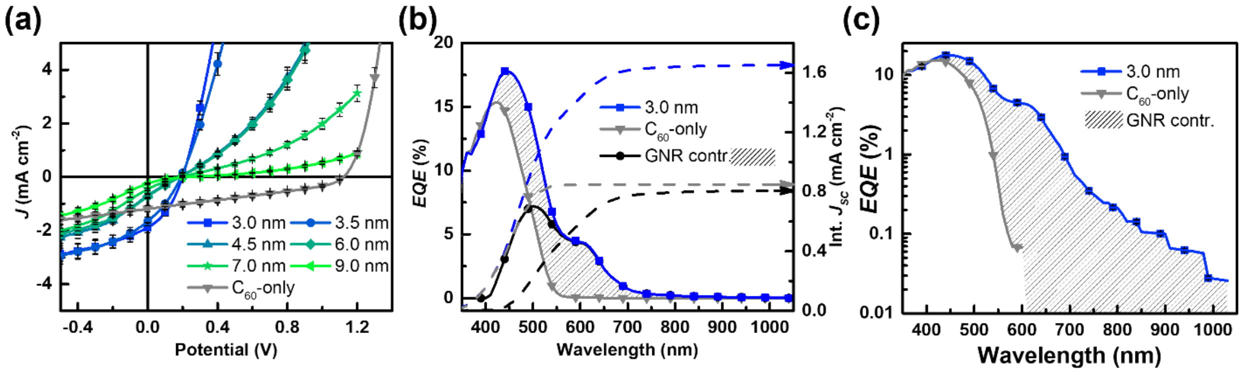

Figure 7.3. Graphene nanoribbon photovoltaic device data. (a) Thickness dependent current-voltage (*J-V*) curves for graphene nanoribbon (GNR)-C_{60} devices of increasing GNR thickness (blue to green) and for a C_{60}-only (gray) control device. **(b)** External quantum efficiency (*EQE*) data for the optimal GNR device with 3.0 nm of GNR (blue) and the C_{60}-only device (gray). The shaded region demonstrates the photocurrent gained by including the GNR layer. The estimated GNR *EQE* (black) was calculated by subtracting the C_{60}-only device from the 3.0 nm GNR bilayer device. Cumulative integrated photocurrents (dashed lines) for the 3.0 nm GNR, C_{60}-only, and GNR contribution. **(c)** *EQE* in the near-infrared region of the 3.0 nm GNR device (blue) and the C_{60} control device (gray). The shaded region is the photocurrent gained in the near-infrared from the GNR. Error bars for *J-V* plots represent the standard deviation from a minimum of 5 measured devices.

total device photocurrent at 3.0 nm GNR, highlighting the broad spectrum absorption due to the low bandgap.

7.2.2 Analysis of EQE trends

To understand the capabilities and limitations of GNR as a photoactive material lying in a flat configuration, we study the GNR thickness dependent *EQE* (Figure 7.4a), which shows three distinct regions for thin films of GNR (3.0 and 3.5 nm). Region 1 consists of the UV and short VIS, where C_{60} produces a large portion of the photocurrent and dominates the absorption profile relative to GNR (Figure 7.5b). In region two, C_{60} absorption quickly falls off, leaving GNR as the primary contributor to the photocurrent seen in the *EQE* shoulder out to 650 nm for 3.0 and 3.5 nm GNR that is absent from the C_{60}-only device. GNR absorption is relatively flat across the UV, VIS, and NIR, however the *EQE* decreases in region 3 to less than 1% at 700 nm. Critically, as the GNR thickness increases beyond 3.5 nm, *EQE* from the C_{60} is greatly diminished to well below

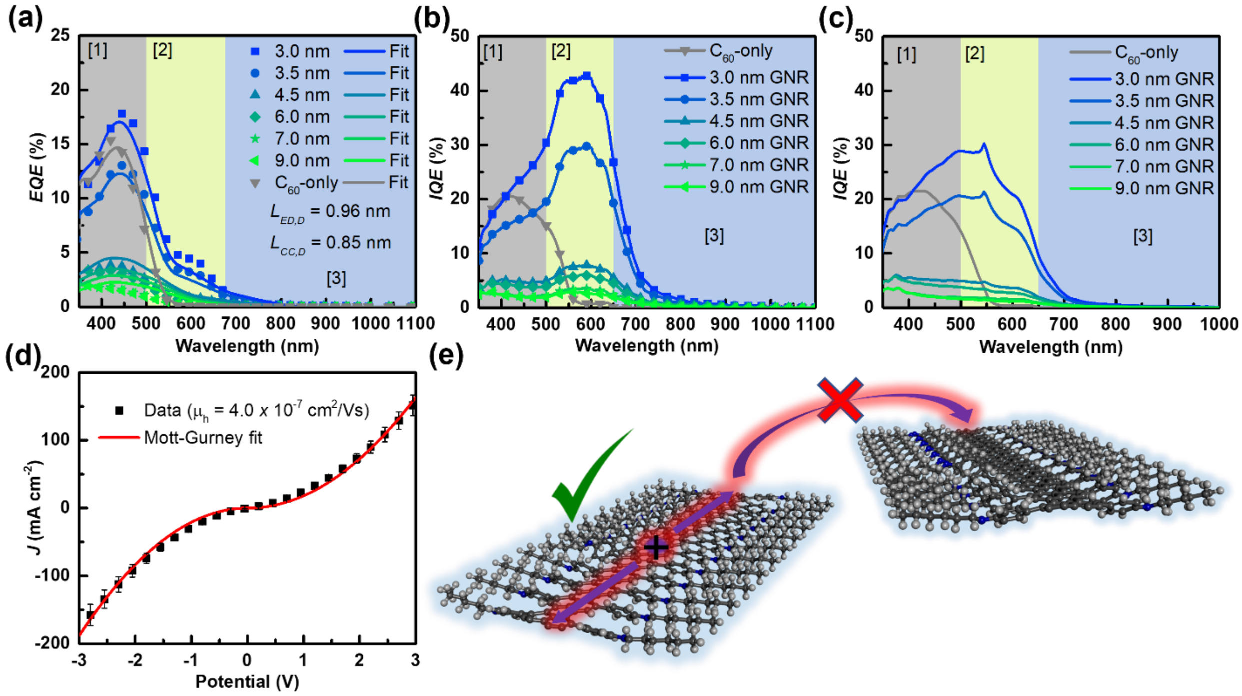

Figure 7.4. Calculation of exciton diffusion and charge collection lengths. (a) External quantum efficiency (*EQE*) thickness dependent data for increasing GNR thickness (data points). Simultaneous fits of GNR thickness dependent *EQE* from transfer matrix optical modeling with the characteristic lengths for exciton diffusion ($L_{ED,D}$) and charge collection ($L_{CC,D}$) of the GNR (solid lines). C_{60}-only device *EQE* was fitted separately (gray line). **(b)** Internal quantum efficiency (*IQE)* calculated from experimental *EQE* and absorption as a function of GNR thickness. **(c)** *IQE* calculated from experimental *EQE* and model generated absorption. **(d)** Hole only device data fitted with the Mott-Gurney equation for space charge limited current to extract the hole mobility for GNR thin films. **(e)** Schematic illustrating the likely cause of poor charge collection efficiency in bulk GNR films relative to the expected high conductivity from graphene-based materials. While hole mobility through a single ribbon's conjugated core may be excellent, experimental data and computational calculations demonstrate poor mobility when charges must transfer between ribbons. Error bars for holy mobility data calculated from the standard error.

the C_{60}-only device *EQE*. This effect is also observed in the thickness dependent J-V curves in both the forward slope (inversely proportional to the resistance) and the J_{SC} with increased GNR thickness, corroborating the observed *EQE* trends through Equation 1.7. *EQE* can be understood as the product of five component efficiencies (Equation 1.8), η_{A}, η_{ED}, η_{CT}, η_{DS}, and η_{CC}. The C_{60}-GNR junction is formed in the same manner for all GNR thicknesses and yields a thickness independent V_{OC}, indicative of minimal band bending and a consistent interface gap between the highest occupied molecular orbital (HOMO) of the GNR and the lowest unoccupied molecular

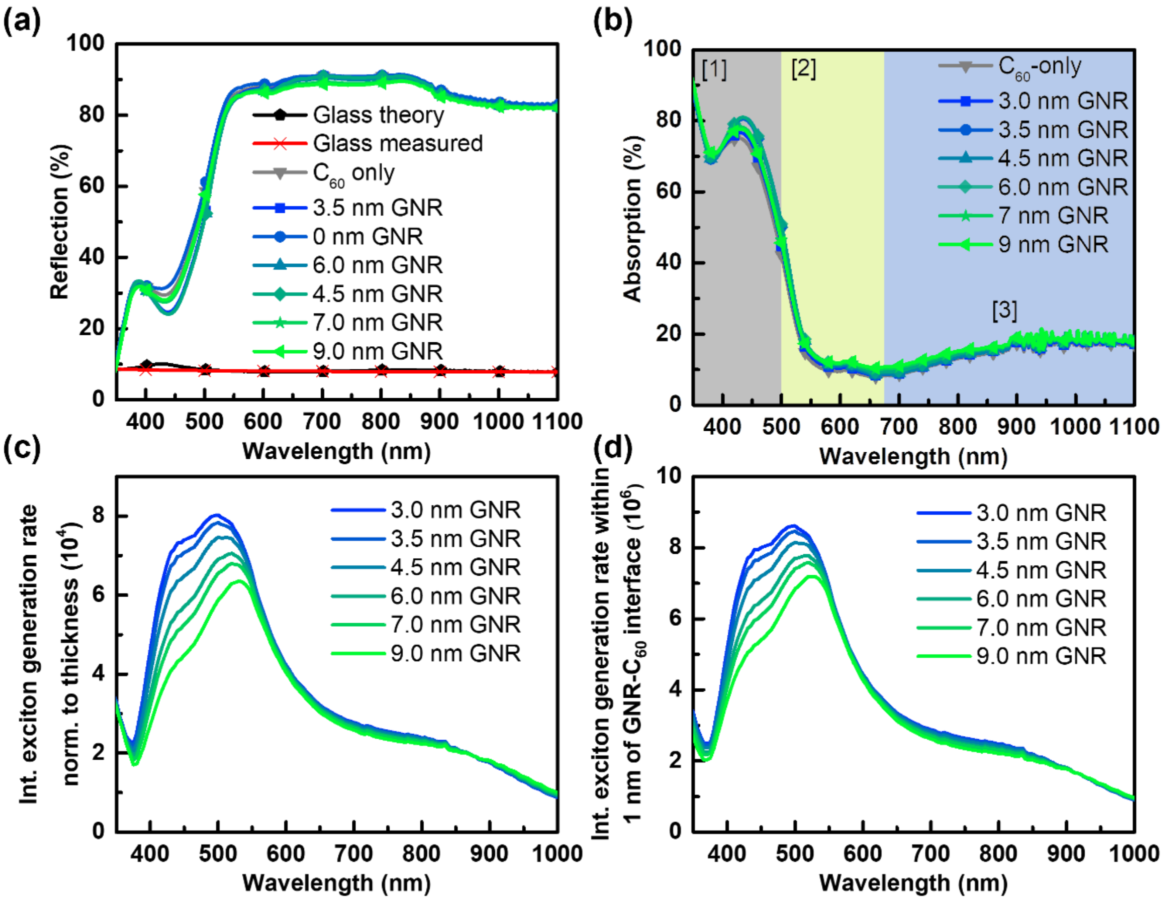

Figure 7.5. Reflection, absorption, and integrated exciton generation rate profiles. (a) Raw reflection data for full device stacks grown on 1.5” x 1.5” substrates used to calculate the device absorption as 100-reflection(%). **(b)** Absorption data (100 - %Reflection) for full device stacks grown on 1.5” x 1.5” substrates with increasing thickness of GNR from 3.0 to 9.0 nm (blue to green). The C_{60}-only device absorption is in gray. **(c)** Integrated exciton generation rates of the GNR layers normalized to the thickness of the layer as a function of wavelength. **(d)** Integrated exciton generation rates in the GNR layer within 1 nm of the GNR-C_{60} interface for different GNR thicknesses as a function of wavelength.

orbital (LUMO) of the C_{60}. Given a stable GNR bandgap, the LUMO-LUMO offset that controls exciton dissociation into free charge carriers will be consistent such that η_{CT} and η_{DS} are independent of GNR thickness. As the C_{60} thickness is constant, this leaves absorption, exciton diffusion, and charge collection losses in the GNR as remaining factors to explain the decrease in *EQE* across the spectrum. To examine the *EQE* trends independent of GNR and C_{60} absorption, we calculate the internal quantum efficiency (*IQE*) (Figure 7.4b) from Equation 1.8 using the experimentally measured *EQE* and absorption. Absorption for the entire device stack is obtained from the measured reflection as 100 – reflection(%) (Figure 7.5a) and used in place of η_A, the absorption efficiency of the active layers. Similar to the *EQE*, we observe three regions of *IQE* behavior, particularly for 3.0 and 3.5 nm GNR devices. In region 1, the *IQE* consists of excitonic and charge carrier processes originating in both the C_{60} and GNR. While *IQE* is generally independent of absorption effects, it can vary spectrally in two key ways. The *IQE* in region 1 is the result of component *IQE*s from the C_{60} and GNR depending on the location of photon absorption. Given the much stronger absorption of C_{60} in this regime (Figure 7.5b), the majority of excitons generated are in the C_{60} layer and thus the resulting overall *IQE* will be heavily weighted towards the efficiency with which excitons formed in C_{60} are extracted as free charge carriers. This analysis is validated by the similar *IQE* of the C_{60}-only and the 3.0 and 3.5 nm GNR devices in region 1. *IQE* increases rapidly for thin layers of GNR as it moves into region 2 as a result of the reversal of the absorption trend from region 1, where GNR now becomes the primary location for exciton formation. Thin layers of GNR allow for the moderately high *IQE*s observed in this region and the strong GNR thickness dependence of the *IQE* in regions 1 and 2 indicates large charge collection limitations that reduce photocurrent from the C_{60} and GNR. Charge collection and exciton diffusion efficiencies are generally independent of the exciting wavelength, which combined with the relatively flat absorption of GNRs would suggest that the *IQE* for a given GNR thickness should be consistent to the GNR bandgap. However, the *IQE* declines into region 3, and in this transition the primary location of exciton formation is still the GNR layer as it was in region 2. The second mechanism for absorption to impact the *IQE* is through optical interference effects, as the *IQE* can vary spectrally based on the location of exciton generation at each wavelength. Excitons generated nearer to a dissociating interface are more likely to successfully diffuse to the interface, increasing η_{ED}. Exciton generation rate is a function of the molecular

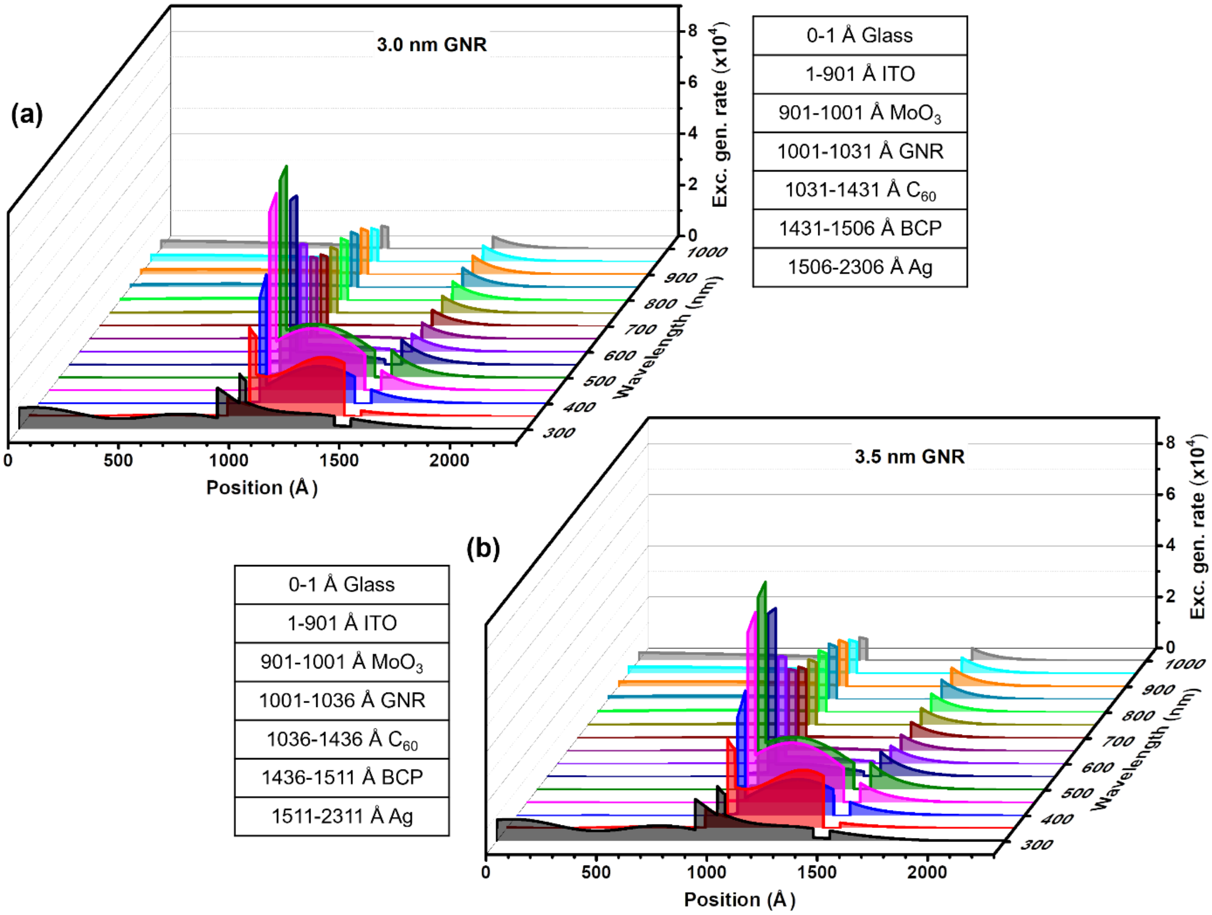

Figure 7.6. Exciton generation rate profiles for 3.0 and 3.5 nm GNR. Exciton generation rates in the **(a)** 3.0 nm and **(b)** 3.5 nm GNR device stack as a function of position and excitation wavelength.

extinction coefficient and the electric field, the latter of which depends in part on the overall device thicknesses. Altering the thickness of an active material can affect the *IQE* by enhancing exciton generation closer to the donor-acceptor interface for a given wavelength independent of the absorption efficiency. To understand the wavelength dependence of the *IQE* in region 3, we turn to transfer matrix optical modeling to calculate the exciton generation rate profiles (Figure 7.6, Figure 7.7, and Figure 7.8).[95] Integrating the exciton generation rate across the GNR layer and normalizing to the GNR thickness yields wavelength resolved profiles (Figure 7.5c) that show strong exciton generation peaking from 400 to 600 nm and then declining consistently to 1000 nm. However, exciton generation rates within 1 nm of the GNR-C_{60} interface (Figure 7.5d) demonstrate

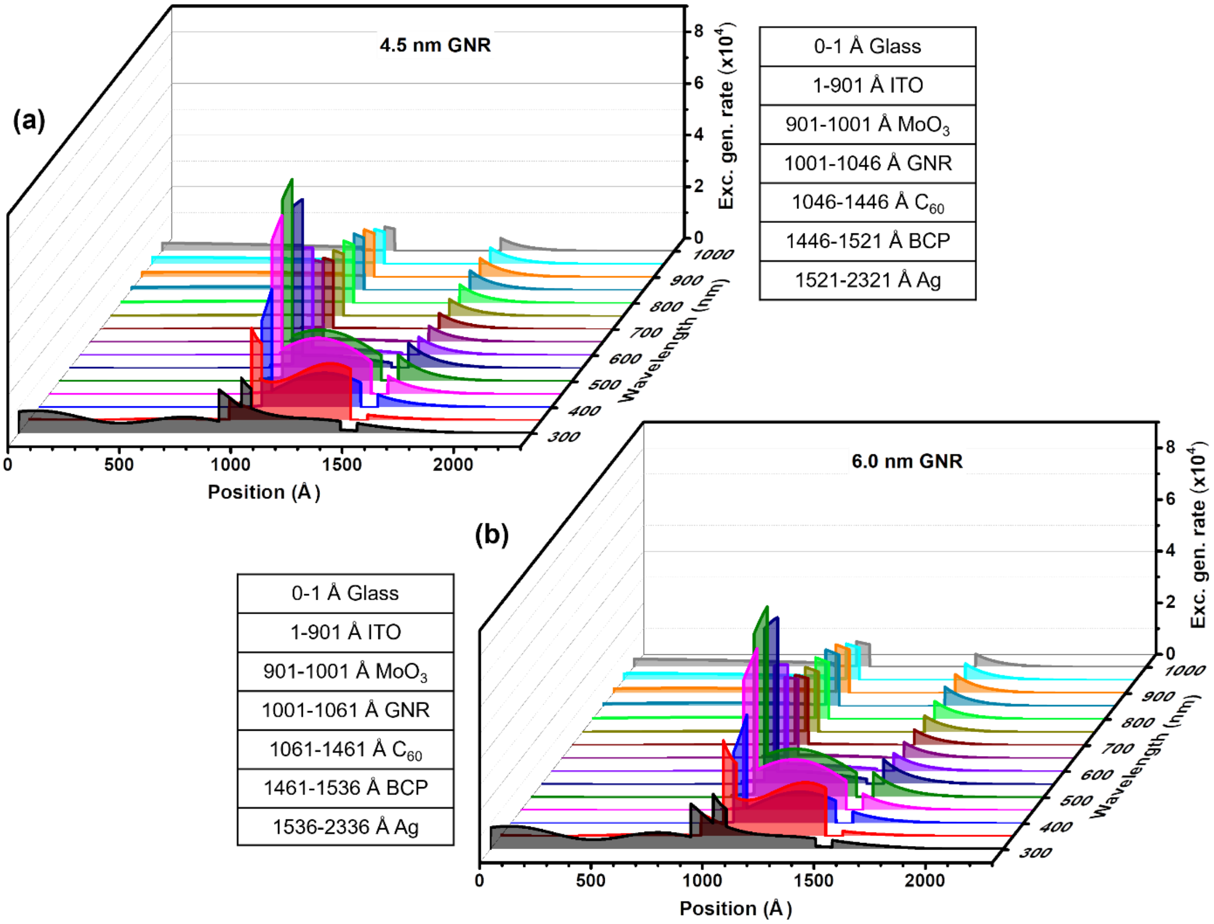

Figure 7.7. Exciton generation rate profiles for 4.5 and 6.0 nm GNR. Exciton generation rates in the **(a)** 4.5 nm and **(b)** 6.0 nm GNR device stack as a function of position and excitation wavelength.

the same overall trend, indicating that while there is heightened exciton generation in the VIS region, it does not lead to preferential generation closer to the interface and therefore will not increase η_{ED}. Enhanced exciton generation throughout the layer will impact the *EQE*, but does not explain the observed *IQE* behavior in region 3. The *IQE* behavior can however be explained by the increased parasitic absorption of the ITO electrode in the NIR, which causes the overall absorption to increase in the NIR (Figure 7.5b, region 3) and the *IQE* to steeply decrease. To investigate this explanation, we calculate the *IQE* using the optical model generated absorption and observe comparable *IQE* in regions 1 through 3 to the experimentally determined *IQE*, further validating this analysis (Figure 7.4c). For thicker GNR layers, the enhancement from favorable

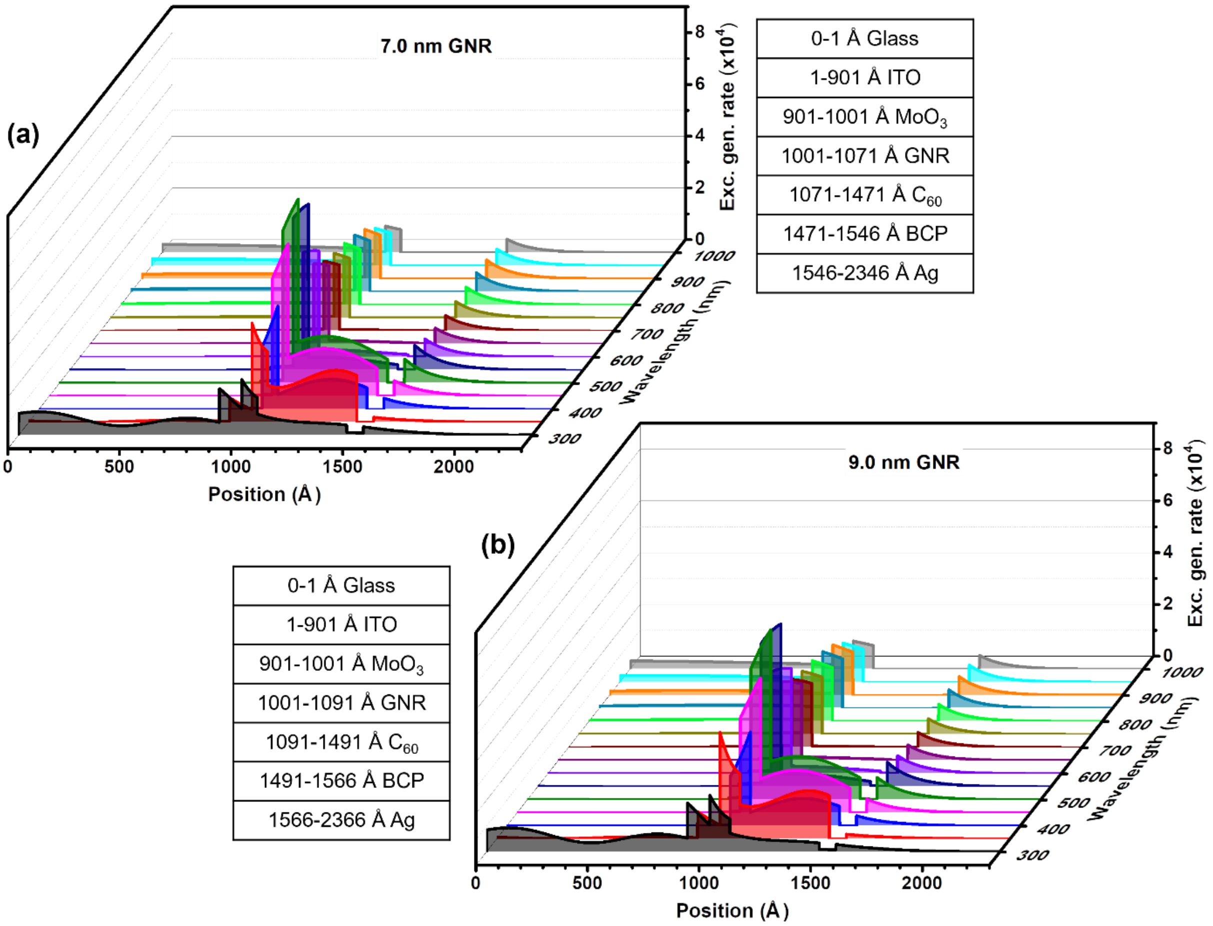

Figure 7.8. Exciton generation rate profiles for 7.0 and 9.0 nm GNR. Exciton generation rates in the **(a)** 7.0 nm and **(b)** 9.0 nm GNR device stack as a function of position and excitation wavelength.

exciton generation is overwhelmed by charge collection losses that sharply reduce the *IQE* and *EQE* across the spectrum, including from the C_{60}. To understand the extent of the limitations imposed by exciton diffusion and charge collection, we pair transfer matrix optical modeling with a nonlinear regression analysis to simultaneously fit the GNR thickness dependent *EQE* for the exciton diffusion length, $L_{ED,D}$, and charge collection length, $L_{CC,D}$, of the GNR.[3] The processes quantified by this model are specifically for exciton diffusion and charge collection occurring vertically through a bulk film of GNRs, and normal to a horizontally or near-horizontally oriented ribbon. Equations for each process are given in Equation 1.10 and Equation 1.18,[3] where d is the GNR thickness. The resulting fit is shown in Figure 7.4a, where the overall *EQE* decay trend with

GNR thickness is well matched by the model. Extracted characteristic lengths of 0.96 nm and 0.85 nm for $L_{ED,D}$ and $L_{CC,D}$ confirm the previous conclusions about the limitations in horizontally oriented GNR PVs and highlight charge collection and exciton diffusion as the key areas for improvement with these materials that would likely (and largely) be overcome with vertical alignment. Importantly, while $L_{ED,D}$ will limit current produced by the GNR, $L_{CC,D}$ limits photocurrent production from both the GNR and C_{60}, making charge collection the limiting factor for horizontally aligned GNR-based photovoltaic performance in this work. Given that a very large degree of anisotropy is expected, vertically oriented GNRs should show dramatically increased exciton diffusion and charge collection lengths.

7.2.3 Hole transport in graphene nanoribbons

To further understand the cause of charge collection losses in GNR based PVs, hole-only devices were fabricated on ITO coated glass substrates with a 20 nm GNR layer sandwiched between two 50 nm MoO_3 layers and capped with an 80 nm Ag top electrode. *J-V* curves were measured in the dark and fit with the Mott-Gurney equation (Equation 4.8) for space charge limited current after confirming *J-V* symmetry (no diode formation or built-in bias) between forward and reverse bias (Figure 7.4d). A hole mobility of $4.0 \pm 0.3 \bullet 10^{-7}$ $cm^2V^{-1}s^{-1}$ was extracted from the fitted data, further evidence of charge collection limitations seen in the *EQE* thickness dependent data. Given the nature of GNRs and other graphene-derived materials, the mobility is notably low. However, this is a measurement of a bulk film of GNRs with transport primarily occurring through stacks of nanoribbons (consistent with the PV device architecture) as opposed to the mobility in-plane of the GNR. The low mobility indicates that hole transport from ribbon to ribbon is not very efficient (Figure 7.4e), while the intra-ribbon transport is still likely to be very high. We estimate that GNR thickness variation from 3.0 nm to 9.0 nm increases the average number of ribbons

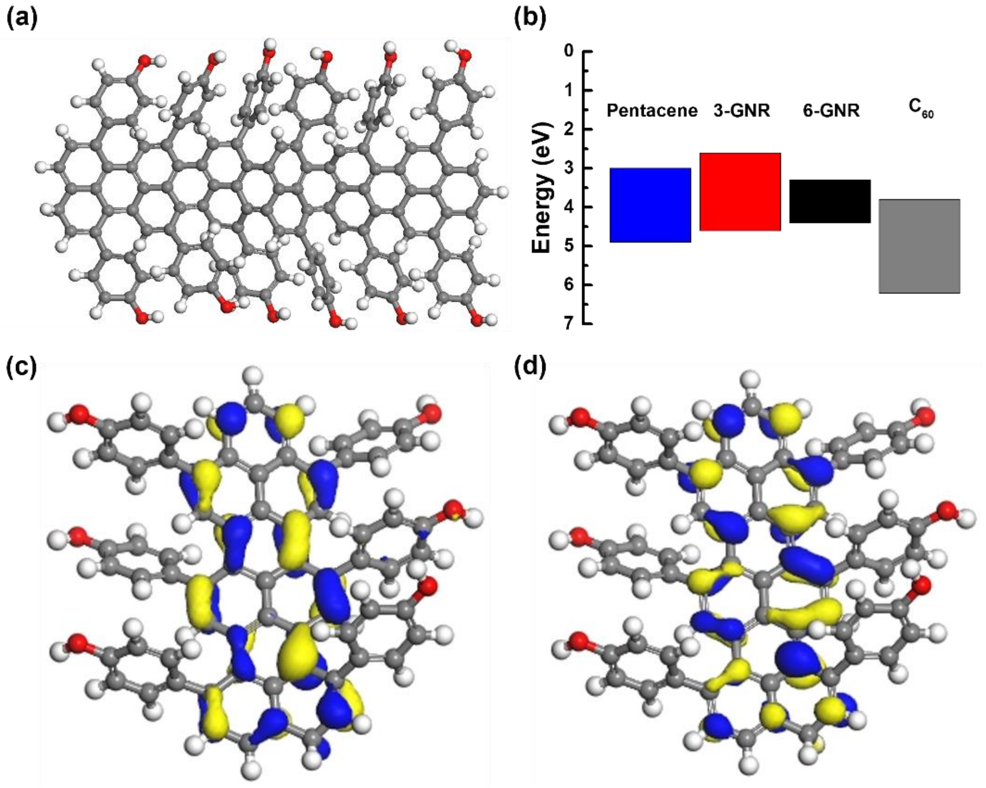

Figure 7.9. Calculation of graphene nanoribbon bandgap and molecular orbitals. (a) Graphene nanoribbon (GNR) used for computational calculations featuring six repeating units (6-GNR) and hydrogen terminated side chains at the oxygen atom. **(b)** Energy diagram of pentacene (control), a three-unit GNR (3-GNR), 6-GNR, and C_{60} bandgaps. Pentacene, 3-GNR, and 6-GNR bandgaps and highest occupied molecular orbital (HOMO) energy levels were adjusted based on pentacene values from literature,[226-227] while C_{60} values were pulled from literature.[90] **(c)** Calculated HOMO of 3-GNR. **(d)** Calculated lowest unoccupied molecular orbital (LUMO) of 3-GNR. The 3-GNR HOMO and LUMO demonstrate the conjugated pathway through the core of the GNR.

stacked in the layer from 9 to 27, assuming well aligned GNRs and a graphite layer separation of 0.335 nm. From this we conclude that inter-ribbon transport is only moderately efficient between fewer than 10 ribbons. Holes traveling between more ribbons face a higher chance of recombination and thus provide lower photocurrent across the solar spectrum. Poor inter-ribbon carrier mobility supports previous conclusions from *EQE* analysis that devices are limited by charge collection losses reducing the photocurrent from both C_{60} and GNRs.

7.2.4 Calculation of the GNR bandgap

The bandgap and frontier molecular orbital energy levels were calculated for GNRs consisting of 3 (3-GNR) and 6 (6-GNR, shown in Figure 7.9a) repeating units due to the large computational cost of the full GNR (~23 repeating units). The extension of the conjugated network from 3-GNR to 6-GNR narrows the bandgap, and after adjusting based on the pentacene control, results in a reasonable estimate for the 6-GNR electronic bandgap of 1.1 eV with a HOMO level at -4.4 eV relative to vacuum. Our calculated bandgap aligns well with the optical bandgap of 1.03 eV and the *EQE*, which shows photocurrent generation to 1050 nm (~1.18 eV).[189] Corrected orbital levels are shown in Figure 7.9b with the levels of C_{60}.[95] The interface gap between the 6-GNR HOMO and C_{60} LUMO is approximately 0.6 eV, yielding an expected voltage of 0.35 V from the SQ limit.[3] The measured V_{OC} of the GNR-C_{60} device (0.2 V) sits 0.15 V below the SQ limit and suggests a loss of 0.4 eV from the optical excitonic bandgap. Calculated HOMO and LUMO for 3-GNR are shown in Figure 7.9c and d, displaying the conjugated network at the core of the GNR.

7.3 Discussion

Graphene and nanostructured graphene derivatives make up an important class of emerging electronic and optoelectronic materials. In this work, we demonstrate graphene-based photovoltaics based on size constrained graphene nanoribbons. This is achieved by fabricating bilayer all carbon (photoactive layer) solar cells with GNR as a donor and C_{60} as an acceptor. Complimentary absorption profiles of the active materials allow us to clearly show GNR contributions to the photocurrent at wavelengths from 450 nm to past 1000 nm deep into the NIR. Devices were primarily limited by the large resistance of the GNR films that increased with thickness, evidenced by the decreasing slope of the forward current in *J-V* curves and declining *EQE* across the UV-VIS and NIR wavelengths. This resistance resulted in charge collection losses due to the small charge collection length and hole mobility of bulk GNR films. Increasing the arrangement of the ribbons (vertically as opposed to horizontally) in the film should improve carrier mobility and charge collection lengths dramatically that would then allow for devices with much thicker GNR layers. Indeed, properly oriented, vertically aligned GNRs synthesized in-situ from the electrode could be a route to achieving the necessary conductivity in a bulk GNR film. Moving forward, characterization and control over GNR orientation and the impact on device performance will be an important step to realizing the full potential of nanoscale graphene materials in these optoelectronic devices. To maximize PV performance, the energy level of the acceptor LUMO with respect to the GNR HOMO should be optimized so as to maximize the V_{OC} while still dissociating excitons at the donor-acceptor interface. As the bandgap size is near-optimal in existing ribbons, increasing the acceptor LUMO while maintaining a GNR bandgap of ~1 eV will be an important step and could be explored by varying acceptors, or even modifying the GRN HOMO with variations in electron donating and accepting capabilities of the side chains. We have successfully integrated photoactive graphene nanoribbons into photovoltaic devices and demonstrated light current production from the GNRs across the UV-VIS and NIR spectrums to the bandgap of the GNR. Utilizing experimental and computational techniques we identified the key area necessary to enhance the performance of GNRs in photovoltaics and provide a route forward to take full advantage of this exciting new class of materials.

7.4 Methods

7.4.1 GNR synthesis

The synthesis scheme is presented in Figure 7.2. All reactions dealing with air- or moisture-sensitive compounds were carried out in a dry reaction vessel under nitrogen. Anhydrous tetrahydrofuran (THF) and dichloromethane (DCM) were obtained by passing the solvent (HPLC grade) through an activated alumina column on a PureSolv MD 5 solvent drying system. ^{1}H and

^{13}C NMR spectra were recorded on Varian 400 MHz or Varian 500 MHz NMR Spectrometers. Spectra were recorded in deuterated chloroform ($CDCl_3$). Chemical shifts were referenced to the residual protio-solvent peaks (7.26 ppm for ^1H and 77.16 ppm for ^{13}C, respectively). Chemical shifts are reported in part per million (ppm) from low to high frequency and referenced to the residual solvent resonance. Coupling constants (J) are reported in Hz. The multiplicity of ^1H signals are indicated as: s = singlet, d = doublet, t = triplet, m = multiplet, br = broad. High resolution APPI mass spectra were recorded using an Agilent 6230 TOF MS. TLC information was recorded on Silica gel 60 F254 glass plates. Purification of reaction products was carried out by flash chromatography using Silica Gel 60 (230-400 mesh).

7.4.2 Device fabrication

Pre-patterned ITO coated glass substrates (Xin Yan) were cleaned via sequential sonication for 10 minutes in deionized water, acetone, and isopropanol. Substrates were dried on a hotplate at 100°C for one minute before plasma cleaning for 10 minutes. Cleaned substrates were loaded into an Angstrom Engineering thermal vapor deposition chamber and 10 nm of MoO_3 (Alfa Aesar) was deposited at a base pressure of $3E^{-6}$ torr. Graphene nanoribbons were dissolved in 1,2,4-trichlorobenzene (Sigma Aldrich) at concentrations from 0.5 to 5 $mgmL^{-1}$ and stirred overnight prior to use. GNR films were spin-coated on top of the MoO_3 at 2000 rpm to yield GNR thin films with thicknesses ranging from 3.0 to 9.0 nm as measured by variable angle spectroscopic ellipsometry (Woollam Ellipsometer) on Si substrates. Substrates with the GNR thin film were loaded into the deposition chamber where 40 nm of C_{60} (MER Corp.), 7.5 nm BCP (Luminescence Technology, Inc.), and 80 nm Ag (Kurt J Lesker Co.) were deposited to complete the device stack. A special mask was used for Ag deposition to define an active area of 4.43 mm^2. Control devices were fabricated as described above without the GNR layer.

7.4.3 Device testing

Current-voltage (*J-V*) curves were acquired under illumination from a Xe arc lamp with intensity calibrated to 1-sun with a NREL-calibrated Si reference cell with KG5 filter. External quantum efficiency (*EQE*) measurements were made with monochromated light from a tungsten halogen lamp chopped at 200 Hz. A Newport-calibrated Si diode was used to calibrate the system prior to taking *EQE* measurements. Error bars for *J-V* plots represent the standard deviation of a minimum of five devices for each GNR thickness.

7.4.4 Optical measurements

Large area ITO coated glass substrates (1.5” x 1.5”) were cleaned via sequential sonication for 10 minutes in deionized water, acetone, and isopropanol. Substrates were dried on a hotplate at 100°C for one minute before plasma cleaning for 10 minutes. The full device stack was created on the substrates as described in the device fabrication section. A Perkin Elmer Lambda 900 UV/VIS/NIR spectrometer was used to make reflection measurements of the devices. The reference slot was empty for the measurements. For solution measurements, GNRs were dissolved in 1,2,4-trichlorobenzene at 0.01 to 0.5 $\mathrm{mgmL^{-1}}$ and a quartz cuvette was used as a solution holder. The reference slot was filled with pure 1,2,4-trichlorobenzene in a second cuvette.

7.4.5 Hole mobility measurements

Hole only devices were fabricated on the same ITO printed glass substrates (Xin Yan) used for devices. 50 nm MoO_3 (Alfa Aesar) was grown on the substrates at $3E^{-6}$ torr after sonication and plasma cleaning. 10 $\mathrm{mgmL^{-1}}$ GNR in 1,2,4-trichlorbenzene (Sigma Aldrich) was spun at 2000 rpm to give 20 nm films. 50 nm MoO_3 was grown on top of the GNR and finally 80 nm Ag (Kurt J Lesker Co.) was grown using a mask to define the active area of 4.43 mm^2. *J-V* testing was performed in the dark by sweeping the voltage from -3 to 3 V. OriginPro was used to fit the device data with the Mott-Gurney equation for Space Charge Limited Current and extract the hole mobility.

7.4.6 Optical modeling

Transfer matrix modeling was performed in MATLAB to calculate absorption and *EQE* based on the device structure and optical constants obtained from ellipsometry.[95] The electric field and exciton generation rate were calculated as a function of wavelength and position within the device stack. Charge collection and exciton diffusion length analysis based on *EQE* fitting was done simultaneously for all GNR thickness dependent *EQE* data.[3]

7.4.7 GNR bandgap calculations

Materials Studio was used to calculate the bandgap and orbital energy levels of pentacene and GNR with 3 and 6 repeating units. GNR side chains were hydrogen terminated at the oxygen atom. This assumption was made based on the understanding that side chains are implemented for solubility and should not affect the conjugated network of sp^2 hybridized carbon that makes up the GNR core and the frontier molecular orbitals. Chemical structures were made in BIOVIA Draw and imported to Materials Studio. Forcite geometry optimization calculations were run first on each structure with a universal forcefield. DMol3 energy calculations were run at medium quality with a DND basis set and a variety of functionals including GGA-PBE with Grimme DFT-D corrections, B3LYP with Grimme DFT-D corrections, m-GGA M06-L, and LDA PWC. GGA-PBE with Grimme produced the most accurate results and was used for the calculations reported in this work. Pentacene was used as a control compound, with an established bandgap of 1.9 eV and HOMO at -4.9 eV,[233,234] that features a chain of sp^2 hybridized carbon. Pentacene was calculated to have a bandgap of 1.1 eV and a HOMO level of -4.04 eV, yielding a bandgap correction factor of 1.75, and a HOMO shift of -0.86 eV for the GNRs studied computationally.

3-GNR and 6-GNR had calculated bandgaps of 1.15 and 0.64 eV, and corrected bandgaps of 2.0 and 1.1 eV. This underestimation of the GNR bandgap in calculations was previously observed by Nguyen et al., whose experimental bandgaps of a chevron GNR and a fluorenone GNR were 2.53 and 2.33 eV, respectively, while the calculated bandgaps were 1.6 and 1.4 eV.[235]

Chapter 8 – Photodynamic Therapy and Fluorescent Imaging with Organic Salts

This chapter was published in *Scientific Reports* as "Modulating cellular cytotoxicity and phototoxicity of fluorescent organic salts through counterion pairing".[143] The research presented here was carried out in collaboration with Dr. Deanna Broadwater, who performed the in vitro and in vivo work.

8.1 Introduction

Previous work with cationic cyanine-based organic salts in PVs (discussed in Chapter 3) had revealed that the counterion could precisely tune the HOMO energy level by up to 1 eV in solid state films.[94,101] Motivated by this discovery, we sought to investigate the effect of the counterion in photodynamic therapy (PDT) and the impact of counterion energy tuning on cellular cytotoxicity (toxicity without light) and phototoxicity (toxicity with light treatment).

Fluorescent dyes offer great potential as both diagnostic and therapeutic agents, and the combined application has been termed "theranostics". These compounds can be used to improve cancer diagnoses, assist with image-guided surgery, and treat tumors by PDT. Ideal theranostic agents localize in tumors and become activated by a specific wavelength of light to either emit a different wavelength of light that can be detected for imaging, or generate reactive species for PDT.[236,237] PDT provides double selectivity through the use of both the dye and light, with the goal of minimizing side effects from the dye or light alone.[238] To realize the full potential of fluorescent dyes in biomedical applications, it is necessary to increase their brightness and tissue penetration in order to detect and treat deeply-embedded tumors, while also eliminating unwanted side effects. Fluorescent dyes that absorb and emit in the near-infrared (NIR) range offer several advantages for both PDT and *in vivo* imaging applications. While visible light (400–650 nm) travels only millimeters in tissues, NIR light (650–1200 nm) can travel centimeters,[239] and 810

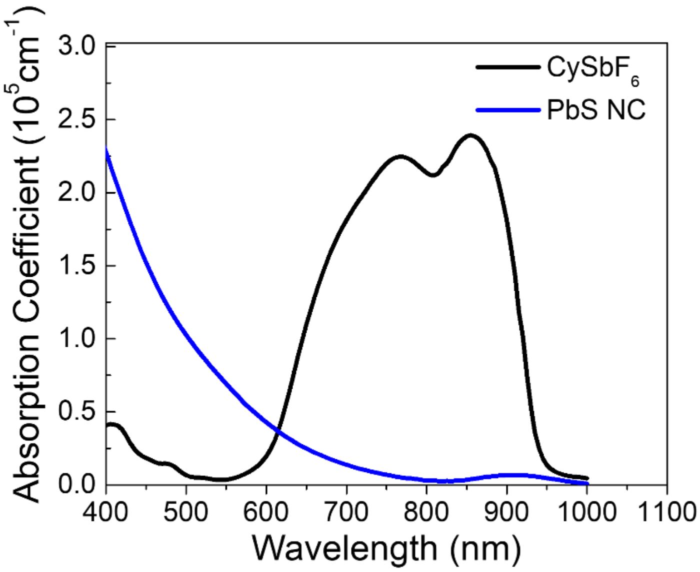

Figure 8.1. Absorption coefficients of an organic salt and nanocrystal. The organic salt (CySbF6) has an absorption coefficient that is orders of magnitude larger than that of the nanocrystal (PbS NC) at wavelengths in the near-infrared around the bandgap (650-950 nm).

nm and 980 nm NIR light have been shown to penetrate 3 cm of skin, skull, and brain tissue.[240] Additionally, visible light absorbance by endogenous biological fluorophores such as heme and flavin groups causes autofluorescence and weak signal intensity.[241] On the other hand, NIR light is minimally absorbed by biological material, drastically reducing background noise and increasing penetrance.[242,243] FDA-approved NIR-responsive fluorescent dyes including indocyanine green, 5-aminolevulinic acid, and methylene blue are available and used in medical diagnostics,[244] but are limited due to their low level of brightness. Other commercially available NIR-responsive fluorescent dyes include heptamethine cyanine (Cy7), Alexa Fluor 750, and heptamethine dye IR-808.[245–247] However, these dyes display low brightness, high toxicity, and poor aqueous stability.[248] Recent PDT-based nanocrystals show energy level tunability via surface ligand modification but have poor biocompatibility due to heavy elements and minute absorbance in the NIR range that stem from a lack of oscillator strength near their bandgap. For example, semiconductor nanocrystals have absorption coefficients of ~10^3/cm for PbS and PbSe compared to ~10^6/cm for cyanines with bandgaps around 850 nm – this translates to 1000 times less absorption per nanometer of material by nanocrystals (Figure 8.1). Fluorescent organic salts, composed of a fluorescent ion and a counterion, have been developed to increase aqueous solubility and photostability.[249,250] The counterion has largely been thought to have little impact on the properties of the fluorescent organic salts. Only a few reports have investigated the impact of the counterion, but have been limited to encapsulated matrices for modestly increasing the quantum yield,[251–254] or have shown no impact on toxicity.[255,256] The latter study investigated two anions with a visible rhodamine dye, but showed no significant difference in cell viability between the two key anions in a range of cell lines (Hs578Bst, Hs578T, and MDA-MB-231) and did not investigate phototoxicity.[255] Here, we focus on NIR-responsive polymethine cyanine dyes, which have been used as effective theranostic agents.[245,257] Heterocyclic polymethine cyanine dyes have been found to preferentially accumulate in tumors and circulating cancer cells even in the absence of bioconjugation to tumor-targeting molecules.[258] This is thought to occur through a mechanism mediated by increased expression of organic anion transporter peptides (OATPs) and hypoxia-inducible factor 1-alpha (HIF1α), both of which are upregulated in cancer cells.[259] HIF1α promotes tumor angiogenesis and expression of OATPs, which facilitate the uptake of polymethine cyanine dyes,[260] as shown by competitive inhibition of OATP1B3.[257] Lipophilic photosensitizers may also associate into circulating low-density lipoproteins (LDLs) and be imported by cells via ATP-mediated endocytosis.[261] Charged molecules taken up by the cell accumulate in negatively charged organelles such as mitochondria and lysosomes, where light irradiation can induce generation of reactive oxygen species (ROS).[262] While the exact mode of uptake and localization varies depending on the chemical characteristics of any given photosensitizer, these mechanisms are uniquely active in tumor cells, leading to tumor-specific accumulation and retention.[263] Cellular toxicity of fluorescent molecules is caused by the

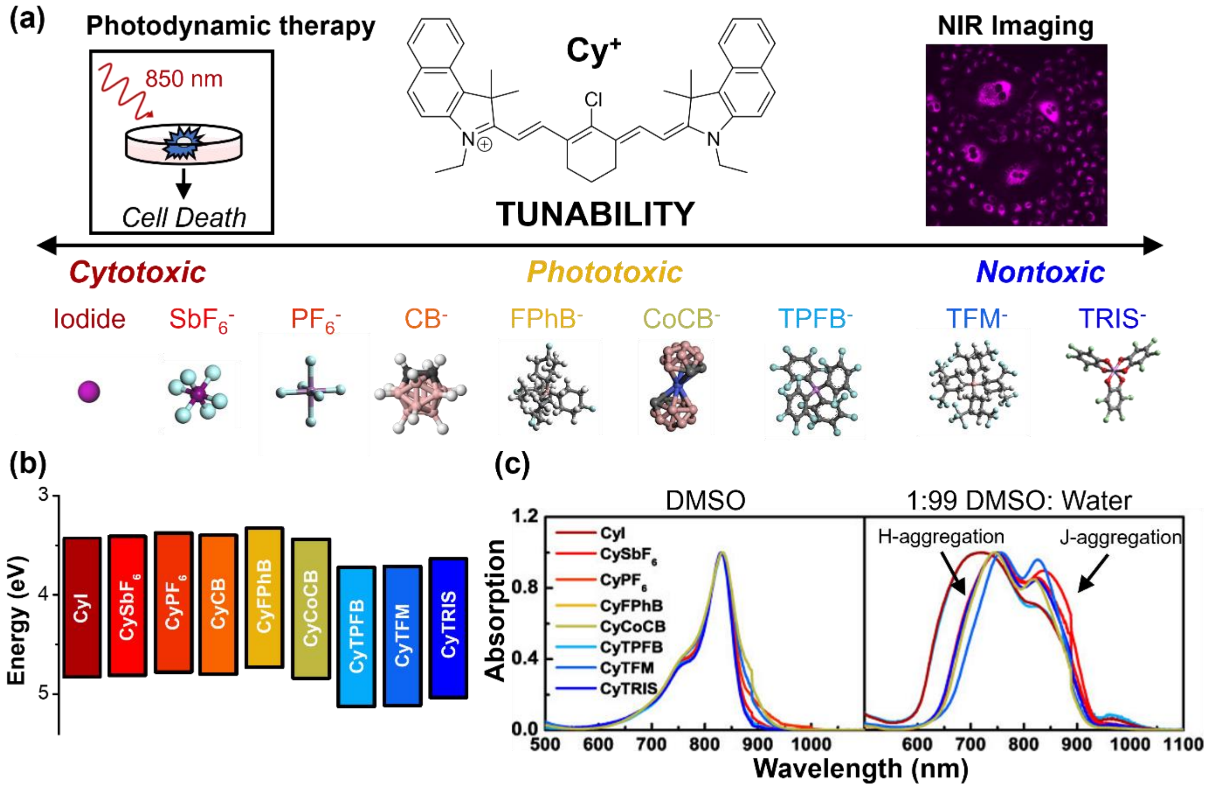

Figure 8.2. Cyanine (Cy^+) with varying counterions enables tunable cellular toxicity. (a) Anions on the left are generally cytotoxic, anions in the middle are selectively phototoxic and ideal for applications in photodynamic therapy, and anions on the right reduce toxicity for applications in fluorescence imaging. Anions: Iodide (I^-); hexafluoroantimonate (SbF_6^-); hexafluorophosphate (PF_6^-); o-carborane (CB^-); tetrakis(4-fluorophenyl)borate ($FPhB^-$); cobalticarborane ($CoCB^-$); tetrakis (pentafluorophenyl) borate ($TPFB^-$); tetrakis[3,5-bis(trifluoro methyl)phenyl]borate (TFM^-); Δ-tris(tetrachloro-1,2-benzene diolato) phosphate(V) ($TRIS^-$). **(b)** The counterion shifts the HOMO energy level while allowing the interference band gap to remain the same. Ultraviolet photoelectron spectroscopy (UPS) was used to measure the frontier energy levels of Cy^+ with indicated counterion pairings in the solid state. Data extracted from Suddard et al[29] and Traverse et al[31]. **(c)** Fluorescent organic salts aggregate in aqueous environments. Organic salts fully dissolved in DMSO have a clear maximum at 830 nm with a leading shoulder when characterized with UV-Vis spectroscopy. However, in aqueous solution combinations of H- and J-aggregation of organic salts can be seen by blue-shifted peaks (lower wavelength) and red-shifted peaks (higher wavelength), respectively.

combination of: (1) cytotoxicity – toxicity in the dark, independent of photoexcitation; and (2) phototoxicity – toxicity with light illumination, or photoexcitation. While the tumor-specific accumulation of polymethine cyanine dyes reduces their nonspecific toxicity, low levels of systemic toxicity remain due to the cytotoxicity of unexcited molecules.[263] For applications in tumor imaging, both cytotoxicity and phototoxicity need to be eliminated to minimize side effects.

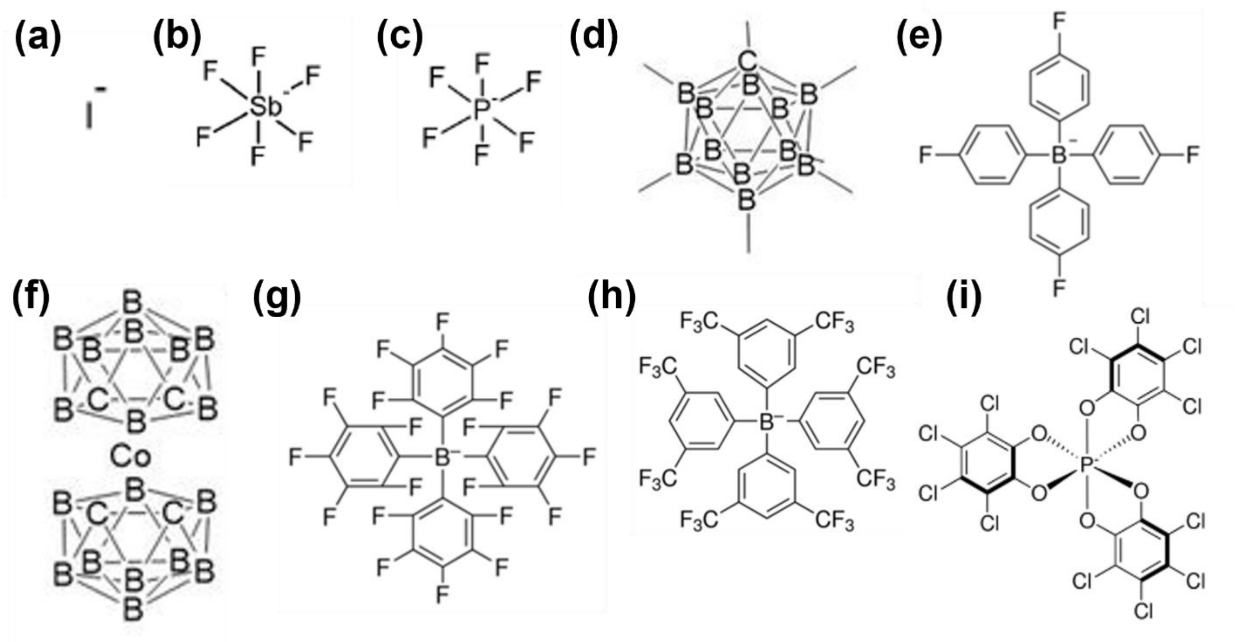

Figure 8.3. Molecular structures of anions investigated in the study. (a) Iodide (I^-) **(b)** Hexafluoroantimony (SbF_6^-) **(c)** Hexafluorophosphate (PF_6^-) **(d)** O-carborane (CB^-) **(e)** Tetrakis(4-fluorophenyl)borate ($FPhB^-$) **(f)** Cobalticarborane ($CoCB^-$) **(g)** Tetrakis (pentafluorophenyl) borate ($TPFB^-$) **(h)** Tetrakis[3,5-bis(trifluoro methyl)phenyl]borate (TFM^-) **(i)** Δ-Tris(tetrachloro-1,2-benzene diolato) phosphate(V) ($TRIS^-$).

For applications in PDT, cytotoxicity must be eliminated, while phototoxicity should be enhanced to selectively kill cancer cells with targeted light therapy. We recently reported that a range of weakly coordinating anions can modulate frontier molecular orbital levels of a photoactive heptamethine cyanine cation (Cy^+) in solar cells without changing the bandgap.[94,95] Thus, we are able to control the electronics (i.e. frontier molecular orbitals) of photoactive molecules independently from their optical properties (i.e. bandgaps). We have subsequently employed this electronic tunability to demonstrate cyanine-based organic salt photovoltaics with >7 year lifetime under typical solar illumination.[102] Here, we demonstrate the impact of the counterion on independently controlling both cytotoxicity and phototoxicity of fluorescent organic salts in cancer cells for enhanced imaging and improved PDT (Figure 8.2a). We achieve this by pairing the NIR-absorbing Cy^+ with various dipole-modulating counterions, and characterizing their effect on human lung carcinoma and metastatic human melanoma cell lines. We find that counterion

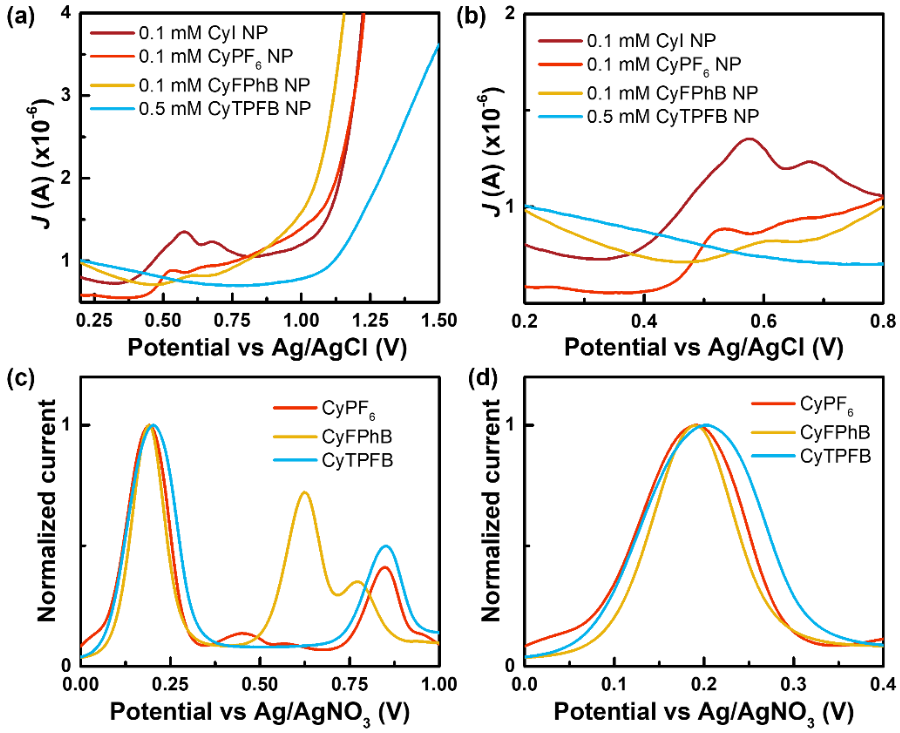

Figure 8.4. Differential pulse voltammetry measurements. (a, b) Nanoparticles (NPs) of the salts at 0.1 mM in 10% DMSO (CyI, CyPF$_6$) and 50% DMSO (CyFPhB) in water. CyTPFB NPs have greater solubility and were tested at 0.5 mM in 50% DMSO. **(c, d)** Monomer solutions of a representative cytotoxic, phototoxic, and nontoxic salt in acetonitrile. None of the differential pulse voltammetry measurements were performed in the presence of cells. Monomers demonstrate similar initial oxidation peaks, while nanoparticles have different peak locations. The CyTPFB nanoparticle oxidation peak is outside the redox window available for DMSO/H$_2$O mixtures. A lower peak potential for CyPF$_6$ compared to CyI and the shift out of the redox window for CyTPFB match anionic effects on the HOMO level shown in the solid state with UPS and correlated to redox levels. CyFPhB nanoparticles show a shift but do not fit the expected redox-HOMO trend. Monomers do not display this trend because their electronic environments are identical after dissociation due to the supporting electrolyte's higher concentration. DMSO/water solutions were measured with a Ag/AgCl reference electrode (-45 mV vs SCE), acetonitrile with a Ag/AgNO$_3$ electrode (0.36 V vs SCE).

pairings with small hard anions lead to high cytotoxicity even at low concentrations. In comparison, counterion pairings with bulkier, halogenated anions can remain nontoxic even at 20x higher concentrations. We further report a distinct intermediate group of anion pairings that are highly phototoxic, but exhibit negligible cytotoxicity, making them ideal photosensitizers for PDT. This concept of tuning the cytotoxicity and phototoxicity of fluorescent organic salts is a new platform for controlling the photoexcited interactions at the cellular level. It opens new

Table 8.1. Zeta potential changes as a function of counterion pairing. Zeta potential of organic salt nanoparticles was calculated from electrophoretic mobility.

Salt	Zeta potential [mV]
CyI	32.87 ± 5.03
$CyPF_6$	30.00 ± 2.13
$CySbF_6$	27.97 ± 0.55
CyFPhB	-29.93 ± 0.95
CyCoCB	-18.53 ± 3.63
CyTPFB	-61.87 ± 1.66
CyTFM	-51.37 ± 2.19
CyTRIS	-32.40 ± 1.93

opportunities for greater tissue penetration and the potential for minimizing side effects. Moreover, this approach may be applied to both novel and existing luminophores, including assembled fluorescent probes, phosphors, nanocrystals, and other hybrid nanoparticles.[264–268]

8.2 Characterization of fluorescent organic salts

Heptamethine cyanine cation (Cy^+, Figure 8.2a) is a photoactive cation that absorbs and emits in NIR wavelengths, with a bandgap of 1.3 eV (Figure 8.2b). A range of anions were tested with Cy^+ and $Cy7^+$ based on our previous studies that demonstrated a full range of valence energy levels tailored by over 1 eV.[94,101,102] These include: hard anions iodide (I^-), hexafluoroantimonate (SbF_6^-), and hexafluorophosphate (PF_6^-), o-carborane (CB^-); and bulkier soft anions tetrakis(4-

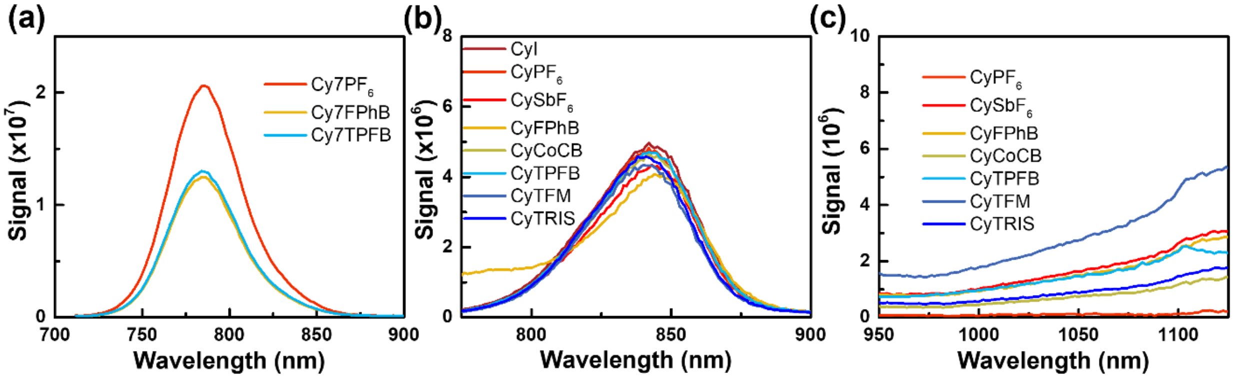

Figure 8.5. Photoluminescence measurements of Cy7X and CyX salts. Absolute scale, background corrected photoluminescence spectra for **(a)** 1 μM Cy7X monomers in DMSO, **(b)** 5 μM CyX monomers in DMSO, and **(c)** 2.5 μM CyX nanoparticles in 1:99 DMSO:H_2O.

Table 8.2. Quantum yields for monomer CyX and Cy7X salts.

Salt	Quantum yield [%]
Cy7PF$_6$	26
Cy7FPhB	26
Cy7TPFB	23
Cy7TRIS	24
CyI	1.7
CyPF$_6$	2.7
CySbF$_6$	1.7
CyFPhB	1.9
CyCoCB	1.4
CyTPFB	2.5
CyTFM	1.4
CyTRIS	1.9

fluorophenyl)borate (FPhB$^-$), cobalticarborane (CoCB$^-$), tetrakis(pentafluorophenyl)borate (TPFB$^-$), tetrakis[3,5-bis(trifluoro methyl)phenyl] borate (TFM$^-$), and Δ-tris(tetrachloro-1,2-benzene diolato) phosphate(V) (referred to as Δ-TRISPHAT$^-$, further abbreviated as TRIS$^-$) (Figure 8.3). The counterion causes distinct shifts in the highest occupied molecular orbital (HOMO) energy levels of heptamethine cyanine salts without changing the size of the bandgap in the solid state (Figure 8.2b). These changes to energy level are found to be consistent for salt nanoparticles in aqueous solution by measuring shifts to the redox potential and zeta potential (Figure 8.4a-b, Table 8.1), both of which have been correlated to HOMO.[125,269] The optical properties of the different ion-counterion pairings remain the same, with equivalent quantum yields and absorbance/emission spectra (Figure 8.2c, Figure 8.5, Table 8.2). In DMSO, fully dissolved

Table 8.3. CyX salt solubility in water and DMSO:H$_2$O mixtures.

Salt	Solubility in water [mg mL^{-1}]	Nanoparticle solubility in 50:50 DMSO:H$_2$O [mg mL^{-1}]
CyI	7×10^{-5}	-
CyPF$_6$	5×10^{-5}	-
CyFPhB	2×10^{-5}	0.1
CyCoCB	2×10^{-5}	0.05
CyTPFB	7×10^{-5}	2.5
CyTFM	1×10^{-4}	0.05

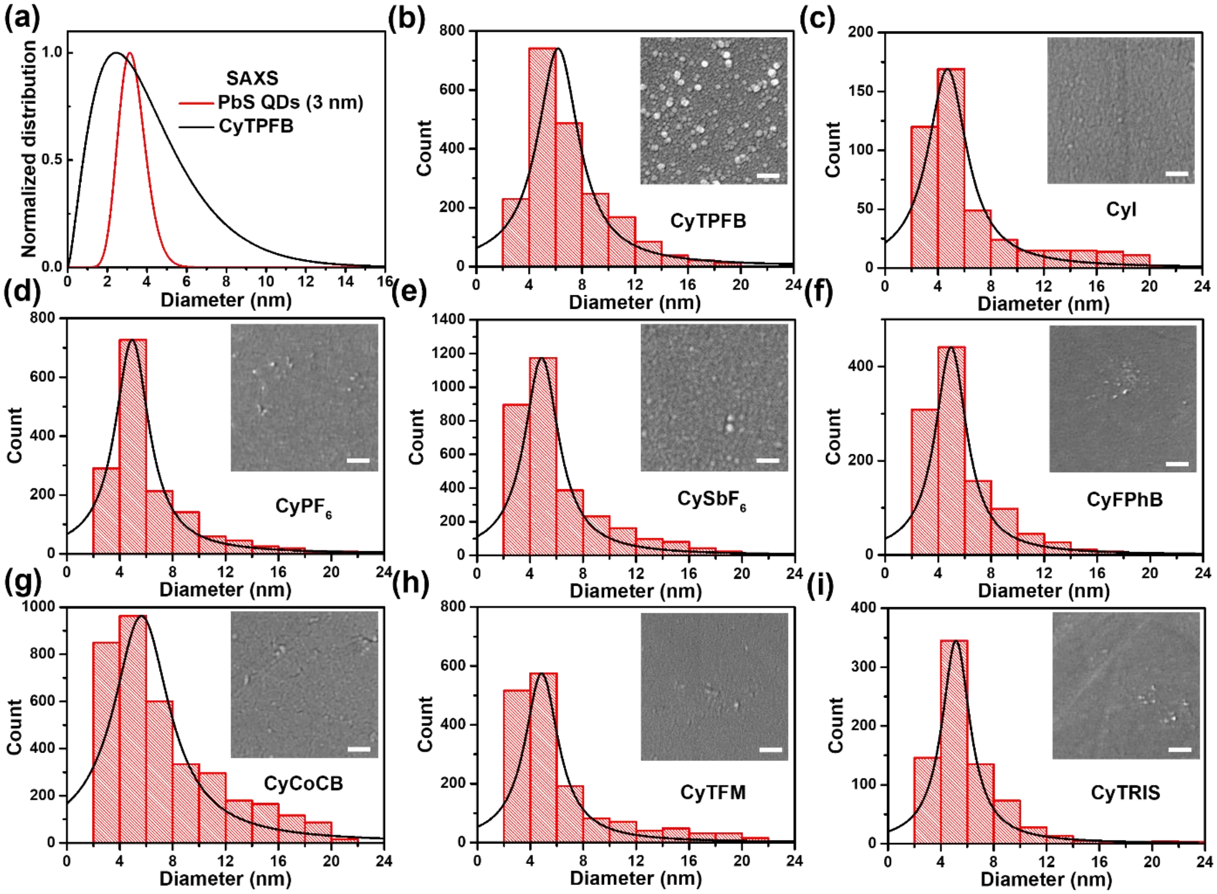

Figure 8.6. Nanoparticle size distribution is similar for all nanoparticles. (a) Nanoparticle aggregation size distribution measurements from SAXS measurements of CyTPFB. Mean particle size is 4.1 ± 0.6 nm. PbS quantum dot size distribution is shown as a control with a nominal size of 3 nm. **(b-i)** Nanoparticle size distribution measurements from SEM images (inset, scale bar = 100 nm) of CyX. Mean aggregate size ranges from 5 to 9 nm with no observable precipitation. Other salts were examined with SAXS but did not produce usable data because of solubility limitations. SAXS requires at least 1 mg/mL of the material of interest, and such concentrations are only obtainable with CyTPFB.

salt monomers display a major peak at 833 nm and a minor shoulder at 764 nm (and no observable shifts in redox potential between various salts as shown in Figure 8.4c-d). Organic salt nanoparticles were formed by diluting these solutions in mixtures of dimethyl sulfoxide and water (DMSO:H_2O). All of the organic salts formed soluble nanoparticles with this approach, which is expected due to their similar solubilities in water (Figure 8.2c, Table 8.3). In aqueous solution, the nanoparticles exhibit distinct peak broadening from the major peak and the minor shoulder. The

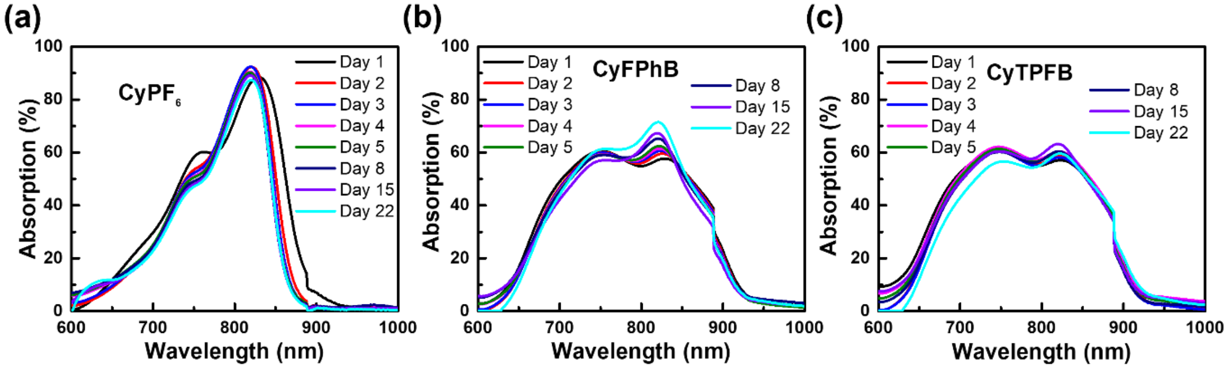

Figure 8.7. Nanoparticle lifetime and stability. $CyPF_6$ does not form nanoparticles in cell media but nonetheless demonstrates a stable chromophore. Lifetime absorption (100-%T) data collected with UV-Vis spectroscopy for **(a)** 5 µM $CyPF_6$, **(b)** CyFPhB, and **(c)** CyTPFB in cell media. All three solutions were measured daily for 5 days and again at 8, 15, and 22 days.

hypsochromic shift of the 764 nm shoulder peak and a bathochromic shift of the 833 nm peak are indicative of both H- and J-aggregation during the nanoparticle formation process. Nanoparticle organization limits the availability for exchange of the ions and preserves salt composition. Nanoparticle size of a typical bulky pairing (CyTPFB) was characterized by small-angle X-ray scattering (SAXS): the mean particle size is 4.1 ± 0.6 nm (Figure 8.6a), a size that is easily taken up by cells.[270] This data was corroborated using scanning electron microscopy (SEM) (Figure 8.6b). Additional nanoparticle size distributions were measured using SEM, and all counterion pairings display similar nanoparticle sizes ranging from 5 to 9 nm (Figure 8.6c-i). Lifetime experiments confirmed that nanoparticle formation remains stable, with no sign of decomposition into monomers for at least 22 days. The nanoparticles also demonstrated colloidal stability, showing no signs of sedimentation or aggregation over the same period (Figure 8.7).

8.3 Tunable cellular toxicity

Human lung carcinoma (A549) and metastatic human melanoma (WM1158) cell lines were used as representative models of two distinct cancer types with increased expression of OATP1B and OATP1B3 but have limited treatment options.[271,272] Cells were treated with multiple Cy^+-anion pairings by diluting organic salts with cell media to generate self-forming nanoparticles.

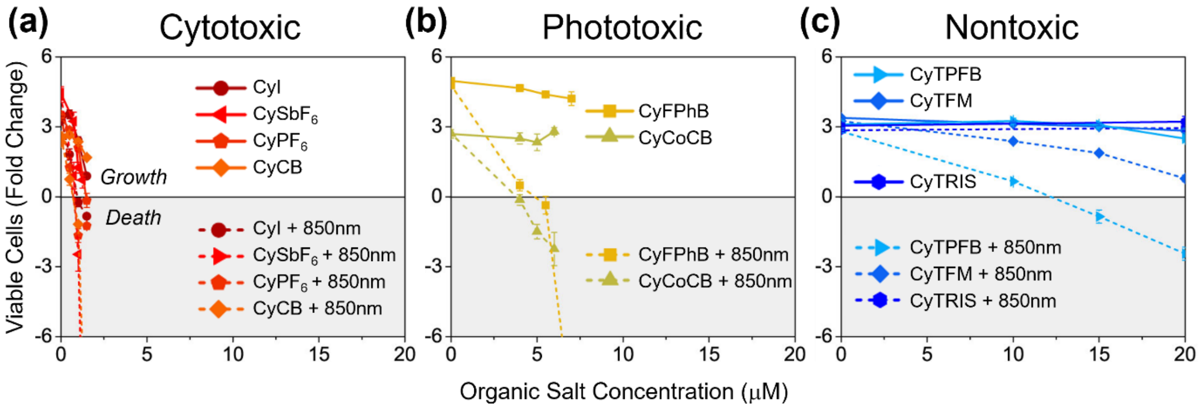

Figure 8.8. Organic salts with tunable toxicity can be used to target human cancer cells. (a) In A549 cells, CyI, CySbF$_6$, CyPF$_6$, and CyCB (red/orange) are toxic at low concentrations (1 μM), and cell death occurs independent of light excitation (cytotoxic). **(b)** CyFPhB and CyCoCB (yellow/green) do not display significant toxicity without light activation, but when photoexcited they induce significant cell death (phototoxic). **(c)** CyTPFB, CyTFM, and CyTRIS (blue) display low toxicity with and without light (nontoxic). Data are displayed as means ± S.E.M., *n* = 3.

Cells were incubated with various concentrations of the salt nanoparticles with or without 850 nm light to assess cytotoxicity in the dark and phototoxicity with 850 nm irradiation. Cell viability assays show that Cy$^+$ is cytotoxic at 1 μM for A549 cells even without exposure to NIR light when paired with small hard anions such as I$^-$, SbF$_6^-$, or PF$_6^-$, and only slightly more phototoxic when exposed to light (Figure 8.8a). In contrast, pairings with anions such as FPhB$^-$ and CoCB$^-$ have little cytotoxicity for concentrations below 7.5 μM but are already highly phototoxic at 5.0 μM and 5.5 μM, respectively (Figure 8.8b). The combination of low cytotoxicity and high phototoxicity is

Table 8.4. Toxicity of photoactive cyanine (Cy$^+$) is determined by counterion pairing. Half maximal inhibitory concentration (IC$_{50}$) values generated by linear regression analysis for A549 cells. The error is displayed as a 95% confidence interval. NA implies no observable toxicity trend.

Salt	IC$_{50}$ Dark [μM]	95% CI	IC$_{50}$ 850nm [μM]	95% CI
CyI	1.0	0.8 - 1.3	0.5	0.2 - 0.7
CyPF$_6$	0.9	0.8 - 1.0	0.5	0.2 - 0.7
CySbF$_6$	0.9	0.7 - 1.0	0.5	0.3 - 0.7
CyCB	1.8	1.4 - 2.6	0.5	0.2 - 0.7
CyFPhB	NA	NA	2.6	1.7 - 3.4
CyCoCB	NA	NA	2.7	2.2 - 3.0
CyTPFB	19.7	15.1 - 31.3	10.2	7.9 - 12.8
CyTFM	NA	NA	13.5	11.9 - 15.2
CyTRIS	NA	NA	NA	NA

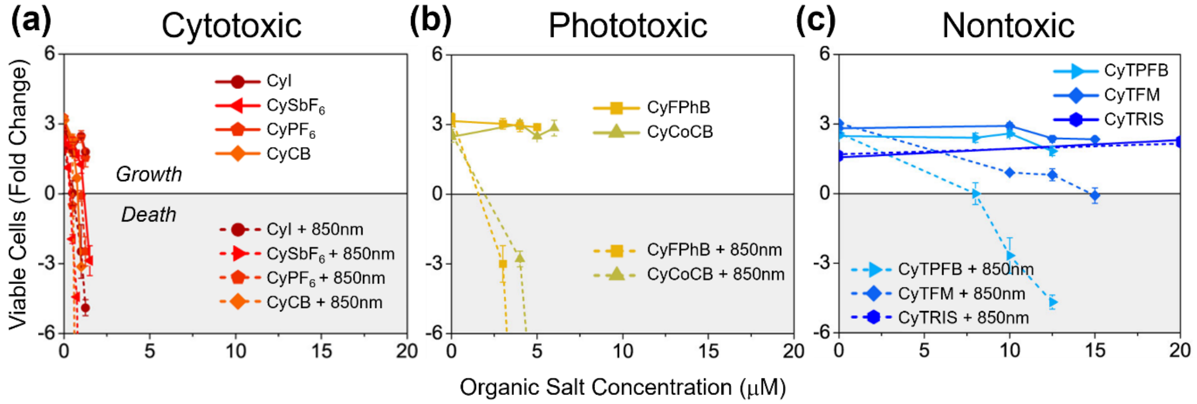

Figure 8.9. Organic salts with tunable toxicity used to target human melanoma cells. (a) CyI, CySbF$_6$, CyPF$_6$, and CyCB (red/orange) are cytotoxic at low concentrations (1μM), with and without NIR excitation (cyototoxic). **(b)** CyFPhB and CyCoCB (yellow/green) do not display significant toxicity without light activation, but when photoexcited they induce significant cell death (phototoxic). **(c)** CyTPFB, CyTFM, and CyTRIS (blue) display low toxicity with and without light (nontoxic). This data agrees with the trend observed in A549 cell toxicity. Data are displayed as means ± S.E.M., $n = 3$.

ideal for photosensitizers in PDT. This starkly contrasts to reports that the anion has no impact on dark cytotoxicity in breast cancer cells when paired with a larger bandgap fluorophore.[255] On the other hand, Cy$^+$ is found to be nontoxic when paired with TPFB$^-$, TFM$^-$, and TRIS$^-$. These pairings display negligible cytotoxicity and only modest phototoxicity at much higher concentrations of >15 μM (CyTPFB), >20 μM (CyTFM), and >30 μM (CyTRIS), making them more ideal for imaging applications (Figure 8.8c). Both cytotoxicity and phototoxicity are shown to be dose-dependent for all ion pairings tested, with the exception of CyTRIS, which displayed no cytotoxicity in the concentrations tested up to 100 μM (Figure 8.8c, Table 8.4). The dose-dependent response observed in A549 cells is also consistent in WM1158 cells (Figure 8.9).

8.4 Mechanism of toxicity

To determine the mechanism of the observed tunability in cytotoxicity and phototoxicity, we investigated salt localization within the cell, which can influence the types of ROS generated and their impact on the cell. Colocalization analysis was done in A549 cells incubated with CyPF$_6$ (Figure 8.10a) and stained with a DNA stain, Hoechst (Ho; Figure 8.10b), and a mitochondrial

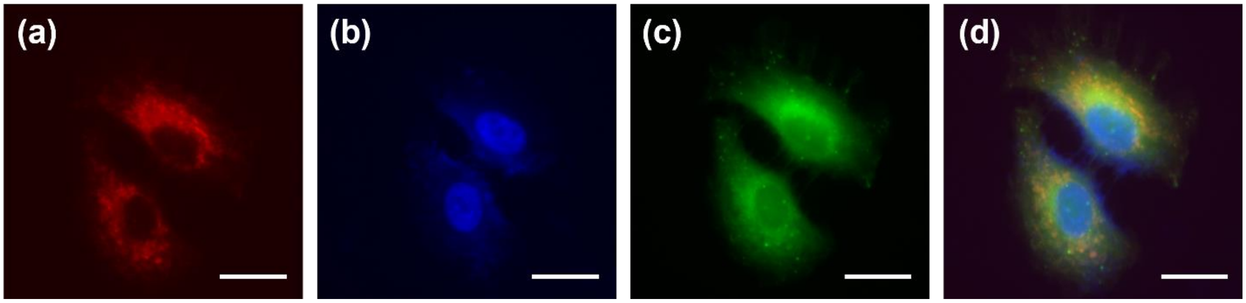

Figure 8.10. CyPF$_6$ preferentially accumulates in mitochondria and lysosomes of cells. (a) CyPF$_6$ staining. **(b)** DNA staining using 2´-[4-ethoxyphenyl]-5-[4-methyl-1-piperazinyl]-2,5´-bi-1H-benzimidazole trihydrochloride trihydrate (Hoechst). **(c)** Mitochondrial staining using Rhodamine 123 (Rho123). **(d)** Superimposed CyPF$_6$ + Hoechst + Rho123 staining. Scale bar = 20 µm (100x).

stain, Rhodamine 123 (Rho123; Figure 8.10c). Colocalization was observed for CyPF$_6$ and mitochondrial tracker Rho123, but not with DNA-specific Ho (Figure 8.10d). This indicates that the salts preferentially localize in the mitochondria, which is expected due to the positive charge of Cy$^+$. Some of the salts that do not colocalize with Rho123 could potentially be found within lysosomes, another negatively charged organelle within the cell. Similar results were observed with CyFPhB and CyTPFB (Table 8.5, Figure 8.11). The mechanism of tunability was further studied by oxidative stress analysis using ROS sensitive probes. MitoSOX was used to measure mitochondrial superoxide, and chloromethyl-2′,7′-dichlorodihydrofluorescein diacetate (Cm-H2DCFDA) was used to analyze general cytoplasmic ROS levels in cells treated with phototoxic levels of organic salts (Figure 8.12). We found that an increase in mitochondrial superoxide is

Table 8.5. Intracellular localization of CyX does not change with the counterion. Variables of colocalization that measure the linear relationship between red (organic salt analog) and green (Rhodamine123) fluorescence (Pearson’s coefficient), overlap of red to green area (Mander’s coefficient 1), and overlap of green to red area (Mander’s coefficient 2). All organic salts show a positive linear correlation with mitochondrial fluorescence, with similar degrees of colocalization in the mitochondria.

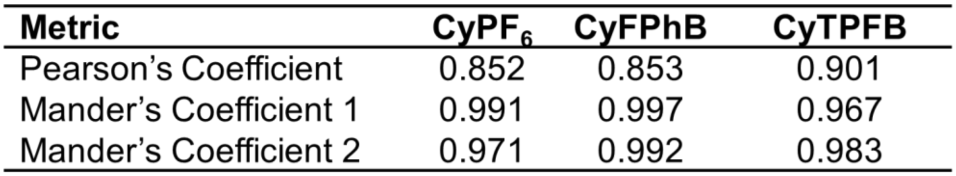

Metric	CyPF$_6$	CyFPhB	CyTPFB
Pearson’s Coefficient	0.852	0.853	0.901
Mander’s Coefficient 1	0.991	0.997	0.967
Mander’s Coefficient 2	0.971	0.992	0.983

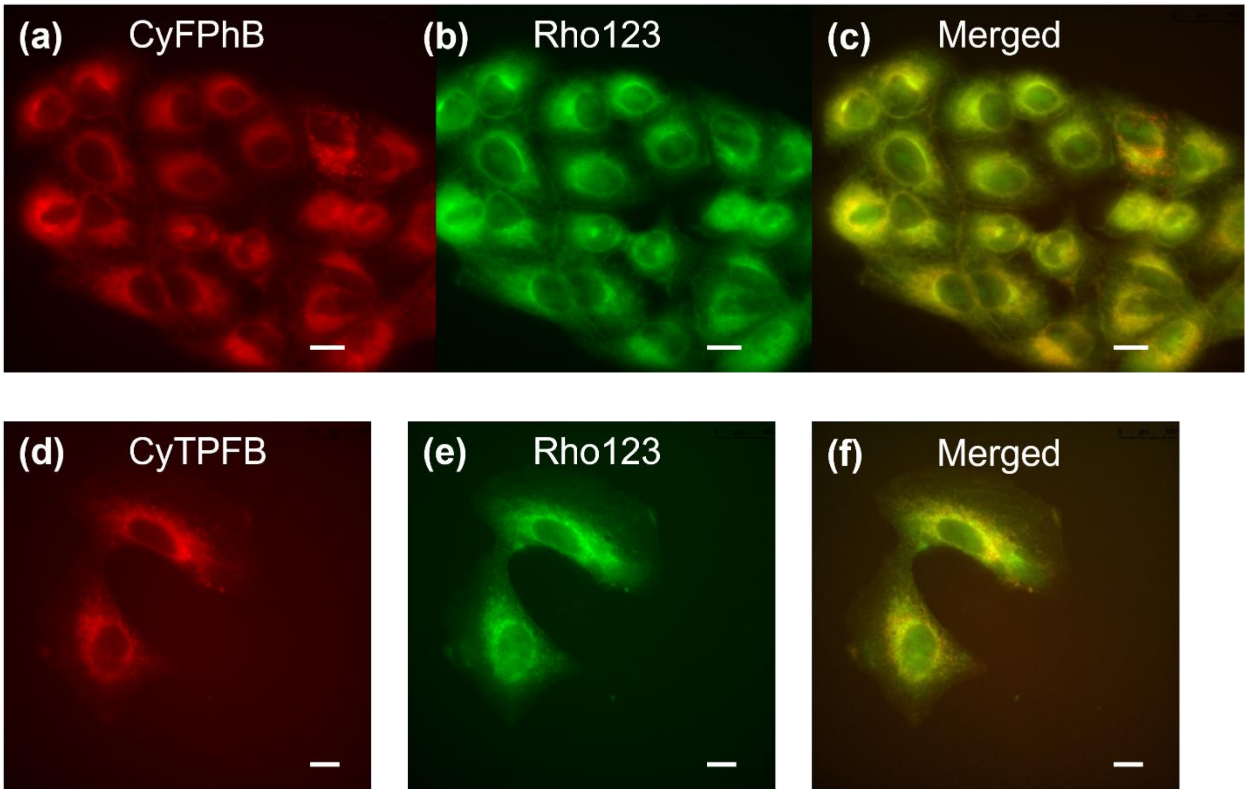

Figure 8.11. CyFPhB and CyTPFB preferentially accumulate in the mitochondria and lysosomes of cells. **(a)** CyFPhB staining. **(b)** Mitochondrial staining using Rhodamine 123 (Rho123). **(c)** Superimposed CyFPhB + Rho123 staining. **(d)** CyTPFB staining. **(e)** Mitochondrial staining using Rho123. **(f)** Superimposed CyTPFB + Rho123 staining. Scale bar = 20 µm (40x).

directly correlated with both cytotoxicity and phototoxicity of organic salts. Cytotoxic CyPF$_6$ generates superoxide with or without light; phototoxic (but not cytotoxic) CyFPhB photo-generates superoxide only with illumination; and nontoxic CyTPFB generates minimal superoxide even with illumination at high concentrations. No cytoplasmic ROS was detected using general cytoplasmic ROS probe Cm-H2DCFDA (Figure 8.12). This data demonstrates that the toxicity of organic salts is caused by localized generation of superoxide within the mitochondria. Mitochondrial superoxide is known to mediate apoptosis through oxidative damage of mitochondrial DNA, hyperpolarization of the mitochondrial membrane potential, and protein modifications leading to the opening of the mitochondrial permeability transition pore.[273] A key difference in cells treated with CyPF$_6$ is the presence of mitochondrial ROS even without light

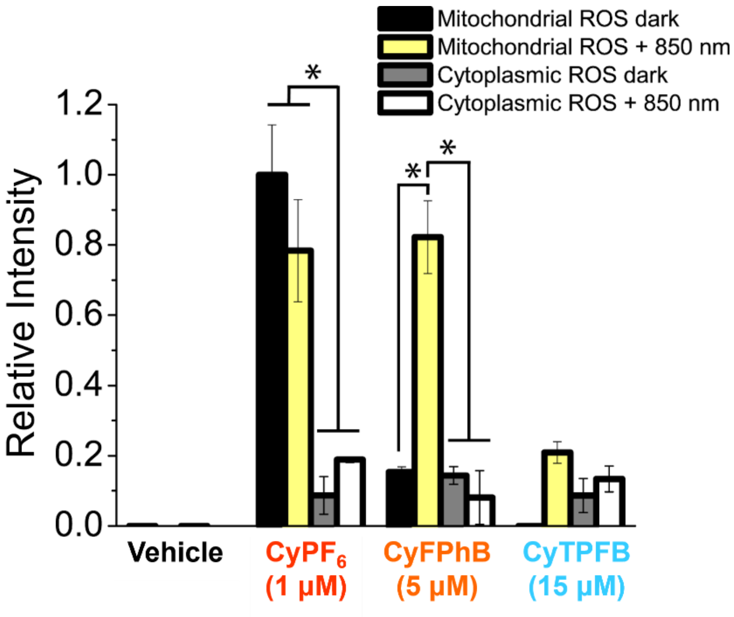

Figure 8.12. Fluorescent organic salts generate mitochondrial superoxide. MitoSOX was used to measure mitochondrial superoxide, and H_2DCFDA for general cytoplasmic ROS in A549 cell treated with organic salts at indicated phototoxic concentrations over 4 days. Phototoxic concentrations were determined from the data in Figure 8.8. This data confirms that $CyPF_6$ is cytotoxic, catalyzing superoxide with or without light; CyFPhB is phototoxic but not cytotoxic, photo-generating superoxide only with illumination; and CyTPFB is nontoxic, generating minimal superoxide even with light at high concentrations ($*P \leq 0.05$). Data are displayed as means ± S.D., $n = 3$.

excitation. This is likely due to the stability of nanoparticles: UV-Vis spectroscopy showed that while pairings with small, hard anions (CyI, $CySbF_6$, and $CyPF_6$,) can form nanoparticles in aqueous solution (Figure 8.2c), they do not form nanoparticles in cell media containing fetal bovine serum (Figure 8.13). Pairings with bulkier halogenated anion pairings formed stable and soluble nanoparticles even in cell media containing fetal bovine serum. Lack of nanoparticle formation may lead to cytotoxic species, which are toxic even without light activation because they are more likely to interfere with mitochondrial electron transport chain complexes, a process known to generate ROS. In contrast, stable nanoparticles with average sizes of <20 nm are still able to enter the cell,[270] but size limitations likely restrict their ability to directly interact and inhibit protein complexes in the mitochondrial membrane. To determine whether the counterion affects cellular uptake of organic salts, intracellular levels of different Cy^+-anion pairings were

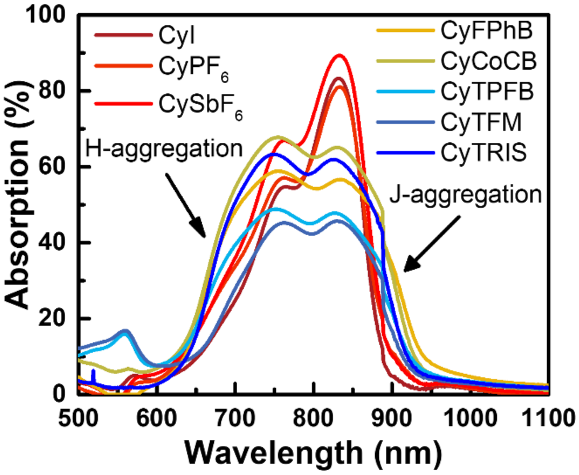

Figure 8.13. Ion pairings display varying degrees of nanoparticle stability in cell media. Organic salts fully dissolved in DMSO have a clear maximum at 830 nm with a leading shoulder when characterized with UV-VIS spectroscopy. After nanoparticle formation and introduction into cell media, combinations of H- and J-aggregation of organic salts can still be seen by blue-shifted peaks (lower wavelength) and red-shifted peaks (higher wavelength), respectively. This is not observed in smaller anions (I^-, SBF_6^-, PF_6^-), indicating a lack of stability in maintaining nanoparticle formation.

measured by high performance liquid chromatography-mass spectrometry (HPLC-MS). No correlation was observed between toxicity and the intracellular concentration of organic salts (Figure 8.14a). This demonstrates that differential anion-mediated uptake is not the cause of the observed modulation in toxicity, even if it is possible that nanoparticle size may be altered upon cellular uptake. In fact, it appears that the opposite may be true: Cy^+ anion pairings with lower cytotoxicity generally had higher intracellular concentrations. However, it should be noted that toxic salts that induce cell death are more likely to rupture and release dyes, potentially decreasing the observed intracellular concentrations. Furthermore, we found that the anions themselves are not toxic: addition of a phototoxic anion such as I^- paired with a non-fluorescent cation such as potassium (K^+) is neither cytotoxic nor phototoxic (Figure 8.14b). Non-cytotoxic anion-cation pairings cannot be made more toxic by addition of toxic anion salts; for example, a nontoxic salt (CyTRIS) does not become cytotoxic or phototoxic by addition of a toxic precursor salt (KI; Figure 8.14b). However, when the reverse experiment was done and a toxic salt (CyPF6) was

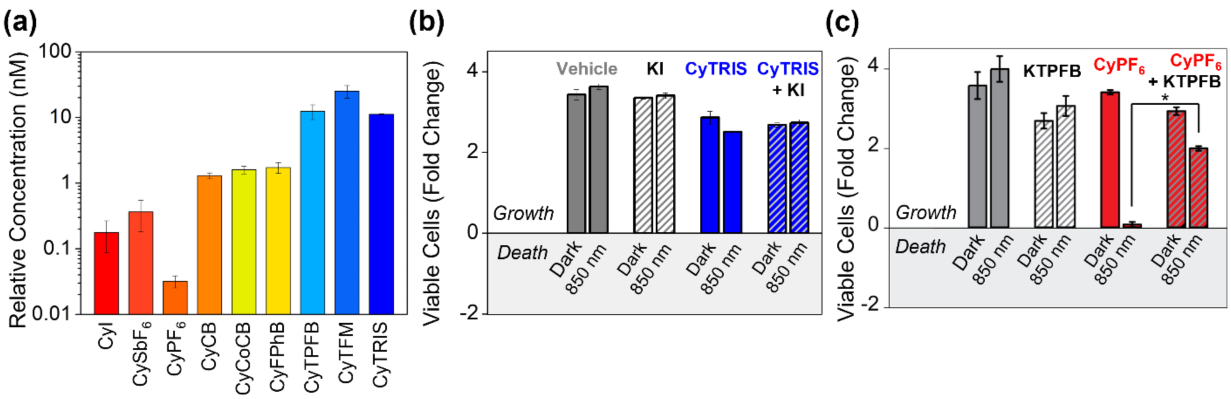

Figure 8.14. Tunable phototoxicity is not due to accumulation or counterion toxicity. (a) Intracellular organic salt accumulation by A549 cells was determined using ultra high-performance liquid chromatography-mass spectrometry. In all cases, cells were incubated with 1 µM of indicated organic salt for 30 hours. Data are displayed as means ± S.D., *n* = 3. **(b)** Iodide (I$^-$) is not toxic when paired with potassium (K$^+$), and KI addition does not make CyTRIS toxic. A549 cells were incubated with vehicle, 1 µM KI, 30 µM CyTRIS, or 1 µM KI + 30 µM CyTRIS with or without NIR (850 nm) excitation. Cell viability determined by trypan blue staining and cell counting. **(c)** The phototoxicity and cytotoxicity of CyPF$_6$ can be mitigated by the addition of KTPFB, which is not found to be toxic. A549 cells were incubated with vehicle, 15 µM KTPFB, 1 µM CyPF$_6$, or 15 µM KTPFB + 0.5 µM CyPF$_6$ with or without NIR (850 nm) excitation. Data are displayed as means ± S.E.M., *n* = 3.

supplemented with a nontoxic precursor salt (KTPFB), toxicity was mitigated (Figure 8.14c). This is likely due to variance in nanoparticle stability in cellular environments: in cell media, nanoparticles become less stable when Cy$^+$ is paired with small, hard anions (I$^-$, SbF$_6^-$, and PF$_6^-$), while nanoparticles remain stable when Cy$^+$ is paired with bulkier anions (FPhB$^-$, CoCB$^-$, TPFB$^-$, TFM$^-$, and TRIS$^-$; Figure 8.13). Thus, CyPF$_6$ may undergo an energetically favorable anion exchange with KTPFB to generate the nontoxic CyTPFB species in cell media, leading to decreased toxicity and increased cell viability. These data indicate that the toxicity of organic salts is not due to the toxicity of the anion itself, or cellular uptake.

8.5 Applications in imaging

We next demonstrated that the concept of counterion-mediated tunability can be used to improve *in vitro* imaging of live cells. Commercially available cyanine molecules used for NIR imaging are typically formulated with halide anions (e.g. chloride or iodide), including the Cy3,

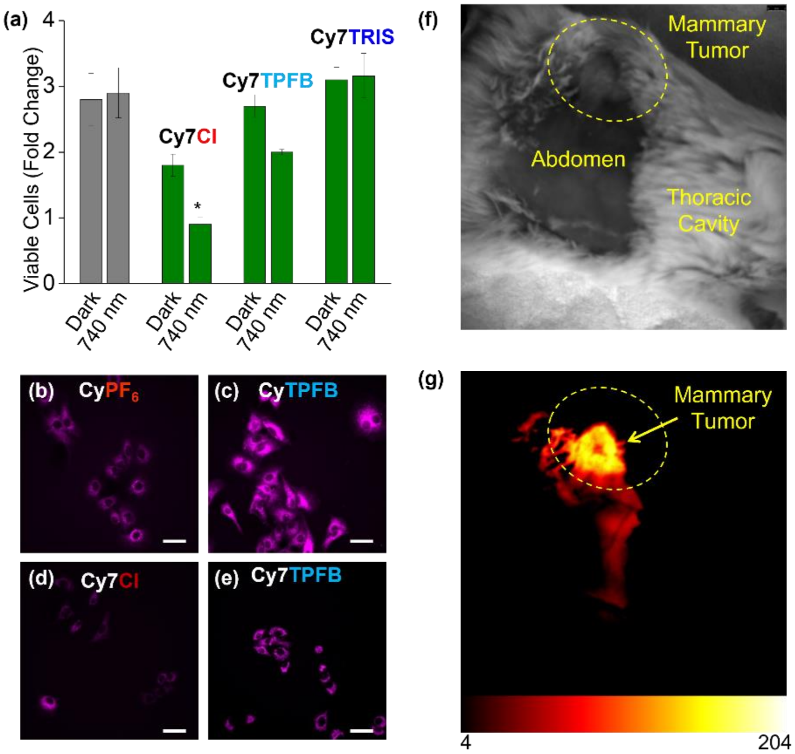

Figure 8.15. Fluorescent dyes tuned to be nontoxic for brighter imaging. (a) Commercially available Cy7, sold as Cy7Cl, can be tuned for toxicity through counterion pairing. A549 cells were incubated with Cy7$^+$ paired with indicated anions at 1 μM. Commercial formulation of Cy7 with Cl$^-$ is found to be cytotoxic; TPFB$^-$ pairing shows a dramatic decrease in cytotoxicity with a minor amount of phototoxicity; TRIS$^-$ pairing eliminates both cytotoxicity and phototoxicity ($*P \leq 0.05$). Data are displayed as means ± S.E.M., $n = 3$. **(b)** Novel fluorescent cation Cy$^+$ paired with PF$_6^-$ is cytotoxic at low concentrations (1.2 μM), leading to dim images. **(c)** However, Cy$^+$ paired with TPFB$^-$ is non-toxic even at increased concentrations (95 μM), and provides brighter images. **(d)** Commercially available Cy7Cl is cytotoxic at 1 μM and provides dim images. **(e)** When Cy7 is paired with counterion TPFB$^-$, it also becomes non-toxic at higher concentrations (6 μM) and provides brighter images. Scale bar = 100 μm (40x). **(f)** Anteroinferior image of supine FVB WT mouse with a MMTV myc-driven mammary tumor. Hair was removed from the abdomen for improved visualization. **(g)** CyPF$_6$ localizes to tumors to enable tumor detection and therapy. Fluorescent images were taken at 41 hours post intraperitoneal injection of 1 mg/kg CyPF$_6$ in PBS. Scale bar represents relative grey value.

Cy5, and Cy7 analogs. We performed anion exchange reactions on Cy7Cl to replace the chloride with the range of anions described above. While Cy7Cl is highly cytotoxic, Cy7+ can be tuned to become less toxic when paired with TPFB$^-$ and TRIS$^-$ (Figure 8.15a). This demonstrates that anionic modulation of toxicity is not limited to a specific fluorescent cation, and this effect can be replicated in alternative organic salt formulations. Reduced toxicity is desirable for live cell

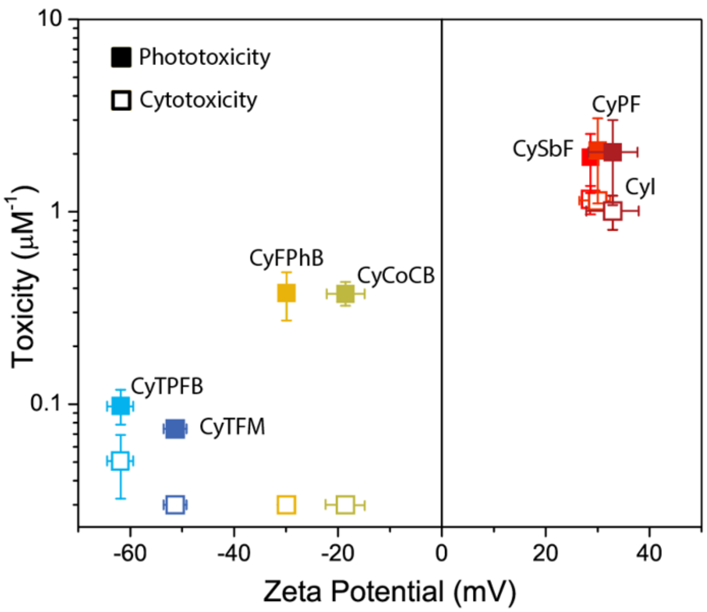

Figure 8.16. Toxicity of organic salts correlates to changes in zeta potential. Toxicity of cyanine counterion pairings is correlated to changes in the electrostatic charge on the nanoparticles as measured by zeta potential. Cytotoxic anion pairings (red) are found to have positive zeta potentials, while non-cytotoxic pairings display negative zeta potentials. Zeta potentials were obtained from Table 8.2, and toxicity values are the inverse of IC_{50} values obtained from Table 8.1. Error displayed as standard deviation.

imaging, as brighter images can be captured with less cellular damage. We have improved live cell imaging using nontoxic anion pairing in both Cy^- and $Cy7^-$. In contrast to the images obtained using toxic $CyPF_6$ and Cy7Cl, brighter images can be captured using nontoxic CyTPFB and Cy7TPFB (Figure 8.15b-e). Due to their high toxicity, $CyPF_6$ and Cy7Cl must be used at low concentrations of 1.2 µM and 1.0 µM, respectively. Nontoxic CyTPFB and Cy7TPFB can be used at higher doses of 95 µM and 6 µM, respectively, allowing for increased absorption and absolute brightness while preserving cell viability. Thus, enhanced brightness and lack of toxicity lead to improved images that capture representative cells under less cellular stress. Finally, an initial *in vivo* demonstration of the tumor-targeting ability of fluorescent organic salts is provided: intraperitoneally injected $CyPF_6$ preferentially localizes to the tumor in a mouse breast cancer model (Figure 8.15f-g).

8.6 Discussion

There is growing interest in developing noninvasive cancer theranostic agents that can detect and target a wide range of tumor types with minimal toxic side effects. This work develops a platform for tuning the toxicity of theranostic agents through counterion pairings for applications in both enhanced imaging and effective therapy. We have demonstrated the ability of weakly coordinating anions to tune cellular toxicity of multiple organic salts by influencing the energy level of the fluorescent cation to impact generation of mitochondrial superoxide. Nanoparticle formation is necessary for the observed modulation of cellular toxicity by the counterion, as it preserves salt composition and prevents ionic dissociation in aqueous solution. We have shown that the tunability in cellular toxicity is independent of intracellular concentration, localization, anionic toxicity, and is not specific to a particular ionic fluorophore. These data demonstrate that electronic modulation via counterion pairing can tune the cytotoxicity and phototoxicity of photosensitizers in cellular environments. We find a correlation between the zeta potential of nanoparticles in aqueous solution and their cyto- and phototoxicity (Figure 8.16). Cytotoxic/phototoxic nanoparticles have positive zeta potentials, while non-cytotoxic/phototoxic nanoparticles have negative zeta potentials, and non-cytotoxic/non-phototoxic nanoparticles have even lower negative zeta potentials (Table 8.1). Interestingly, nanoparticles with negative zeta potentials have distinct cyto- and phototoxicities, while nanoparticles with positive zeta potentials have overlapping cyto- and phototoxicities (Figure 8.16). Zeta potential has been correlated to HOMO level,[269] and these shifts in HOMO are likely the driving force for dictating phototoxicity. While we have demonstrated the correlation between energy level modulation and phototoxicity, the mechanism by which valence energy levels effect cellular toxicity remains an open question for future studies. We hypothesize that the degree of phototoxicity is dictated by energy level resonance with components in the mitochondria. For example, CyFPhB with a lower absolute HOMO is highly phototoxic, while CyTPFB with a higher absolute HOMO is not phototoxic even at orders of magnitude higher concentrations. This is likely due to the ability of the photoactivated fluorophore to resonately perform electron transfer reactions within the mitochondria and therefore produce varying amounts and types of particular radical and reactive species. Energy level modulation is only achievable with nanoparticle formulation, as free salts show the same redox potential and therefore the same energy level (Figure 8.4c-d).[94] Non-toxic pairing with anions such as $TPFB^-$ and TFM^- can be used to reduce cellular toxicity during diagnostic imaging. In contrast, we have selectively enhanced phototoxicity in response to NIR excitation while eliminating dark cytotoxicity of Cy^+ across a range of cell lines by pairings with anions such as $FPhB^-$ and $CoCB^-$. This approach has the potential to increase targeting efficacy in tumors while minimizing nonspecific toxicity in healthy tissue. In addition to having broad clinical applications, this work gives insight into a novel method for modulating the electronic characteristics of fluorescent cation-anion pairings, and provides a rational strategy for enhancing existing photodynamic drugs and imagers.

8.7 Experimental methods

8.7.1 Synthesis

Synthesis of $CyPF_6$, CySbF6, CyFPhB, and CyTPFB: Precursor salts (CyI and $NaPF_6$, $NaSbF_6$, NaFPhB, or KTPFB) were dissolved in methanol:dichloromethane (MeOH:DCM) mixtures and stirred at room temperature under nitrogen. The counterion precursor was added in 100% molar excess to drive the exchange of ions. The product compounds were formed as solid precipitates after approximately 5 minutes. They were collected using vacuum filtration and rinsed with MeOH. The crude product was dissolved in minimal DCM and run through a silica gel plug with DCM as the eluent to remove unreacted precursors and other impurities. The product compound exiting the silica was recognized by its color and collected. Excess DCM was removed in a rotary evaporator. Reaction yield and purity were confirmed using a high mass accuracy time-of-flight mass spectrometer coupled to an ultra-high performance liquid chromatography (UHPLC-MS) in positive mode to quantify cations, and in negative mode to quantify anions. For ion purity measurements, solutions of precursors and products were prepared in various known concentrations and analyzed by UHPLC-MS. Typical reactions led to products yields of >60% with purities >95%. Reaction schemes and purification procedures described previously were used.[95,102]

Synthesis of CyTRIS and CyTFM: Precursor salts (CyI and TBA-TRIS or NaTFM) were dissolved in DCM in a 1:2 molar ratio and stirred at room temperature under nitrogen for 1 hour. The reaction contents were passed through a silica gel plug using DCM as the eluent, where the purified product was collected and quantified with UHPLC-MS as described for the salts above. Similar yields and purities were achieved for CyTRIS and CyTFM as other salts.

Synthesis of CyCoCB: Precursor salts CyI and NaCoCB were dissolved in MeOH in a 1:2 molar ratio and stirred at room temperature under nitrogen. CyCoCB formed and precipitated out of solution after approximately 5 minutes. The crude product was collected using vacuum filtration and rinsed with MeOH. It was then purified with silica gel chromatography and the purity was quantified with UHPLC-MS as detailed previously. Reaction yield and purity of CyCoCB was similar to that of the other salts discussed here30,31.[95,101]

Synthesis of Cy7PF$_6$, Cy7FPhB, Cy7TPFB, and Cy7TRIS: Precursor salts (Cy7Cl and NaPF$_6$, NaFPhB, KTPFB, and TBA-TRIS) were dissolved in DCM in a 1:2 molar ratio and stirred at room temperature under nitrogen for 1 hour. Reaction contents were passed through a silica gel plug using DCM as the eluent, where the purified product was collected and quantified with UHPLC-MS. Reaction yields were 45–50% with similar purity to other salts. Cyanine7 NHS ester (Cy7) was utilized as received (Lumiprobe), as a commercial reference.

8.7.2 Cell culture

Human lung carcinoma (A549) and metastatic human melanoma (WM1158) cells were cultured in Dulbecco's Modified Eagle's Medium (DMEM) with 4.5 g L^{-1} glucose without sodium pyruvate with 10% heat inactivated fetal bovine serum supplemented with 2 mM glutamine and 1% penicillin and streptomycin. Cells were incubated in 37 °C with 5% CO_2 without light exposure.

8.7.3 Viability studies

A549 and WM1158 cells were seeded at a density of 50,000 cells per well in 6-well tissue culture plates. After 24 hours of incubation, media was aspirated and replaced with media containing fluorescent dyes at indicated concentrations. Each well was irradiated with an 850 nm LED lamp with an illumination flux of 526 mW cm^{-2} for an hour in the incubator, and control cells were left in a dark incubator without irradiation. For studies using Cy7, a custom made 740 nm LED lamp was used, but with the same illumination flux. Immediately after irradiation, the media was replenished with fresh dye-laced media and allowed to incubate for another 24 hours. The same procedure was done at 48 and 72 hours, but the cells received no further dye-laced media after 72 hours. Viable cell number was determined at 24 and 96 hours using 4% trypan blue and a Nexcelom Cellometer Auto T4 cell counter. All assays were done with 3 biological replicates. The fold change in cell proliferation over days of treatment was calculated using Equation 8.1:[274]

$$\text{Fold change} = \log_2\left(\frac{Day\ 4\ viable\ cell\ count}{Day\ 1\ viable\ cell\ count}\right) \tag{8.1}$$

The half maximal inhibitory concentration (IC_{50}) was calculated by linear regression analysis of cell viability versus concentration data.

8.7.4 Fluorescent imaging

Images were obtained using a Leica DMi8 microscope with a PE4000 LED light source, DFC9000GT camera, and LAS X imaging software. A549 cells were seeded in 3 cm tissue culture plates at a density of 50,000 cells per well in DMEM containing fluorescent organic salts at indicated concentrations. The cells were incubated for 2 days at 37 °C with 5% CO_2 until the day of imaging. For live cell imaging, the media was aspirated, and the cells were washed with phosphate buffered saline (PBS, Sigma-Aldrich) 5 times before being imaged in PBS.

For colocalization analysis, A549 cells were grown on 0.5 mm coverslips placed in 3 cm tissue culture plates containing media for 3 days. Cells were then fixed by aspirating media, washing with PBS 5 times, then submerging the coverslip in cold methanol and incubating on ice for 15 minutes. The fixed cells were stained with 1 μM 2′-[4-ethoxyphenyl]-5-[4-methyl-1-piperazinyl]−2,5′-bi-1H-benzimidazole trihydrochloride trihydrate (Hoechst 33342, Invitrogen) for 5 minutes, washed with PBS, and then incubated with 15 μM of 3,6-diamino-9-(2-(methoxycarbonyl)phenyl chloride (Rhodamine123) and 1 μM $CyPF_6$ for 15 minutes before being washed and mounted to slides with Fluoromount-G (Invitrogen). Cells were analyzed using a Leica DMi8 microscope with a PE4000 LED light source, DFC9000GT camera, and LAS X imaging software.

8.7.5 Flow cytometry

Cells were incubated with phototoxic concentrations of $CyPF_6$ (1 μM), CyFPhB (5 μM), or CyTPFB (15 μM) and exposed to NIR light for 4 days as described above. Each day, cells were collected for analysis by trypsinization from plates (prior to any illumination), spun down and resuspended in a staining buffer consisting of Hank’s buffered salt solution (HBSS, Sigma-

Aldrich) with 10 mM 4-(2-Hydroxyethyl) piperazine-1-ethanesulfonic acid (HEPES, Sigma-Aldrich) and 2% FBS. Cells were separated into 2 populations for staining with 15 µM of chloromethyl-2′, 7′-dichlorodihydrofluorescein diacetate (cm- H2DCFDA, Invitrogen) for 60 minutes, or 2.25 µM of MitoSOX (Invitrogen) for 20 minutes. Hydrogen peroxide was used as a positive control for H2DCFDA. Cells were analyzed on a BD LSR II using FITC and PE-A channels and 30,000 events counted. Fluorescence was normalized to the initial value.

8.7.6 Ultraviolet-visible and near-infrared light spectroscopy

Cyanine dyes were diluted to a concentration of 5 µM in cell media. All dyes were characterized using a Perkin Elmer Lambda 900 UV/VIS/NIR spectrometer in the wavelength range from 500–1100 nm in normal incidence transmission mode with a resolution of 1 nm and a 1.27 cm path length. A pure solvent reference was utilized to remove reflections so that the absorption is calculated as 1-transmission.

8.7.7 Zeta potential measurements

A Zetasizer Nano Z (Malvern Instruments, UK) at 25 °C with a 633 nm laser was used to calculate zeta-potential measurements (ζ) using laser Doppler micro-electrophoresis. Measured electrophoretic mobilities (μ_e) were converted to zeta potentials from the Henry equation (Equation 8.2):

$$\zeta = \frac{\mu_e 3\eta}{2\varepsilon_\tau \varepsilon_0 f(Ka)} \tag{8.2}$$

where ε_τ is the dielectric constant of the medium, ε_0 is the permittivity of the vacuum, *f(Ka)* is Henry's function, and η is the viscosity of the colloid. Samples were run in triplicate at a concentration of 10 µM organic salt in 10% PBS and 1% DMSO.

8.7.8 Scanning electron microscopy

Scanning electron microscopy (SEM) was used to study the size of organic salt nanoparticles. Polished glass substrates (Xin Yan Technology LTD) were cleaned by sequential sonication in soap, deionized water and acetone, and boiling in isopropanol for six minutes each followed by oxygen plasma cleaning for three minutes. CyX nanoparticles were spun at 2000 rpm for 30 s from 0.5 µM solutions (1% DMSO, 99% DI H_2O) using 50 µL of solution. Substrates were then coated with a thin layer of platinum to improve conductivity prior to measurements, and

for 30 s from 0.5 µM solutions (1% DMSO, 99% DI H_2O) using 50 µL of solution. Substrates were then coated with a thin layer of platinum to improve conductivity prior to measurements, and

carbon black was used to provide a conductive path from the substrate stage to the sample on a corner of each substrate. A Carl Zeiss EVO LS 25 Variable Pressure Scanning Electron Microscope and a Tescan Mira3 Scanning Electron Microscope were used to capture images of the organic salt nanoparticles. Images were then analyzed using ImageJ software to produce size distributions for each organic salt.[275]

8.7.9 Small-angle x-ray scattering

To verify organic salt nanoparticle size, small-angle X-ray scattering (SAXS) was used to measure CyTPFB nanoparticle size in solution. A Rigaku Ultima IV X-ray Diffractometer in the Robert B. Mitchell Electron Microbeam Analysis Lab at the University of Michigan was used to make SAXS measurements. Solutions were loaded into boron-rich glass capillaries with 1.5 mm outside diameter (Charles Supper Company) Parallel beam and SAXS alignment procedures were performed to prepare the diffractometer for measurements. PbS quantum dots (Millipore Sigma, 3 nm nominal size) were used as a control sample and 2.6 mg/mL CyTPFB in 50% DMSO, 50% DI H_2O was the experimental sample, along with a 50% DMSO, 50% DI H_2O blank. CyTPFB was the only organic salt measured using SAXS due to solubility issues with other salts. CyTPFB was known to form nanoparticles at 50% DMSO from previously collected UV-VIS data.[143]

8.7.10 Differential pulse voltammetry

DPV was used to measure the oxidation potentials of organic salts as monomers and as nanoparticles to elucidate changes to the HOMO level (which correlates to the oxidation potential) upon formation of nanoparticles.[125] DPV measurements were made with a µAutoLabIII potentiostat using glassy carbon and platinum mesh as the working and counter electrodes, respectively. For monomer measurements, a $Ag/AgNO_3$ (0.36 V vs SCE) reference electrode was used while nanoparticle measurements were made with a Ag/AgCl (-45 mV vs SCE) reference electrode. Monomer salts were dissolved at 1 mM in acetonitrile with 100 mM TBA-PF_6 as the supporting electrolyte. Nanoparticle DPV measurements were made with salts dissolved in 10% DMSO and 90% DI H_2O (CyI and CyPF_6) and in 50% DMSO, 50% DI H_2O (CyFPhB and CyTPFB). Nanoparticle solutions were made at the maximum solubility that could be sustained for the duration of the measurement, which was 0.1 mM for CyI, CyPF_6, and CyFPhB, and 0.5 mM for CyTPFB.[143]

8.7.11 Photoluminescence and quantum yield

Photoluminescence (PL) spectra were collected using a PTI Spectrofluorometer for monomers of Cy7X and CyX salts, as well as nanoparticles of CyX salts. For Cy7X monomers, solutions at 1 µM salt in DMSO were used. Solutions of 5 µM CyX salts were prepared in DMSO for PL measurements. Nanoparticles of CyX salts were made at 2.5 µM in 1% DMSO, 99% water. A mounted Thorlabs 735 nm LED was used at approximately 5% power as the excitation source for the PL spectra of the CyX monomers and nanoparticles, while a monochromated Xenon lamp (700 nm) was used as the excitation source for Cy7X PL.

Quantum yield (Φ) data was gathered using a PTI Spectrofluorometer with an integrating sphere (350–900 nm) for monomers of Cy7X and CyX salts. A Thorlabs 735 nm LED was used at approximately 5% power as the excitation source for all quantum yield measurements. Cy7X solutions were made at 1 μM in DMSO, while CyX salts were prepared at 2.5 μM in DMSO.

8.7.12 Determination of intracellular organic salt concentrations

Cells were seeded at a density of 50,000 cells per well in 6-well plates in media containing 1 μM of indicated dye. Cells were allowed to incubate for 3 days at 37 °C with 5% CO_2 with a media change to fresh dye-laced media on day 2. For extraction, media was aspirated from each well, and cells were washed with PBS. The cells were removed from the plate using 0.05% trypsin/EDTA (Thermo Fisher) and centrifuged at 1,500 rpm for 6 minutes. The supernatant was aspirated, and the cell pellet was washed with saline. Saline was aspirated, and the pellets were resuspended with room temperature HPLC-grade 3:7 methanol:acetonitrile (Sigma Aldrich) and centrifuged at 13,000 rpm for 5 minutes. The supernatant was collected in a separate tube, and the pellet was again resuspended in HPLC grade 3:7 methanol:acetonitrile and centrifuged at 13,000 rpm for 10 minutes. The supernatant was combined with the first supernatant for analysis by liquid chromatography-mass spectrometry.

Cell extracts were analyzed the day of extraction using a Waters Xevo G2-XS QToF mass spectrometer coupled to a Waters Acquity UPLC system. The UPLC parameters were as follows: autosampler temperature, 10 °C; injection volume, 5 μL; column temperature, 50 °C; and flow rate, 300 μL min^{-1}. The mobile solvents were Solvent A: 10 mM ammonium formate (Sigma-Aldrich) and 0.1% formic acid (Sigma-Aldrich) in 60:40 acetonitrile:water; and Solvent B: 10 mM ammonium formate and 0.1% formic acid in 90:10 isopropanol:acetonitrile. Elution from the column was performed over 5 minutes with the following gradient: t = 0 minutes, 5% B; t = 3 minutes, 95% B; t = 4 minutes, 95% B; t = 5 minutes, 5% B. ESI spray voltage was 3,000 V. Nitrogen was used as the sheath gas at 30 psi and as the auxiliary gas at 10 psi, and argon as the collision gas at 1.5 mTorr, with the capillary temperature at 325 °C. Data were acquired and analyzed using MassLynx 4.1 and QuanLynx software. Cy^+, which typically elutes at 2.5 minutes, was analyzed in positive mode. Standards of each anion-cation pair were run at concentrations of 5, 10, 25, 50, and 100 nM to generate standard curves for quantitation. Blanks were run before each sample to minimize sample carryover.

8.7.13 In Vivo imaging

All animal protocols were approved and performed in accordance with guidelines set by the Institute of Animal Care and Use Committee (IACUC) of Michigan State University. Primary MMTV-Myc papillary tumors were donated by Dr. Eran Andrechek and have been previously described.[276] Viable frozen tumor chunks (1 mm3) were implanted into the right fourth mammary fat pad of FVB/NJ female mice (purchased from Jackson Laboratories, Bar Harbor, ME, USA) at 6–8 weeks of age. Tumors were monitored with calipers twice a week. Once tumors reached 7.5 mm by the longest axis, mice were given a 1 mg kg^{-1} intraperitoneal injection of $CyPF_6$ in 200 μL of sterile PBS and 1% DMSO. Mice were anesthetized with 3% isoflurane and fluorescent images were taken at 41 hours post injection using a Leica M165FC stereoscope with a 740 nm PE4000 LED light source, DFC9000GT camera, and LAS X imaging software.

8.7.14 Statistical analysis

Statistical analysis was done using OriginPro 8 software. For analyses with more than two group comparisons, a one-way ANOVA analysis was performed with an ad hoc Bonferroni test. To assess the homogeneity of variance and suitability for ANOVA analysis, a Levene’s test was performed. P-values < 0.05 are reported as statistically significant.

Chapter 9 – *In Vivo* Photodynamic Therapy with Organic Salts

The work presented in this chapter was submitted for publication and is in review. This research was carried out in collaboration with Dr. Deanna Broadwater, who performed the in vitro and in vivo work.

9.1 Introduction

The lack of targeted therapy options remains a major problem for effective treatment of many cancer types, and non-specific chemotherapy leads to harsh side effects due to unintended toxicity in normal tissue.[277] A promising solution is PDT, which uses light-activated photosensitizers (PSs) to treat tumors by the generation of reactive oxygen species (ROS) upon photo-excitation.[144,236] PSs that absorb and emit in the near-infrared (NIR) range (650-1200 nm) display superior tissue penetration and reduced photodamage by avoiding visible light wavelengths (400-650 nm) absorbed by biological tissue components. [239,278]

Cyanines are commonly used NIR scaffolds due to their ease of synthesis, structural tunability, and biocompatibility.[279–281] For example, indocyanine green is an NIR heptamethine cyanine used in diagnostic clinical cancer studies for sentinel lymph node mapping to detect metastasis.[282] However, it suffers from poor chemical stability, nonspecific binding, and off-target toxicity, resulting in limited medical usage.[283,284] Indeed, this is a common problem in cancer therapy: even with tumor-targeting approaches such as nanoparticle formulation or antibody-conjugation, chemotherapeutics can still accumulate in healthy tissue, notably the liver.[285–288] PDT with PSs such as Photofrin (porfimer sodium) and Foscan (mTHPC, temoporfin) have displayed off-site cytotoxicity (toxicity without light irradiation), preventing their use in treatment of many cancers.[289–291] Therefore, despite advances in tumor targeting, there is a need for NIR-PSs with selective phototoxicity (toxicity with light irradiation) and minimal cytotoxicity in normal tissue.

In addition to their improved NIR optical properties, cyanines have inherent tumor targeting capabilities, in large part due to their uptake by organic anion transporter polypeptides (OATPs, human; Oatps, rodent).[292,293] OATPs are cellular transporters that mediate uptake of numerous amphipathic endogenous and exogenous molecules; they are expressed throughout the body in a wide range of tissues and play a critical role in drug uptake and biodistribution.[294] OATPA1/B1 and OATP2B1 transporters, which mediate uptake of cancer chemotherapeutics, are upregulated in a number of cancer cells and are regulated by hypoxia-inducible factor 1α (HIF-1α), a transcription factor commonly expressed in the hypoxic tumor environment.[260,295] PDT *in vitro* studies with cyanine dyes frequently assess cancer uptake specificity with inhibition assays of OATPA1/B1 and OATP2B1 transporters.[257,296] In addition to OATPs, recent studies suggest that serum albumin may be an overlooked mediator of cyanine's tumor-targeting capabilities. Albumin is the predominant protein in the blood and is responsible for maintaining osmotic pressure and chaperoning endogenous molecules through the vascular system.[297] Albumin is reported to have increased tumor accumulation due to upregulated albumin catabolism that fuels cancer growth.[298] Recent studies report meso-chlorinated cyanines can covalently bind to albumin, and that cyanine albumin adducts accumulate within the tumor interstitium.[299,300] Albumin is a commonly used targeting moiety for chemotherapeutics and nanomaterials; thus, albumin conjugation may contribute to the tumor targeting ability of cyanine dyes.[301,302] To assess the mechanisms of tumor targeting, biodistribution, and potential translatability of our findings to additional cancers and preclinical models, we also characterize uptake mediated by mouse Oatps and albumin *in vitro*.

In Chapter 8, we reported a platform to modulate the toxicity of NIR photoactive heptamethine cyanine cation (Cy^+) by counterion pairing with weakly coordinating anions in nanoparticle formulations.[143] The dipole-modulating counterions modify the frontier molecular orbital energy without changing the bandgap. This allows for independent modification of electronic properties from optical properties, resulting in the ability to adjust the toxicity of organic salts without affecting their optical properties such as absorption, emission, and Stokes shift. The composition of photoactive salts is locked in cellular environments by formation of nanoparticles (average diameter of ~4 nm) that prevent cation-anion dissociation.[143] Indeed, pairing Cy^+ with small, hard anions produce organic salts that are cytotoxic, while pairing with bulky, weakly coordinating halogenated anions produces organic salts that are either phototoxic and non-cytotoxic, or non-phototoxic and non-cytotoxic, in human lung carcinoma cells and metastatic human melanoma cell lines.[143] This novel engineering platform through counterion pairing could be used to design PS agents specifically for PDT with low cytotoxicity and high phototoxicity.

Here, we tested the hypothesis that our toxicity-tuning platform via counterions can be used to design a PS with low cytotoxicity and high phototoxicity for *in vivo* PDT. We used a clinically relevant orthotopic mouse model of metastatic breast cancer: 6DT1 cells derived from an MMTV-Myc driven tumor injected into the fourth mammary fat pad of syngeneic FVB mice.[303] This model allowed for testing of counterion-tuned PSs in a physiologically relevant tumor microenvironment in immunocompetent mice, as both the tumor microenvironment and a functional immune system are both critical for metastasis and PDT pharmacodynamics studies.[304–307] Furthermore, metastatic breast cancer has poor patient prognoses with limited targeted therapies available only for specific subtypes, making it an attractive candidate for PDT.[308] Using an orthotopic mouse model of breast cancer, we tested PDT *in vivo* using Cy^+ paired with three different representative toxicity-tuning anions: PF_6^-, $FPhB^-$, and $TPFB^-$ (Figure 9.1a). We found

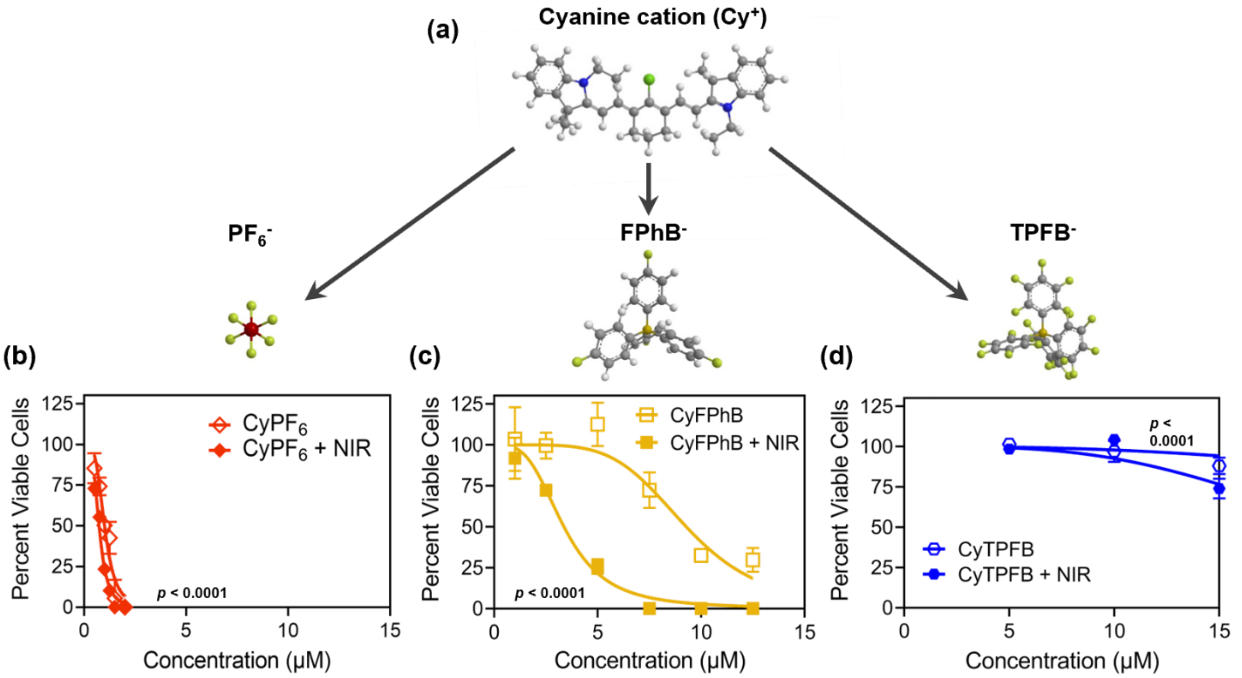

Figure 9.1. Fluorescent organic salts can be used as photosensitizing agents to treat breast cancer cells. Mouse mammary cancer cells (6DT1) were incubated with the indicated concentrations of organic salt pairings with or without near-infrared (NIR, 850 nm) irradiation to determine half maximal inhibitory concentrations (IC_{50}). **(a)** Photoactive heptamethine cyanine cation (Cy^+) is tuned with counterions to modulate toxicity. Percent of viable cells was determined for **(b)** $CyPF_6$, **(c)** CyFPhB, and **(d)** CyTPFB. Data are displayed as means ± S.E.M., $n = 3$. Statistical significance (p-values) of IC_{50} shifts (Dark IC_{50} vs NIR IC_{50}) are displayed on graphs.

that our previous *in vitro* results in human lung carcinoma and melanoma cell lines were reproducible both *in vitro* and *in vivo* in a metastatic breast cancer model, with comparable trends for cytotoxic ($CyPF_6$), phototoxic (CyFPhB), and less toxic (CyTPFB) anion pairings. We further assessed all three organic salts based on *in vivo* pharmacokinetics, antitumor efficacy with light irradiation, and off-site toxicity. Organic salts all displayed tumor-specific accumulation *in vivo*, and CyFPhB was the most potent PS agent with enhanced phototoxicity that eliminates tumor growth upon NIR excitation with minimal side effects in mice. These *in vivo* results validate our counterion tuning strategy, which has potential to expand the clinical applications of cancer PDT agents.

Table 9.1. Half maximal inhibitory concentrations (IC$_{50}$) of fluorescent organic salts with and without NIR irradiation in 6DT1 cells. IC$_{50}$ values were generated by nonlinear regression analysis using GraphPad Prism. Error is displayed as a 95% confidence interval.

Compounds	Dark IC$_{50}$ (mM)	95% CI	NIR IC$_{50}$ (mM)	95% CI
CyPF$_6$	1.0	0.9 – 1.1	0.7	0.7 – 0.8
CyFPhB	9.3	8.0 – 10.8	3.4	2.9 – 3.9
CyTPFB	45.2	33.2 – 149.4	21.6	19.5 – 23.4

9.2 Results

9.2.1 Counterion tuning of organic salts controls toxicity during PDT of mouse metastatic mammary cancer cells in vitro

To confirm that our previous *in vitro* findings from A549 human lung cancer and WM1158 melanoma cell lines can be translated to a *in vivo* mouse model of breast cancer, we first performed *in vitro* PDT on 6DT1 mouse mammary carcinoma cells following incubation with various concentrations of CyPF6, CyFPhB, and CyTPFB with or without 850 nm light irradiation.[143] Consistent with our previous results in A549 and WM1158 cells, we found CyPF$_6$ to be cytotoxic,

Table 9.2. 6DT1 gene expression values. Gene expression data for genes of interest (solute carrier organic anion transporter family member 1B2, Slco1b2; Secreted Protein Acidic and Rich in Cysteine, Sparc) and levels of relative controls (Glyceraldehyde-3-phosphate dehydrogenase, GAPDH; Actin) in 6DT1 tumors (*n* = 4 biological replicates) and cultured cells.

Geoset	Sample ID	Sample	Gene	ID	Mean Value	Value ID
GSE69006	GSM1689995, GSM1689996, GSM1689997, GSM1689998	6DT1 Tumors	GAPDH	10386947	12.68333	0.305307
GSE69006	GSM1689995, GSM1689996, GSM1689997, GSM1689998	6DT1 Tumors	Sparc	10386058	13.13948	0.288961
GSE69006	GSM1689995, GSM1689996, GSM1689997, GSM1689998	6DT1 Tumors	Slco1b2	10542615	4.599253	0.046681
GPL6096	GSM1703590	6DT1 Cell line	Actin	6964030	7.86698	NA
GPL6096	GSM1703590	6DT1 Cell line	Sparc	6788410	11.7504	NA
GPL6096	GSM1703590	6DT1 Cell line	Slco1b2	6950727	4.02566	NA

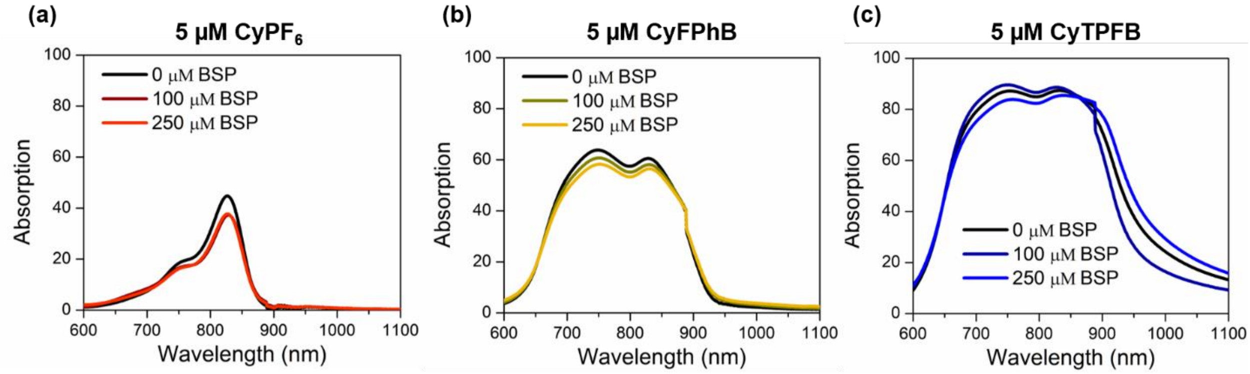

Figure 9.2. Addition of Oatps inhibitor bromosulfophthalein (BSP) does not affect organic salt nanoparticle composition or absorption in cell media. Absorption (100-%T) data collected with UV-Vis spectroscopy for 5 μM **(a)** CyPF$_6$, **(b)** CyFPhB, and **(c)** CyTPFB with increasing concentrations of BSP.

CyFPhB phototoxic, and CyTPFB minimally toxic in 6DT1 cells. CyPF$_6$ is cytotoxic in 6DT1 cells at low concentrations: cell death occurs independent of NIR irradiation with similar half-maximal inhibitory concentration (IC$_{50}$) values of 1 μM (dark IC$_{50}$) and 0.7 μM (NIR IC$_{50}$) without and with light irradiation, respectively (Figure 9.1b, Table 9.1). CyFPhB is highly phototoxic with low cytotoxicity, with a dark IC$_{50}$ of 9 μM and NIR IC$_{50}$ of 3 μM (Figure 9.1c, Table 9.1). With a dark IC$_{50}$ that is three times the concentration of the NIR IC$_{50}$, CyFPhB is a promising candidate for *in vivo* PDT applications. CyTPFB displayed minimal cytotoxicity and minor phototoxicity with a dark IC$_{50}$ of 45 μM and NIR IC$_{50}$ of 22 μM (Figure 9.1d, Table 9.1). While there is a two-fold difference in dark and NIR IC$_{50}$ of CyTPFB, a NIR IC$_{50}$ concentration of 22 μM is too high to achieve *in vivo* and is therefore not ideal for PDT applications.[309]

9.2.2 Oatps and albumin mediate cellular uptake of fluorescent organic salts

Next, we investigated the roles of Oatps and albumin on mediating cancer cell uptake of fluorescent organic salts and verified their relevance in our model. As discussed above, human OATPs and albumin have been shown to mediate uptake of cyanine dyes. Data from Gene Expression Omnibus (GEO) shows that 6DT1 tumors and cells in culture express the gene product of mouse Oatp1b2 (Slco1b2), which has 65% amino acid sequence homology with human

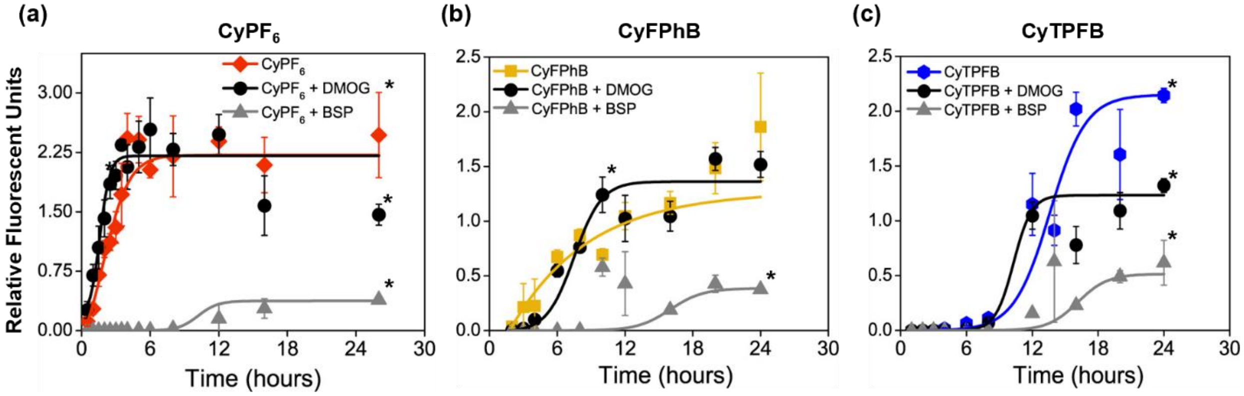

Figure 9.3. Oatps mediate cellular uptake of $CyPF_6$, but only partially account for CyTPFB and CyFPhB uptake. 6DT1 cells were preincubated with 1 mM dimethyloxalylglycine (DMOG), a HIF-1α stabilizer, or 250 μM bromosulfophthalein (BSP), a competitive Oatps inhibitor. Following pre-incubation with Oatps modulating drugs, cells were incubated with the indicated organic salt over 25 hours. Relative fluorescence units were measured for **(a)** 1 μM $CyPF_6$, **(b)** 5 μM CyFPhB, and **(c)** 15 μM CyTPFB. Data are displayed as means ± S.D., $n = 3$. Statistically significant differences (p-value < 0.05) are marked with asterisks. Curves were fit using a sigmoidal dose-response function using Origin Pro8. Sigmoidal curve fitting values are shown in Table 9.3.

OATP1B1 (Table 9.2).[310] In addition to Oatp1b2 expression, 6DT1 tumors and cells express higher levels of proteins that uptake albumin, including Secreted Protein Acidic and Rich in Cysteine (Sparc), compared to surrounding breast tissues (Table 9.2).[311,312] These expression data show that our 6DT1 model reflects expression trends found in human breast cancer and is therefore appropriate and clinically relevant for investigating Oatp- and albumin-mediated cellular uptake of cyanine organic salts.

To assess the role of Oatps on organic salt uptake in our breast cancer model, 6DT1 cells were pre-incubated in cell media with 250 μM bromosulfophthalein (BSP), a competitive inhibitor of Oatps, or 1 mM dimethyloxalylglycine (DMOG), a HIF-1α stabilizer to increase expression of Oatps.[260,299,313,314] Following drug pre-incubation, organic salts were added to cell media, and intracellular fluorescence was measured at various time points to determine cellular uptake. Fluorescence over time was plotted and fitted with a sigmoidal curve to determine uptake kinetics. Nanoparticle absorption spectra were monitored using UV-VIS spectroscopy to confirm that the

Table 9.3. Sigmoidal curve fitting values. Curve fitting values for graphs in Figure 9.3 were generated using a dose-response sigmoidal function in Origin Pro8.

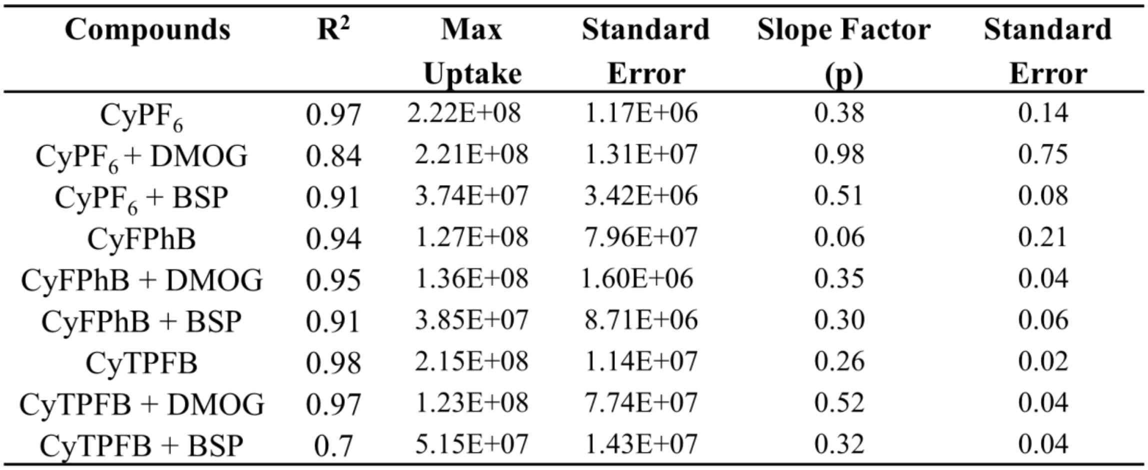

Compounds	R^2	Max Uptake	Standard Error	Slope Factor (p)	Standard Error
CyPF$_6$	0.97	2.22E+08	1.17E+06	0.38	0.14
CyPF$_6$ + DMOG	0.84	2.21E+08	1.31E+07	0.98	0.75
CyPF$_6$ + BSP	0.91	3.74E+07	3.42E+06	0.51	0.08
CyFPhB	0.94	1.27E+08	7.96E+07	0.06	0.21
CyFPhB + DMOG	0.95	1.36E+08	1.60E+06	0.35	0.04
CyFPhB + BSP	0.91	3.85E+07	8.71E+06	0.30	0.06
CyTPFB	0.98	2.15E+08	1.14E+07	0.26	0.02
CyTPFB + DMOG	0.97	1.23E+08	7.74E+07	0.52	0.04
CyTPFB + BSP	0.7	5.15E+07	1.43E+07	0.32	0.04

addition of chemical agents did not affect nanoparticle composition or stability (Figure 9.2). Cellular uptake of CyPF$_6$ increased rapidly upon addition to media, reached maximal uptake at 4 hours, and plateaued after 6 hours (Figure 9.3a, Table 9.3). Consistently, addition of BSP stopped CyPF$_6$ uptake for the first 8 hours, with 84% ± 12% decrease in CyPF$_6$ uptake after 24 hours. Moreover, DMOG addition increased the rate of CyPF6 uptake. Compared to CyPF$_6$, CyFPhB displayed delayed cellular uptake with a steady increase over 24 hours (Figure 9.3b, Table 9.3). Addition of BSP decreased cellular uptake of CyFPhB by 80% ± 14% of uptake at 24 hours. Furthermore, DMOG treatment increased the initial rate of uptake and plateaued at 12 hours. Cellular uptake of CyTPFB was significantly retarded compared to that of CyPF$_6$, reaching maximal uptake at 24 hours. Addition of BSP decreased cellular uptake of CyTPFB by 71% ± 6% (Figure 9.3c, Table 9.3). These results indicate that Oatps mediate cellular uptake of CyPF$_{6,}$ CyFPhB and CyTPFB in 6DT1 cells.

Noting the differences cellular uptake kinetic trends for CyPF$_6$, CyFPhB, and CyTPFB and previously reported zeta potentials, which could cause differences in protein affinity,[143] we examined additional endocytotic mechanisms of cellular uptake. No difference in organic salt

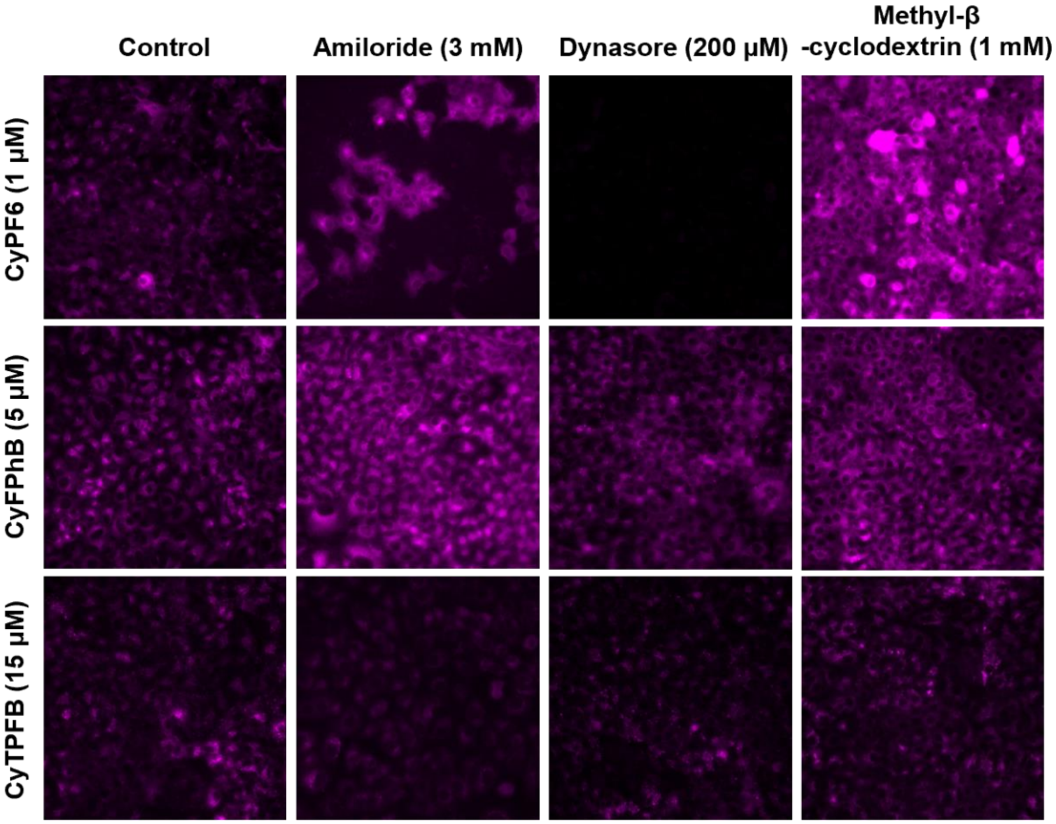

Figure 9.4. Endocytotic inhibition does not inhibit uptake of organic salts. 6DT1 cells were pretreated with amiloride, dynasore, or methyl-β-cyclodextrin. Control samples were treated with an equivalent volume of DMSO. Cells were then incubated with 1 µM CyPF$_6$, 5 µM CyFPhB, or 15 µM CyTPFB and fluorescence intensity was measured at 8 hours. While there is a decrease in fluorescence intensity for CyPF$_6$ + Dynasore, this has been found to be due to an interaction between the molecules themselves and not a decrease in cellular uptake.

uptake was observed upon incubation with various endocytotic inhibitors including dynasore, methyl-β-cyclodextrin, and amiloride (Figure 9.4). Interestingly, notable differences in uptake were observed in serum-free culture medium: CyFPhB uptake decreased dramatically when cells were incubated in culture medium without serum, while CyPF$_6$ and CyTPFB showed similar levels of uptake (Figure 9.5a). To determine if this increase in cellular uptake was mediated by changes to organic salt structure in the presence of serum, UV-VIS spectroscopy was performed on organic salts in DMEM, DMEM + serum, and DMEM with increasing concentrations of bovine serum albumin, the most abundant protein in serum.[315] The results showed that albumin and serum

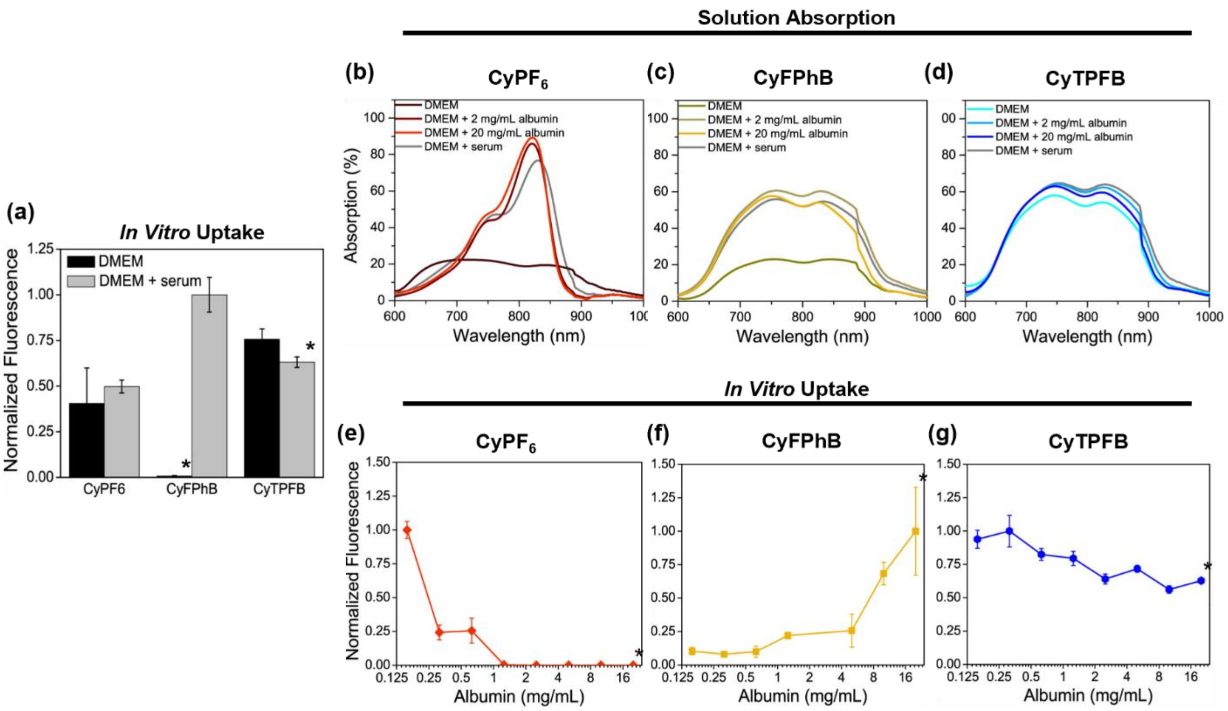

Figure 9.5. Albumin plays a critical role in organic salt stability and uptake. (a) 6DT1 cells were incubated in serum-free media (DMEM) and complete media (DMEM + serum) over 24 hours with indicated organic salts. UV-vis spectroscopy was used to characterize 5 μM **(b)** $CyPF_6$, **(c)** CyFPhB, and **(d)** CyTPFB in DMEM with increasing amounts of bovine serum albumin. Complete spectra can be found in Fig. 9.6. 6DT1 cells were incubated with albumin in DMEM with **(e)** 1 μM $CyPF_6$, **(f)** 5 μM CyFPhB, and **(g)** 15 μM CyTPFB. Data are displayed as means ± S.D., $n = 3$. Statistically significant differences (p-value < 0.05) between initial albumin concentration and final albumin concentration are marked with asterisks.

destabilized $CyPF_6$ nanoparticles to form monomers, as can be seen by spectral narrowing of the peaks (Figure 9.5b). In contrast, albumin increased CyFPhB nanoparticle solubility based on the increase in overall absorption (Figure 9.5c); however, albumin did not impact nanoparticle stability (Figure 9.6). CyTPFB maintained a stable nanoparticle solubility in all solutions with only a minimal increase in the solubility with increasing albumin (Figure 9.5d). These trends were also observed in complete cell media, indicating that albumin interaction has a significant impact in biological systems.

To further determine the effect of albumin on cellular uptake of organic salts, 6DT1 cells were incubated in serial dilutions of purified bovine serum albumin in culture medium with each

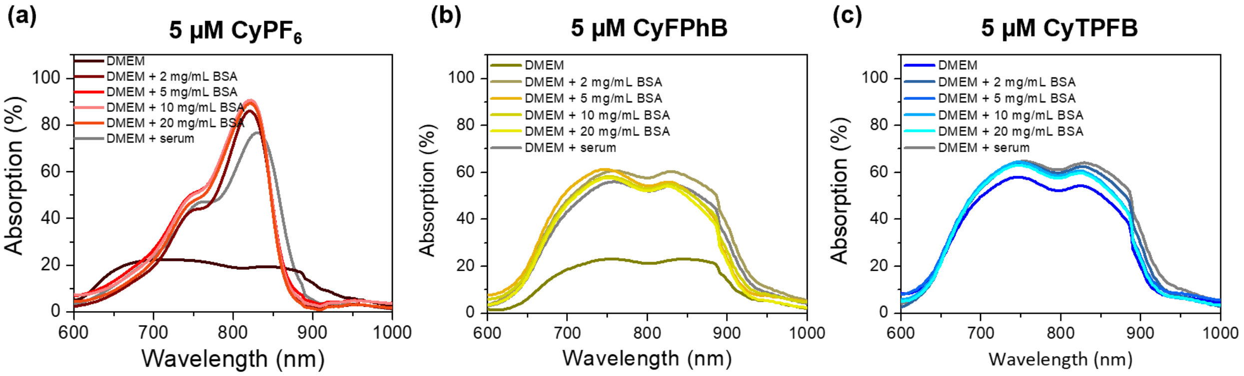

Figure 9.6. Impact of BSA on absorption profiles of organic salts. Absorption (100-%T) data collected with UV-Vis spectroscopy for 5 μM **(a)** CyPF$_6$, **(b)** CyFPhB, and **(c)** CyTPFB with increasing concentrations of bovine serum albumin (BSA) in serum free DMEM, and complete cell media (DMEM + serum). DMEM destabilizes CyPF$_6$ and CyFPhB nanoparticles. BSA stabilizes the CyFPhB nanoparticle, but only the Cy$^+$ monomer from CyPF$_6$.

organic salt. Albumin was not required for cellular uptake of CyPF$_6$, as intracellular fluorescence decreased with increasing albumin concentrations (Figure 9.5e). In contrast, albumin was required for CyFPhB uptake; the intracellular fluorescence signals were increased with increasing albumin concentrations in a dose-dependent manner (Figure 9.5f). CyTPFB cellular uptake was independent of albumin concentrations, as uptake declined with the addition of albumin (Figure 9.5g). We further verified that albumin had no significant effects in decreasing the fluorescent quantum yields of organic salts (Figure 9.7). These results imply that Oatps mediate cellular uptake of CyPF$_6$, CyFPhB, and CyTPFB. Moreover, albumin further mediates uptake of CyFPhB.

9.2.3 Organic salts display differential in vivo biodistribution

To verify trends observed *in vitro* and demonstrate potential clinical applications, we further performed *in vivo* experiments. FVB mice received an orthotopic injection of 10,000 syngeneic 6DT1 mammary cancer cells into the fourth mammary fat pad. At 9 days post injection, a palpable tumor was formed, and mice received an intravenous injection of CyPF$_6$, CyFPhB, or CyTPFB through the tail vein. Biodistribution of organic salts was tracked using a fluorescent stereo microscope, which allowed monitoring of tumor localization and PS clearance from normal

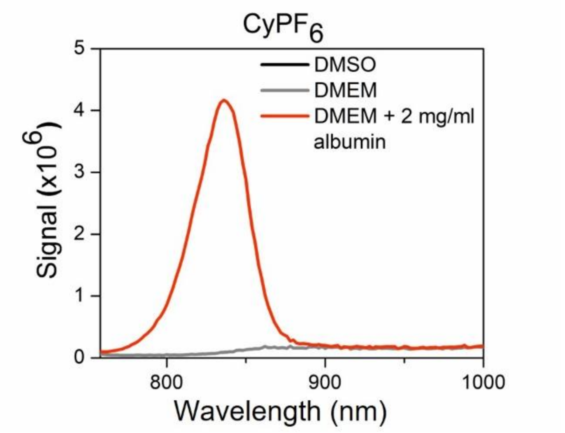

Figure 9.7. Photoluminescence spectra of CyPF$_6$ monomers. Background corrected photoluminescence spectra for 1 μM CyPF$_6$ monomers in DMSO, DMEM, and DMEM + 2 mg/mL bovine serum albumin demonstrates that albumin association does not significantly influence fluorescent quantum yields.

tissue. To assess *in vivo* biodistribution, fluorescence intensity was measured over 5 days from the tumor (located on the right mammary fat pad), the non-tumor bearing left mammary fat pad, and the liver (Figure 9.8a).

CyPF$_6$ was rapidly uptaken by all measured tissue within the first 12 hours, with initial localization in the liver for 1.5 to 6 hours, predominately. Maximal tumor uptake was at 24 hours with modest tumor retention over 48 hours before gradually diminishing after 72 hours. Observed tumor clearance was slower than from normal tissue, with a difference in fluorescence at 48 hours of 25% ± 5%; however, tumor fluorescence cleared rapidly with poor overall retention (Figure 9.8b). Tumor uptake of CyFPhB was found to be slower compared to CyPF$_6$ which reached maximal uptake at 48 hours (Figure 9.8c). The liver uptake of CyFPhB was negligible with similar levels of fluorescence signal to background tissue (i.e., non-tumor bearing right mammary fat pad). Moreover, CyFPhB showed exceptional tumor specific uptake, reaching 45% ± 10% increase in fluorescence signal from surrounding tissues over 48 to 72 hours and stably retained for more than 120 hours, demonstrating promising therapeutic potential for PDT. Furthermore, tumor and liver showed significantly reduced uptake of CyTPFB compared to both CyPF$_6$ and CyFPhB (Figure

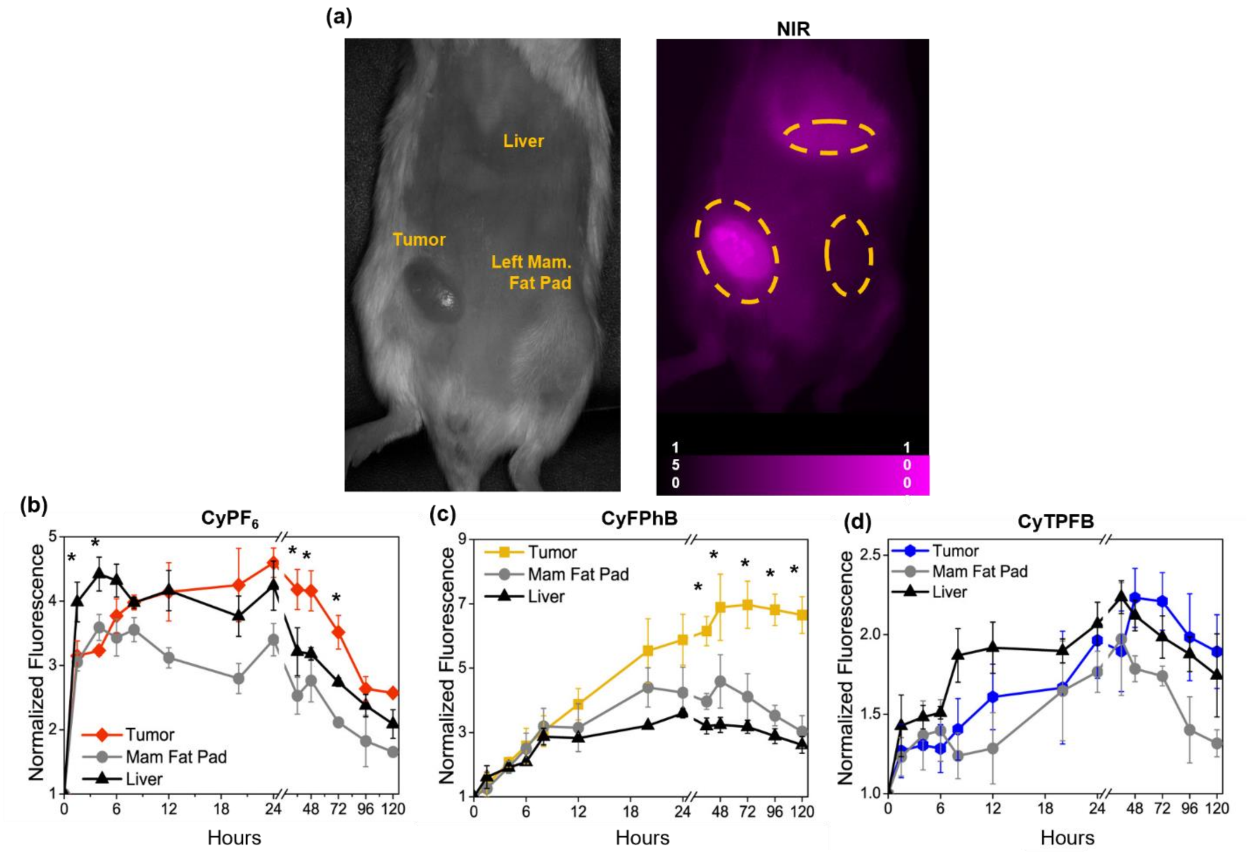

Figure 9.8. In vivo biodistribution data shows organic salts preferentially accumulate and are retained within 6DT1 mammary tumors. Following 6DT1 mammary tumor formation, mice received a tail vein injection of 1 μmol/kg CyPF$_6$, 3 μmol/kg CyFPhB, or 5 μmol/kg CyTPFB. **(a)** NIR fluorescence from the tumor-bearing fourth right mammary fat pad (Tumor), liver (Liver), and left fourth mammary fat pad (Left Mam. Fat Pad) was measured to determine biodistribution of organic salts. Picture is a mouse dosed with 1 μmol/kg CyPF$_6$ at 48 hours. Fluorescence intensity was normalized to a vehicle control. Normalized fluorescence of **(b)** CyPF$_6$, **(c)** CyFPhB, and **(d)** CyTPFB were measured in the tumor-bearing fourth right mammary fat pad (Tumor), liver (Liver), and left fourth mammary fat pad (Mam Fat pad). Data are displayed as means ± S.D., $n = 3$. Statistically significant differences (p-value < 0.05) between tissue fluorescent intensity are marked with asterisks.

9.8d). Collectively, these *in vivo* biodistribution results indicate that organic salts preferentially accumulate and are retained within 6DT1 tumors.

9.2.4 CyFPhB is a selectively phototoxic antitumor agent when combined with NIR irradiation

To explore the potential effects of fluorescent organic salts as potent PSs for PDT, we further performed *in vivo* studies in FVB mice orthotopically injected with 6DT1 mammary cancer cells. Tumor-bearing mice were dosed with 1 to 5 μmol/kg of the indicated organic salt or vehicle

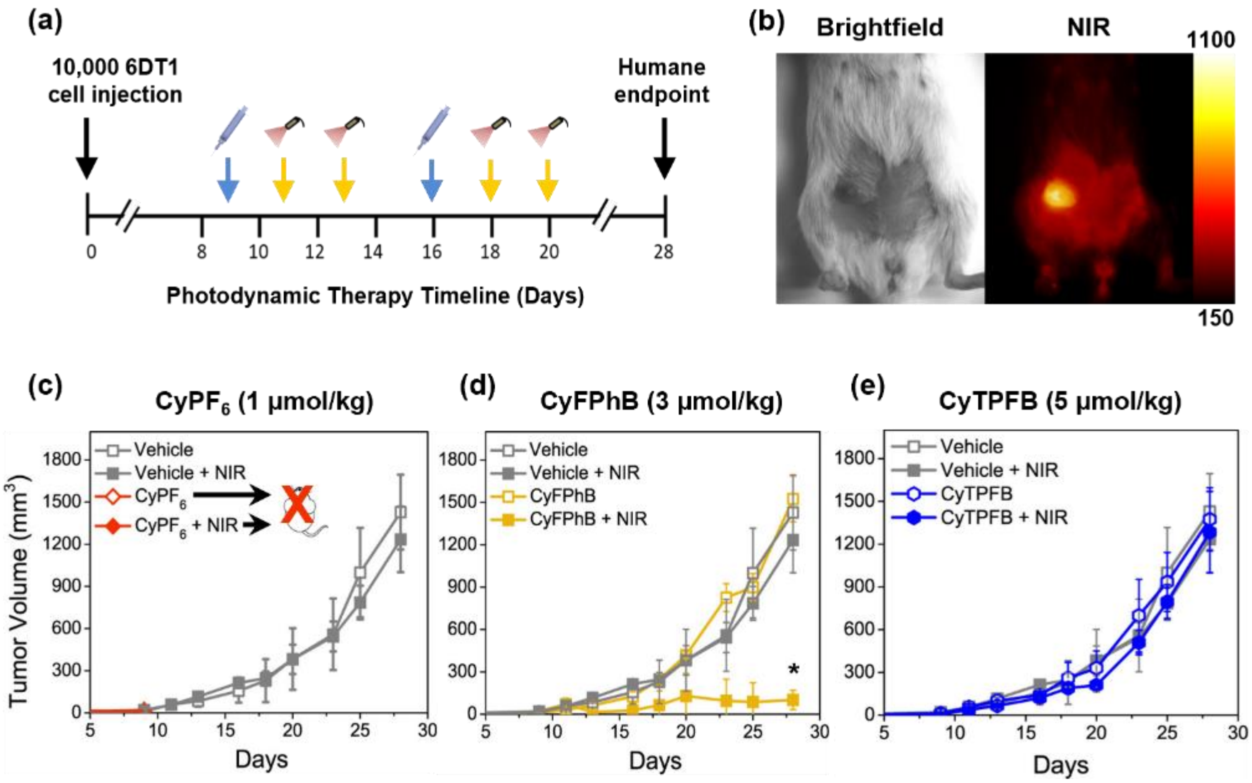

Figure 9.9. Counterion tuning of organic salts produces a potent photosensitizer (PS) for photodynamic therapy (PDT) in a mouse model of breast cancer. (a) Experimental overview of photodynamic therapy experimental timeline. FVB mice were injected with 10,000 6DT1 cells into the fourth right mammary fat pad. After 9 days, when a palpable tumor was present, mice were dosed with an organic salt via intravenous tail vein injection. After 2 days the organic salt localized within the tumor and cleared from the surrounding offsite tissue. Mice were then irradiated with 150 J/cm^2 of 850 nm near-infrared light (NIR) at 48 and 96 hours following organic salt administration. This PDT regimen was repeated one week after the first organic salt injection. Tumor growth was monitored throughout the course of the experiment with manual caliper measurement for 28 days, when mice are euthanized due to tumor burden. **(b)** Representative image of tumor specific localization of organic salts prior to NIR light irradiation. Pictured is an FVB mouse 44 hours post IV injection of 5 μmol/kg CyFPhB. Tumor volume was measured in tumor-bearing mice treated with vehicle (Veh) or **(c)** 5 μmol/kg CyPF$_6$, **(d)** 3 μmol/kg CyFPhB, or **(e)** 5 μmol/kg CyTPFB with (+NIR) or without NIR irradiation. Data are displayed as means ± S.D., $n = 4$. Error bars represent S.D. Statistically significant differences (p-value < 0.05) in CyFPHB + NIR tumor volumes from control groups at endpoint are marked with asterisks (*).

control (Veh) and further irradiated with 150 J cm^{-2} of 850 nm light (Veh + NIR, CyX + NIR) at 48 and 96 hours following organic salt administration (Figure 9.9a-b). Tumor volume was monitored with caliper measurements, and mice were euthanized on day 28 due to tumor burden in control groups. Mouse health was monitored throughout the experiment by weight and visual

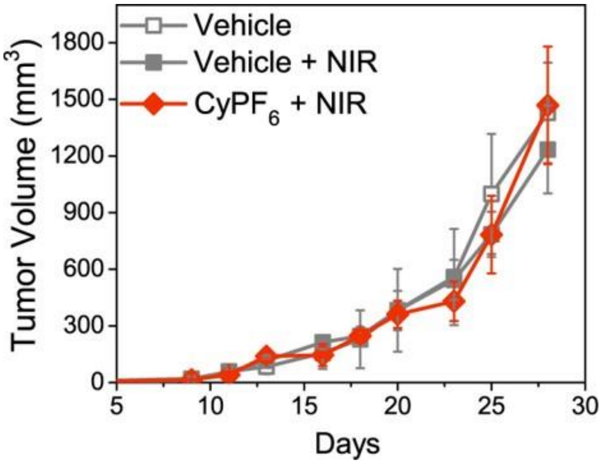

Figure 9.10. Tumor growth with 3 µmol/kg CyPF$_6$ in a mouse model of breast cancer. Tumor volume was measured in tumor-bearing mice treated with vehicle, vehicle + NIR irradiation, or 3 µmol/kg CyPF$_6$. Severe tail swelling after the first injection of 3 µmol/kg CyPF$_6$ limited the treatment protocol to one organic salt injection and two light treatments. Data are displayed as means ± S.D., *n* = 3. Error bars represent S.D.

inspection every other day as well as blood chemistry assays at endpoint.

Mice in the 5 µmol/kg CyPF$_6$ + NIR treatment group were all died within 24 hours post-injection (Figure 9.9c). Mice in the 3 µmol/kg CyPF$_6$ + NIR treatment group exhibited severe tail swelling, limiting treatment to only one course of the PDT protocol, and there were no observable changes to tumor growth or appearance following light irradiation (Figure 9.10). Mice treated with 1 µmol/kg CyPF$_6$ with or without NIR light irradiation did not display any discernable effect on tumor growth compared to control groups (Figure 9.11). Similar lack of effect was observed *in vivo* with CyI at low dosage (Figure 9.12), another highly cytotoxic combination we previously reported *in vitro*.[143] A higher dosage (5 µmol/kg CyPF$_6$) of either cytotoxic compound led to mouse death.

CyFPhB + NIR treatment (3 µmol/kg) showed a potent antitumor effect in mice, with a 93% reduction in tumor volume compared to control groups at experimental endpoint (Figure 9.9d). Following the first light treatment on day 11, a bruise developed around the tumor, which then formed a black eschar. This is indicative of vascular specific-PDT, a combination of direct

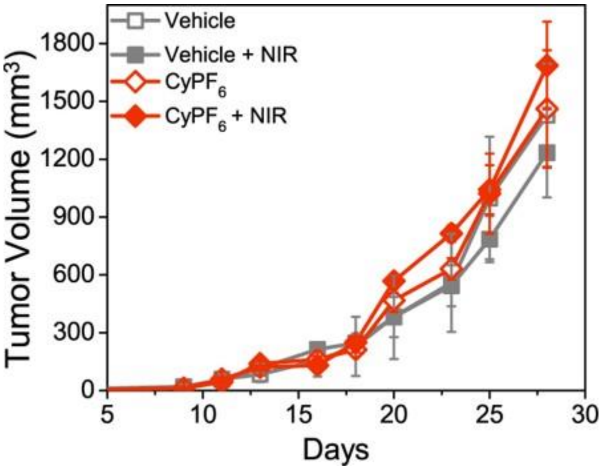

Figure 9.11. Tumor growth with 1 μmol/kg CyPF$_6$ in a mouse model of breast cancer. Tumor volume was measured in tumor-bearing mice treated with vehicle or 1 μmol/kg CyPF$_6$ with (+NIR) or without NIR irradiation. Data are displayed as means ± S.D., *n* = 4. Error bars represent S.D.

photodamage to the cancer cells and ablation of the tumor vascular, which starves the tumor of nutrients.[316] Mice in the CyFPhB + NIR group, in which tumor growth was stopped, were all visually healthy at experimental endpoint. In contrast, mice in the remaining three control groups, which were treated with CyFPhB (without NIR irradiation), Veh (without NIR irradiation), and Veh + NIR, all displayed severe labored breathing and decreased activity by day 28 from unrestricted tumor growth.

Treatment with 5 μmol/kg CyTPFB with or without NIR light did not exhibit any antitumor

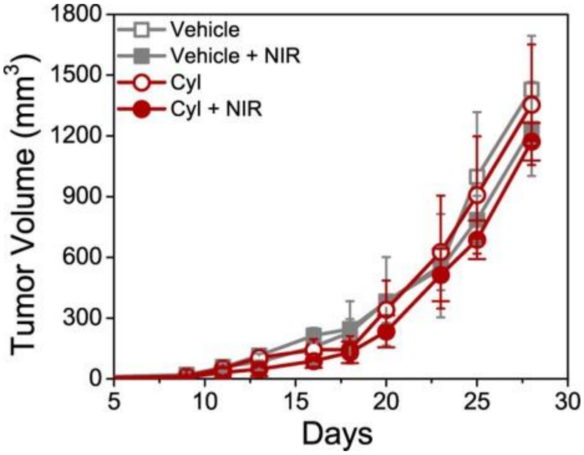

Figure 9.12. Tumor growth with 1 μmol/kg CyI in a mouse model of breast cancer. Tumor volume was measured in tumor-bearing mice treated with vehicle or 1 μmol/kg CyI with (+NIR) or without NIR irradiation. Data are displayed as means ± S.D., *n* = 4. Error bars represent S.D.

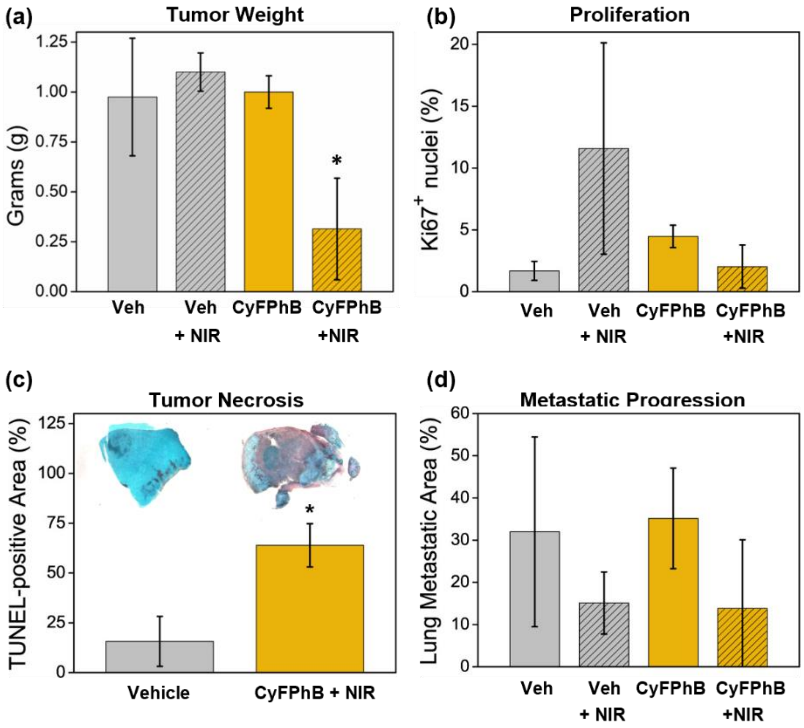

Figure 9.13. CyFPhB irradiated with NIR light induces an antitumor effect via tumor necrosis and impedes cancer progression in a breast cancer mouse model. At the end of the PDT experiment, tumor tissue was collected for further analysis of disease progression by **(a)** tumor weight, **(b)** Ki67 staining, **(c)** terminal deoxynucleotidyl transferase dUTP nick end labeling (TUNEL), and **(d)** lung histology, $n = 3$. Representative images of each group are shown in **(c)**. Error bars represent S.D. Statistically significant differences (p-value < 0.05) in CyFPhB + NIR values from control groups are marked with asterisks (*).

effect in mice, and no differences in tumor volume were observed between any of the groups (Figure 9.9e). Additionally, all mice were visually healthy at experimental endpoint, suggesting that CyTPFB is non-toxic *in vivo* at approved maximum doses.

At experimental endpoint, mice were sacrificed, and tumors were collected, weighed, and analyzed histologically for further assessment of treatment response. The CyFPhB + NIR group displayed 69% decrease in tumor weight compared to control groups, confirming volume calculations from caliper measurements (Figure 9.13a). A concern with many cancer treatments is that the treatment may drive selection to induce increased tumor malignancy, leading to recurrence and drug resistance.[317,318] To assess this, healthy margins of tumors were stained for Ki67, a

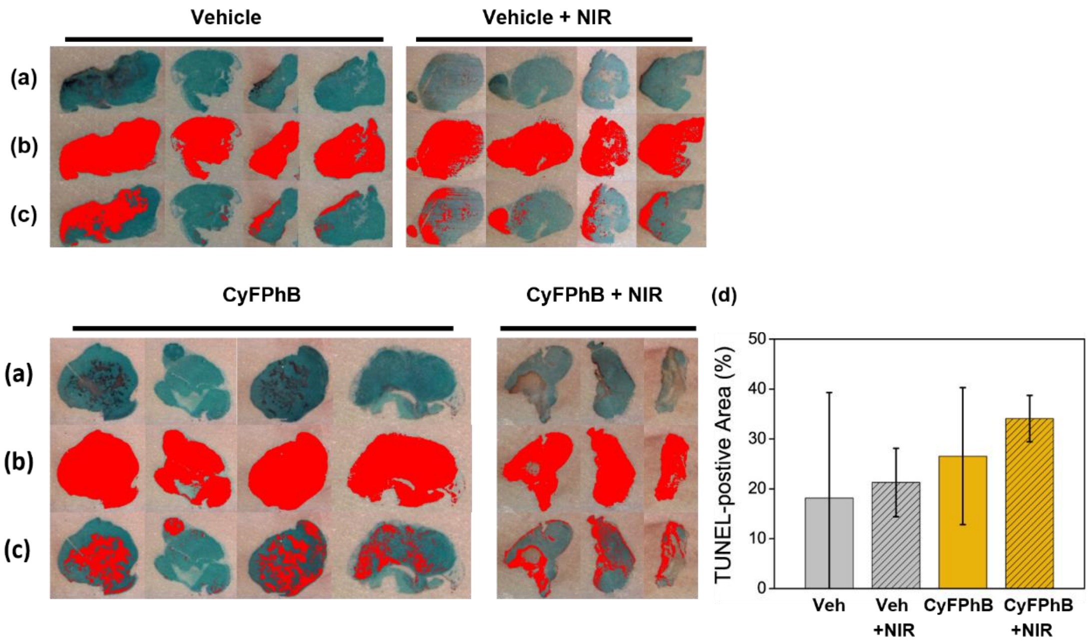

Figure 9.14. TUNEL assay color thresholds for treatment groups at experimental endpoint (28 days). (a) Cross-section of tumors after TUNEL staining. Images with **(b)** TUNEL^{+} area highlighted, and **(c)** full tumor area highlighted were used to calculate the percent area of TUNEL^{+} staining shown in **(d)**.

proliferation biomarker commonly used to prognose tumor aggressiveness.[319,320] There was no increase in Ki67^{+} nuclei in the FPhB + NIR group compared to the control groups, and all tumors were Ki67^{+}-low by percent-positive nuclei (Figure 9.13b). Additionally, terminal deoxynucleotidyl transferase dUTP nick end labeling (TUNEL) assays were used to determine apoptotic and necrotic regions within the CyFPhB-NIR treated tumors.[321] TUNEL-stained cells were identified by brown staining within tumor cross-sections. Samples taken at the experimental end point of 28 days no longer had any relevant necrotic regions (Figure 9.14). However, samples taken 72 hours after PDT treatment displayed extensive TUNEL-staining, indicating tumor necrosis and apoptosis (Figure 9.13c, Figure 9.15).

To determine efficacy against metastatic disease, we further investigated the ability of CyFPhB + NIR to inhibit lung metastasis. Lungs were harvested, fixed in formalin, and sectioned for hematoxylin and eosin (H&E) staining. To quantify the extent of metastasis, we analyzed the

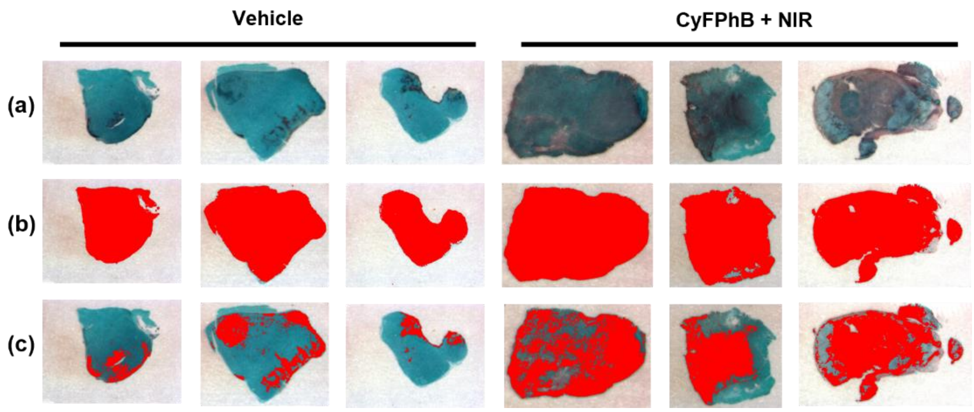

Figure 9.15. Representative TUNEL assay color thresholds for Vehicle and CyFPhB + NIR treatment groups three days after PDT treatment. (a) Cross-section of tumors after TUNEL staining. **(b)** TUNEL$^+$ area highlighted, and **(c)** full tumor area highlighted was used to calculate the percent area of TUNEL$^+$ staining shown in Figure 9.13c.

percent metastatic area, which was identified by high hematoxylin (blue) staining in nuclei-dense regions. While the average percentage of metastatic area was lower in the CyFPhB + NIR group, the difference was not statistically significant due to a wide degree of variation within groups (Figure 9.13d). Altogether, these results indicate that the combination of CyFPhB with NIR is an ideal PS for PDT *in vivo*, displaying a potent anti-tumor effect by triggering tumor apoptosis and necrosis in an orthotropic mouse model of breast cancer.

9.2.5 CyFPhB + NIR antitumor treatment has minimal side effects on normal tissue

To examine acute toxic side effects, we further monitored mouse weight and skin irritation at the site of light irradiation throughout the course of the experiment. Due to the aggressiveness of the 6DT1 breast cancer model, control tumors displayed minor ulceration prior to experimental endpoint. The CyFPhB + NIR group developed an eschar overlying the tumor following treatment, but otherwise appeared to be in good overall condition at experimental endpoint with no significant decrease in mouse weight observed throughout the treatment course (Figure 9.16a). The minor difference in final weight observed at the end of the experiment was not statistically significant and could be accounted for by the lack of a large tumor in CyFPhB + NIR mice. No mouse lost

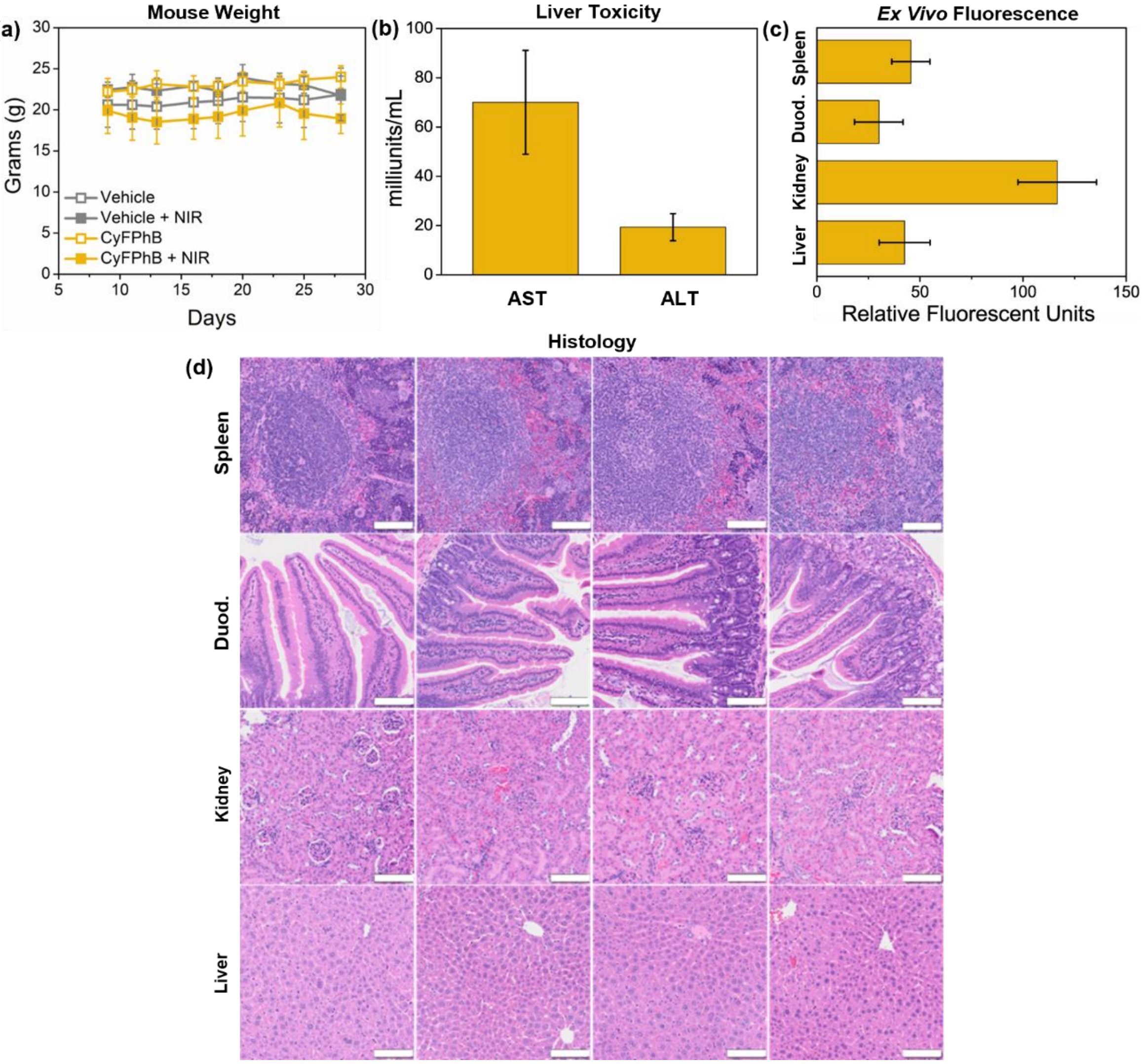

Figure 9.16. Minimal systemic toxicity observed with CyFPhB + NIR treatment in mice. (a) Mouse weight was monitored throughout the experiment. **(b)** Aspartate aminotransferase (AST) and alanine aminotransferase (ALT) serum levels were measured to assess liver damage at experimental endpoint in CyFPhB + NIR treatment mice. All measurements were within normal serum levels. **(c)** Residual fluorescence of normal biological tissue (spleen, duodenum, kidney, liver) were measured from CyFPhB + NIR treatment mice. **(d)** Representative histological images from each treatment group are shown. Scale bars: 100 µm. Data are displayed as means ± S.D., *n* = 4.

more than 10% of body weight throughout the course of the experiment.

Other clinical parameters were also examined to assess for evidence of end organ dysfunction affecting the kidneys and liver. Proteinuria was not detected in any group as measured by urine reagent test strips. Liver injury was assessed at the end of the experiment by measuring

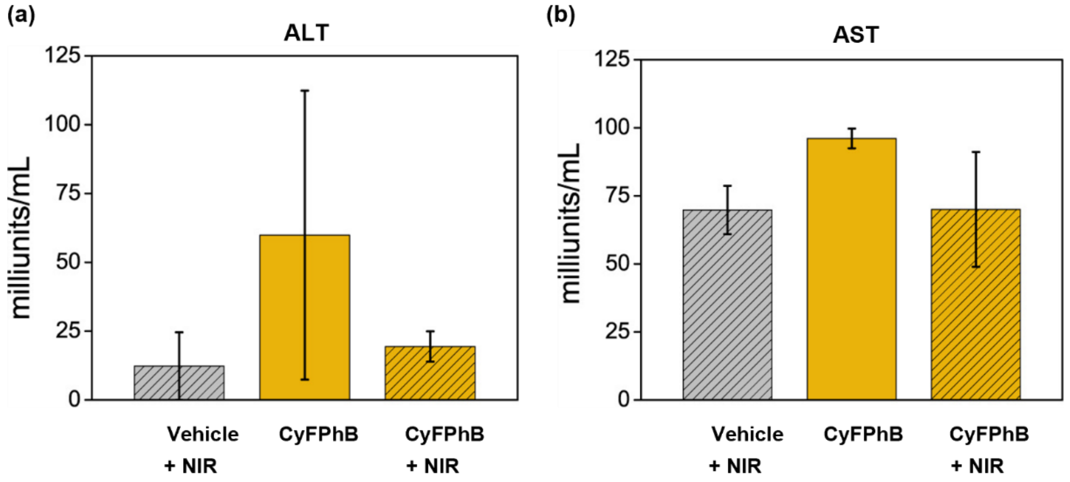

Figure 9.17. Serum levels of liver enzymes ALT and AST. At experimental endpoint, **(a)** alanine aminotransferase (ALT) and **(b)** aspartate aminotransferase (AST) serum levels were measured to assess liver damage. All treatment groups fall within normal serum levels.

serum levels of aspartate aminotransferase (AST) and alanine aminotransferase (ALT), biochemical markers of liver damage. All CyFPhB + NIR treatment mice displayed serum values within normal ranges and were unchanged compared to control treatment mice serum values (Figure 9.16b, Figure 9.17).[322]

Additional potential offsite toxicity was assessed from tissue where residual fluorescence was noted upon *ex vivo* organ extraction, notably the spleen, kidneys, duodenum, and liver (Figure 9.16c). These tissues were fixed in formalin and underwent H&E staining. The CyFPhB + NIR group did not display any morphological alterations or increased inflammatory exudation (Figure 9.16d). Collectively, this data demonstrates that CyFPhB nanoparticles are a promising photosensitizing anticancer agent with minimal side effects.

9.3 Discussion

In this study, we report the utility of counterion-tuned organic salt nanoparticles for *in vivo* PDT in a mouse model of breast cancer. We developed an *in vivo* PDT regimen for assessment of counterion-tuned organic salts antitumor efficacy, biodistribution, and off-site toxicity to normal tissue. Counterion modulation is required to control the cyto- and photo-toxicities of organic salt nanoparticles for *in vivo* therapeutic applications. Consistent with our findings *in vitro*,[143] phototoxic CyFPhB is an ideal candidate for *in vivo* PDT. Cytotoxic CyI and $CyPF_6$ are too toxic for *in vivo* PDT, while CyTPFB displays little phototoxicity. By using counterion $FPhB^-$ to decrease cytotoxicity while maintaining phototoxicity of Cy^+, we have reduced off-target cytotoxicity and improved phototoxicity to inhibit tumor growth in an aggressive breast cancer model. We report CyFPhB has improved characteristics for a therapeutic PS including: high NIR absorption coefficient, prolonged tumor retention, and high phototoxicity relative to cytotoxicity with a reduction in tumor growth by 93% and minimal toxicity to normal tissue.

Following CyFPhB treatment, we observed shrinking of tumors in mice and formation of necrotic and apoptotic regions, determined by TUNEL-staining. This is likely due to a combination of PDT-induced photodamage directly to tumor and indirectly to the vasculature, which leads to tumor starvation and necrosis.[323] We have previously demonstrated that fluorescent organic salts preferentially accumulate in the mitochondria of cancer cells and generate mitochondrial superoxide.[143] Vasculature-PDT has been reported in clinically approved PS talaporfin sodium and is characterized by bruising at the irradiation site.[324]

We report a lower trend of lung metastasis in CyFPhB treatment groups, despite directly treating only the primary tumor site. This could be due to the reduced tumor growth, ablation of the tumor vasculature preventing cancer cell intravasation, and/or antitumor immune activation. Certain PDT regimens have been shown to induce damage-associated molecular patterns (DAMPs), which stimulate the innate immune system and generate a systemic antitumor surveillance response to inhibit metastasis.[325] The influence of the immune system on PDT and anticancer treatment is crucial and should be accounted for when identifying appropriate models for studies.[326] Future work will further investigate the potential role of counterion-tuned organic salt nanoparticles for treatment of metastatic disease.

We also assessed potential uptake mechanisms *in vitro* to elucidate the cause of tumor-specific accumulation and assess translatability to alternative cancer models and diseases. We find that through a combination of serum albumin interaction and Oatp uptake, the organic salt nanoparticles preferentially concentrate within tumors. We find a higher degree of liver accumulation for $CyPF_6$ and CyTPFB, likely due to their strong reliance on cellular uptake by Oatps, which are also expressed in the liver.[327] *In vitro*, $CyPF_6$ displays albumin-induced monomeric formation; however, increasing concentrations of albumin lead to decreased uptake. Conversely, CyFPhB is dependent on albumin for cellular uptake. We report lower levels of CyFPhB liver accumulation *in vivo*, and significantly higher levels of tumor retention over time.

9.4 Conclusions

Our findings demonstrate that our counterion tuning strategy has clinical potential and could transform PS engineering. We have demonstrated efficacious PDT in an immunocompetent mouse model of metastatic breast cancer, paving the way for translation to human cancer. Additional tumor-targeting may be achieved by stable incorporation of these organic salt nanoparticles with antibody conjugation, which are common engineering platforms for multi-agent tumor delivery. Indeed, NIR-PSs are promising components for multimodal synergistic cancer therapy, as they have deep tissue imaging capabilities.[328,329] Reducing the nonspecific cytotoxicity and improving phototoxic yields of NIR organic salts with counterion tuning is a promising engineering strategy to advance tumor-specific PDT and cancer treatment.

9.5 Materials and methods

9.5.1 Synthesis and purification of organic salts

Precursor salts (CyI and $NaPF_6$, NaFPhB, or KTPFB) were dissolved in 5:1

methanol:dichloromethane (MeOH:DCM) mixtures and stirred at room temperature under inert nitrogen gas. The counterion precursor was added in 100% molar excess to drive the exchange of ions, and the product compounds precipitate out of solution after 5 minutes. Product was collected using vacuum filtration and rinsed with MeOH. Crude product was dissolved in minimal DCM and run through a silica gel plug with a DCM wash to remove unreacted precursors, side products, and other impurities. The product compound exiting the silica was identified by its color and elution time and collected. Excess DCM was removed in a rotary evaporator. Reaction yield and purity were confirmed using a high mass accuracy time-of-flight mass spectrometer coupled to an ultra-high performance liquid chromatography (UHPLC-MS) in positive mode to quantify cations, and in negative mode to quantify anions. Typical reactions led to products yields of >60% with purities >95%. Reaction schemes and purification procedures described previously were used.[95,102]

9.5.2 Cell culture conditions

Mouse mammary carcinoma cells (6DT1) were cultured in Dulbecco's Modified Eagle's Medium (Cat. No. 10-017CM, Corning, NY, USA) with 4.5 g/L glucose without sodium pyruvate with 10% heat inactivated fetal bovine serum (Cat. No. F0392, Sigma, St. Louis, MO, USA) supplemented with 2 mM glutamine and 1% penicillin and streptomycin (Cat. No. 15323671, Corning, NY, USA). Cells were incubated in 37 °C with 5% CO_2 without light exposure. Fluorescent organic salts were dissolved to 5.6 mM in dimethyl sulfoxide (Cat. No. D4540, Millipore Sigma, St. Louis, MO, USA), and then further diluted in aqueous solution to form nanoparticles for various experiments.

9.5.3 Cell viability studies

6DT1 cells were seeded at a density of 40,000 cells per well in 6-well tissue culture plates, in dye-laced or vehicle (DMSO) media. After 24 hours of incubation, media was aspirated and replaced with untreated media. Each well was irradiated with an 850 nm LED lamp with an irradiation flux of 425 mW/cm^2 for 30 minutes in the incubator, and control cells were left in a dark incubator without irradiation. Following irradiation treatment, the media was replenished with fresh dye-laced media and allowed to incubate for another 24 hours. The same procedure was done at 48 and 72 hours, but the cells received no further dye-laced media after 72 hours. Viable cell number was determined at 96 hours using 4% trypan blue and a Nexcelom Cellometer Auto T4 cell counter. All assays were done with three biological replicates. The half maximal inhibitory concentration (IC$_{50}$) was determined by plotting percent inhibition versus concentration and fitting using a nonlinear regression with GraphPad Prism.

9.5.4 Kinetic inhibition studies

6DT1 cells were seeded at a density of 25,000 cells per well in 24-well tissue culture plates. After 24 hours, cells were pre-incubated for 15 minutes with 250 µM bromosulfophthalein (Cat. No. 21058, Cayman Chemical, Ann Arbor, MI, USA), or 12 hours with 1 mM dimethyloxalylglycine (Cat. No. D3695, Sigma-Aldrich, St. Louis, MO, USA). Following the indicated pre-incubation with each inhibitor, the inhibitor-laced media was replaced with organic salts and inhibitor-laced media. For live cell imaging, the cells were washed three times with PBS and excited with 740 nm light. Fluorescence was measured using a Leica DMi8 microscope with a Cy7 filter cube, PE4000 LED light source, DFC9000GT camera, and LAS X imaging software. Cellular fluorescence was measured at the indicated timepoints, and all conditions were done in triplicate. Fluorescence was quantitated using ImageJ software. Curve fitting was performed with Origin Pro8 software by plotting relative fluorescent units versus time and using a dose-response sigmoidal equation.

9.5.5 Endocytosis inhibition studies

6DT1 cells were seeded at a density of 25,000 cells per well in 24-well tissue culture plates. After reaching 80-90% confluency, cells were serum starved for 2 hours. Following serum starvation, cells were pre-incubated either for 30 minutes in 3 mM amiloride (Cat. No. A7410, Sigma-Aldrich, St. Louis, MO, USA), 1 hour in 1 mM methyl-β-cyclodextrin (Cat. No. C4555, Sigma-Aldrich, St. Louis, MO, USA), or for 20 minutes with 200 µM dynasore (Cat. No. 120192, Abcam). Following pre-incubation with various endocytotic inhibitors, inhibitor-laced media was replaced with organic salts and inhibitor-laced media. After 24 hours, cellular fluorescence was measured as described above.

9.5.6 Ultraviolet-visible light spectroscopy

Organic salts were diluted to a concentration of 5 µM in cell media and combined with the indicated concentrations of inhibitors. For albumin characterization, organic salts were diluted to a concentration of 5 µM in cell media, serum free media (DMEM), and DMEM with the indicated concentrations of BSA. All dyes were characterized using a 25 UV-Vis spectrometer (Perkin-Elmer, Waltham, MA, USA) in the wavelength range from 500-1100 nm in normal incidence transmission mode with a resolution of 1 nm and a 1.27 cm path length. Cell media with inhibitors was used as the solvent reference to remove reflections so that the absorption is calculated as 1-transmission.

9.5.7 Bovine serum albumin (BSA) uptake studies

Purified bovine serum albumin (Cat. No. A7030. Sigma-Aldrich, St. Louis, MO, USA) was resuspended in serum-free media (DMEM) and was serially diluted to create the indicated concentrations. Indicated concentrations of fluorescent organic salts were added to solutions, and after 14 hours cellular fluorescence was measured as described above.

9.5.8 Photoluminescence

Photoluminescence (PL) spectra were collected using a Photon Technology International (PTI) Spectrofluorometer for monomers of 5 μM $CyPF_6$ that was completely solubilized in DMSO or associated with 2 mg/mL BSA in DMEM without phenol red.

9.5.9 Orthotopic cancer model

All animal protocols were approved and performed in accordance with guidelines set by the Institute of Animal Care and Use Committee (IACUC) of Michigan State University (license number: 201900200). 6DT1 cells were harvested for tumor implantation at 80% confluence while in the logarithmic phase of growth. 10,000 6DT1 cells in 50 μL of sterile saline were inoculated into the right fourth mammary fat pad of 6-8 week-old syngeneic FVB/NJ female mice (purchased from Jackson Laboratories, Bar Harbor, ME, USA), as described previously.[330] Tumor growth was monitored every other day with external caliper measurements to determine tumor length and width to calculate volume, $V = L \times W^2/2$. Animal wellbeing was also monitored by recording mouse weight every other day and watching for potential skin irritation at the tumor site. The presence of protein in urine was monitored using urine reagent test strips (URS-1B/G/K/P, Cortez Diagnostics). Mice were euthanized at a 28-day endpoint, when majority of control mice exhibit excessive morbidity due to tumor burden. Following euthanasia by carbon dioxide asphyxiation and subsequent cervical dislocation, tissues of interest were collected for further analysis.

9.5.10 In vivo imaging

For biodistribution studies, at 11 days post orthotopic injection tumor bearing mice were dosed with 1 μmol/kg $CyPF_6$, 3 μmol/kg CyFPhB, or 5 μmol/kg CyTPFB via intravenous tail vein injection. For imaging, mice were anesthetized with 2.5% isoflurane and brightfield and NIR fluorescent images were taken at the indicated time points using a Leica M165FC stereoscope with a 740 nm PE4000 LED light source, DFC9000GT camera, and LAS X imaging software. Using ImageJ, brightfield images were used to determine regions of interest (ROIs) for the tumor in the right fourth mammary fat pad, the liver, and the left fourth mammary fat pad. ROIs were then overlaid on the NIR fluorescent image for blinded quantitation of fluorescence intensity and normalized to a vehicle injected mouse. The study ended after 5 days upon tumor ulceration due to rapid tumor growth.

9.5.11 Photodynamic therapy

At 9 days post orthotopic injection tumor-bearing mice were randomly divided into four treatment groups: 1. vehicle injection (Veh), 2. organic salt injection (CyX), 3. vehicle injection with NIR light irradiation (Veh + NIR), and 4. organic salt injection with NIR light irradiation (CyX + NIR). For organic salt injection treatment groups (2 and 4), mice were given a 1-5 µmol/kg intravenous injection of a fluorescent organic salt dissolved in 5% DMSO and 0.03% Tween 20 in 100 µL of sterile saline prior to injection through the lateral tail vein. Vehicle groups (1 and 3) received a tail vein injection of 5% DMSO and 0.03% Tween 20 in 100 µL of sterile saline. ImageJ software was used to quantitate relative brightness and localization within tumor tissue relative to normal tissue at various time points throughout the experimental study. At 48 hours post IV injection of the organic salt, NIR light irradiation groups (3 and 4) were anesthetized with 2.5% isoflurane, placed on a heated pad, and underwent tumor irradiation with an 850 nm LED. Mice received a 120-150 J/cm^2 dose over 15-20 minutes, depending on previously decided treatment conditions. This was repeated 48 hours later. A week following the first organic salt IV injection, the PDT treatment was repeated.

9.5.12 Histology

All histologic preparation and immunohistochemistry staining was performed by the

Investigative HistoPathology Laboratory at Michigan State University. Tumor, lung, spleen, kidney, liver, and duodenum were harvested, fixed in formalin, embedded in paraffin, sectioned, and stained with hematoxylin and eosin (H&E) for qualitative analysis. Tissues were visualized using an Olympus VS200 research slide scanner at 20x magnification.

9.5.13 Ki67 nuclei staining assessment

Ki67 staining was measured using images taken from healthy cross-sections of tumors. Image processing was performed in ImageJ. The color images were first deconvoluted into hematoxylin (H) and diaminobenzidine (DAB) color channels using Color Deconvolution (“H DAB” deconvolution matrix). Deconvoluted H and DAB images were saved as new TIFF images. For each image, smoothing was applied 5 times, then Auto Local Threshold was performed using Phansalkar’s's algorithm to detect stained nuclei. Stained nuclei were counted using Analyze Particles (minimum size 30, minimum circularity 0.3). To check that threshold parameters were appropriate, several output images were manually inspected to confirm that visually identifiable nuclei were properly counted. The percent Ki67$^+$ nuclei were calculated as the ratio of DAB-stained nuclei counts (representing proliferating cells) to H-stained nuclei counts (representing all cells) for each tumor.

9.5.14 TUNEL-area quantification

Terminal deoxynucleotidyl transferase–mediated dUTP nick end labeling (TUNEL) assays were evaluated using ImageJ to determine the percentage of necrotic to total area of each tumor cross-section. Images were acquired using a Leica M165FC stereo microscope operated at 1.6x magnification. Images were duplicated, smoothed to reduce artifacts, and color thresholding was used to select either the TUNEL$^+$ area or the entire tumor area. Representative thresholding can be found in Figure 9.14 and Figure 9.15.

9.5.15 Metastatic lung area assessment

Microscope images of lung histology slides were analyzed using ImageJ. Colors were converted using “Dichromacy > Tritanope” filter then split into three channels, and the “blue” channel showing high overall intensity was subtracted from the “red” channel showing high selective intensity in high-hematoxylin tumor tissue regions. Resultant images showing selective highlighting of tumor tissue region was then smoothed to reduce thresholding artifacts and finally thresholding applied using Auto Local Threshold with Phansalkar’s's algorithm to quantitate area of tumor tissue regions. Image processing workflows described previously were used.[331]

9.5.16 Alanine aminotransferase (ALT) and aspartate aminotransferase (AST) assays

Serum levels for alanine aminotransferase (Cat. No. MAK052, Sigma-Aldrich, St. Louis, MO, USA) and aspartate aminotransferase (Cat. No. MAK055, Sigma-Aldrich, St. Louis, MO, USA) were measured using commercially available kits according to the manufacturer's protocol. Samples were run in duplicate and averaged for analysis, before averaging levels for each treatment group.

9.5.17 Statistical analyses

Statistical analyses were performed using an unpaired student’s t-test and all error bars are representative of standard deviation, except where otherwise noted. All displayed data has a minimum of three biological replicates. Curve fittings were done using Origin Pro8 and GraphPad Prism software. P-values < 0.05 are reported as statistically significant (*).

Chapter 10 - Future Directions for Research

In this chapter, we present future directions of research for the four projects discussed in this thesis. We consider general approaches, specific next steps, and long-term goals to achieve high efficiency devices and produce more organic salt anti-cancer agents.

10.1 Organic salt photovoltaics

Future work with organic salt-based photovoltaics could investigate two subsequent routes, 1) systematic exploration of novel near-infrared absorbing organic salt formulations utilizing a conventional bilayer approach, and 2) new architectures and deposition routes enabling higher efficiency PVs and TPVs. The following sections outline pathways to explore each of these routes.

10.1.1 New organic salts

To directly build on the newly understood relationship between charge character on anionic chromophores and charge transfer through bulk organic salt films there are three key research areas to explore, 1) the effect of the counterion on charge transfer for anionic chromophore based organic salts, 2) the relationship between charge character and cationic chromophores, and 3) the proper counterion and charge character selection to optimize exciton diffusion and charge transfer for organic salts with cationic or anionic chromophores.

One of the remaining unknowns from our study on the impact of charge character on charge transfer in anionic heptamethine based OPVs was the nature of hole transport and the route that holes take to travel through an organic salt film. To fully understand this, counterion exchanges could be made for the sodium (NaCy1 to XCy1) and the subsequent devices analyzed using similar experimental and computational methods to quantify exciton diffusion and charge collection. Counterion exchange to a series of cations with increasing size, halogenation, or charge character could all provide interesting studies and reveal more about charge transfer in anionic cyanines.

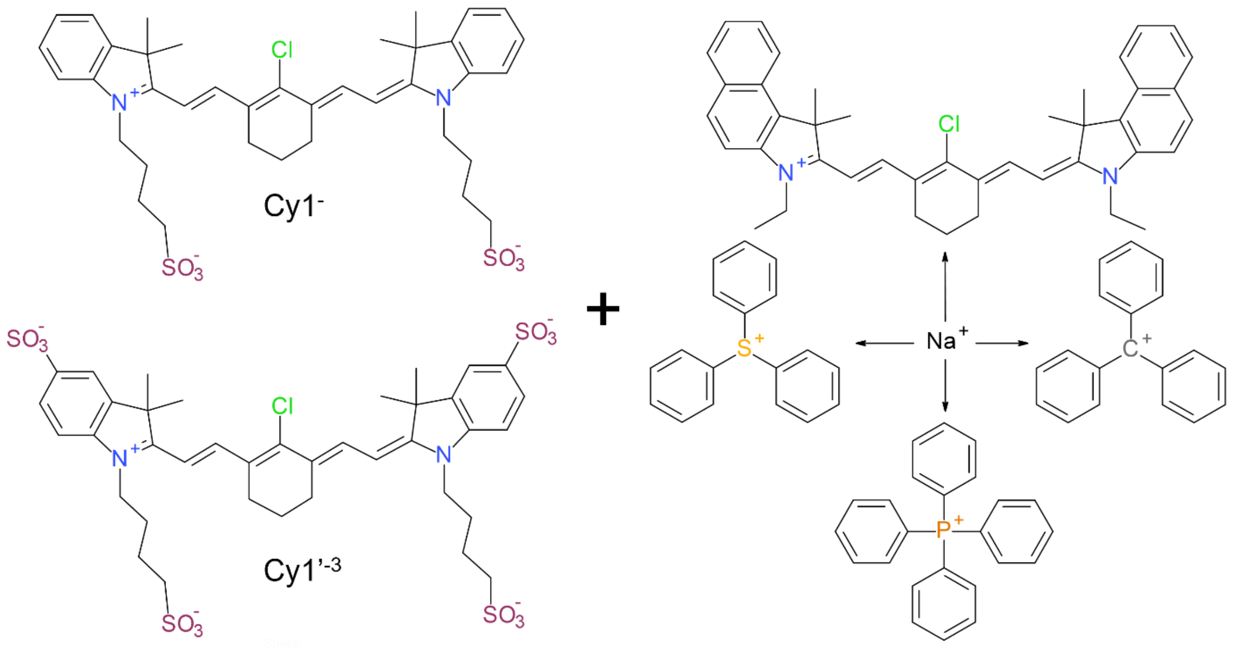

Figure 10.1. Potential counterion exchanges for anionic heptamethine cyanines. Future work with anionic heptamethine cyanines will focus on ion exchanges to pair cyanines such as Cy1$^-$ and Cy1'$^{-3}$ (left) with new counterions (right). Deploying these new salts in photovoltaic devices will reveal more about how exciton diffusion and charge collection processes relate to charge character on the chromophore and the nature of the counterion.

Several possible candidates for ion exchange are shown in Figure 10.1. Weakly coordinating counterions such as tetraphenyl phosphonium could be expected to tune the HOMO level and alter film packing and morphology based on previous work.[94,101] Counterions with increased character, yielding organic salts with compositions such as XCy1$_2$ and X$_3$Cy1'$_2$ (vs. NaCy1 and Na$_3$Cy1') could be another interesting platform from which to observe charge transfer.

We presented the first study on the effects of charge character on carrier transport using anionic heptamethine cyanines, and while cationic cyanines have seen much higher usage in OPVs and TPVs, the analogous study for cationic chromophore-based salts has not yet been demonstrated. Cationic cyanines with increased charge character (either existing compounds or newly synthesized) should be explored in bilayer devices with C$_{60}$ for analysis of charge transfer properties. Ion exchanges are well understood with cationic cyanines and will allow for a direct comparison of the established L_{ED} enhancement and any charge character-based effect that is revealed.

Last, the most promising NIR absorbing anionic and cationic cyanine chromophores based on charge character and observed device performance could be paired with ideal counterions to maximize charge collection and exciton diffusion efficiencies. Achieving this optimization will further emphasize the unique facile tunability that organic salts possess and bring these exciting materials closer to being NIR light harvesters in highly transparent and efficient TPVs.

10.1.2 New architectures and deposition routes

The platform developed in this thesis for the analysis of exciton diffusion and charge collection from a single photovoltaic device is a powerful tool for the optimization of selectively NIR absorbing materials. Pairing that approach with the appropriate characterization techniques such as transient photovoltage and carrier mobility measurements leads to a more complete understanding of how organic salts function in PVs. Ultimately, to achieve high efficiency industrial-scale TPVs, organic salts will need to be 1) demonstrated in new architectures that can achieve higher efficiencies than a C_{60}-paired bilayer and 2) deposited with high efficiency via methods other than spin-coating.

Even with ideal cyanine selection and counterion pairing, it is unlikely that organic salts will possess L_{ED} >> 10-20 nm, as is typical with organic semiconductors.[8] The architectures that organic salts are used in and the active material they are paired with must yield higher *EQE* from the organic salt. Two approaches worth investigating are a BHJ and a mixed planar HJ. Successfully pairing organic salts with either an NFA or an NIR absorbing polymer (if the salt is an acceptor, or with a small bandgap polymer) in a BHJ or a mixed planar HJ would be a great step forward. Both architectures could minimize the consequences of a low L_{ED} and allow organic salts to reach higher *EQE*s. In practice, organic salt-based BHJs are notably difficult to form for reasons that remain unclear, as neutrally charged fluorescent dyes with similar chemical composition and size are routinely demonstrated in BHJs. Organic salt-based BHJs with soluble fullerenes (including ionic fullerenes) as well as several NFAs failed to demonstrate a functional PV device. Understanding this limitation would be an important area of future work. As an initial demonstration, utilizing organic salts as a dopant in ternary BHJs or planar mixed HJs could take advantage of the high extinction coefficient while minimizing the current limitations for organic salts in non-bilayer structures. The organic salt dopant route could also be an effective means to study the impact of an organic salt on an established BHJ architecture.

Ideally, the BHJ or planar mixed HJ would be formed with solid state deposition, a more scalable and environmentally friendly approach than high volume solution processing. Routes to evaporable organic salts would likely need to focus on salts with lower molecular weight and improved thermal stability, perhaps using other evaporable organic semiconductors as a guide. The role of the counterion on evaporation feasibility and on the composition and order of the thin film will be important to explore and understand.

We have outlined numerous studies focused on improving the fundamental understanding of what makes an organic salt an effective material in TPVs and how to deploy organic salts with more scalable methods in higher efficiency TPV architectures. Progress in these areas will greatly assist in elevating this class of semiconducting materials.

10.2 Transparent photovoltaics

In this work we demonstrate high efficiency LBL TPVs with *AVT* > 40%. Key next steps for devices with this approach include 1) improving optical performance by reducing visible absorption of the polymer or substituting the Ag/Alq_3 top contact with a more transparent layer

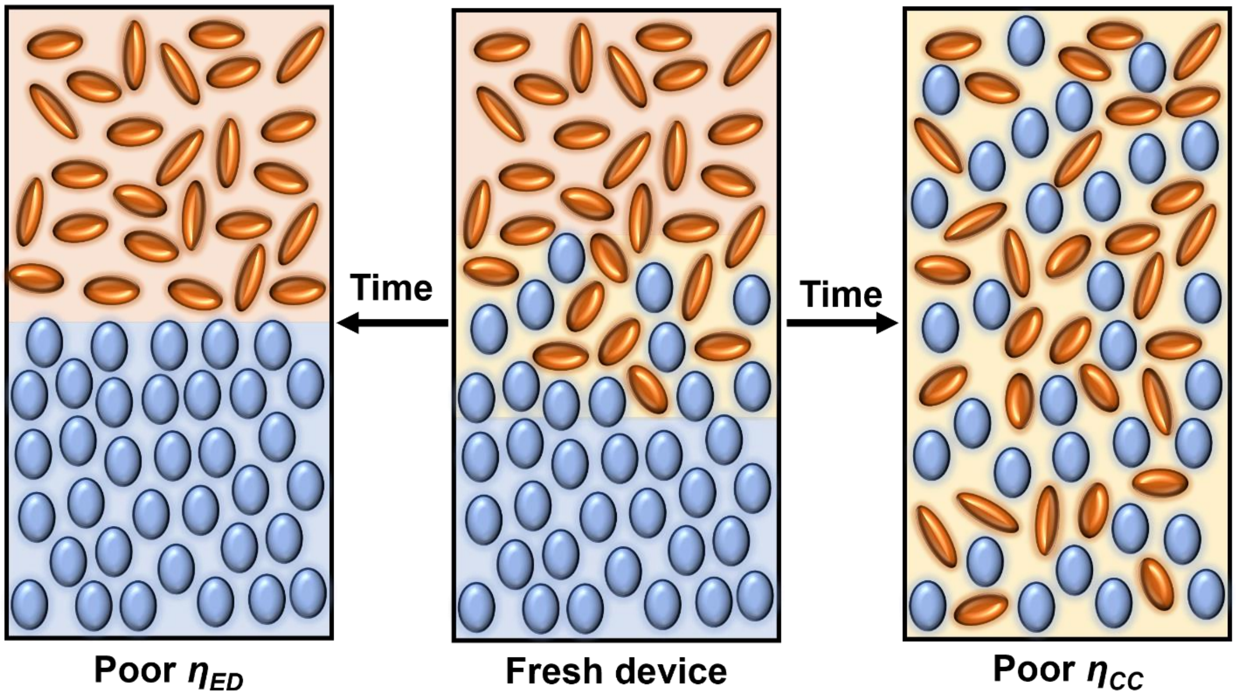

Figure 10.2. Potential failure mechanisms for LBL TPVs. A schematic of the mixed planar heterojunction (HJ) in layer-by-layer deposited transparent photovoltaics (TPVs) after device fabrication (middle). Over time, thermodynamically driven phase segregation could result in the formation of a true bilayer architecture, reducing the interfacial area and exciton diffusion efficiency (left). Alternatively, if the relatively pure domains break down over time leading to increased mixing, the path for charge collection through the HJ could become arduous, reducing charge collection efficiency (right).

such as sputtered ITO, 2) an in-depth study of the lifetime to understand failure mechanisms for LBL planar mixed HJs, and 3) introducing a scaled-up approach to LBL deposition that does not rely on spin-coating.

As discussed in Chapter 5, thin films of PTB7-Th feature a strong absorptive shoulder in the visible spectrum resulting in blue tinted TPVs. Chemical modification of PTB7-Th to increase conjugation and narrow the bandgap will improve the optical performance of the devices at a slight cost to the current and voltage. Replacing PTB7-Th with an already established deep NIR absorbing polymer is a second option. Additionally, replacing the Ag/Alq_3 top contact with ITO can improve the aesthetics with only a small cost to the photocurrent. Given the material and time costs involved, optical simulations of the TPVs with a top ITO contact should be utilized to gain an understanding of the ideal ITO thickness range for optical performance. ITO sputtering should first be attempted on stand-in devices with simpler processing (bilayer devices with an organic salt and C_{60}) to learn the thickness required of the sacrificial layer, likely MoO_3, required to protect the active layers in the LBL TPV from sputtered ITO molecules. Subsequent LBL TPVs will be evaluated as demonstrated in this thesis for electrical and optical performance.

The shelf life of LBL TPVs has been reported several times, including here, however the constant illumination lifetime has not yet been demonstrated. This will be an important study to understand the failure mechanisms and determine if they differ under 1 sun illumination. A mechanistic study should utilize UV-VIS-NIR spectroscopy and AFM to study active material absorption and film morphology in addition to daily *J-V*, dark *J-V*, and *EQE* measurements. Active materials stored as dry powders showed no signs of degradation under inert conditions for up to a year. Two possible routes for a breakdown of the active layer structure are shown in Figure 10.2. Phase segregation could cause losses in exciton diffusion efficiency with decreased interfacial area (left), or an increase in mixing could result in limited pathways for charge collection (right). If material degradation is evident, UHPLC-MS could be used to assess stability, in which case the planar mixed HJs must be made on separate substrates to allow for the active materials to be redissolved. Understanding the lifetime of LBL TPVs and how it might be improved will be critical for future development of this approach.

In addition to improved lifetime, moving to a scalable thin film deposition technique is an important step forward. Solution processing approaches for commercial scale production could include printing or spray-coating. However, the large amount of solvent required in combination with the sensitivity of the active layers to CN and challenge of nm level uniformity are significant barriers to a successful scaled-up solution approach. A solid-state technique such as high vacuum thermal vapor deposition is an ideal approach for uniform film deposition over large areas (2-10 ft^2 or more), and deposition rates for two materials could be optimized to yield a mixed region between two single-component layers. The inherent challenge in moving to vapor deposition is the presence of a polymer and relatively large discrete molecule (MW = 1808 g/mol) in PTB7-Th and IEICO-4F. A key study for this route will be to understand how the morphology changes if PTB7-Th polymer is reduced to a monomer, dimer, trimer, etc.and at which molecule length most of the properties of the bulk polymer are preserved. Conceptually, it is reasonable to assume that the morphology and device performance would change significantly, but the rise of all-small molecule devices to *PCE*s similar to polymer-NFA OPVs lends credence to the possibility of a highly efficient TPV based on small-molecule versions of PTB7-Th and IEICO-4F.[17] The development of organic semiconductors for all-solid state processed TPVs is an open field of research and will be crucial to realizing commercially viable LBL TPVs.

10.3 Graphene nanoribbons

We demonstrated the first GNR-based photovoltaic device and thoroughly evaluated current limitations resulting from out of plane carrier mobility and exciton diffusion losses when hopping between ribbons. The primary objective in future work with GNRs should be to improve the alignment of ribbons either via solution processing and post deposition treatment techniques, or by a new deposition route. The simplest path to ideal alignment is by orienting the ribbons vertically such that carriers and excitons move along the length of the ribbon (Figure 10.3), however horizontally aligned ribbons with ideal stacking for π-π* overlap could also be a powerful approach.

For solution synthesized GNRs, vertical alignment could be achieved by docking GNRs to the underlying electrode or contact layer. Given the level of aggregation observed in GNR

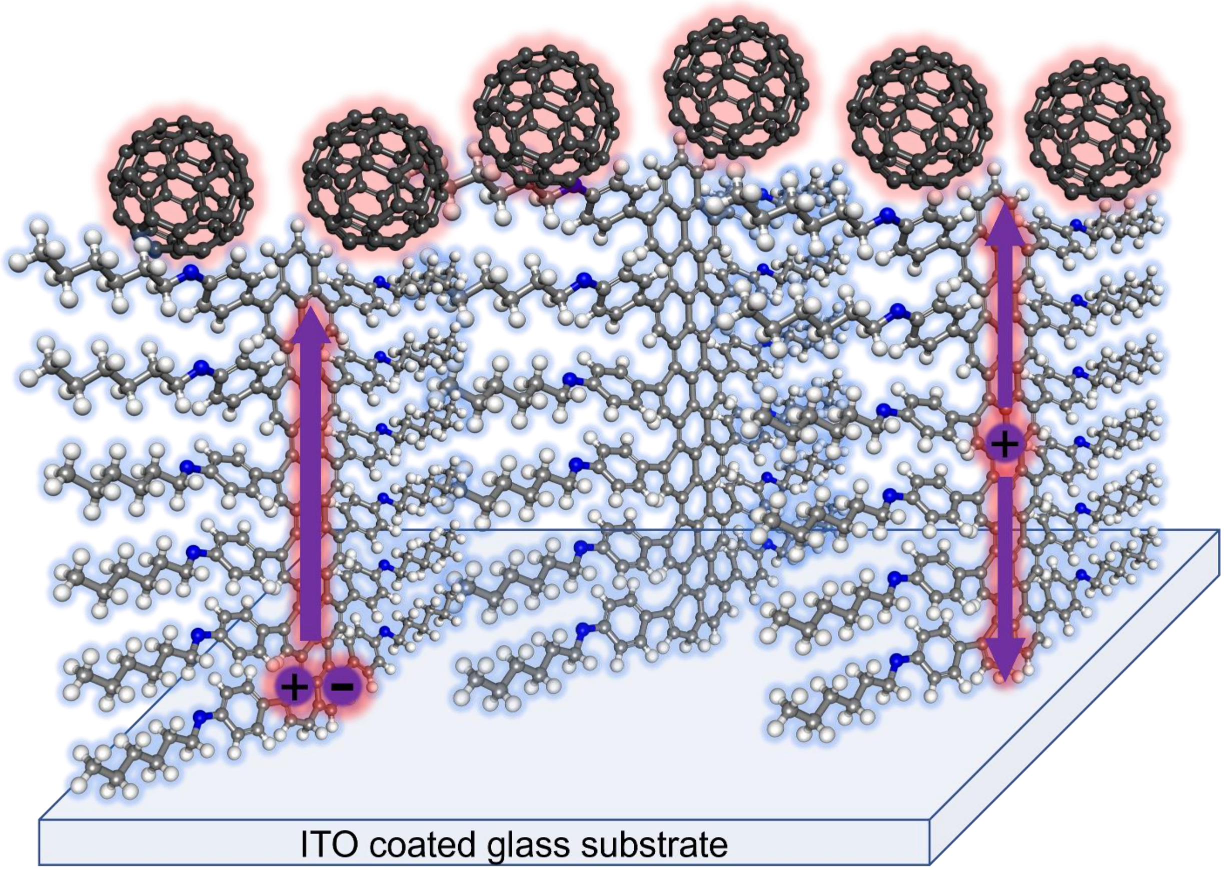

Figure 10.3. Vertically aligned graphene nanoribbons. A schematic of how vertically aligned graphene nanoribbons (GNRs) grown on an ITO coated glass substrate can facilitate exciton diffusion and charge collection with high intra-ribbon conductivity. A thin layer of fullerene as an acceptor is shown deposited on top of the GNR.

solutions in TCB, alternative solvents should be explored to study inter-ribbon interactions and how that may impact film morphology during spin-coating. Post-deposition techniques should also be considered, including thermal annealing in an inert environment, under solvent vapor, and under vacuum. Characterization of different film formation and treatment techniques should be carried out using traditional *J-V* and *EQE* measurements, as well as carrier mobility in hole-only devices and microscopy techniques such as AFM and SEM. Alternative GNR synthesis routes should also be investigated with a focus on in-situ growth of GNRs onto the device substrate as a route to vertically aligned ribbons.

Deployment of GNRs in different architectures and with non-fullerene materials is a second area of study. GNR films or domains may form entirely different orientations in a BHJ with a polymer or NFA. However, the complication with using such high efficiency materials is that it may become difficult to clearly elucidate the role of the GNR in the PV performance, as many NIR selectively absorbing polymers and NFAs still yield *EQE* > 30% in the VIS and UV regions of opaque PVs. For this reason, the initial focus going forward should be on GNR orientation in PV devices, utilizing different synthesis or deposition routes to achieve a more favorable alignment.

10.4 Organic salts in photodynamic therapy and fluorescent imaging

We have successfully developed a series of cationic cyanine based organic salts that demonstrate the full range of cellular toxicity based on the counterion selection. Of that series, CyFPhB was shown to be an excellent active agent for cancer treatment in a mouse model. Future work should primarily focus on three routes, 1) the development of new theranostics agents based on novel counterion pairings, 2) synthesis of higher Φ organic salts, and 3) advancement of CyFPhB as a PDT active agent.

An entirely new series of carborane counterion based organic salts has already been synthesized as part of this work, and analysis of these materials as PDT and bioimaging agents is underway. Carboranes in the original study were CyCoCB and CyCB, with CyCoCB presenting as a selectively phototoxic salt alongside CyFPhB and CyCB as a cyto- and phototoxic salt on the edge of selective phototoxicity. The new series of carborane salts spans a wide range of sizes, degree and identity of halogenation, and even net charge (Figure 10.4). This carborane series has already demonstrated the solid-state HOMO level shift seen in the previous CyX series (Figure 10.4c and d).[94,101] The goals of future work with this series could be to elucidate the impact of these various physical properties on toxicity that will inform subsequent counterion ion syntheses

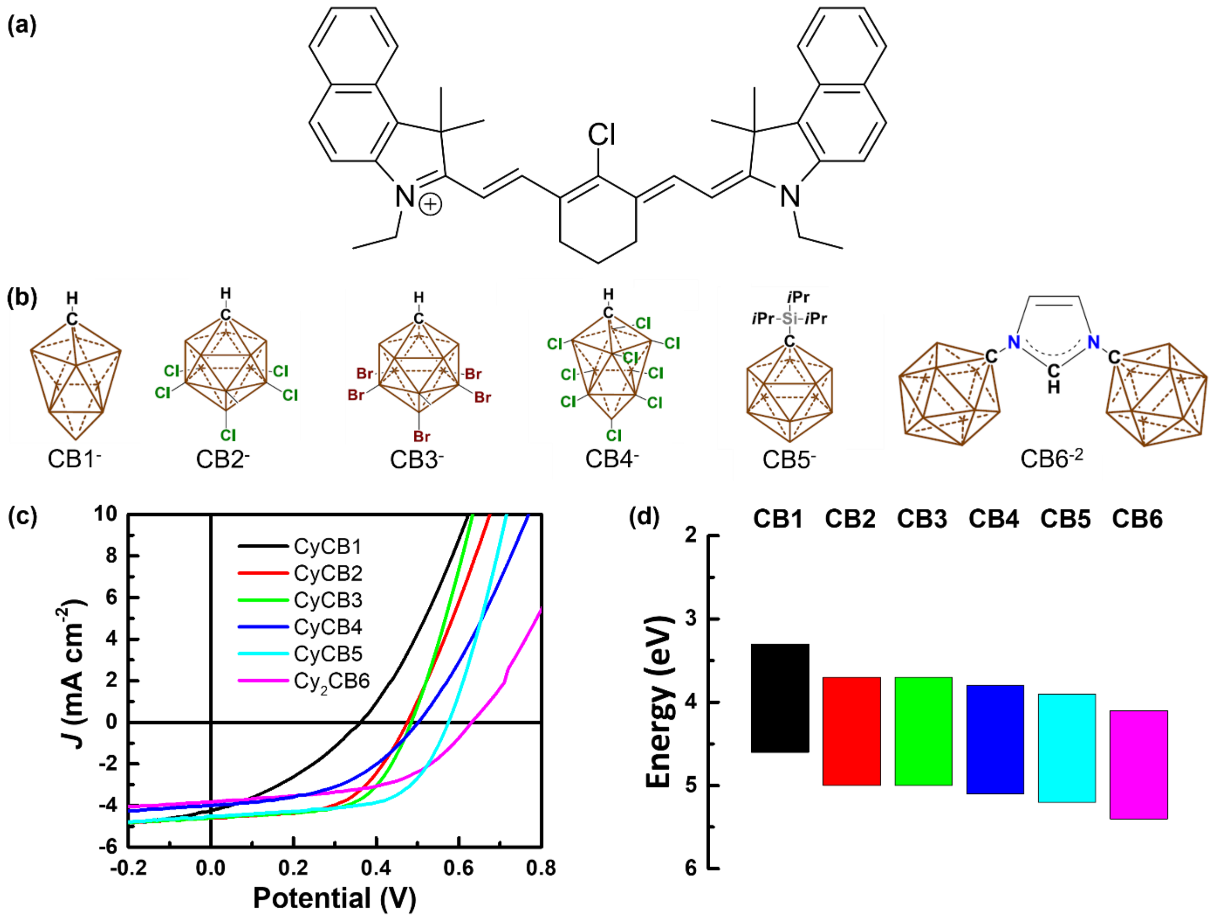

Figure 10.4. New series of carborane anions for PDT. (a) The cationic cyanine Cy$^+$. **(b)** A new series of carborane anions that have been synthesized paired with Cy$^+$. **(c)** *J-V* curves for the new carborane salts. **(d)** Estimated energy levels of new carborane salts based on preliminary *J-V* data in **(c)** and previously measured energy levels of CyX salts.[13,14]

and identify at least 1-2 candidates as selectively phototoxic agents for future in vivo cancer treatment studies.

Cancer diagnosis via bioimaging is a powerful application of the tunable cellular toxicity we observe with cyanine based organic salts. The reduced toxicity of cyanines paired with bulkier counterions in CyTPFB, CyTRIS, and CyTFM allows for a higher dosage of an imaging compound to be used leading to increased fluorescence and imaging power. To further take advantage of this discovery, NIR absorbing salts with a similar peak absorption range and $\Phi > 10\%$ should be synthesized. A higher Φ will increase the imaging brightness, and paired with the outstanding lifetime and stability that salts such as CyTPFB have shown would make for an outstanding fluorescent bioimaging candidate.[102]

Finally, CyFPhB should be advanced as a strong candidate for clinical PDT. One of the strengths of PDT as a cancer treatment approach is that it does not rely on a singular cancer mechanism for targeting and treatment. We have shown CyFPhB via intravenous injection in a mouse model to treat metastatic breast cancer and will now endeavor to demonstrate CyFPhB as an effective treatment agent in other cancer types. Through the work discussed above, we expect other selectively phototoxic cyanine salts to join CyFPhB as successful anti-cancer agents and expand the field of candidates for future studies.

10.5 Final conclusions

In this thesis, we use organic semiconductors as active materials for projects in OPVs, TPVs, bioimaging, and PDT. We start by revealing a strong relationship between charge character on a cyanine and the mobility of charge carriers in organic salt-based PVs. We next demonstrate excellent electronic and optical performance in LBL TPVs, achieving 8.8% *PCE*, 40.9% *AVT*, and 3.6% *LUE*. In the third project, GNRs are introduced as the first graphene derived photoactive material in a PV. Last, organic salts from OPV studies are translated to cancer research and demonstrated to be highly tunable anti-cancer materials in PDT or fluorescent bioimaging agents for diagnostics. Material synthesis, device fabrication, and material and device characterization are all key aspects of this work. A wide range of experimental techniques are utilized to characterize materials and devices leading to a better understanding of functionality and clear routes forward. The research discussed here presents new advances in OPVs, TPVs, and PDT, demonstrating the importance of organic semiconductors to providing renewable energy and effective cancer diagnosis and treatment.

BIBLIOGRAPHY

[1] P. Rhodes, E. C. Stoner, *Proc. R. Soc. Lond. Ser. Math. Phys. Sci.* **1950**, *204*, 396.

[2] S. Hubbard, *Photovolt. Sol. Energy*, **2016**, pp. 54–66.

[3] R. R. Lunt, V. Bulović, T. P. Osedach, P. R. Brown, J. A. Rowehl, *Adv. Mater.* **2011**, *23*, 5712.

[4] K.-L. Wong, J.-C. G. Bünzli, P. A. Tanner, *J. Lumin.* **2020**, *224*, 117256.

[5] C. W. Tang, *Appl. Phys. Lett.* **1986**, *48*, 183.

[6] C. Yang, D. Liu, M. Bates, M. C. Barr, R. R. Lunt, *Joule* **2019**, *3*, 1803.

[7] R. Wilson, *Phys. Sci. Int. J.* **2021**, *25*, 41.

[8] R. R. Lunt, N. C. Giebink, A. A. Belak, J. B. Benziger, S. R. Forrest, *J. Appl. Phys.* **2009**, *105*, 053711.

[9] C. Yang, J. Zhang, W.-T. Peng, W. Sheng, D. Liu, P. S. Kuttipillai, M. Young, M. R. Donahue, B. G. Levine, B. Borhan, R. R. Lunt, *Sci. Rep.* **2018**, *8*, 16359.

[10] R. R. Lunt, R. J. Holmes, *Org. Sol. Cells*, **2014**, pp. 71–125.

[11] J. Xue, B. P. Rand, S. Uchida, S. R. Forrest, *J. Appl. Phys.* **2005**, *98*, 124903.

[12] M. L. Tietze, J. Benduhn, P. Pahner, B. Nell, M. Schwarze, H. Kleemann, M. Krammer, K. Zojer, K. Vandewal, K. Leo, *Nat. Commun.* **2018**, *9*, 1182.

[13] Q. Wan, X. Guo, Z. Wang, W. Li, B. Guo, W. Ma, M. Zhang, Y. Li, *Adv. Funct. Mater.* **2016**, *26*, 6635.

[14] W. Li, J. Cai, F. Cai, Y. Yan, H. Yi, R. S. Gurney, D. Liu, A. Iraqi, T. Wang, *Nano Energy* **2018**, *44*, 155.

[15] D. Li, F. Geng, T. Hao, Z. Chen, H. Wu, Z. Ma, Q. Xue, L. Lin, R. Huang, S. Leng, B. Hu, X. Liu, J. Wang, H. Zhu, M. Lv, L. Ding, M. Fahlman, Q. Bao, Y. Li, *Nano Energy* **2022**, *96*, 107133.

[16] L. Zhu, M. Zhang, J. Xu, C. Li, J. Yan, G. Zhou, W. Zhong, T. Hao, J. Song, X. Xue, Z. Zhou, R. Zeng, H. Zhu, C.C. Chen, R. C. I. MacKenzie, Y. Zou, J. Nelson, Y. Zhang, Y. Sun, F. Liu, *Nat. Mater.* **2022**, *21*, 656.

[17] J. Qin, Z. Chen, P. Bi, Y. Yang, J. Zhang, Z. Huang, Z. Wei, C. An, H. Yao, X. Hao, T. Zhang, Y. Cui, L. Hong, C. Liu, Y. Zu, C. He, J. Hou, *Energy Environ. Sci.* **2021**, *14*, 5903.

[18] W. Zhang, C. Sun, I. Angunawela, L. Meng, S. Qin, L. Zhou, S. Li, H. Zhuo, G. Yang, Z.-G. Zhang, H. Ade, Y. Li, *Adv. Mater.* **2022**, *34*, 2108749.

[19] J. Qin, Q. Yang, J. Oh, S. Chen, G. O. Odunmbaku, N. A. N. Ouedraogo, C. Yang, K. Sun, S. Lu, *Adv. Sci.* **2022**, *9*, 2105347.

[20] P. Gagnon, R. Margolis, J. Melius, C. Phillips, R. Elmore, *Rooftop Solar Photovoltaic Technical Potential in the United States. A Detailed Assessment*, **2016**.

[21] R. R. Lunt, *Appl. Phys. Lett.* **2012**, *101*, 043902.

[22] C. J. Traverse, R. Pandey, M. C. Barr, R. R. Lunt, *Nat. Energy* **2017**, *2*, 849.

[23] P. Fissette, "Windows: Understanding Energy Efficient Performance", **2003**.

[24] J. Mescher, S. W. Kettlitz, N. Christ, M. F. G. Klein, A. Puetz, A. Mertens, A. Colsmann, U. Lemmer, *Org. Electron.* **2014**, *15*, 1476.

[25] C. Yang, M. C. Barr, R. R. Lunt, *Phys. Rev. Appl.* **2022**, *17*, 034054.

[26] C. Yang, W. Sheng, M. Moemeni, M. Bates, C. K. Herrera, B. Borhan, R. R. Lunt, *Adv. Energy Mater.* **2021**, *11*, 2003581.

[27] M. Bates, R. R. Lunt, *Sustain. Energy Fuels* **2017**, *1*, 955.

[28] R. Hany, B. Fan, F. A. de Castro, J. Heier, W. Kylberg, F. Nüesch, *Prog. Photovolt. Res. Appl.* **2011**, *19*, 851.

[29] X. Chen, J. Guo, X. Peng, M. Guo, Y. Xu, L. Shi, C. Liang, L. Wang, Y. Gao, S. Sun, S. Cai, *J. Photochem. Photobiol. Chem.* **2005**, *171*, 231.

[30] B. Feng, D. Wan, L. Yan, V. D. Kadam, J. You, G. Gao, *RSC Adv.* **2016**, *6*, 66407.

[31] T. Geiger, H. Benmansour, B. Fan, R. Hany, F. Nüesch, *Macromol. Rapid Commun.* **2008**, *29*, 651.

[32] B. Jędrzejewska, B. Michalak, *Color. Technol.* **2011**, *127*, 288.

[33] J. R. Lenhard, B. R. Hein, A. A. Muenter, *J. Phys. Chem.* **1993**, *97*, 8269.

[34] M. A. Bedics, K. R. Mulhern, D. F. Watson, M. R. Detty, *J. Org. Chem.* **2013**, *78,* 8885.

[35] W. Zhan, W. Wu, J. Hua, Y. Jing, F. Meng, H. Tian, *Tetrahedron Lett.* **2007**, *48*, 2461.

[36] J. H. Lim, O. V. Przhonska, S. Khodja, S. Yang, T. S. Ross, D. J. Hagan, E. W. Van Stryland, M. V. Bondar, Y. L. Slominsky, *Chem. Phys.* **1999**, *245*, 79.

[37] K. Funabiki, K. Yagi, M. Ueta, M. Nakajima, M. Horiuchi, Y. Kubota, M. Mastui, *Chem. Eur. J.* **2016**, *22*, 12282.

[38] A. S. Tatikolov, A. A. Ishchenko, S. Ghelli, G. Ponterini, *J. Mol. Struct.* **1998**, *471*, 145.

[39] W. H. Zhan, J. L. Hua, Y. H. Jin, X. Teng, H. Tian, *Res. Chem. Intermed.* **2008**, *34*, 229.

[40] J. L. Bricks, A. D. Kachkovskii, Y. L. Slominskii, A. O. Gerasov, S. V. Popov, *Dyes Pigments* **2015**, *121*, 238.

[41] J. Fabian, H. Nakazumi, M. Matsuoka, *Chem. Rev.* **1992**, *92*, 1197.

[42] M. Henary, A. Levitz, *Dyes Pigments* **2013**, *99*, 1107.

[43] A. Mishra, R. K. Behera, P. K. Behera, B. K. Mishra, G. B. Behera, *Chem. Rev.* **2000**, *100*, 1973.

[44] P. A. Bouit, E. Di Piazza, S. Rigaut, B. Le Guennic, C. Aronica, L. Toupet, C. Andraud, O. Maury, *Org. Lett.* **2008**, *10*, 4159.

[45] C. Z. Li, C. C. Chueh, F. Ding, H. L. Yip, P. W. Liang, X. Li, A. K. Y. Jen, *Adv. Mater.* **2013**, *25*, 4425.

[46] I. Krossing, I. Raabe, *Angew. Chem. Int. Ed.* **2004**, *43*, 2066.

[47] S. Jenatsch, L. Wang, M. Bulloni, A. C. Véron, B. Ruhstaller, S. Altazin, F. Nüesch, R. Hany, *ACS Appl. Mater. Interfaces* **2016**, *8*, 6554.

[48] C. A. Bertolino, G. Caputo, C. Barolo, G. Viscardi, S. Coluccia, *J. Fluoresc.* **2006**, *16*, 221.

[49] H. Jia, Y. Lv, S. Wang, D. Sun, L. Wang, *RSC Adv.* **2014**, *5*, 4681.

[50] A. L. Ellis, J. Christian Mason, H. W. Lee, L. Strekowski, G. Patonay, H. Choi, J. J. Yang, *Talanta* **2002**, *56*, 1099.

[51] Flanagan James H., S. H. Khan, S. Menchen, S. A. Soper, R. P. Hammer, *Bioconjug. Chem.* **1997**, *8*, 751.

[52] W. Zhan, H. N. Barnhill, K. Sivakumar, H. Tian, Q. Wang, *Tetrahedron Lett.* **2005**, *46*, 1691.

[53] F. Hu, L. Jiang, M. Cao, Z. Xu, J. Huang, D. Wu, W. Yang, S. H. Liu, J. Yin, *RSC Adv.* **2014**, *5*, 5982.

[54] H. Mustroph, M. Stollenwerk, V. Bressau, *Angew. Chem. Int. Ed.* **2006**, *45*, 2016.

[55] R. B. Mujumdar, L. A. Ernst, S. R. Mujumdar, C. J. Lewis, A. S. Waggoner, *Bioconjug. Chem.* **1993**, *4*, 105.

[56] N. Siraj, F. Hasan, S. Das, L. W. Kiruri, K. E. Steege Gall, G. A. Baker, I. M. Warner, *J. Phys. Chem. C* **2014**, *118*, 2312.

[57] L. Strekowski, M. Lipowska, G. Patonay, *J. Org. Chem.* **1992**, *57*, 4578.

[58] T. P. Osedach, A. Iacchetti, R. R. Lunt, T. L. Andrew, P. R. Brown, G. M. Akselrod, V.

Bulović, *Appl. Phys. Lett.* **2012**, *101*, 113303.

[59] Y. Zhao, G. A. Meek, B. G. Levine, R. R. Lunt, *Adv. Opt. Mater.* **2014**, *2*, 606.

[60] B. P. Regmi, W. I. S. Galpothdeniya, N. Siraj, M. H. Webb, N. C. Speller, I. M. Warner, *Sens. Actuators B Chem.* **2015**, *209*, 172.

[61] M. Levitus, S. Ranjit, *Q. Rev. Biophys.* **2011**, *44*, 123.

[62] J. N. Tisserant, R. Brönnimann, R. Hany, S. Jenatsch, F. A. Nüesch, R. Mezzenga, G.-L. Bona, J. Heier, *ACS Nano* **2014**, *8*, 10057.

[63] J. S. Lee, X. Wang, H. Luo, G. A. Baker, S. Dai, *J. Am. Chem. Soc.* **2009**, *131*, 4596.

[64] O. Ostroverkhova, *Chem. Rev.* **2016**, *116*, 13279.

[65] A. W. Hains, Z. Liang, M. A. Woodhouse, B. A. Gregg, *Chem. Rev.* **2010**, *110*, 6689.

[66] Y. Lin, Y. Li, X. Zhan, *Chem. Soc. Rev.* **2012**, *41*, 4245.

[67] A. K. Ghosh, T. Feng, *Photovoltaic Device Containing an Organic Layer*, **1978**, US4127738A.

[68] G. A. Stepanova, L. S. Volkova, M. A. Gainullina, F. F. Yumakulova, *ZHURNAL Fiz. KHIMII* **1977**, *51*, 7.

[69] D. Wöhrle, D. Meissner, *Adv. Mater.* **1991**, *3*, 129.

[70] A. K. Jana, *J. Photochem. Photobiol. Chem.* **2000**, *132*, 1.

[71] F. Meng, K. Chen, H. Tian, L. Zuppiroli, F. Nuesch, *Appl. Phys. Lett.* **2003**, *82*, 3788.

[72] M. Kawasaki, S. Aoyama, *Chem. Commun.* **2004**, *8*, 988.

[73] F. Nüesch, G. Tornare, L. Zuppiroli, F. Meng, K. Chen, H. Tian, *Sol. Energy Mater. Sol. Cells* **2005**, *87*, 817.

[74] F. Nüesch, A. Faes, L. Zuppiroli, F. Meng, K. Chen, H. Tian, *J. Mater. Sci.* **2005**, *40*, 1353.

[75] F. Meng, J. Hua, K. Chen, H. Tian, L. Zuppiroli, F. Nüesch, *J. Mater. Chem.* **2005**, *15*, 979.

[76] F. A. Castro, A. Faes, T. Geiger, C. F. O. Graeff, M. Nagel, F. Nüesch, R. Hany, *Synth. Met.* **2006**, *156*, 973.

[77] B. Fan, R. Hany, J. E. Moser, F. Nüesch, *Org. Electron.* **2008**, *9*, 85.

[78] B. Fan, F. A. de Castro, J. Heier, R. Hany, F. Nüesch, *Org. Electron.* **2010**, *11*, 583.

[79] P. A. Bouit, D. Rauh, S. Neugebauer, J. L. Delgado, E. D. Piazza, S. Rigaut, O. Maury, C.

Andraud, V. Dyakonov, N. Martin, *Org. Lett.* **2009**, *11*, 4806.

[80] B. Fan, F. A. de Castro, B. T. T. Chu, J. Heier, D. Opris, R. Hany, F. Nüesch, *J. Mater. Chem.* **2010**, *20*, 2952.

[81] E. Berner, T. Jäger, T. Lanz, F. Nüesch, J. N. Tisserant, G. Wicht, H. Zhang, R. Hany, *Appl. Phys. Lett.* **2013**, *102*, 183903.

[82] O. Malinkiewicz, T. Grancha, A. Molina-Ontoria, A. Soriano, H. Brine, H. J. Bolink, *Adv. Energy Mater.* **2013**, *3*, 472.

[83] C. C. Yap, M. Yahaya, M. M. Salleh, *Sol. Energy* **2011**, *85*, 95.

[84] N. S. Sabri, C. C. Yap, M. Yahaya, M. Mat Salleh, *J. Mater. Sci. Mater. Electron.* **2013**, *24*, 2183.

[85] L. Wang, C. Hinderling, S. Jenatsch, F. Nüesch, D. Rentsch, R. Steim, H. Zhang, R. Hany, *Polymer* **2014**, *55*, 3195.

[86] A. C. Véron, H. Zhang, A. Linden, F. Nüesch, J. Heier, R. Hany, T. Geiger, *Org. Lett.* **2014**, *16*, 1044.

[87] S. Jenatsch, T. Geiger, J. Heier, C. Kirsch, F. Nüesch, A. Paracchino, D. Rentsch, B. Ruhstaller, A. C Véron, R. Hany, *Sci. Technol. Adv. Mater.* **2015**, *16*, 035003.

[88] J. Zhao, X. Yang, M. Cheng, S. Li, X. Wang, L. Sun, *J. Mater. Chem. A* **2013**, *1*, 2441.

[89] F. M. Jradi, X. Kang, D. O'Neil, G. Pajares, Y. A. Getmanenko, P. Szymanski, T. C. Parker, M. A. El-Sayed, S. R. Marder, *Chem. Mater.* **2015**, *27*, 2480.

[90] F. M. Jradi, D. O'Neil, X. Kang, J. Wong, P. Szymanski, T. C. Parker, H. L. Anderson, M. A. El-Sayed, S. R. Marder, *Chem. Mater.* **2015**, *27*, 6305.

[91] D. Saccone, S. Galliano, N. Barbero, P. Quagliotto, G. Viscardi, C. Barolo, *Eur. J. Org. Chem.* **2016**, *2016*, 2244.

[92] Y. Ooyama, Y. Harima, *Eur. J. Org. Chem.* **2009**, *2009*, 2903.

[93] S. P. Singh, G. D. Sharma, *Chem. Rec.* **2014**, *14*, 419.

[94] J. Suddard-Bangsund, C. J. Traverse, M. Young, T. J. Patrick, Y. Zhao, R. R. Lunt, *Adv. Energy Mater.* **2016**, *6*, 1501659.

[95] M. Young, J. Suddard-Bangsund, T. J. Patrick, N. Pajares, C. J. Traverse, S. Y. Lunt, M. C. Barr, R. R. Lunt, *Adv. Opt. Mater.* **2016**, *4*, 1028.

[96] T. A. Engesser, M. R. Lichtenthaler, M. Schleep, I. Krossing, *Chem. Soc. Rev.* **2016**, *45*, 789.

[97] K. Landskron, *Chem. Eur. J.* **2015**, *21*, 14258.

[98] M. I. Demchuk, A. A. Ishchenko, V. P. Mikhailov, V. I. Avdeeva, *Chem. Phys. Lett.* **1988**, *144*, 99.

[99] P. A. Bouit, C. Aronica, L. Toupet, B. Le Guennic, C. Andraud, O. Maury, *J. Am. Chem. Soc.* **2010**, *132*, 4328.

[100] G. V. Bulavko, N. A. Davidenko, N. A. Derevyanko, A. A. Ishchenko, *High Energy Chem.* **2015**, *49*, 331.

[101] C. J. Traverse, M. Young, J. Suddard-Bangsund, T. Patrick, M. Bates, P. Chen, B. Wingate, S. Y. Lunt, A. Anctil, R. R. Lunt, *Sci. Rep.* **2017**, *7*, 16399.

[102] C. J. Traverse, P. Chen, R. R. Lunt, *Adv. Energy Mater.* **2018**, *8*, 1703678.

[103] H. Benmansour, F. A. Castro, M. Nagel, J. Heier, R. Hany, F. Nüesch, *CHIMIA* **2007**, *61*, 787.

[104] M. Lenes, H. J. Bolink, *ACS Appl. Mater. Interfaces* **2010**, *2*, 3664.

[105] S. Jenatsch, J. Groenewold, M. Döbeli, R. Hany, R. Crockett, J. Lübben, F. Nüesch, J. Heier, *Adv. Mater. Interfaces* **2017**, *4*, 1600891.

[106] D. A. Higgins, P. J. Reid, P. F. Barbara, *J. Phys. Chem.* **1996**, *100*, 1174.

[107] T. K. Mullenbach, K. A. McGarry, W. A. Luhman, C. J. Douglas, R. J. Holmes, *Adv. Mater.* **2013**, *25*, 3689.

[108] S. Jenatsch, R. Hany, A. C. Véron, M. Neukom, S. Züfle, A. Borgschulte, B. Ruhstaller, F. Nüesch, *J. Phys. Chem. C* **2014**, *118*, 17036.

[109] J. D. Jonghe-Risse, J. Heier, F. Nüesch, J. E. Moser, *J. Mater. Chem. A* **2015**, *3*, 10935.

[110] A. Devižis, J. De Jonghe-Risse, R. Hany, F. Nüesch, S. Jenatsch, V. Gulbinas, J. E. Moser, *J. Am. Chem. Soc.* **2015**, *137*, 8192.

[111] Th. B. Singh, N. Marjanović, G. J. Matt, S. Günes, N. S. Sariciftci, A. Montaigne Ramil, A. Andreev, H. Sitter, R. Schwödiauer, S. Bauer, *Org. Electron.* **2005**, *6*, 105.

[112] T. D. Anthopoulos, B. Singh, N. Marjanovic, N. S. Sariciftci, A. Montaigne Ramil, H. Sitter, M. Cölle, D. M. de Leeuw, *Appl. Phys. Lett.* **2006**, *89*, 213504.

[113] K. Tennakone, P. K. D. D. P. Pitigala, A. G. U. Perera, *RSC Adv.* **2013**, *3*, 2770.

[114] P. K. D. Duleepa Pitigala, M. M. Henary, E. A. Owens, A. G. UnilPerera, K. Tennakone, *J. Photochem. Photobiol. Chem.* **2016**, *325*, 39.

[115] N. Blouin, A. Topley, L. Nanson, S. Tierney, T. Cull, P. Tiwana, S. Berny, M. Carrasco-Orozco, F. E. Meyer, *Conjugated Polymers*, **2013**, WO2013135339A2.

[116] N. Karl, K. H. Kraft, J. Marktanner, M. Münch, F. Schatz, R. Stehle, H. M. Uhde, *J. Vac. Sci. Technol. A* **1999**, *17*, 2318.

[117] N. Karl, *Synth. Met.* **2003**, *133*, 649.

[118] P. A. Bouit, C. Aronica, L. Guy, A. Martinez, C. Andraud, O. Maury, *Org. Biomol. Chem.* **2009**, *7*, 3086.

[119] R. R. Lunt, V. Bulovic, *Appl. Phys. Lett.* **2011**, *98*, 113305.

[120] H. Zhang, G. Wicht, C. Gretener, M. Nagel, F. Nüesch, Y. Romanyuk, J. N. Tisserant, R. Hany, *Sol. Energy Mater. Sol. Cells* **2013**, *118*, 157.

[121] J. D. Zimmerman, V. V. Diev, K. Hanson, R. R. Lunt, E. K. Yu, M. E. Thompson, S. R. Forrest, *Adv. Mater.* **2010**, *22*, 2780.

[122] G. Wicht, S. Bücheler, M. Dietrich, T. Jäger, F. Nüesch, T. Offermans, J. N. Tisserant, L. Wang, H. Zhang, R. Hany, *Sol. Energy Mater. Sol. Cells* **2013**, *117*, 585.

[123] H. Zhang, A. Borgschulte, F. A. Castro, R. Crockett, A. C. Gerecke, O. Deniz, J. Heier, S. Jenatsch, F. Nüesch, C. Sanchez-Sanchez, A. Zoladek-Lemanczyk, R. Hany, *Adv. Energy Mater.* **2015**, *5*, 1400734.

[124] W. S. Saad, R. K. Prud'homme, *Nano Today* **2016**, *11*, 212.

[125] B. W. D'Andrade, S. Datta, S. R. Forrest, P. Djurovich, E. Polikarpov, M. E. Thompson, *Org. Electron.* **2005**, *6*, 11.

[126] J. A. Woollam, B. D. Johs, C. M. Herzinger, J. N. Hilfiker, R. A. Synowicki, C. L. Bungay, *Opt. Metrol. Crit. Rev.*, **1999**, pp. 3–28.

[127] J. Xiao, Z. Chen, G. Zhang, Q. Y. Li, Q. Yin, X. F. Jiang, F. Huang, Y. X. Xu, H. L. Yip, Y. Cao, *J. Mater. Chem. C* **2018**, *6*, 4457.

[128] C. G. Shuttle, B. O'Regan, A. M. Ballantyne, J. Nelson, D. D. C. Bradley, J. de Mello, J. R. Durrant, *Appl. Phys. Lett.* **2008**, *92*, 093311.

[129] M. Young, C. J. Traverse, R. Pandey, M. C. Barr, R. R. Lunt, *Appl. Phys. Lett.* **2013**, *103*, 133304.

[130] P. Peumans, A. Yakimov, S. R. Forrest, *J. Appl. Phys.* **2003**, *93*, 3693.

[131] M. Bates, S. Y. Lunt, R. R. Lunt, *J. Appl. Phys.* **2022**, *132*, 085501.

[132] Y. Huo, H. L. Zhang, X. Zhan, *ACS Energy Lett.* **2019**, *4*, 1241.

[133] Z. Zhang, Y. Wang, C. Sun, Z. Liu, H. Wang, L. Xue, Z. G. Zhang, *Nano Sel.* **2022**, *3*, 233.

[134] B. Kan, Y. Kan, L. Zuo, X. Shi, K. Gao, *InfoMat* **2021**, *3*, 175.

[135] G. Zhang, J. Zhao, P. C. Y. Chow, K. Jiang, J. Zhang, Z. Zhu, J. Zhang, F. Huang, H. Yan, *Chem. Rev.* **2018**, *118*, 3447.

[136] A. Devižis, A. Gelzinis, J. Chmeliov, M. Diethelm, L. Endriukaitis, D. Padula, R. Hany, *Adv. Funct. Mater.* **2021**, *31*, 2102000.

[137] M. Makha, P. Schwaller, K. Strassel, S. B. Anantharaman, F. Nüesch, R. Hany, J. Heier, *Sci. Technol. Adv. Mater.* **2018**, *19*, 669.

[138] D. Gesevičius, A. Neels, S. Jenatsch, E. Hack, L. Viani, S. Athanasopoulos, F. Nüesch, J. Heier, *Adv. Sci.* **2018**, *5*, 1700496.

[139] D. Gesevičius, A. Neels, L. Duchêne, E. Hack, J. Heier, F. Nüesch, *J. Mater. Chem. C* **2019**, *7*, 414.

[140] L. Wang, S. Jenatsch, B. Ruhstaller, C. Hinderling, D. Gesevičius, R. Hany, F. Nüesch, *Adv. Funct. Mater.* **2018**, *28*, 1705724.

[141] D. Gesevičius, A. Neels, S. Yakunin, E. Hack, M. V. Kovalenko, F. Nüesch, J. Heier, *ChemPhysChem* **2018**, *19*, 3356.

[142] H. Zhang, B. Niesen, E. Hack, S. Jenatsch, L. Wang, A. C. Véron, M. Makha, R. Schneider, Y. Arroyo, R. Hany, F. Nüesch, *Org. Electron.* **2016**, *30*, 191.

[143] D. Broadwater, M. Bates, M. Jayaram, M. Young, J. He, A. L. Raithel, T. W. Hamann, W. Zhang, B. Borhan, R. R. Lunt, S. Y. Lunt, *Sci. Rep.* **2019**, *9*, 15288.

[144] D. Broadwater, H. C. D. Medeiros, R. R. Lunt, S. Y. Lunt, *Annu. Rev. Biomed. Eng.* **2021**, *23*, 29.

[145] Y. Zhao, A. M. Nardes, K. Zhu, *J. Phys. Chem. Lett.* **2014**, *5*, 490.

[146] A. T. Marin, D. Muñoz-Rojas, D. C. Iza, T. Gershon, K. P. Musselman, J. L. MacManus-Driscoll, *Adv. Funct. Mater.* **2013**, *23*, 3413.

[147] F. Moscatelli, A. Scorzoni, A. Poggi, M. Bruzzi, S. Lagomarsino, S. Mersi, S. Sciortino, R. Nipoti, *Nucl. Instrum. Methods Phys. Res. Sect. Accel. Spectrometers Detect. Assoc. Equip.* **2005**, *546*, 218.

[148] Y. Terao, H. Sasabe, C. Adachi, *Appl. Phys. Lett.* **2007**, *90*, 103515.

[149] Z. Li, P. Zhao, S. Tofighi, R. Sharma, T. R. Ensley, S. H. Jang, D. J. Hagan, E. W. Van Stryland, A. K.-Y. Jen, *J. Phys. Chem. C* **2016**, *120*, 15378.

[150] A. Roth, C. Schierl, A. Ferrer-Ruiz, M. Minameyer, L. Rodríguez-Pérez, C. Villegas, M. Á. Herranz, N. Martín, D. M. Guldi, *Chem* **2017**, *3*, 164.

[151] L. Rodríguez-Pérez, C. Villegas, M. Á. Herranz, J. L. Delgado, N. Martín, *ACS Omega* **2017**, *2*, 9164.

[152] C. Villegas, E. Krokos, P.-A. Bouit, J. Luis Delgado, D. M. Guldi, N. Martín, *Energy Environ. Sci.* **2011**, *4*, 679.

[153] Q. Liu, L. G. Gerling, F. Bernal-Texca, J. Toudert, T. Li, X. Zhan, J. Martorell, *Adv. Energy Mater.* **2020**, *10*, 1904196.

[154] J. Lee, H. Cha, H. Yao, J. Hou, Y. H. Suh, S. Jeong, K. Lee, J. R. Durrant, *ACS Appl. Mater. Interfaces* **2020**, *12*, 32764.

[155] L. Zuo, X. Shi, W. Fu, A. K. Y. Jen, *Adv. Mater.* **2019**, *31*, 1901683.

[156] Y. Liu, P. Cheng, T. Li, R. Wang, Y. Li, S. Y. Chang, Y. Zhu, H. W. Cheng, K. H. Wei, X. Zhan, B. Sun, Y. Yang, *ACS Nano* **2019**, *13*, 1071.

[157] Y. Li, J. D. Lin, X. Che, Y. Qu, F. Liu, L. S. Liao, S. R. Forrest, *J. Am. Chem. Soc.* **2017**, *139*, 17114.

[158] X. Liu, Z. Zhong, R. Zhu, J. Yu, G. Li, *Joule* **2022**, *6*, 1918.

[159] R. Sun, Q. Wu, J. Guo, T. Wang, Y. Wu, B. Qiu, Z. Luo, W. Yang, Z. Hu, J. Guo, M. Shi, C. Yang, F. Huang, Y. Li, J. Min, *Joule* **2020**, *4*, 407.

[160] Y. Cui, S. Zhang, N. Liang, J. Kong, C. Yang, H. Yao, L. Ma, J. Hou, *Adv. Mater.* **2018**, *30*, 1802499.

[161] K. Weng, L. Ye, L. Zhu, J. Xu, J. Zhou, X. Feng, G. Lu, S. Tan, F. Liu, Y. Sun, *Nat. Commun.* **2020**, *11*, 2855.

[162] Y. Song, K. Zhang, S. Dong, R. Xia, F. Huang, Y. Cao, *ACS Appl. Mater. Interfaces* **2020**, *12*, 18473.

[163] C. Xu, K. Jin, Z. Xiao, Z. Zhao, Y. Yan, X. Zhu, X. Li, Z. Zhou, S. Y. Jeong, L. Ding, H. Y. Woo, G. Yuan, F. Zhang, *Sol. RRL* **2022**, *6*, 2200308.

[164] H. Fu, W. Gao, Y. Li, F. Lin, X. Wu, J. H. Son, J. Luo, H. Y. Woo, Z. Zhu, A. K. Y. Jen, *Small Methods* **2020**, *4*, 2000687.

[165] W. Xu, X. Li, S. Y. Jeong, J. H. Son, Z. Zhou, Q. Jiang, H. Y. Woo, Q. Wu, X. Zhu, X. Ma, F. Zhang, *J. Mater. Chem. C* **2022**, *10*, 5489.

[166] X. Li, L. Cao, X. Yu, X. Du, H. Lin, G. Yang, Z. Chen, C. Zheng, S. Tao, *Sol. RRL* **2022**, *6*, 2200076.

[167] Y. Wang, Q. Zhu, H. B. Naveed, H. Zhao, K. Zhou, W. Ma, *Adv. Energy Mater.* **2020**, *10*, 1903609.

[168] S. Karuthedath, Y. Firdaus, A. D. Scaccabarozzi, M. I. Nugraha, S. Alam, T. D. Anthopoulos, F. Laquai, *Small Struct.* **2022**, *3*, 2100199.

[169] B. P. Rand, D. P. Burk, S. R. Forrest, *Phys. Rev. B* **2007**, *75*, 115327.

[170] A. Foertig, J. Rauh, V. Dyakonov, C. Deibel, *Phys. Rev. B* **2012**, *86*, 115302.

[171] T. H. Lee, S. Y. Park, W. W. Park, X. Du, J. H. Son, N. Li, O. H. Kwon, H. Y. Woo, C. J. Brabec, J. Y. Kim, *ACS Energy Lett.* **2020**, *5*, 1628.

[172] Y. Wei, J. Yu, L. Qin, H. Chen, X. Wu, Z. Wei, X. Zhang, Z. Xiao, L. Ding, F. Gao, H. Huang, *Energy Environ. Sci.* **2021**, *14*, 2314.

[173] Y. Firdaus, V. M. Le Corre, S. Karuthedath, W. Liu, A. Markina, W. Huang, S. Chattopadhyay, M. M. Nahid, M. I. Nugraha, Y. Lin, A. Seitkhan, A. Basu, W. Zhang, I. McCulloch, H. Ade, J. Labram, F. Laquai, D. Andrienko, L. J. A. Koster, T. D. Anthopoulos, *Nat. Commun.* **2020**, *11*, 5220.

[174] X. Wang, L. Zhang, L. Hu, Z. Xie, H. Mao, L. Tan, Y. Zhang, Y. Chen, *Adv. Funct. Mater.* **2021**, *31*, 2102291.

[175] P. Xue, S. Dai, T. K. Lau, J. Yu, J. Zhou, Y. Xiao, K. Meng, Z. Xie, G. Lu, X. Lu, R. P. S. Han, X. Zhan, *Sol. RRL* **2020**, *4*, 2000115.

[176] L. J. A. Koster, V. D. Mihailetchi, R. Ramaker, P. W. M. Blom, *Appl. Phys. Lett.* **2005**, *86*, 123509.

[177] X. Huang, L. Zhang, Y. Cheng, J. Oh, C. Li, B. Huang, L. Zhao, J. Deng, Y. Zhang, Z. Liu, F. Wu, X. Hu, C. Yang, L. Chen, Y. Chen, *Adv. Funct. Mater.* **2022**, *32*, 2108634.

[178] Y. Chang, X. Zhu, L. Zhu, Y. Wang, C. Yang, X. Gu, Y. Zhang, J. Zhang, K. Lu, X. Sun, Z. Wei, *Nano Energy* **2021**, *86*, 106098.

[179] D. H. Lim, J. W. Ha, H. Choi, S. C. Yoon, B. R. Lee, S. J. Ko, *Nanoscale Adv.* **2021**, *3*, 4306.

[180] Y. Sun, J. H. Seo, C. J. Takacs, J. Seifter, A. J. Heeger, *Adv. Mater.* **2011**, *23*, 1679.

[181] K. S. Novoselov, A. K. Geim, S. V. Morozov, D. Jiang, M. I. Katsnelson, I. V. Grigorieva, S. V. Dubonos, A. A. Firsov, *Nature* **2005**, *438*, 197.

[182] C. Lee, X. Wei, J. W. Kysar, J. Hone, *Science* **2008**, *321*, 385.

[183] K. Cao, S. Feng, Y. Han, L. Gao, T. Hue Ly, Z. Xu, Y. Lu, *Nat. Commun.* **2020**, *11*, 284.

[184] X. Wang, L. Zhi, K. Müllen, *Nano Lett.* **2008**, *8*, 323.

[185] J. Wu, H. A. Becerril, Z. Bao, Z. Liu, Y. Chen, P. Peumans, *Appl. Phys. Lett.* **2008**, *92*, 263302.

[186] S. S. Li, K. H. Tu, C. C. Lin, C. W. Chen, M. Chhowalla, *ACS Nano* **2010**, *4*, 3169.

[187] Y. Wang, S. W. Tong, X. F. Xu, B. Özyilmaz, K. P. Loh, *Adv. Mater.* **2011**, *23*, 1514.

[188] P. You, Z. Liu, Q. Tai, S. Liu, F. Yan, *Adv. Mater. Deerfield Beach Fla* **2015**, *27*, 3632.

[189] Wenlong Yang, A. Lucotti, M. Tommasini, W. A. Chalifoux, *J. Am. Chem. Soc.* **2016**, *138*, 9137.

[190] J. A. Velten, J. Carretero-González, E. Castillo-Martínez, J. Bykova, A. Cook, R. Baughman, A. Zakhidov, *J. Phys. Chem. C* **2011**, *115*, 25125.

[191] M. S. Arnold, J. D. Zimmerman, C. K. Renshaw, Xin Xu, R. R. Lunt, C. M. Austin, S. R. Forrest, *Nano Lett. Print* **2009**, *9*, 3354.

[192] D. J. Bindl, N. S. Safron, M. S. Arnold, *ACS Nano* **2010**, *4*, 5657.

[193] D. J. Bindl, M. Y. Wu, F. C. Prehn, M. S. Arnold, *Nano Lett. Print* **2011**, *11*, 455.

[194] R. M. Jain, R. Howden, K. Tvrdy, S. Shimizu, A. J. Hilmer, T. P. McNicholas, K. K. Gleason, M. S. Strano, *Adv. Mater. Deerfield Beach Fla* **2012**, *24*, 4436.

[195] M. J. Shea, M. S. Arnold, *Appl. Phys. Lett.* **2013**, *102*, 243101.

[196] D. V. Kosynkin, A. L. Higginbotham, A. Sinitskii, J. R. Lomeda, A. Dimiev, B. K. Price, J. M. Tour, *Nature* **2009**, *458*, 872.

[197] L. Jiao, L. Zhang, X. Wang, G. Diankov, H. Dai, *Nature* **2009**, *458*, 877.

[198] L. Jiao, X. Wang, G. Diankov, H. Wang, H. Dai, **2010**, *5*, 321.

[199] J. Carretero-González, E. Castillo-Martínez, M. Dias-Lima, D. M. Rogers, J. Sovich, C. S. Haines, X. Leprõ, M. Kozlov, A. Zhakidov, R. H. Baughman, M. Acik, Y. Chabal, *Adv. Mater.* **2012**, *24*, 5695.

[200] Q. F. Zheng, Y. Guo, Y. Liang, Q. Shen, *ACS Appl. Nano Mater.* **2020**, *3*, 4708.

[201] M. Liu, C. Zhang, W. W. Tjiu, Z. Yang, W. Wang, T. Liu, *Polymer* **2013**, *54*, 3124.

[202] M. Y. Han, B. Oezyilmaz, Y. Zhang, P. Kim, *Phys. Rev. Lett.* **2007**, *98*, 206805.

[203] R. M. Jacobberger, K. M. McElhinny, G. J. Brady, R. Rojas Delgado, S. Singha Roy, M. G. Lagally, P. G. Evans, M. S. Arnold, B. Kiraly, A. Mannix, N. P. Guisinger, M. C. Hersam, M. Fortin-Deschenes, P. Desjardins, P. L. Levesque, R. Martel, *Nat. Commun.* **2015**, *6*, 9006.

[204] X. Yang, X. Dou, A. Rouhanipour, L. Zhi, H. J. Räder, K. Müllen, *J. Am. Chem. Soc.* **2008**, *130*, 4216.

[205] J. Cai, P. Ruffieux, R. Jaafar, M. Bieri, T. Braun, S. Blankenburg, M. Muoth, A. P. Seitsonen, M. Saleh, X. Feng, K. Mullen, R. Fasel, *Nature* **2010**, *466*, 470.

[206] A. Narita, X. Feng, Y. Hernandez, S. A. Jensen, M. Bonn, H. Yang, I. A. Verzhbitskiy, C. Casiraghi, M. R. Hansen, A. H. R. Koch, G. Fytas, O. Ivasenko, B. Li, K. S. Mali, T. Balandina, S. Mahesh, S. De Feyter, K. Müllen, *Nat. Chem.* **2014**, *6*, 126.

[207] T. H. Vo, M. Shekhirev, M. D. Morton, E. Berglund, P. M. Wilson, A. Sinitskii, D. A. Kunkel, L. Kong, P. A. Dowben, A. Enders, *Nat. Commun.* **2014**, *5*, 4189.

[208] T. H. Vo, M. Shekhirev, A. Sinitskii, D. A. Kunkel, A. Enders, F. Orange, M. J. F. Guinel, *Chem. Commun.* **2014**, *50*, 4172.

[209] A. Kimouche, R. Drost, J. Sainio, P. Liljeroth, M. M. Ervasti, A. Harju, S. Halonen, P. M. Joensuu, *Nat. Commun.* **2015**, *6*, 10177.

[210] L. Talirz, P. Ruffieux, R. Fasel, *Adv. Mater.* **2016**, *28*, 6222.

[211] W. A. Chalifoux, *Angew. Chem. - Int. Ed.* **2017**, *56*, 8048.

[212] G. Li, K. Y. Yoon, J. Wang, G. Dong, X. Zhong, X. Y. Zhu, R. Zhang, J. R. Guest, J. Wen, *Nat. Commun.* **2018**, *9*, 1687.

[213] K. Sun, X. Li, H. Zhang, L. Chi, L. Chen, *J. Phys. Chem. C* **2020**, *124*, 11422.

[214] T. H. Vo, M. Shekhirev, A. Lipatov, A. Sinitskii, R. A. Korlacki, *Faraday Discuss.* **2014**, *173*, 105.

[215] M. Mehdi Pour, A. Lashkov, A. Radocea, X. Liu, T. Sun, A. Lipatov, R. Korlacki, M. Shekhirev, N. Aluru, J. Lyding, V. Sysoev, A. Sinitskii, *Nat Commun.* **2017**, *8*, 820.

[216] Y. C. Chen, T. Cao, C. Chen, Z. Pedramrazi, D. Haberer, D. G. de Oteyza, F. R. Fischer, S. G. Louie, M. F. Crommie, **2015**, *10*, 156.

[217] P. Bennett, Z. Pedramrazi, A. Madani, Y. Chen, D. De Oteyza, C. Chen, F. Fischer, M. Crommie, J. Bokor, **2013**, *103*, 253114.

[218] Y. Hata, T. Sawada, T. Serizawa, *ACS Appl. Bio Mater.* **2020**, *3*, 3210.

[219] S. Rostami, A. Mehdinia, A. Jabbari, *Mater. Sci. Eng. C* **2020**, *114*, 111034.

[220] F. Pan, Y. Gang, X. Xiang, Z. Du, Y. Li, B. Li, G. Wang, E. Sarnello, H. T. Nguyen, T. Li, Y. Fei, Y. H. Hu, P. Zhang, H. C. Zhou, *ACS Nano* **2020**, *14*, 5506.

[221] C. Rogers, W. S. Perkins, G. Veber, T. E. Williams, R. R. Cloke, F. R. Fischer, **2017**, *139*, 4052.

[222] L. Wang, H. Dong, Z. Guo, L. Zhang, T. Hou, Y. Li, *J. Phys. Chem. C* **2016**, *120*, 17427.

[223] L. Li, G. Ruan, Z. Peng, Y. Yang, H. Fei, A. R. O. Raji, E. L. G. Samuel, J. M. Tour, *ACS Appl. Mater. Interfaces* **2014**, *6*, 15033.

[224] J. Liu, Y. Xue, L. Dai, G. H. Kim, J. Y. Kim, J. B. Baek, M. Durstock, *Adv. Mater.* **2014**, *26*, 786.

[225] J. Kim, M. A. Mat Teridi, Abd. R. bin Mohd Yusoff, J. Jang, **2016**, *6*, 27773.

[226] E. Castro, E. L. Romero, L. Echegoyen, T. J Sisto, F. Liu, S. R. Peurifoy, J. Wang, X. Zhu, C. Nuckolls, *Angew. Chem. Int. Ed.* **2017**, *56*, 14648.

[227] X. Meng, X. Cui, M. Rager, S. Zhang, Z. Wang, J. Yu, Y. W. Harn, Z. Kang, B. K. Wagner, Y. Liu, C. Yu, J. Qiu, Z. Lin, *Nano Energy* **2018**, *52*, 123.

[228] A. R. Bin Mohd Yusoff, D. Kim, J. Jang, F. K. Schneider, W. J. Da Silva, *Energy Environ. Sci.* **2015**, *8*, 1523.

[229] C. Xie, B. Nie, T. Yan, Q. Li, P. Lv, F. Li, M. Wang, C. Wu, L. Wang, L. Luo, J. Jie, *Appl. Phys. Lett.* **2012**, *100*, 193103.

[230] R. Denk, M. Hohage, P. Zeppenfeld, J. Cai, C. A. Pignedoli, H. Söde, R. Fasel, P. Ruffieux, X. Feng, K. Müllen, S. Wang, D. Prezzi, A. Ferretti, A. Ruini, E. Molinari, *Nat. Commun.* **2014**, *5*, 4253.

[231] G. Soavi, S. D. Conte, C. Manzoni, D. Viola, A. Narita, Y. Hu, X. Feng, U. Hohenester, E. Molinari, D Prezzi, K. Müllen, G. Cerullo, *Nat. Commun.* **2016**, *7*, 11010.

[232] A. Tries, S. Osella, P. Zhang, F. Xu, M. Kläui, Y. Mai, D. Beljonne, H. I. Wang, **2019**, *20*, 2993.

[233] P. Sullivan, T. S. Jones, *Org. Electron.* **2008**, *9*, 656.

[234] S. Yoo, B. Domercq, B. Kippelen, *Appl. Phys. Lett.* **2004**, *85*, 5427.

[235] G. D. Nguyen, H. Z. Tsai, A. A. Omrani, M. Wu, D. J. Rizzo, G. F. Rodgers, F. Liou, A. S. Aikawa, S. G. Louie, M. F. Crommie, T. Marangoni, R. R. Cloke, R. A. Durr, F. R. Fischer, Y. Sakai, J. R. Chelikowsky, *Nat. Nanotechnol.* **2017**, *12*, 1077.

[236] T. J. Dougherty, C. J. Gomer, B. W. Henderson, G. Jori, D. Kessel, M. Korbelik, J. Moan, Q. Peng, *JNCI J. Natl. Cancer Inst.* **1998**, *90*, 889.

[237] H. Mojzisova, S. Bonneau, D. Brault, *Eur. Biophys. J.* **2007**, *36*, 943.

[238] B. C. Wilson, *Can. J. Gastroenterol.* **2002**, *16*, 393.

[239] B. Chance, *Ann. N. Y. Acad. Sci.* **1998**, *838*, 29.

[240] T. A. Henderson, L. D. Morries, *Neuropsychiatr. Dis. Treat.* **2015**, *11*, 2191.

[241] O. I. Kolenc, K. P. Quinn, *Antioxid. Redox Signal.* **2019**, *30*, 875.

[242] N. J. Patel, Y. Chen, P. Joshi, P. Pera, H. Baumann, J. R. Missert, K. Ohkubo, S. Fukuzumi,

R. R. Nani, M. J. Schnermann, P. Chen, J. Zhu, K. M. Kadish, R. K. Pandey, *Bioconjug. Chem.* **2016**, *27*, 667.

[243] J. V. Frangioni, *Curr. Opin. Chem. Biol.* **2003**, *7*, 626.

[244] A. L. Vahrmeijer, M. Hutteman, J. R. van der Vorst, C. J. H. van de Velde, J. V. Frangioni, *Nat. Rev. Clin. Oncol.* **2013**, *10*, 507.

[245] X. Tan, S. Luo, D. Wang, Y. Su, T. Cheng, C. Shi, *Biomaterials* **2012**, *33*, 2230.

[246] T. Shen, X. Xu, L. Guo, H. Tang, T. Diao, Z. Gan, G. Zhang, Q. Yu, *Biomacromolecules* **2017**, *18*, 217.

[247] B. Sui, G. Zhong, J. Sun, *Sci. Rep.* **2016**, *6*, 33443.

[248] L. Yuan, W. Lin, K. Zheng, L. He, W. Huang, *Chem. Soc. Rev.* **2012**, *42*, 622.

[249] L. Benov, *Med. Princ. Pract.* **2015**, *24*, 14.

[250] T. S. Wiedmann, A. Naqwi, *Asian J. Pharm. Sci.* **2016**, *11*, 722.

[251] V. N. Kilin, H. Anton, N. Anton, E. Steed, J. Vermot, T. F. Vandamme, Y. Mely, A. S. Klymchenko, *Biomaterials* **2014**, *35*, 4950.

[252] I. Shulov, Y. Arntz, Y. Mély, V. G. Pivovarenko, A. S. Klymchenko, *Chem. Commun.* **2016**, *52*, 7962.

[253] A. Reisch, P. Didier, L. Richert, S. Oncul, Y. Arntz, Y. Mély, A. S. Klymchenko, *Nat. Commun.* **2014**, *5*, 4089.

[254] I. Shulov, S. Oncul, A. Reisch, Y. Arntz, M. Collot, Y. Mely, A. S. Klymchenko, *Nanoscale* **2015**, *7*, 18198.

[255] P. K. S. Magut, S. Das, V. E. Fernand, J. Losso, K. McDonough, B. M. Naylor, S. Aggarwal, I. M. Warner, *J. Am. Chem. Soc.* **2013**, *135*, 15873.

[256] N. Siraj, P. E. Kolic, B. P. Regmi, I. M. Warner, *Chem. Eur. J.* **2015**, *21*, 14440.

[257] X. Yang, C. Shi, R. Tong, W. Qian, H. E. Zhau, R. Wang, G. Zhu, J. Cheng, V. W. Yang, T. Cheng, M. Henary, L. Strekowski, L. W. K. Chung, *Clin. Cancer Res.* **2010**, *16*, 2833.

[258] Y. Wang, T. Liu, E. Zhang, S. Luo, X. Tan, C. Shi, *Biomaterials* **2014**, *35*, 4116.

[259] C. Shi, J. B. Wu, D. Pan, *J. Biomed. Opt.* **2016**, *21*, 050901.

[260] J. B. Wu, C. Shao, X. Li, C. Shi, Q. Li, P. Hu, Y. T. Chen, X. Dou, D. Sahu, W. Li, H. Harada, Y. Zhang, R. Wang, H. E. Zhau, L. W. K. Chung, *Biomaterials* **2014**, *35*, 8175.

[261] S. P. Wu, I. Lee, P. P. Ghoroghchian, P. R. Frail, G. Zheng, J. D. Glickson, M. J. Therien,

Bioconjug. Chem. **2005**, *16*, 542.

[262] M. Garcia-Diaz, Y. Y. Huang, M. R. Hamblin, *Methods* **2016**, *109*, 158.

[263] C. Zhang, Y. Zhao, H. Zhang, X. Chen, N. Zhao, D. Tan, H. Zhang, C. Shi, *Int. J. Mol. Sci.* **2017**, *18*, 1332.

[264] X. Dang, L. Gu, J. Qi, S. Correa, G. Zhang, A. M. Belcher, P. T. Hammond, *Proc. Natl. Acad. Sci.* **2016**, *113*, 5179.

[265] J. Ge, Q. Jia, W. Liu, M. Lan, B. Zhou, L. Guo, H. Zhou, H. Zhang, Y. Wang, Y. Gu, X. Meng, P. Wang, *Adv. Healthc. Mater.* **2016**, *5*, 665.

[266] A. A. Burns, J. Vider, H. Ow, E. Herz, O. Penate-Medina, M. Baumgart, S. M. Larson, U. Wiesner, M. Bradbury, *Nano Lett.* **2009**, *9*, 442.

[267] E. Phillips, O. Penate-Medina, P. B. Zanzonico, R. D. Carvajal, P. Mohan, Y. Ye, J. Humm, M. Gönen, H. Kalaigian, H. Schöder, H. W. Strauss, S. M. Larson, U. Wiesner, M. S. Bradbury, *Sci. Transl. Med.* **2014**, *6*, 260149.

[268] Q. Chen, C. Wang, L. Cheng, W. He, Z. Cheng, Z. Liu, *Biomaterials* **2014**, *35*, 2915.

[269] A. Mikolajczyk, A. Gajewicz, B. Rasulev, N. Schaeublin, E. Maurer-Gardner, S. Hussain, J. Leszczynski, T. Puzyn, *Chem. Mater.* **2015**, *27*, 2400.

[270] S. Zhang, J. Li, G. Lykotrafitis, G. Bao, S. Suresh, *Adv. Mater.* **2009**, *21*, 419.

[271] J. Gao, B. A. Aksoy, U. Dogrusoz, G. Dresdner, B. Gross, S. O. Sumer, Y. Sun, A. Jacobsen, R. Sinha, E. Larsson, E. Cerami, C. Sander, N. Schultz, *Sci. Signal.* **2013**, *6*, 11.

[272] E. Cerami, J. Gao, U. Dogrusoz, B. E. Gross, S. O. Sumer, B. A. Aksoy, A. Jacobsen, C. J. Byrne, M. L. Heuer, E. Larsson, Y. Antipin, B. Reva, A. P. Goldberg, C. Sander, N. Schultz, *Cancer Discov.* **2012**, *2*, 401.

[273] M. Redza-Dutordoir, D. A. Averill-Bates, *Biochim. Biophys. Acta BBA - Mol. Cell Res.* **2016**, *1863*, 2977.

[274] D. Y. Gui, L. B. Sullivan, A. Luengo, A. M. Hosios, L. N. Bush, N. Gitego, S. M. Davidson, E. Freinkman, C. J. Thomas, M. G. Vander Heiden, *Cell Metab.* **2016**, *24*, 716.

[275] J. Schindelin, I. Arganda-Carreras, E. Frise, V. Kaynig, M. Longair, T. Pietzsch, S. Preibisch, C. Rueden, S. Saalfeld, B. Schmid, J. Y. Tinevez, D. J. White, V. Hartenstein, K. Eliceiri, P. Tomancak, A. Cardona, *Nat. Methods* **2012**, *9*, 676.

[276] E. R. Andrechek, R. D. Cardiff, J. T. Chang, M. L. Gatza, C. R. Acharya, A. Potti, J. R. Nevins, *Proc. Natl. Acad. Sci.* **2009**, *106*, 16387.

[277] C. H. Lee, K. W. Kim, S. M. Lee, S. Y. Kim, *Int. J. Mol. Sci.* **2021**, *22*, 113.

[278] S. Wäldchen, J. Lehmann, T. Klein, S. van de Linde, M. Sauer, *Sci. Rep.* **2015**, *5*, 15348.

[279] S. M. Usama, S. Thavornpradit, K. Burgess, *ACS Appl. Bio Mater.* **2018**, *1*, 1195.

[280] J. Wu, D. Pan, L. W. K. Chung, *Transl. Androl. Urol.* **2013**, *2*, 25464.

[281] P. Bhattarai, Z. Dai, *Adv. Healthcare Mater.* **2017**, *6*, 1700262.

[282] E. L. Jewell, J. J. Huang, N. R. Abu-Rustum, G. J. Gardner, C. L. Brown, Y. Sonoda, R. R. Barakat, D. A. Levine, M. M. Leitao, *Gynecol. Oncol.* **2014**, *133*, 274.

[283] M. Hope-Ross, L. A. Yannuzzi, E. S. Gragoudas, D. R. Guyer, J. S. Slakter, J. A. Sorenson, S. Krupsky, D. A. Orlock, C. A. Puliafito, *Ophthalmology* **1994**, *101*, 529.

[284] H. Wang, X. Li, B. W. C. Tse, H. Yang, C. A. Thorling, Y. Liu, M. Touraud, J. B. Chouane, X. Liu, M. S. Roberts, X. Liang, *Theranostics* **2018**, *8*, 1227.

[285] C. H. J. Choi, C. A. Alabi, P. Webster, M. E. Davis, *Proc. Natl. Acad. Sci.* **2010**, *107*, 1235.

[286] J. Bolleddula, A. Shah, M. Shadid, A. Kamali, M. D. Smith, S. K. Chowdhury, *Drug Metab. Dispos.* **2020**, *48*, 1239.

[287] D. K. Shah, N. Haddish-Berhane, A. Betts, *J. Pharmacokinet. Pharmacodyn.* **2012**, *39*, 643.

[288] S. Khoee, A. Sadeghi, *RSC Adv.* **2019**, *9*, 39780.

[289] T. J. Dougherty, M. T. Cooper, T. S. Mang, *Lasers Surg. Med.* **1990**, *10*, 485.

[290] S. S. Yom, T. M. Busch, J. S. Friedberg, E. P. Wileyto, D. Smith, E. Glatstein, S. M. Hahn, *Photochem. Photobiol.* **2003**, *78*, 75.

[291] R. Ghanbarinia Firozjah, A. Sadeghi, S. Khoee, *ACS Omega* **2020**, *5*, 27119.

[292] E. Cooper, P. J. Choi, W. A. Denny, J. Jose, M. Dragunow, T. I. H. Park, *Front. Oncol.* **2021**, *11*.

[293] C. Shi, J. B. Wu, G. C.-Y. Chu, Q. Li, R. Wang, C. Zhang, Y. Zhang, H. L. Kim, J. Wang, H. E. Zhau, D. Pan, L. W. K. Chung, *Oncotarget* **2014**, *5*, 10114.

[294] B. Hagenbuch, B. Stieger, *Mol. Aspects Med.* **2013**, *34*, 396.

[295] R. R. Schulte, R. H. Ho, *Mol. Pharm.*, **2019**, *5*, 490.

[296] Y. Guan, Y. Zhang, J. Zou, L. P. Huang, M. D. Chordia, W. Yue, J. J. Wu, D. F. Pan, *Molecules* **2019**, *24*, 4120.

[297] A. M. Merlot, D. S. Kalinowski, D. R. Richardson, *Front. Physiol.* **2014**, *5*, 12.

[298] S. M. Davidson, O. Jonas, M. A. Keibler, H. W. Hou, A. Luengo, J. R. Mayers, J. Wyckoff, A. M. Del Rosario, M. Whitman, C. R. Chin, K. J. Condon, A. Lammers, K. A. Kellersberger, B. K. Stall, G. Stephanopoulos, D. Bar-Sagi, J. Han, J. D. Rabinowitz, M. J. Cima, R. Langer, M. G. Vander Heiden, *Nat. Med.* **2017**, *23*, 235.

[299] S. M. Usama, G. K. Park, S. Nomura, Y. Baek, H. S. Choi, K. Burgess, *Bioconjug. Chem.* **2020**, *31*, 248.

[300] Y. Matsumura, H. Maeda, *Cancer Res.* **1986**, *46*, 6387.

[301] X. Han, X. Xu, Y. Tang, F. Zhu, Y. Tian, W. Liu, D. He, G. Lu, Y. Gu, S. Wang, *Front. Mol. Biosci.* **2020**, *7*, 610084.

[302] E. Miele, G. P. Spinelli, E. Miele, F. Tomao, S. Tomao, *Int. J. Nanomedicine* **2009**, *4*, 99.

[303] X. Fang Pei, M. S. Noble, M. Antonietta Davoli, E. Rosfjord, M. T. Tilli, P. A. Furth, R. Russell, M. D. Johnson, R. B. Dickson, *Vitro Cell. Dev. Biol. Anim.* **2004**, *40*, 14.

[304] C. Ross, K. Szczepanek, M. Lee, H. Yang, C. J. Peer, J. Kindrick, P. Shankarappa, Z.-W. Lin, J. D. Sanford, W. D. Figg, K. W. Hunter, *Mol. Cancer Res.* **2020**, *18*, 1278.

[305] F. Faraji, Y. Pang, R. C. Walker, R. N. Borges, L. Yang, K. W. Hunter, *PLOS Genet.* **2012**, *8*, e1002926.

[306] C. Donohoe, M. O. Senge, L. G. Arnaut, L. C. Gomes-da-Silva, *Biochim. Biophys. Acta BBA - Rev. Cancer* **2019**, *1872*, 188308.

[307] Y. Yang, H. H. Yang, Y. Hu, P. H. Watson, H. Liu, T. R. Geiger, M. R. Anver, D. C. Haines, P. Martin, J. E. Green, M. P. Lee, K. W. Hunter, L. M. Wakefield, *Oncotarget* **2017**, *8*, 30621.

[308] A. A. Abdul Pari, M. Singhal, H. G. Augustin, *J. Exp. Med.* **2020**, *218*, e20190218.

[309] J. Chen, Y. Wang, Y. Fang, Z. Jiang, A. Wang, A. Wang, J. Xue, *Biomed. Opt. Express* **2020**, *11*, 3900.

[310] I. L. Csanaky, H. Lu, Y. Zhang, K. Ogura, S. Choudhuri, C. D. Klaassen, *Hepatology* **2011**, *53*, 272.

[311] N. Desai, V. Trieu, B. Damascelli, P. Soon-Shiong, *Transl. Oncol.* **2009**, *2*, 59.

[312] N. Ghinea, *Diseases* **2021**, *9*, 28.

[313] N. Zhao, C. Zhang, Y. Zhao, B. Bai, J. An, H. Zhang, J. B. Wu, C. Shi, *Oncotarget* **2016**, *7*, 57277.

[314] S. Zhang, K. Ma, Y. Liu, X. Pan, Q. Chen, L. Qi, S. Li, *J. Cardiovasc. Pharmacol.* **2016**, *67*, 68.

[315] M. T. Larsen, M. Kuhlmann, M. L. Hvam, K. A. Howard, *Mol. Cell. Ther.* **2016**, *4*, 3.

[316] Z. S. Silva Jr, S. K. Bussadori, K. P. S. Fernandes, Y. Y. Huang, M. R. Hamblin, *Biosci. Rep.* **2015**, *35*, e00265.

[317] S. Branford, Z. Rudzki, S. Walsh, I. Parkinson, A. Grigg, J. Szer, K. Taylor, R. Herrmann, J. F. Seymour, C. Arthur, D. Joske, K. Lynch, T. Hughes, *Blood* **2003**, *102*, 276.

[318] S. Venkatesan, C. Swanton, B. S. Taylor, J. F. Costello, *Cold Spring Harb. Perspect. Med.* **2017**, *7*, a026617.

[319] R. Stuart-Harris, C. Caldas, S. E. Pinder, P. Pharoah, *The Breast* **2008**, *17*, 323.

[320] E. de Azambuja, F. Cardoso, G. de Castro, M. Colozza, M. S. Mano, V. Durbecq, C. Sotiriou, D. Larsimont, M. J. Piccart-Gebhart, M. Paesmans, *Br. J. Cancer* **2007**, *96*, 1504.

[321] M. Yang, D. J. Antoine, J. L. Weemhoff, R. E. Jenkins, A. Farhood, B. K. Park, H. Jaeschke, *Liver Transpl.* **2014**, *20*, 1372.

[322] Y. P. Sher, M. C. Hung, *Bio-Protoc.* **2013**, *3*, e931.

[323] P. Harrod-Kim, *J. Vasc. Interv. Radiol.* **2006**, *17*, 1441.

[324] T. Suzuki, M. Tanaka, M. Sasaki, H. Ichikawa, H. Nishie, H. Kataoka, *Cancers* **2020**, *12*, 2369.

[325] A. D. Garg, D. V. Krysko, P. Vandenabeele, P. Agostinis, *Photochem. Photobiol. Sci.* **2011**, *10*, 670.

[326] Y. Yang, Y. Hu, H. Wang, *Oxid. Med. Cell. Longev.* **2016**, *2016*, e5274084.

[327] K. Alam, T. Farasyn, K. Ding, W. Yue, *Drug Metab. Lett.* **2018**, *12*, 24.

[328] Q. Chen, L. Feng, J. Liu, W. Zhu, Z. Dong, Y. Wu, Z. Liu, *Adv. Mater.* **2016**, *28*, 7129.

[329] Q. Zhang, L. Li, *J. BUON* **2018**, *23*, 561.

[330] G. L. Zhang, Y. Zhang, K. X. Cao, X. M. Wang, *JoVE J. Vis. Exp.* **2019**, e58604.

[331] S. T. Teoh, M. P. Ogrodzinski, C. Ross, K. W. Hunter, S. Y. Lunt, *Front. Oncol.* **2018**, *8*.

Appendix – Photon balance checks for TPVs

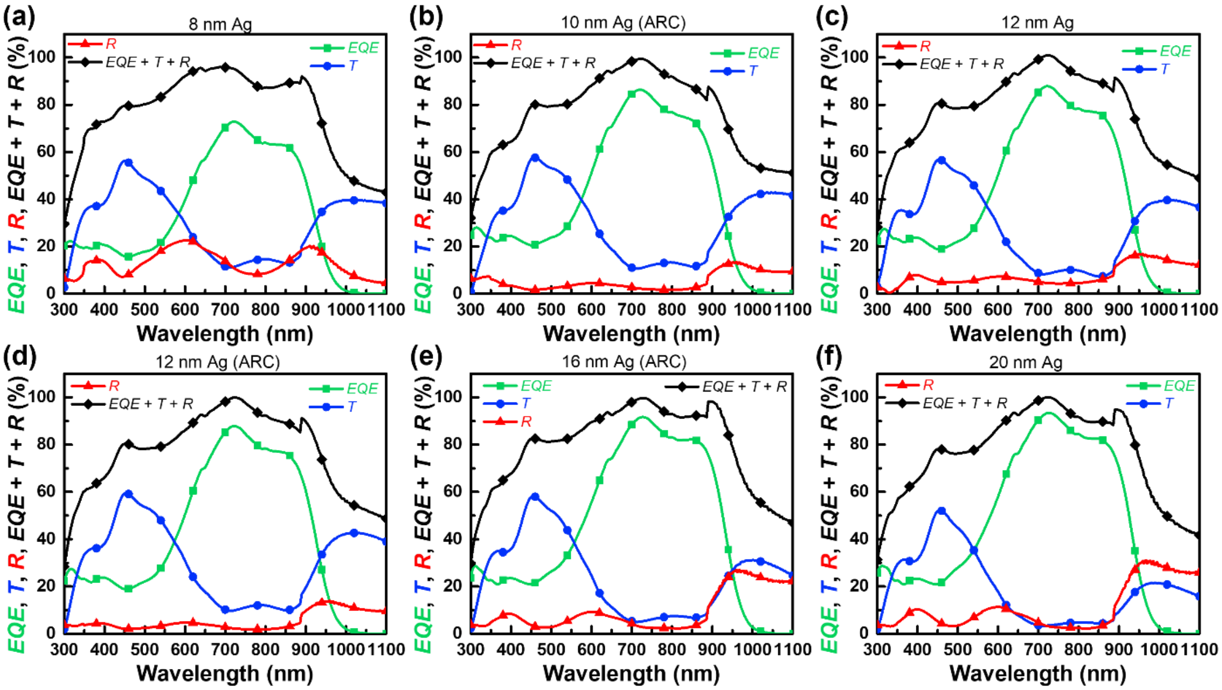

Figure A.1. Photon balances for Ag thickness dependent TPVs. External quantum efficiency (*EQE*), transmission (*T*), reflection (*R*), and the photon balance (*EQE* + *T* + *R*) data for devices with different Ag thickness.

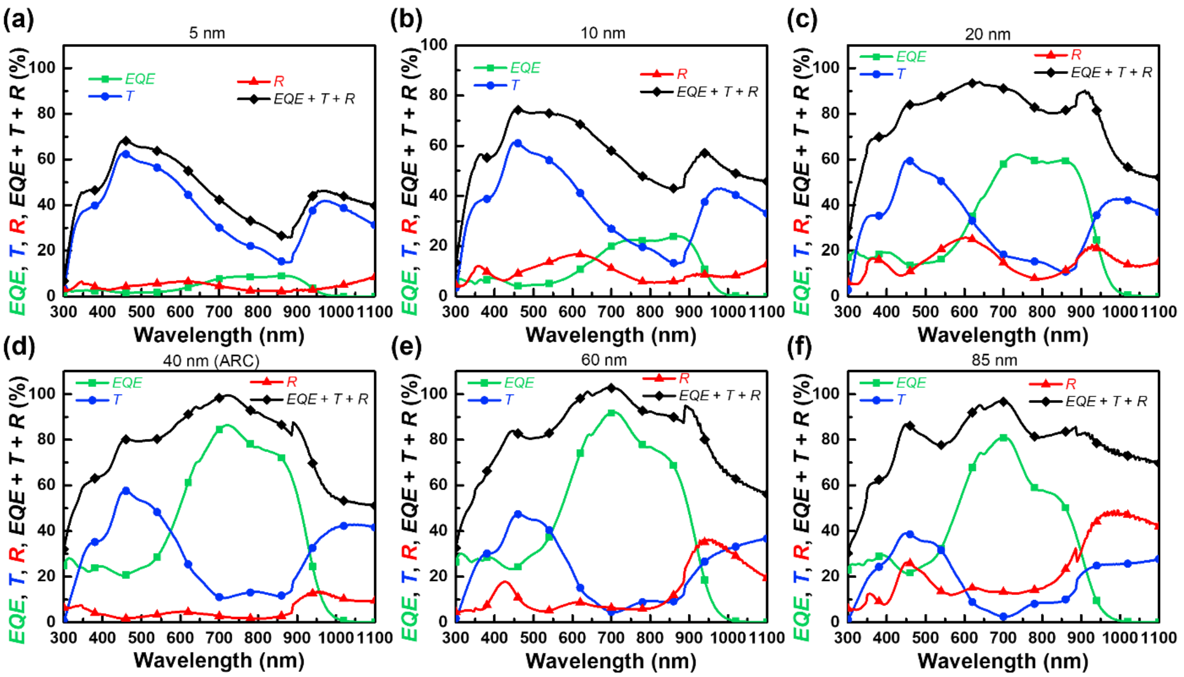

Figure A.2. Photon balances for PTB7-Th thickness dependent TPVs. External quantum efficiency (*EQE*), transmission (*T(%)*), reflection (*R(%)*), and the photon balance (*EQE* + *T(%)* + *R(%)*) data for devices with different PTB7-Th thickness.

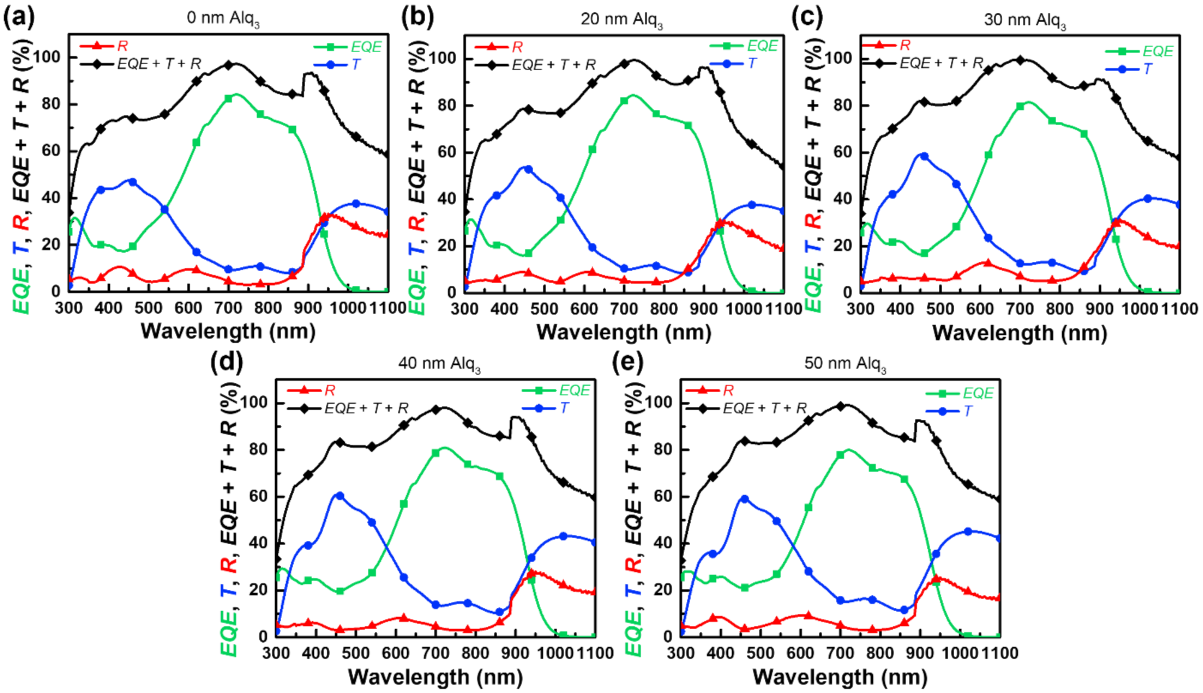

Figure A.3. Photon balances for Alq$_3$ thickness dependent TPVs. External quantum efficiency (*EQE*), transmission (*T*), reflection (*R*), and the photon balance (*EQE* + *T* + *R*) data for devices with different Alq$_3$ thickness and an antireflection coating on the glass side of the device.